Numerical Studies of Propagation of L_g Waves across Ocean Continent Boundaries Using the Representation Theorem

Thesis by
Janice Regan

In Partial Fulfillment of the Requirements
for the Degree of
Doctor of Philosophy

California Institute of Technology
Pasadena, California

1987

(submitted February 10, 1987)

Acknowledgements

Many thanks to my thesis advisor, David G. Harkrider, for guidance, support, and encouragement. Thanks, also to the students, faculty, and staff of the Seismo. Lab. for their friendship and encouragement.

Abstract

The methods for Representation Theorem (RT) coupling of finite element (FE) or finite difference calculations and Harkrider's (Harkrider 1964, 1970) propagator matrix method calculations to produce a hybrid method for propagation of SH mode sum seismograms across paths that contain regions of non plane-layered structure are explained and developed. The coupling methods explained in detail use a 2-D Cartesian FE formulation. Analogous methods for the 3-D method follow directly. Extensive tests illustrating the validity and accuracy of the implementation of these coupling methods are discussed. These hybrid techniques are developed to study the propagation of surface waves across regional transition zones or other heterogeneities that exist in part of a longer, mostly plane-layered, path. The effects of a thinning or thickening of the crustal layer on the propagation of L_g mode sum seismograms have been examined in this study. The thinning or thickening of the crustal layer is used as a simple model of ocean continent transitions. The L_g phase is of particular interest since it is used in several important applications such as mapping the extent of continental crust, magnitude determination, and discrimination between explosive and earthquake sources. The understanding of the observations that L_g wave is attenuated completely when the propagation path includes an oceanic portion of length greater than one hundred to two hundred kilometers or a region of complex crustal structure is not complete, and a clear explanation of these phenomena could have important consequences for all these types of studies. The transition model calculations done in this study show that passage through a region of thinning crustal thickness, the model for a continent to ocean transition, increases the amplitude and coda length of the L_g wave at the surface, and allows much of the modal energy

trapped in the crust, which forms the L_g phase, to escape into the subcrustal layers as body waves or other downgoing phases. The magnitude of both these effects increases as the length of the transition increases or the slope of the layer boundaries decrease. The passage of the wavefront exiting the continent to ocean transition region through the oceanic structure allows further energy to escape from the crustal layer, and produces a decrease in L_g amplitude at the surface as the length of the oceanic path increases. The amplitude decrease is maximum near the transition region and decreases with distance from it. Passage through a region of thickening crust, the model of a ocean to continent transition, causes a rapid decrease in the L_g amplitude at the surface of the crust. The energy previously trapped in the oceanic crustal layer spreads throughout the thickening crustal layer, and any amplitude which has been traveling through the subcrustal layer but has not reached depths below the base of the continental crust is transmitted back into the continental crust. The attenuation of L_g at the crustal surface along a partially oceanic path occurs in the oceanic structure and in the ocean to continent transition region. The attenuation at the surface depends in part on the escape of energy at depth through the continent to ocean transition region into the underlaying half-space. The total attenuation of Lg due to propagation through a forward transition followed by a reverse transition is at most a factor of four to six. This is inadequate to explain the observed attenuation of Lg. Thus, additional effects, other than geometry must be considered to provide a complete explanation of the attenuation of Lg.

Table of Contents

Introduction

This thesis presents a study of the propagation of L_g waves across ocean continent transition regions. The transition regions are represented by a simplified model consisting of a crustal layer with thickness that increases or decreases smoothly between oceanic and continental values. The distance over which this smooth variation occurs is referred to as the length of the transition region. The changes to a L_g wavefield, when it travels through one of these simple transition regions, are modeled using a hybrid method which is explained and developed in sections four, five, and six of chapter one. The hybrid method combines the Finite Element method and the Propagator Matrix technique through application of the Seismic Representation Theorem. These two methods are explained and the notation associated with them is defined in section two and three of chapter one. In the regions of complex structure, those regions containing the transition regions, the Finite Element method is used to transmit the L_g waves. In the regions of plane layered structure either the Propagator Matrix technique is used to directly determine the seismograms for a source in the layers being considered, or it is used to determine the Green's functions for propagation from the interface between the complex region and the layered region to the receiver. In the first case, displacement time histories are determined at a set of points equally spaced in depth along a vertical plane. These time histories are used as boundary conditions for the Finite Element method. Extensive tests of the accuracy of producing a Finite Element wavefield by specifying the displacements as a function of time along the vertical plane defining the Finite Element grid edge are presented in sections seven and eight of chapter one. The results of these tests are useful in understanding the sources of uncertainty due to truncation of the vertical plane at some depth less than infinity. In the case where the propagator method is used to determine Green's functions the Green's functions are combined with the stress and displacement time histories recorded at the boundary between the plane layered region

and the complex region according to the Representation Theorem. Tests of the validity and accuracy of this method of coupling are discussed in section two of chapter three. The results of the study on the effects of transition length on the propagation of L_g waves are reported, discussed and interpreted in chapter two. The results of the study of the effects of the length of the intermediate oceanic path on the propagation of L_g are mentioned in chapter two and again in the first and last sections of chapter three. In order to understand why the models used were chosen for this study, and why this study is important, it is useful to discuss and review the the different types of studies that use L_g data. In the remainder of this section the background of the problem will be discussed.

In order to choose a reasonable form for a simple model of a ocean continent or continent ocean transition region it is useful to examine existing observations of such regions. Structures of transition regions have been studied using many techniques, both geological and geophysical. These techniques include reflection and refraction seismic surveys, gravity studies, and geologic mapping and interpretation. Many such studies have been completed so only a few examples will be cited here to support the choice of the model structure used. A review of studies of the continental margins of the eastern and western coasts of Canada by Keen and Hyndman (1979) shows sample sections of the transition regions along the passive margins of the eastern coast. The transition lengths observed vary between about fifty and two hundred kilometers with the average being about one hundred kilometers. Sheridan et al. (1979) and Grow et al. (1979) discuss refaction studies off the northeastern United States coast which show similar transition geometries and transition lengths of one to three hundred kilometers. Uchupi and Austin (1979) examine reflection profiles off the eastern coast of North America which indicate that the length of the upper surface of the transition region is about one hundred kilometers. Hinz et al. (1979) present the same types of

results off Labrador and Greenland showing transition lengths of about one hundred kilometers. Studies off northern Alaska by Eittreim and Grantz (1979) and Grantz et al. (1979) show transition lengths of the upper transition surface of between fifty and one hundred kilometers. Barton et al. (1984) derive a structure beneath the North Sea which shows similar transition regions. Le Douaran et al. (1984) examine the crustal structure in the northwestern Mediterranean Basin, and Makris et al. (1983) and Makris and Stobbe (1984) derive structures in the Eastern Mediterranean. In the Mediterranean region the transition regions are fifty to one hundred fifty kilometers in length. Most of the transition region structures mentioned above show similarities. In all cases the crustal layer thins from the continent toward the ocean. In most cases this thinning is fairly constant. The thicknesses of the continental and oceanic crustal layers vary somewhat. The resolution and detail in the models vary considerably. The details would need to be accounted for if cases of detailed waveform modeling were to be undertaken, but, they are not critical for this study. The lengths of transition regions suggested by the observations are between fifty and three hundred kilometers. These studies all indicate that the simplified models used in this investigation are reasonable. These models use a thirty two kilometer crustal layer over a half-space as a model of the continental structure and a five kilometer ocean over a five kilometer crust over a half-space as a model of the oceanic structure. The thickness of the crustal layer varies smoothly between the oceanic and continental values as one passes through a transition region. Model transition regions are constrained by computational limits to lengths of one hundred kilometers or less.

The wavefields transmitted through these models are synthesized to model the L_g arrivals in a seismogram. The L_g arrival was first defined by Press and Ewing (1952). Based on studies of seismograms recorded in North America, they defined L_g to have periods of 0.5 to 6 seconds, phase velocities between 2.0 and 3.5 km/s, reverse

dispersion at distances greater than 20°, and a sharp high amplitude onset. They noted that L_g arrivals are visible for purely continental paths and are gradually eliminated as the oceanic portion of the path increases in length beyond one hundred kilometers. The arrivals are visible on all three components but are larger on the horizontals. They suggested two possible interpretations of L_g, then abandoned the one which explained L_g in terms of higher mode Love waves in favor of one which explained them as channel waves trapped in the crust above a low velocity layer. The idea that L_g was a crustal channel wave was expanded and discussed by Press and Gutenburg (1956) and Gutenburg (1955) but even they stated that such an explanation was at best tentative. The interpretation of L_g in terms of higher mode Love waves was abandoned by Press and Ewing (1952) because of the motions on the vertical and longitudinal components and the long coda. Oliver and Ewing (1957, 1958a, 1958b) and Oliver et al. (1959) studied higher mode Love waves and Rayleigh waves and concluded that the vertical and longitudinal components of L_g are composed of higher mode Rayleigh waves and that higher mode Love waves could account for the transverse component. They considered only the first two higher modes and thus did not explain the long coda, but only its initial portion. Kovach and Anderson (1964) showed in detail that L_g could be interpreted using higher mode Rayleigh and Love waves. Panza et al. (1972) related the higher mode Rayleigh wave interpretation to the channel wave explanation. Panza and Calcagnile (1974, 1975) compare models with and without a low velocity channel below the crustal waveguide and conclude that such a channel is not necessary for the existence of L_g waves. Thus, the L_g arrival is clearly explained as a superposition of the higher mode Love waves and Rayleigh waves.

All the studies of higher mode Rayleigh waves and Love waves discussed above are based on analysis of group velocities, and phase velocities, with the L_g arrivals

corresponding to the group velocities of the extrema of the group velocity curves. Knopoff et al. (1975) used the higher mode interpretation of L_g to calculate synthetic seismograms for L_g. These seismograms further establish the validity of the previous interpretations based on group velocities of higher mode Love and Rayleigh waves by matching not only arrival times but also relative amplitudes. These seismograms also establish that the observed properties of L_g waves can be produced without including a low velocity channel. Knopoff et al. (1975) continued their studies using synthetic L_g waves to define properties of L_g that can be used to discriminate differences in crustal structure. Bouchon (1981,1982) used an alternate method for determining L_g synthetics at short distances (150 - 350 km) to model data from an earthquake in France. He concluded that the L_g arrivals were composed of multiply reflected post-critical SH and SV rays and that synthetics modeled the data well for group velocities between 3.5 and 2.8 km/s. Several other workers have used the fact that Love waves can be expressed as the superposition of post-critical multiply reflected SH rays in the crust to investigate the L_g arrivals. Herrin and Richmond (1960) along with corrections in Herrin (1961) used ray theory to show L_g could be modeled using multiply reflected and refracted ray in a thin crustal layer. This type of approach was also used by Pec (1967) and Kennett (1986) to address some properties of L_g. Cara and Minster (1981) developed a method to analyze Rayleigh type L_g seismograms recorded along a linear array. Cara et al. (1981) applied this method to data recorded in the northwestern Sierra Nevada and in southern California. They conclude that representation of L_g as a single multimode wavetrain is an oversimplified approach which can explain observations in the initial portions of the wavetrain (group velocity $>$ 3.2 km/s), while the later portions of the waveform are strongly affected by reflections and diffractions from any discontinuities in structure. Other phases previously defined in terms of the channel model have also been modeled using the higher mode surface wave model. Schwab

et al. (1974), Mantovani et al. (1977), Nakanishi et al. (1977), and Mantovani (1978) considered S_a, Stephens and Isacks (1977) considered the transverse component of S_n, and Cansi and Bethoux (1985) investigate the T phase which converted to L_g at the continental margin. In light of all the evidence the higher mode interpretation of L_g best explains the observed properties of L_g, even though variations in the crustal structure may cause a longer coda than that calculated using a simple layered structure. The SH L_g seismograms used to produce the wavefields used to drive the FE calculations in this study are determined as mode sums over the fundamental and first five higher modes.

One of the important uses of L_g has been to distinguish regions with oceanic crustal structures from those with continental crustal structures and to map regions where sudden changes in crustal structure occur. While the theoretical interpretation of L_g were being debated many observational studies of L_g waves were being conducted. These studies were conducted to map regions of oceanic crustal structure and regions of complex crustal structure on continents which caused the L_g arrival to be heavily attenuated or vanish. The studies considered a strong L_g to indicate continental structure and a missing or highly attenuated L_g to indicate passage through oceanic crust. Intermediate cases were included in one group or the other depending on the workers, but none used a quantitative scale.

Bath (1954,1958) collected a large sample of L_g data along Euroasiatic paths and fashioned explanations of his data based on the guided wave interpretation of L_g. He also defined two arrivals he called L_{g_1} and L_{g_2} with distinctly different phase velocities of 3.54 km/s and 3.37 km/s. His observations supported the conclusion of Press and Ewing (1952) that partially oceanic paths resulted in attenuation of the L_g phase. However, he interpreted some portions of the Arctic Ocean where L_g was not attenuated as being continental in structure. This approach, of defining paths which

pass under oceans but do not attenuate L_g as continental paths has also been used in most of the more recent studies of this type since that time. These studies used L_g recorded in many regions of the world. Press et al. (1956) considered paths in Africa, Press (1956) used paths in California, Savarensky and Valdner (1960) studied the Black Sea region, Bolt (1957) studied data from Australia, Utsu (..) considered Japan and the region surrounding it, and Lehmann (1952, 1957) studied significant events in North America and Europe. Oliver et al. (1955) considered L_g propagation in the Arctic region, Herrin and Minton (1960) in the Southwestern United States and Mexico, and Wetmiller (1974) investigated the crustal structure in the Baffin Bay area. Gregersen (1984) studied the crustal structure near Denmark and in the North Sea. Additional data for this area were presented by Kennett and Mykkeltveit (1984) who used the supplemented data set and the method of Kennett (1984a) to produce synthetics and an interpretation of the data in terms of a multimode wavetrain traveling through a crustal 'pinch'.

As originally noted by Bath, some purely continental paths show attenuated L_g and the later studies mapped these regions. Gumper and Pomeroy (1970) made a more extensive study of L_g and other phases in Africa. They found L_g velocities between 3.48 and 3.60 km/s and a discontinuity in the crust near the rift zone. Ruzaikin et al. (1977) mapped regions of L_g propagation in Asia and saw attenuation in Tibet and regions of China. Kadinsky-Cade et al. (1981) conducted a detailed study of L_g, S_n, P_g, and P_n propagation in India, the Himalayan Arc and the Tibetan Plateau producing a more detailed map than Ruzaikin et al., and agreeing with their observations and the sparse observations of Bath that showed the absence of L_g on paths crossing or originating in Tibet. Finally, Ni and Barazangi (1983) report the results of a detailed study in India, Tibet, and the Himalayan Arc which agrees with other results. Chinn et al. (1980) studied L_g and S_n in western South America and

observed that L_g propagation was efficient only parallel to the strike of the Andes. They also observed conversion of Oceanic S_n to L_g in areas of crustal thickening. Isacks and Stephens (1975) also observed conversion of S_n to L_g both in earthquakes from the West Indies observed in Eastern North America and in earthquakes near southernmost Mexico observed on the northern coast of the Gulf of Mexico. Some of their claims of observed conversions are disputed by Shurbet (1962, 1974, 1976). Gregersen (1978) discusses conversion between different modes of Love waves and between Love and Rayleigh waves at an ocean continent boundary. These studies illustrate the importance of a clear understanding of the mechanisms of attenuation of L_g along mixed paths. Simply stating that a path which passes under an ocean but is not attenuated implies that the floor of that ocean has a continental structure could be misleading. A clearer understanding of the effects of structural transitions on the attenuation of L_g is important.

Another major use of L_g waves is the determination of magnitudes of explosions and earthquakes and of regional attenuation properties. These magnitudes, usually referred to as m_{bL_g}, and other types of magnitudes are compared to discriminate between the two types of sources (Blandford, 1982, and Pomeroy et al. 1982). The ratio of body wave magnitude, m_b, to surface wave magnitude, M_S, is one such discriminant whose physical basis is explained by Stephens and Day (1985). In order to examine whether this type of discriminant can be generalized to periods shorter than than those considered when using the twenty second surface wave magnitude, new empirical relations for short period phases such as L_g (Baker, 1970) and R_g (Basham, 1971) were derived to measure short period surface wave magnitudes. Nuttli (1973) used observed attenuation of short period Rayleigh waves (L_g, and R_g) to present a theoretical explanation and generalization of the empirical relations and defined their limitations. He explained how to use data of L_g amplitude versus

distance to determine the value of γ, the coefficient of anelastic attenuation. Nuttli (1978) extended the definitions from one second waves to frequencies as high as ten Hertz. These studies provided a more quantitative method for mapping the attenuation of L_g than simply recording whether L_g was observed, not observed, or attenuated. Thus, a series of studies mapping the attenuation of L_g using the determination of γ were initiated. An extensive study of the United States at 0.5 to 2 Hz. had previously been completed by Sutton et al. (1967) using other methods. Nuttli (1973) developed an L_g magnitude scale for the central United States. Herrmann and Nuttli (1982) studied the relation of this scale, m_{bL_g}, to the local magnitude scale, M_L. The attenuation observed was used to model ground motions at regional distances due to earthquakes and assess the possible destructiveness of the L_g part of the wavetrain (Herrmann and Nuttli, 1975a, 1975b). An additional study of this type of problem using added data was done by Street (1984). Street et al. (1975) studied L_g spectra of United States earthquakes. The results were the basis of a study of L_g moments, magnitudes, and intensities (Street and Turcotte, 1977) and the development of an L_g magnitude scale analogous to that of Nuttli (1973) for the northeastern United States and southeastern Canada (Street, 1976). Jones et al. (1977) studied attenuation of L_g in the southeastern United States. Nuttli (1980) considered a region including Iran. Bollinger (1979) again studied the northeastern United States obtaining results consistent with Street (1976). Nuttli (1981) examined attenuation of L_g in western and central Asia for both earthquakes and explosions. Barker et al. (1981) studied the crustal structure at the Nevada Test Site using L_g and P_g. Chung and Bernreuter (1981) reviewed the studies of regional relations between various magnitude scales including m_{bL_g}. Nicolas et al. (1982) studied attenuation of regional phases in western Europe. Gupta et al. (1980) considered both earthquakes and explosions in western Russia, and Gupta et al. (1982) studied variations in horizontal to vertical L_g

amplitude ratios. Ebel (1982) criticizes the m_{bL_g} scale as being inappropriate at five to ten Hertz for earthquakes in the northeastern United States. Dwyer et al. (1983) presented a frequency dependent study of L_g in the central United States which addresses this criticism of the m_{bL_g} scale. Singh and Herrmann (1983) present a regionalized map of L_g attenuation in the continental United States for periods between 0.5 and 3.5 Hz. Herrmann and Kijko (1983a, 1983b) also investigate necessary changes to the L_g magnitude scale to allow use of data for instruments with predominant periods other than the one second period of the WWSSN instrument. Campillo et al. (1984) studied the excitation of spectra and geometrical attenuation of regional phases including L_g. Der et al. (1984) studied the coherence of the L_g wave crossing a given region. All these studies are based on the interpretation of L_g as a superposition of higher mode Love and Rayleigh waves. They all assume that the L_g waves are traveling through a relatively constant thickness crustal layer, and most do not account for reflection of diffraction of L_g energy from changes in thickness of the crust. Clearly, it is important to understand if such changes will produce significant effects not accounted for in the interpretations given.

Many attempts to understand the propagation of seismic disturbances across regions of varying structure such as transition zones have been made. First, simple models were used and analytic solutions were derived for soluble special cases, then increasingly complicated models were considered as available computational power increased. The types of models that have been used to approximate transition regions can be separated into several types which are illustrated in Figure 1.

The simplest type of model (Figure 1a) consists of two homogeneous layered regions, 1 1', and 3 3', with layer over half-space structures separated by a vertical boundary or a region 2 2' in which density, ρ, rigidity μ, and SH wave velocity , β, vary smoothly between their values in the regions 1 1' and 3 3'. Sato (1961a) discusses

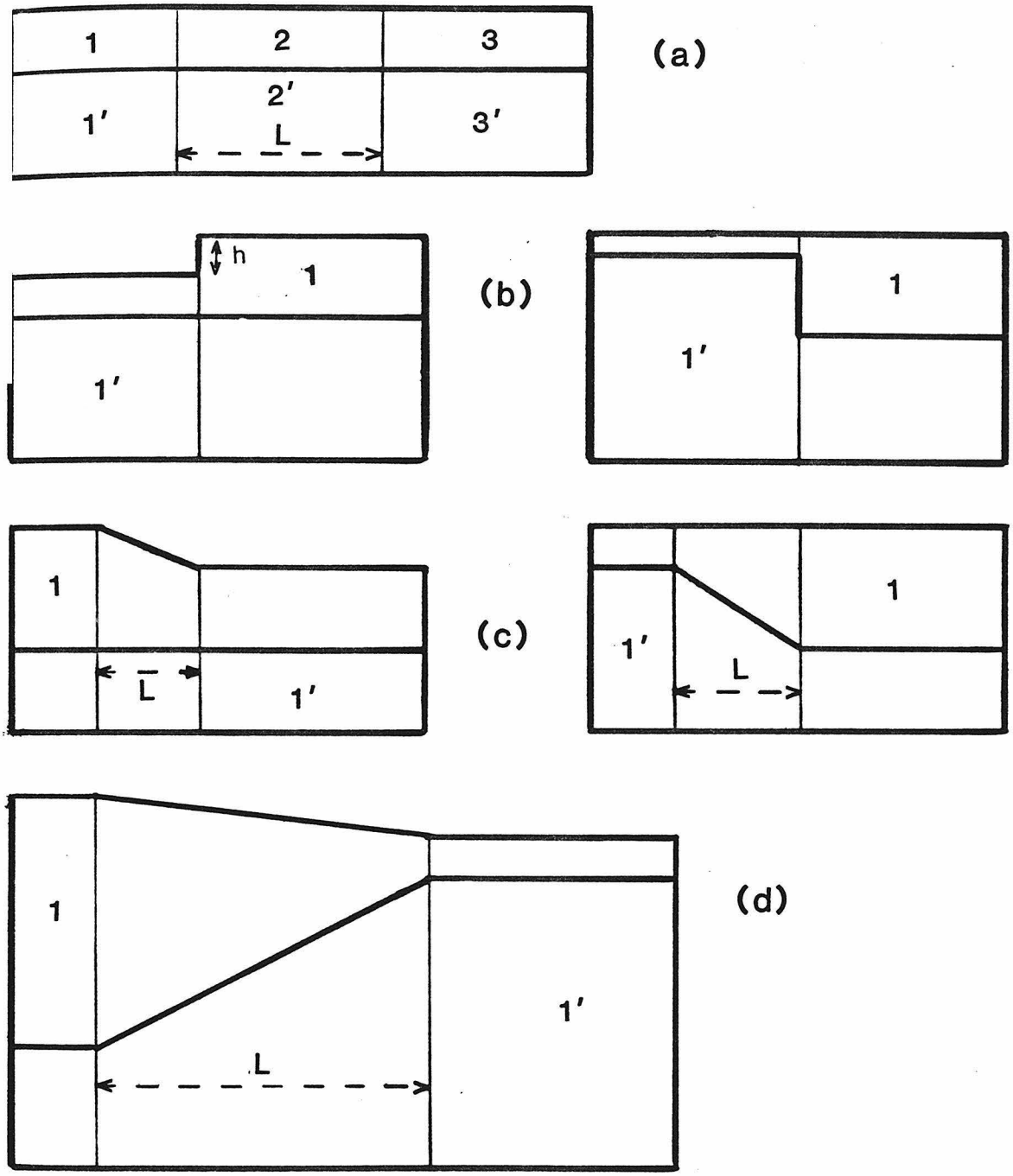

Figure 1: Types of models used in studies of propagation of Love waves across continent ocean boundaries. Part a) shows the simplest model, two regions labeled 1 and 3 separated by a vertical boundary or a intermediate region, 2, of varying properties. Part b) shows another type of simple model, a layer of a half-space with a sudden step change in the thickness of the layer. Part c) shows a more general type of simplified model with a more gradual change in thickness rather than a step. Part d) shows the type of model used in this study, which includes smooth thickness variation both at the surface and the base of the crustal layer.

both these cases applying the conditions

$$\frac{\mu_3}{\mu_1} = \frac{\mu_{3'}}{\mu_{1'}} \qquad \beta_1^{-2} - \beta_{1'}^{-2} = \beta_2^{-2} - \beta_{2'}^{-2}$$

to assure the transmission of fundamental mode Love waves across the boundary without modal conversion. He derives analytic expressions for the transmitted and reflected waves, the phase and group velocities, and the reflection and transmission coefficients in each case. The case for which no transition regions is present has since been used by Alsop (1966), Boore (1970), and Gregersen and Alsop (1974, 1976) as a test case for more generalizable numerical methods. More recently, Kennett (1973) has developed a numerical technique to consider the problem of seismic waves interacting with a layer or layers in which properties change across a surface perpendicular to or at a specified angle from the layering.

The next level of complexity that can be introduced into the model is the inclusion of a change in the thickness of the surface layer at the discontinuity between the two structures. This type of model is illustrated in Figure 1b. In most cases the material properties do not change when the layer thickness changes. Sato (1961b) used the Wiener-Hopft technique to obtain analytic expressions for the transmitted and reflected waves for a model with a surface step with height h much less than the wavelength of the incident wavefield λ. Using these solutions he obtained approximate expressions for energy reflection and transmission coefficients for a surface step model using a Green's function method. Hudson and Knopoff (1964) calculated expression for the motion and the reflection and transmission coefficients for the surface step model. They did not need or use the $h << \lambda$ approximation. Alsop (1966) developed an approximate method for determining Love wave transmission and reflection coefficients in a model of type 1b. This method assumes that all energy remains in Love waves, introducing errors, particularly at intermediate periods, if any

energy is converted between modes or into forms other than modal energy. The latter two methods had the advantage that higher modes could be used and that no specific interrelation of elastic properties between the different layers or regions was necessary. Gregersen and Alsop (1974, 1976) extended the method of Alsop (1966,1968) to the determination of transmission coefficients for the case of non-normally incident Love waves. At normal incidence results correspond well to those found in previous studies, for oblique incidence at angles less than forty degrees normal incidence is a good approximation. Bose (1975) solves the surface step problem using an integral equation formulation which yields asymptotic solutions for large distances from the step. His results show increases in amplitude for a step down and decrease in amplitude for a step up, consistent with results derived for the step models in this study. Kazi (1978a, 1978b) uses the variational method of Schwinger-Levine to derive solutions to the surface step problem that account for the Love waves converted to body waves at the surface step. He determines the reflection and transmission coefficients by way of a scattering matrix and evaluates them for the same cases as Alsop (1966) and Knopoff and Hudson (1964) showing that the transmission coefficients increased after the cutoff frequency rather than decreasing as was observed in earler studies that neglected the body waves. Lapwood, Hudson, and Kembhavi (1973, 1975) and Lapwood and Hudson (1975) used a similar variational technique to study normally and obliquely incident plane waves incident on a layer between two uniform half-spaces. Hudson (1977) extended their method to the surface step problem but concluded that the numerical implementation of the method would not be more efficient than existing techniques. Martel (1980) used a finite element technique to evaluate propagation of Love waves across a Moho step. Spatial filtering of the transmitted and reflected modes to determine transmission and reflection coefficients allowed the isolation of the diffracted body wave component.

Studies using the surface step model and the Moho step model have been generalized in several ways. First, and most relevant to this study, the step can be replaced by a transition region as discussed in the next paragraph. Other types of generalization allow the study of the effect of topography, of a short section if thinner crust referred to as a crustal 'pinch', or of continuous but small variations in crustal thickness on the incident wavefield. Gilbert and Knopoff (1960) used a method similar to a Born approximation to study seismic scattering from topography and to produce approximations valid for pulses with duration short with respect to the horizontal travel time across the irregularity. Hudson (1967) extended the method of Gilbert and Knopoff (1960) to variations in elastic properties at the surface such as sediment filled depressions, as well as surface distortions. The method can be used to obtain a rough estimate of the dimension of the scatterer. Boore et al. (1971) and Boore (1972) study the effect of topography on SH waves using the Finite Difference method to propagate a simple pulse through the structure. This approach, unlike the previously discussed methods, allows the consideration of steep topography or topography with wavelength similar to or smaller than that of the incident waves. Herrera (1964a, 1964b) developed a perturbation method to study the effects on a propagating seismic disturbance of a crustal layer with slowly varying thickness. Mal and Herrera (1965) studied the effect of a short section of thinner crust, where the difference in crustal thickness between the thin and the thick crust is small compared with the wavelength of the incident energy.

The next increase in the complexity of the transition model is the introduction of a transition region in which the crustal thickness varies smoothly between the crustal thicknesses at its ends. The simplest models of this type are shown in figure 1c. In these models either the surface or the Moho have a smooth slope in the transition region. Knopoff and Mal (1967), and Knopoff et al. (1970) explained an analytic

solution for this type of model when the slope of the surface (or Moho) of the transition region is small. They also assumed that the local phase velocity was the same as that in a layered structure with the local layer thickness. They found forward scattering to be much less important than back scattering. Pec (1967) calculated the dispersion of Love waves propagating in a wedge shaped layer such as the transition region in models of type 1c. He considered Love waves in terms of the constructive interference of multiply reflected SH rays and found that the inclination of the Moho caused the largest changes in phase velocity and amplitudes at short periods. Boore(1970) studied the propagation of a simple low frequency Love wave across the type of structure shown in figure 1c. He specified the displacements at t=0 and t=dt throughout the grid such that the displacement at t=0 at the surface of the layer over a half-space portion of the model was a Ricker wavelet. The Finite Difference method was then used to calculate phase velocities and transmission coefficients at various points along the grid surface for a one hundred twenty kilometer long transition region. Periods of twenty to one hundred thirty seconds were used. Phase velocities were lower for propagation from continent to ocean than from ocean to continent. He noted that in the region of the transition that mode conversions and conversion to other types of waves seemed to be important. Lysmer and Drake (1971, 1972) and Drake(1972), who discusses mainly Rayleigh wave results but states that they also apply to Love waves, use a Finite Element method based on Zienkiewicz and Cheung (1967) which includes a rigid grid bottom and thus allows no energy to escape the grid. The formulation also requires that the incident modal energy is exactly equal to the sum of the reflected and transmitted modal energy, thus disallowing conversion to other types of waves. Lysmer and Drake (1971) use this method to study the effect of a transition of type 1c, with length one hundred twenty kilometers, or 1d, with a length of one hundred kilometers, on the incident fundamental mode Love wave

energy. With their constraint no difference in continent to ocean and ocean to continent phase velocities is seen, so they attribute the differences to body wave interference. They estimate that about one percent of the energy at 25s period is transmitted without mode conversion and about 35% is transmitted in other modes. Drake(1971) discusses mainly Rayleigh wave results but states that they also apply to Love waves. Drake and Bolt (1980) used the method of Lysmer and Drake (1972) to study a more complicated model with the upper and lower transition surfaces having different lengths to model phase velocity data of events normally incident on the California continental margin. They considered periods between 4.4 and 60 seconds and modeled only incident fundamental mode waves. They discuss the period ranges over which fundamental mode transmission is small and conversion to particular higher modes is large. They conclude that the ocean continent boundary strongly increases the attenuation of fundamental mode Love waves. Schlue (1979) shows some simple examples of a three dimensional Finite Element solution for Love wave propagation.

All the studies discussed in the previous paragraph used periods much longer than those that will be considered in the following discussions. The shorter periods used in this study allow the examination of the effects of transition regions with length many times the wavelength of the incident energy. Most previous studies considered transition regions with lengths comparable the wavelength of the incident energy. The method of Lysmer and Drake (1972) purposely excluded the possibility of conversion from modal energy to body waves, and thus excludes the possible escape of energy from the system as these body waves travel out the bottom of the grid. This escaping energy is shown in this study to be an important component of the explanation of the attenuation of the L_g phase traveling on partially oceanic paths. The studies using the method of Lysmer and Drake (1972) used periods shorter than other studies but longer than those used here. They also considered only fundamental mode Love wave input

and calculated each mode separately, while the driving functions used in this study are a sum over a range of frequencies on the fundamental and first five higher branches. In fact most of the earlier studies with Finite Element or Finite Difference considered the fundamental mode at one frequency rather than over a range of frequencies. None of these studies has generated realistic seismograms, but instead they all concentrated on measuring phase velocities and transmission and reflection coefficients. In light of these facts it is clear that the results discussed in this thesis can give a significant addition to the understanding of the propagation of L_g waves across transition regions.

Finally, the content of each chapter will be summarized. The first four sections of chapter one present the basics of and the notation associated with the Propagator Matrix and FE techniques. Sections five and six discuss the theory of the two coupling methods. The remainder of the chapter is a series of tests of the accuracy of the coupling technique discussed in section five and used in chapter two. Sections one to three of chapter two discuss the design of the numerical experiments presented in the remainder of that chapter, and in section two of chapter three. The remainder of chapter two discussed the effects of transition of L_g wavetrains and the dependence of those effects on transition length. Chapter three first presents FE results investigating the effect of the length of the oceanic path on the L_g wavefield. Then examples of the accuracy and efficiency of the coupling method discussed in section six of chapter one are presented. Finally, this method is used to determine seismograms after propagation through a transition and then oceanic paths of different lengths. Reasons for the attenuation of L_g for oceanic path lengths longer than 100-200 kilometers are discussed.

Chapter 1

Representation Theorem Coupling of the Finite Element and Modal Propagator Matrix Methods

Intoduction

In this chapter the methods for Representation Theorem (RT) coupling of finite element (FE) or finite difference calculations and Harkrider's (Harkrider 1964, 1970) propagator matrix method calculations to produce a hybrid method for propagation of SH mode sum seismograms across paths that contain regions of non plane-layered structures are explained and developed. The FE method used in this study is an extensively modified version of the Stress Waves in Solids code (Frazier, Alexander and Petersen, 1973). The coupling methods explained in detail in this chapter use a 2-D Cartesian FE formulation. Analogous methods for the 3-D method follow directly. The hybrid method linking propagator matrix results to FE calculations assumes that the wavefield arrives at the edge of the FE grid after propagating many wavelengths in the layered structure. Extensive tests illustrating the validity and accuracy of the implementation of this method are presented in this chapter. These tests use a structure consisting of a layer over a half-space. This simple structure allows the calculation of synthetic seismograms using only the propagator matrix technique. These synthetic seismograms can be directly compared to the hybrid results to ascertain the accuracy and the limitations of the coupling technique. After propagation through a path of length much less than the source to FE grid distance in the FE grid the wavefields can be coupled back into a layered medium. The layering in the second layered medium need not be identical to that in the first layered medium. The tests of coupling from FE to propagator matrix are discussed in chapter 3. This sequence of

procedures can be repeated any number of times, thus including several regions of complexity in the source to receiver path.

These hybrid techniques are developed to study the propagation of surface waves across regional transition zones or other heterogeneities that exist in part of a longer, mostly plane-layered, path. Examples of structures of interest through which surface waves can be propagated using these techniques include, regions of crustal thickening or thinning such as continent ocean transitions or basins, anomalous bodies of any shape located in the path, topography, and sudden transitions from one structure to another. In fact, any arbitrary structure of interest can be placed in the FE portion of the path.

To clearly explain the methods used to couple finite element (FE) and propagator matrix methods, enabling transmission of a disturbance along part of its path from the source to the receiver by each method, it is useful to first discuss some of the foundations on which each method is based, and some of the details of the implementation of each method. The propagator matrix technique is used to transmit mode sum synthetics through sections of their paths that consist of simple plane layered structures. The theory used to derive this technique is explained in detail by Harkrider (Harkrider 1964). His numerical implementation of these ideas forms the basis for the slightly modified codes used in this study. The fundamentals of this method which are central to the understanding of the Representation Theorem coupling techniques and the generation of the mode sum synthetics and the Green's Function synthetics used in these techniques will be discussed below. The modifications to the numerical implementation of Harkrider will also be discussed. The FE calculations discussed here are done using an extensively modified version of the Stress Waves in Solids (SWIS) code developed by Frazier, Alexander, and Petersen (Frazier et al. 1973, Frazier and Petersen 1974). The basic structure of SWIS code is retained, but many options in the code

are removed, and the detailed implementation is changed in order to produce a large increase in the speed of execution. Further options not available in the version of the SWIS code used were added to enable grid points to be constrained to move with a given time history, to allow the production of time slices, and to implement hourglass corrections for the SH case. Details of these changes and their impact will be discussed later, as will the basic formulation of the SWIS FE method.

The Propagator Matrix Technique

The basic idea behind the propagator matrix method as implemented by Harkrider is to transmit the disturbance produced by a source within a layered half-space structure through that structure by combining terms that describe the source, the medium response, and the propagation effects. The terms that apply the effects for the propagation path in the z direction are in the form of propagator matrices. For source and receiver both at depth, they are separated into two parts, the propagation in z from the source to the surface, and the propagation in z from the surface to the receiver. An additional propagation term adds the effect of the propagation in the r coordinate. In most cases the general form of a modal displacement at a receiver at depth is

$$v(r,\phi,z) = S\ \underline{A}_L \left[\frac{v_S(h)}{v_0}\right]_H \left[\frac{v_R(z)}{v_0}\right]_H P \qquad (1)$$

where S is a function of the source strength and geometry, $\underline{A}_L$ represents the medium response for a surface source and a surface receiver, P expresses the propagation effects in direction r, $\left[\frac{v_S(h)}{v_0}\right]_H$ is the term for transmitting the disturbance from the source depth to the surface which because of reciprocity can be expressed as a modal propagator from the surface to the source depth, and $\left[\frac{v_R(z)}{v_0}\right]_H$ is the propagator from the surface to the receiver depth. The subscript H on the terms which transmit the modal

disturbances in z denotes homogeneous, that is independent of and not containing a source. The expressions within the square brackets of these terms represent matrix quantities, not simple ratios. If the source is a stress source rather than a displacement source then $\left[\frac{v_S(h)}{v_0}\right]_H$ is replaced by $\frac{k_L}{\mu_S}\left[\frac{\tau^*(h)}{\dot{v}_0 / c_L}\right]_H$, where μ_S is the rigidity at the depth of the source. If stress rather than displacement is to be recorded at the receiver, then $\left[\frac{v_R(z)}{v_0}\right]_H$ is replaced by $\frac{k_L}{\mu_R}\left[\frac{\tau^*(z)}{\dot{v}_0 / c_L}\right]_H$. In this expression μ_R is the rigidity at the depth of the receiver. As an example of a specific case of this type of representation, the displacement expressions for a double couple source of arbitrary orientation will be stated in terms of the propagator formulation. This expression will then be used to obtain the expressions for displacements from a dip slip and a strike slip source. These expressions will be used extensively in subsequent discussions. Following this discussion the modifications made to the propagator matrix codes will be explained.

The displacement for an arbitrary double couple source follows directly from the expression for the SH displacement at the free surface produced by a double couple source of arbitrary orientation at depth h (Harkrider 1964, 1970).

$$\left\{\overline{v}_0\right\} = 2i\pi\, K_{\#} k_\beta^2 \mu \underline{A}_L \left\{ \left[\cos\lambda \sin\delta \cos 2\phi - \sin\lambda \frac{\sin 2\delta}{2} \sin 2\phi\right] \left[\frac{v_S(h)}{v_0}\right]_H \frac{\partial H_2^{(2)}(k_L r)}{\partial r} \right.$$

$$\left. - \left[\sin\lambda \cos 2\delta \cos\phi + \cos\lambda \cos\delta \sin\phi\right] \left(\frac{1}{\mu_S}\left[\frac{\tau^*(h)}{\dot{v}_0 / c_L}\right]_H\right) \frac{\partial H_1^{(2)}(k_L r)}{\partial r} \right. \tag{2}$$

where

$$K_{\#} = \frac{-\overline{M}(w)}{4\pi\rho\omega^2} = \frac{iM_0}{4\pi\rho\omega^3} \qquad \dot{v}_0 = i\omega v_0 \tag{3}$$

$$k_\beta^2 = \frac{\omega^2}{\beta^2} = \frac{\rho_s \omega^2}{\mu_s} \qquad k_L = \frac{\omega}{c_L} \qquad \tau = i\tau^* \tag{4}$$

In equations (2), (3), and (4), λ is the strike of the double couple source, δ is the dip, ϕ is the azimuth to the station, β is the SH wave velocity, ρ_s is the density at the depth of the source, h is the source depth, ω is the frequency, r is the distance from the source to the receiver, c_L is the Love wave velocity, μ_S and μ_R are respectively the rigidity at the source depth and at the receiver depth, $\underline{A}_L$ is the medium response for a surface source and receiver, $\left[\frac{v_S(h)}{v_0}\right]_H$ and $\left[\frac{\tau^*(h)}{\dot{v}_0 / c_L}\right]_H$ are the terms that transmit the source disruption in z from the source to the surface receiver, and the term containing the Hankel function is the propagation term in r. The source term is defined to contain all the angular dependence on δ, λ, and ϕ, as well as the term $2i\pi k_\beta^2 K_\#$, and the factors of μ. The second equality in the first expression of equation (3) assumes a step moment, that is $\overline{M}(\omega) = \frac{M_0}{i\omega}$.

It is well known that a double couple of arbitrary orientation can be expressed in terms of a linear combination of double couple sources of three types, vertical strike slip, vertical dip slip and 45° dip slip. Thus, results for these three fault types can be added to produce results for an arbitrary orientation, removing the necessity to repeat the entire procedure for each orientation to be studied. Substituting (3) and (4) into (2) and evaluating the expression for each of the three basic fault types yields, (5), the expressions used to determine displacement at the surface. For a vertical strike slip fault $\delta = 90°$, and $\lambda = 0°$. In the following development part a of each set of equations will be the expression for the strike slip fault. For a vertical dip slip fault $\delta = 90°$, and $\lambda = 90°$. Part b of each set of equations below will be the appropriate expression for the vertical dip slip fault. For a 45° dip slip fault $\delta = 45°$, and $\lambda = 90°$. Part c of the next group of equations is for a 45° dip slip fault.

$$\left\{\overline{v}_0\right\} = -\frac{M_0}{2\omega} A_L \cos 2\phi \left[\frac{v_S(h)}{v_0}\right]_H \frac{\partial H_2^{(2)}(k_L r)}{\partial r} \tag{5a}$$

$$\left\{\overline{v}_0\right\} = -\frac{M_0}{2\omega} A_L \sin\phi \frac{1}{\mu_S} \left[\frac{\tau^*(h)}{\dot{v}_0 \,/\, c_L}\right]_H \frac{\partial H_1^{(2)}(k_L r)}{\partial r} \tag{5b}$$

$$\left\{\overline{v}_0\right\} = -\frac{M_0}{2\omega} A_L \frac{(-\sin 2\phi)}{2} \left[\frac{v_S(h)}{v_0}\right]_H \frac{\partial H_2^{(2)}(k_L r)}{\partial r} \tag{5c}$$

Examining equations (5) shows that, for SH waves, any fault geometry can be modeled using a linear combination of only the vertical dip slip and the vertical strike slip faults. This follows from the observation that the vertical dip slip and the 45° dip slip expressions differ only by a function of the azimuth ϕ. For the remainder of this development only vertical dip slip and vertical strike slip fault types will be considered. This is equivalent to setting $\sin\phi = \cos 2\phi = 1$, and $\sin 2\phi = 0$, that is $\phi = 90°$. For a given value of ϕ any fault geometry can be reconstructed by reintroducing the appropriate values of $\sin\phi$, $\cos 2\phi$, and $\sin 2\phi$ into the coefficients of the linear combination of the remaining two factors. The displacements determined by equation (5) are those produced at the surface by a double couple source at depth h. To determine the displacements at depth, a term propagating the energy from the surface to the depth of the receiver must be included. For a receiver at depth z the modal displacement expressions become

$$\left\{\overline{v}(z)\right\} = -\frac{M_0}{2\omega} A_L \frac{\partial H_2^{(2)}(k_L r)}{\partial r} \left[\frac{v_S(h)}{v_0}\right]_H \left[\frac{v_R(z)}{v_0}\right]_H \tag{6a}$$

$$\left\{\overline{v}(z)\right\} = -\frac{M_0}{2\omega} A_L \frac{1}{\mu_S} \frac{\partial H_1^{(2)}(k_L r)}{\partial r} \left[\frac{\tau^*(h)}{\dot{v}_0 \,/\, c_L}\right]_H \left[\frac{v_R(z)}{v_0}\right]_H \tag{6b}$$

Most of the changes made to the propagator matrix codes of Harkrider were minor. The only major changes were the addition of an option to evaluate the

analytic expressions for the stresses and the implementation of an alternate code which uses the line source rather than the point force, double couple, or explosive sources already available. The implementation of the stress calculation will be discussed later. The construction of the line source code required changes to the source terms and the modal propagation terms that propagate in r. The basic form of the z dependent modal propagator terms is identical regardless of the source used, so no changes were necessary in the calculation of $\left[\frac{v_S(h)}{v_0}\right]_H$, $\left[\frac{v_R(z)}{v_0}\right]_H$, $\left[\frac{\tau^*(h)}{\dot{v}_0 / c_L}\right]_H$, or $\left[\frac{\tau^*(z)}{\dot{v}_0 / c_L}\right]_H$. The line source code is set up to calculate displacement, stress, and displacement and stress Green's functions. The minor changes made to the codes include the restructuring of the order of operations to allow the efficient calculation of particular types of sets of seismograms. To efficiently calculate sets of displacement and stress seismograms in which successive seismograms are at the same horizontal distance r, and at a series of receiver depths at intervals of Δz, the operations were reordered to avoid unnecessary recalculation of intermediate results. The propagation terms in r need to be calculated only once, as does the source to surface term. To efficiently calculate sets of displacement and stress line source Green's functions the calculations were reordered in a different manner so that the surface to receiver propagator term and the propagation term in r needed to be evaluated only once. The codes still retain the ability to calculate seismograms for sets of receivers or Green's functions for sets of sources which do not form depth sections. However, for these sets the order of operations is not necessarily optimal and extra time may be taken in calculation of displacements or stresses.

The Modified SWIS Finite Element Code

The SWIS FE program is a flexible code capable of calculating the propagation of stress waves through solids of arbitrary complexity. Properties such as density, and elastic wave velocity are defined at a grid of nodes whose locations can be defined in

curvilinear coordinates. These properties are then used to determine the location, stress, and motion of the nodes in the grid as a function of time. Next, it is useful to give a simple step by step outline of the procedures used in the SWIS FE code.

First, several quantities are defined at each node or at each element in the grid to provide the initial conditions. In particular, the properties that are initialized at each node before the first time step are, the nodal position $\underline{X}(t)$, nodal displacement $\underline{U}(t)$, and nodal velocity $\dot{U}\left(t - \frac{\Delta t}{2}\right)$. The properties defined for each element are the force as a function of time, $\underline{F}(t)$, resulting from body forces $\underline{f}(t)$ within the element and from tractions $\underline{\tau}(t)$ applied to the surface of the element, and the elastic constants as determined by specification of density and elastic wave velocities. The values, within a element, of the variables initialized on each node are defined by interpolation between the nodal values at the nodes surrounding that element. In order to define the form of the interpolation functions the coordinate systems which define the location of a point within an element and the location of an element within the body must be defined and related. The 'natural' or local coordinate system defines the location of any point in the element with respect to the nodes surrounding that element. Each node is defined to be a unit distance, in each coordinate, from the element center. Let z_i be the coordinates of a point in element e in this 'natural' coordinate system, and let Z_i^m be the coordinates of node m, one of the nodes bordering element e, in the 'natural' coordinate system. This means that Z_i^m is always ± 1. A Cartesian coordinate system is defined within the volume V containing the body composed of the elements. In this Cartesian coordinate system, the i^{th} component of the position of node m bordering element e will be denoted X_i^m, and the i^{th} coordinate of a point z within element e will be denoted x_i. The Cartesian coordinates x_i and X_i^m can be transformed to an arbitrary curvilinear coordinate system y_i and Y_i^m using the well known relations for the transformation of quantities between Cartesian and general curvilinear coordinates.

Since all calculations in this study are performed in Cartesian coordinates, the transformation to general curvilinear coordinates will be omitted in further discussion of the SWIS FE method. Now it is possible to define the interpolation function used to determine positions, dislocations, velocities, accelerations and stresses within an element. In 'natural' coordinates the interpolation function used to define the coordinates of a point z within element e has the form

$$P^m(\underline{z}) = \frac{1}{2^D}\prod_{i=1}^{D}(1 + z_i Z_i^m) \tag{7}$$

where

$P^m(\underline{z})$ the interpolation function at point z for position of node m bordering element e

D number of space dimensions

Using the interpolation function it is possible to define the value of any of the quantities initially defined at each node at any point within an element, in terms of the Cartesian coordinates of the nodes surrounding the element. The location of the evaluation point within the element is expressed in the 'natural' coordinate system, For the position, displacement, applied force, or velocity at any point in an element surrounded by 2^D nodes the relation is or is analogous to equation (9).

$$x_i = \sum_{m=1}^{2^D} P^m(\underline{z}) X_i^m \tag{8}$$

For the stresses the relation is

$$\sigma_{ij} = \sum_{m=1}^{2^D} \frac{\partial P^m(\underline{z})}{\partial z_j} X_i^m \tag{9}$$

The SWIS code is based upon a one point quadrature integration rule, so the point $\underline{z}$ used to evaluate these expressions is the centroid of the element. Given the initial values the SWIS code uses one of several series of calculations to advance the properties of the nodes of the grid one time step, Δt. Only the option used for the

calculations in this study is discussed below. To update the values of the initialized quantities by Δt, thus yielding the configuration of the grid at time $t+\Delta t$ the following time centered explicit FE integration procedure is used;

(1) Compute strain and thus stress at the centroid of each element m

$$\sigma_{ij}(\underline{x},t) = 2\mu\left\{\frac{1}{2}\frac{\partial P^m(\underline{z})}{\partial z_j}U_i(t) + \frac{1}{2}\frac{\partial P^m(\underline{z})}{\partial z_j}U_j(t)\right\} + \lambda\delta_{ij}\frac{\partial P^m(\underline{z})}{\partial z_k}U_k(t) \qquad (10)$$

(2) Compute the restoring forces for each element m

$$R_i^m(t) = \sigma_{ij}(\underline{x},t)\frac{\partial P^m(\underline{z})}{\partial z_i} \qquad (11)$$

Then use the values of restoring force R_i^m at each element m surrounding a given node to determine a net restoring force R_i at each node.

(3) Integrate the equation of motion to give the values of location, stress and motion at each node at time $t + \Delta t$.

$$U_i(t + \Delta t) = U_i(t) + \Delta t\left\{\dot{U}\left[t - \frac{\Delta t}{2}\right] + \Delta t\frac{\left(F_i(t) + R_i(t)\right)}{M}\right\} \qquad (12)$$

The basic series of calculations described above form the core of the SWIS code and were retained in principle in the modified and accelerated version of SWIS used in this study.

In the discussion of the basics of the FE method used no mention was made of the exact method by which a source can be introduced into the FE calculations. In the basic version of SWIS a point source or a source of finite spatial dimension can be defined by constraining a node or nodes in the grid to have a specified displacement at time zero. Alternately, given body forces, F_i, can be applied at the centroids of one or more elements at time zero to create a source. Clearly, a more general source would

be desirable, and in fact necessary for the RT coupling of Propagator Matrix or other results into a FE calculation. To couple energy from a source outside the FE grid into the FE calculation it is necessary to specify the displacement time history of a column of nodes. An additional option to allow the specification of displacement as a function of time for any node or nodes within the grid was added to the basic SWIS code. This option allows the specification of a time history constraint at up to two hundred nodes. However, if time history constraints are specified at more than one node, they must have a common duration at all nodes used. Constraints used to define boundary conditions are defined separately and persist for the entire calculation. The time history constraints can have any duration. If the duration of the constraint is less than the duration of the calculations then the constrained nodes are released when the time t within the calculation exceeds the duration of the constraint. If the duration of the constraint exceeds the duration used to define the length of the calculation then only the first portion of the constraining displacement time histories are used.

A second modification to the SWIS FE code was added to enable the production of time slices, or 'snapshots' of the motions at each node within the grid at a chosen time t. This option allows the code to write a file which contains the displacements at every node in the grid, or at every node in a decimated grid every n time steps. If a decimated grid is chosen it is specified by an integer decimation factor. If this factor has a value l then in a given row (l-1) nodes are skipped between each node for which a value is recorded, and (l-1) rows of nodes are skipped between each row where displacements are recorded. These displacements are then plotted to produce a series of figures showing the displacement as a function of location within the grid at a selection of times. The sequence of plots illustrates how the energy propagates through the grid as a function of time.

The final, and most important addition to the SWIS code was the SH hourglass correction terms. The finite element (FE) code uses a one-point quadrature integration rule so stresses are evaluated only at the center of mass of each element. Consequently any stress state that produces non-constant stress within an element is not treated completely in the calculation. Such a stress state can be decomposed into the sum of a constant stress state, which the one point integration represents exactly, and a non-constant stress state with zero stress at the centroid, known as the hourglass mode. To account for the hourglass modes in a code which uses one point integration an additional term is added to the restoring force. The form of this term for SH or antiplane motion is explained and derived below. For the in plane or P-SV problem corresponding hourglass modes occur as discussed by Kosloff and Frazier (1978). In all cases the hourglass term in the restoring force is calculated using similar procedures.

Figure 1a) shows a 2-D rectilinear element of the type used in the SH Finite Element calculations, and the form of the hourglass deformation present for SH motion of such an element. This deformation lifts one pair of diagonally opposite element corners and depresses the other pair of corners by the same amount, producing no stress or dispacement at the centroid of the element. Since the Finite Element code depends upon evaluation of stress only at the centroid of each element, it is singular with respect to such deformation. A correction to the restoring forces must be made to offset this hourglass motion. This correction must be singular with respect to constant stress states and rigid body translations. The constant-stress states produce motions as shown in Figure 1b) and 1c). It is clear that no sum of these motions and a translation in y will produce the deformation shown in 1a). Thus, the hourglass deformation is indeed singular with respect to translations and constant-stress states.

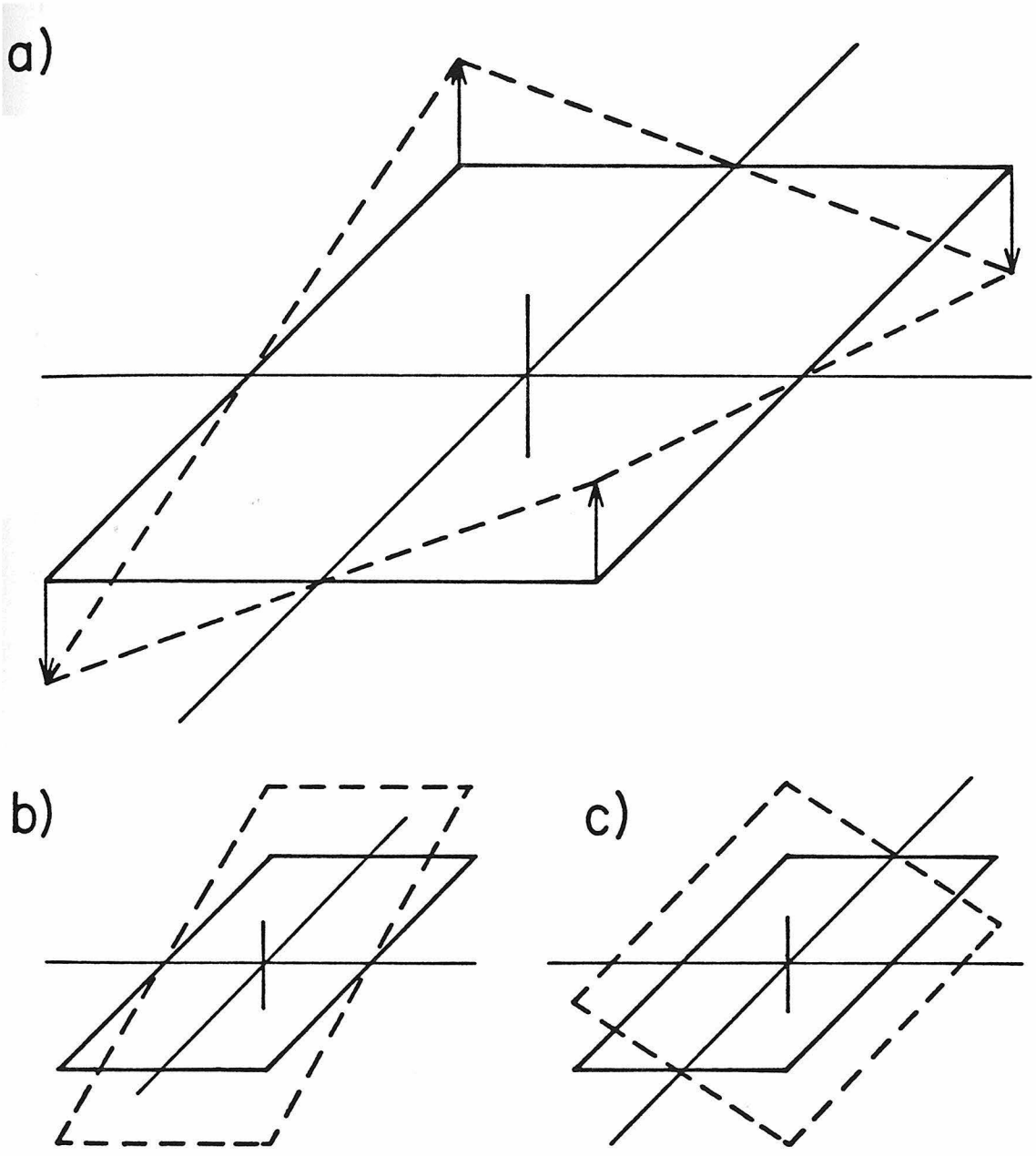

Figure 1: Types of SH motion of a 2-D rectilinear element. a) shows the hourglass mode for SH motion. Arrows at the element corners show the direction of displacement in y. The displacement and stress at the centroid (coordinate origin) of the element are zero. b) and c) show the motions accounted for in the uncorrected stiffness matrix, the constant stress modes.

For a body undergoing pure antiplane (SH) deformation, perpendicular to the x-z plane, the following conditions are satisfied:

$$\begin{aligned} &\text{a)} \quad u_x = u_z = 0. \\ &\text{b)} \quad \sigma_{ii} = 0. = \sigma_{xz} \\ &\text{c)} \quad \sigma_{xy} = \mu \frac{\partial u_y}{\partial x} \\ &\text{d)} \quad \sigma_{zy} = \mu \frac{\partial u_y}{\partial z} \end{aligned} \tag{13}$$

These relations are used as a basis to derive the form of this hourglass correction factor to the restoring forces for the case of SH motion. Using equations (7), (8) and (9) and the equation (14) below, from Zienkiewicz (1971), the hourglass correction to the restoring force at node m, R_i^m, can be calculated. The details of this calculation are given in the following paragraphs. Equation (14) expresses the hourglass restoring forces on each node in terms of the interpolation functions, the tractions on the surfaces of the surrounding elements and the body forces in those elements.

$$R_i^m = \sum_{e_m} \int_{V_e} h_i P^m(\underline{z}) dV + \sum_{e_m} \int_{S_\sigma} P^m(\underline{z}) T_i dS \tag{14}$$

where

h_i — body forces in volume V, i component i=1, ..., D

S_σ — the portion of the element surface S on which tractions T_i are specified

$\sum_{e_m}$ — sum over all elements bounding the node

To calculate the hourglass restoring forces the traction, T_i, on the element surfaces are needed. The quantities used as tractions for the purpose of calculating hourglass restoring forces are the stresses σ_{xy} and σ_{zy}. Consider the 2-D rectilinear element illustrated in Figure 2, with a linear varying traction σ_{zy} applied to its sides at $z=\pm b$ and σ_{xy} applied to its sides at $x=\pm a$. Let the form of the tractions σ_{xy} be

$$\sigma_{xy} = \mu \frac{\partial u_y}{\partial x} = \sigma_0 z \tag{15}$$

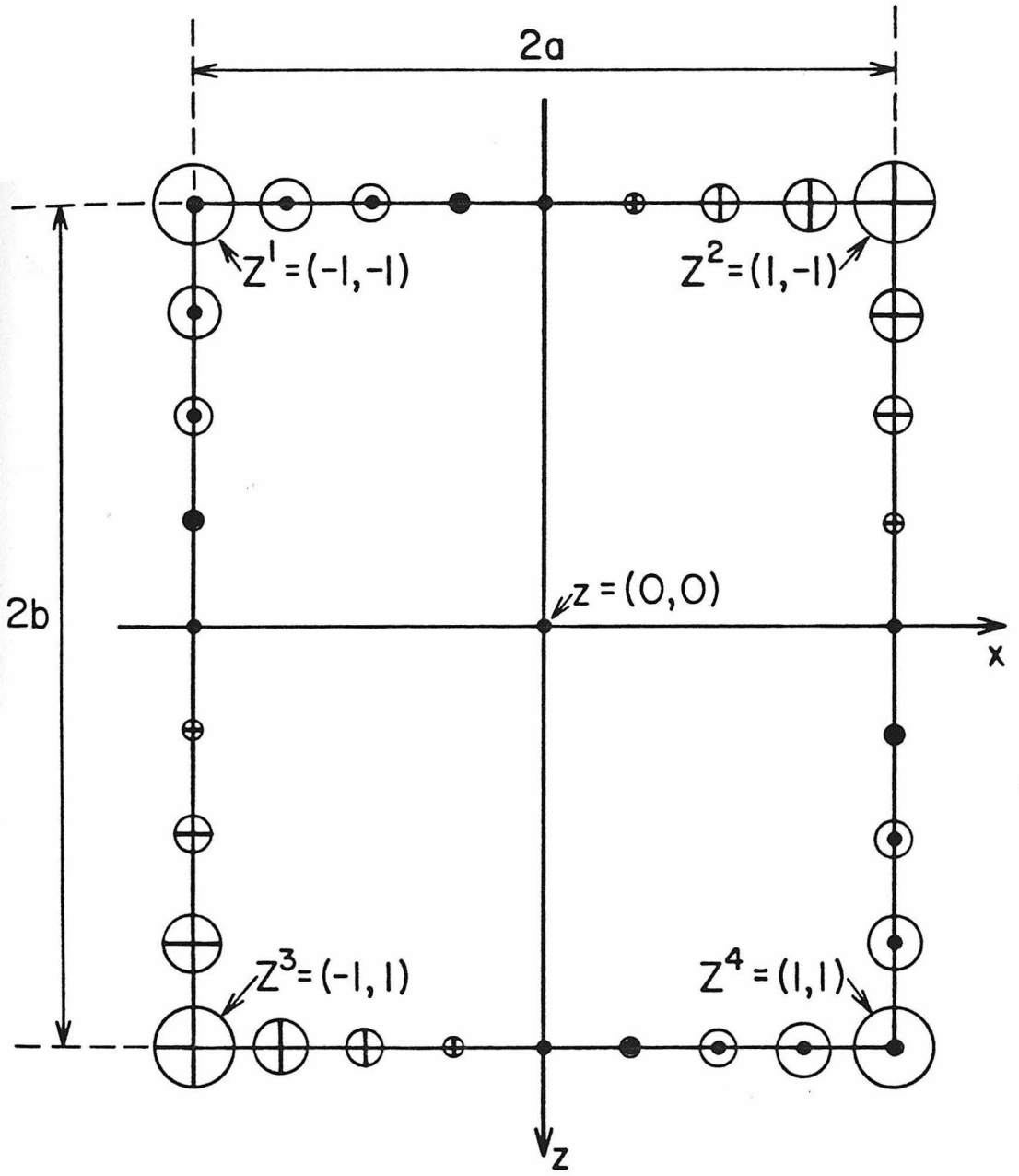

Figure 2: Configuration of an element used to calculate hourglass restoring forces for 2-D SH motion. The diameters of the circles on the element edges indicate the amplitudes of the applied tractions T_i ($T_i = \sigma_{xy}$, $x=\pm a$, $T_i = \sigma_{zy}$, $z=\pm b$) at selected points. Variation between illustrated points is linear. Circles with embedded crosses indicate motion into the page. Those with embedded dots indicate motion out of the page. Z_i are the natural coordinates of the nodes. The lengths a, b are the dimensions of the element in the Cartesian coordinate system.

From this relation u_y can be determined by integrating σ_{xy} with respect to x.

$$u_y = \int \sigma_0 z dx. = \sigma_0 zx + f(z) \tag{16}$$

However, at x=0, z=b, u_y=0 so f(z)=0. Now u_y at each of the j nodes surrounding element e may be determined. Expressing the u_y for node m, m=1,..,j, as the m^{th} element of a vector $\{U_y\}$, and defining the unit vector $\{1\}$ to carry the sign information as

$$\left\{1\right\}^T = \left\{-1,\ 1,\ 1,\ -1\right\} \tag{17}$$

enables the y displacements at the nodes to be written

$$\left\{U_y\right\} = \begin{Bmatrix} u_y(-1,\ 1) \\ u_y(\ 1,\ 1) \\ u_y(-1,-1) \\ u_y(\ 1,-1) \end{Bmatrix} = \frac{\sigma_0 ab}{\mu}\left\{1\right\} \tag{18}$$

Simple manipulation of (18) leads to the following expression for σ_0

$$\sigma_0 = \frac{\mu}{4ab}\left\{1\right\}^T\left\{U_y\right\} \tag{19}$$

It should also be noted that equations (16), (13a), and (13d) lead directly to an expression for σ_{zy}

$$\sigma_{zy} = \mu\frac{\partial u_y}{\partial z} = \sigma_0 x \tag{20}$$

Now we have the expression for the traction $T_i = \sigma_{zy}, \sigma_{xy}$ to be used in equation (9) to calculate the restoring forces. For a 2-D quadrilateral element subject to (13) the body forces h_i are zero so the first term in (9) vanishes and the interpolation functions become

$$P^m(\underline{z}) = \frac{1}{4}\left(1 + z_1 Z_1^m\right)\left(1 + z_2 Z_2^m\right) \tag{21}$$

Substituting (21) into (14) gives the following expressions for R^m, the hourglass restoring forces.

$$R^1 = -\int_{-a}^{a} \frac{1}{2}(1-z_1)\,\sigma_0 x\,dx + \int_{-b}^{b} \frac{1}{2}(1+z_2)\,\sigma_0 z\,dz = \sigma_0 \frac{(a^2+b^2)}{3}$$

$$R^2 = \int_{-a}^{a} \frac{1}{2}(1+z_1)\,\sigma_0 x\,dx + \int_{-b}^{b} \frac{1}{2}(1+z_2)\,\sigma_0 z\,dz = -\sigma_0 \frac{(a^2+b^2)}{3}$$

$$R^3 = -\int_{-a}^{a} \frac{1}{2}(1-z_1)\,\sigma_0 x\,dx - \int_{-b}^{b} \frac{1}{2}(1-z_2)\,\sigma_0 z\,dz = -\sigma_0 \frac{(a^2+b^2)}{3} \tag{22}$$

$$R^4 = \int_{-a}^{a} \frac{1}{2}(1+z_1)\,\sigma_0 x\,dx - \int_{-b}^{b} \frac{1}{2}(1-z_2)\,\sigma_0 z\,dz = \sigma_0 \frac{(a^2+b^2)}{3}$$

Thus, in vector form the restoring forces are

$$\left\{R\right\} = -\sigma_0 \frac{(a^2+b^2)}{3}\left\{1\right\} \tag{23}$$

Substituting (15) in (19) gives the value of the restoring forces used in the SH FE code. Square elements were used, that is a=b, so the final form of the hourglass restoring force corrections are:

$$\left\{R\right\} = \frac{\mu}{6}\left\{1\right\}\left\{1\right\}^T\left\{U_y\right\} \tag{24}$$

This restoring force has been implemented in the version of SWIS used for all subsequent calculations

It remains to be shown that these corrections are necessary and adequate to allow the FE code to produce accurate results. To illustrate the effect of the corrections two test examples were completed, each of them with and without the hourglass restoring

force terms. The first example uses a point source located at one of the nodes within the grid. This source configuration is known to be a severe test of the stability of a FE or finite difference (FD) calculation. The second example uses a two step procedure, the validity of which will be demonstrated later, to couple energy propagated from a distant line source into the FE calculation through the edge of the FE grid. This procedure produces a more stable source and introduces hourglass instabilities only in the FE portion of the path. Consequently, smaller differences are introduced into the results when hourglass restoring forces are omitted.

Results of the first set of calculations, using the line source within the grid, are shown in Figure 3. The line source is located at a depth of 10 km from the free surface and a horizontal distance of fifty kilometers from the left hand grid edge. The grid has dimensions of 200x100 nodes, and node spacing of dx=dy=0.5 km. All calculations use a time step of 0.05s. The displacement time history of the source is a triangle eight time steps wide with a rise time of four time steps. Each group of three seismograms shown in Figure 3 is recorded at a given node. The nine nodes for which seismograms are illustrated surround four adjacent elements that share a common node. That common node is 12.5 km from the source, at the same depth as the source. The geometric arrangement of the groups of seismograms in Figure 3 is identical to that of the nodes at which they are recorded. The maximum amplitude of each trace is normalized to one. The uppermost seismograms in each group of three seismograms in Figure 3 is calculated by direct numerical evaluation of the analytic expression for the propagation of waves from a line source through a half-space. This expression is

$$u_y(x,z,t) = \int_{r_1/v}^{t} \frac{f(t-\tau)}{\left[\tau^2 - r_1^2/v^2\right]} d\tau + \int_{r_2/v}^{t} \frac{f(t-\tau)}{\left[\tau^2 - r_2^2/v^2\right]} d\tau \qquad (25)$$

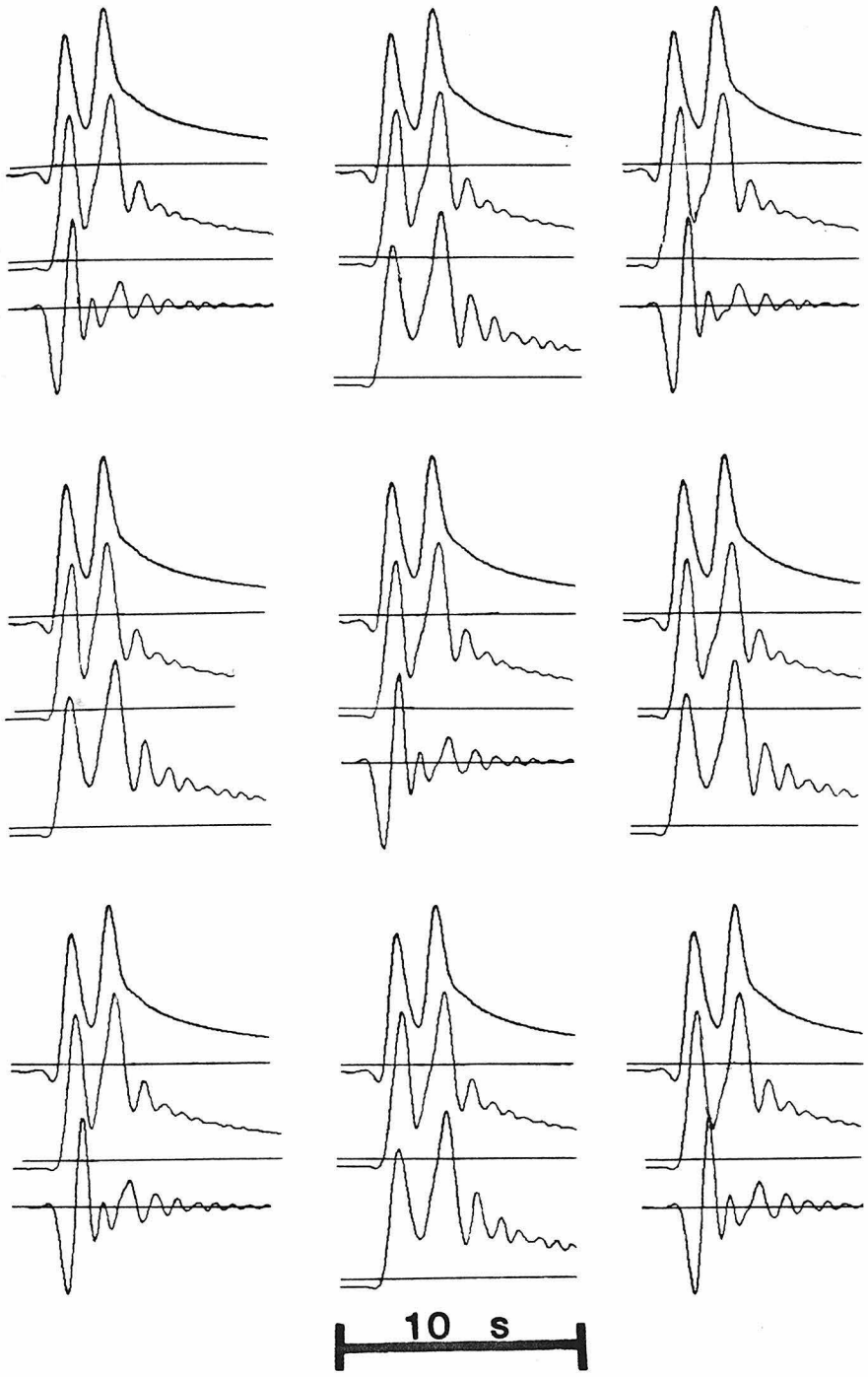

Figure 3: Waveforms for synthetic and FE seismograms calculated at nine adjacent nodes. Amplitude of each trace is normalized to one. Each group of three traces is recorded at one node. The groups of traces are displayed in the same geometrical arrangement as the nodes at which they are recorded. The central node is at a depth of 10 km, 12.5 km from a 10 km deep source. The spacing between the illustrated nodes is 0.5 km. In each group the top trace is synthetic, the second trace is a FE result including hourglass restoring forces, and the third trace is a FE result without hourglass restoring forces.

Where r_1 is the direct source to receiver distance, r_2 is the source to receiver distance for the reflection from the free surface, v is the SH wave velocity in the half-space, t is the time of observation with t=0 being the origin time, and x and z are the receiver coordinates. The first term on the right hand side of this equation gives the direct arrival, the second term the reflection from the free surface. The first peak in each synthetic is the direct arrival, the second peak is the free surface reflection. The central seismogram in each group is the FE result including the hourglass restoring forces. The last seismogram in each group is the FE solution omitting the hourglass terms. The waveforms and amplitudes for the first two traces in each group differ mainly in that some spurious oscillations are present in the FE solution. These oscillations are due to instabilities caused by the finiteness and high frequency of the source. The waveforms for the FE solution without hourglass corrections show marked discrepancies when compared to either the corrected FE solutions or the synthetics. For alternate nodes in any row or column these discrepancies have a different character. In one case the shape of the waveform shows only a small discrepancy and the peak amplitude is increased by more than 10%. In the other case the entire character of the waveform changes and the amplitude decreases by at least 20%. Clearly the hourglass corrections are necessary if accurate results are to be determined.

The second example used a 100x100 node FE grid whose first column is 1500 km from a ten kilometer deep line source in a layer over a half space. The layer has density 2.7 g/cm^3 and SH wave velocity 3.5 km/s and the half space has density 3.2 g/cm^3 and SH wave velocity 4.5 km/s. The time step size and the vertical and horizontal spacing of nodes in the FE grid were identical to those used in the previous example. Seismograms were calculated for a group of nodes along the surface and down depth sections at twenty five, forty and sixty five nodes from the grid edge using a two step procedure. First, synthetic seismograms were generated at a horizontal

distance of 1500 km from the source, at the surface and at half kilometer depth intervals to a depth of thirty kilometers. These seismograms were used to constrain the displacement time histories of the leftmost column of nodes in the FE grid. It will be shown that applying such constraints completely specifies the distant source. Analytic synthetic seismograms were also generated at the same locations. The two step seismograms, which have been propagated through a FE grid for thirty to thirty five kilometers between 1500 km and the receiver should be identical to the analytic synthetics at the same receivers if the FE calculation is stable. Results from this test are shown in Figure 4. The pairs of two step seismograms illustrated show how the introduction of the hourglass corrections effects the waveform and amplitude of the results. The upper trace in each pair includes the hourglass restoring force the lower trace does not. At the scale of the figure the corresponding analytic synthetics are indistinguishable from the two step results with hourglass restoring terms. The uppermost number to the right of each trace is the ratio of the peak to peak amplitude of the illustrated trace to that of a synthetic calculated for the same location. The lower number is the same type of ratio using an RMS amplitude measure discussed in detail later. These three pairs of seismograms were recorded at the free surface at distances of 30, 32.5, and 35 km from the left hand grid edge. These distances illustrate the behavior of the amplitudes at adjacent nodes within the grid. Some intermediate nodes have been omitted, but the alternation of higher and lower amplitudes for the uncorrected synthetics is seen as long as an even number of nodes are skipped between illustrated nodes. Examining the illustrated results shows that adding the hourglass restoring force term makes a small but perceptible change to the waveform. This change produces a slight improvement to the already excellent correspondence between the FE and analytic waveforms. However, the important improvement made when hourglass restoring force terms are included is in the amplitude correspondence between the FE and synthetic results. When no hourglass corrections are made the amplitudes of FE

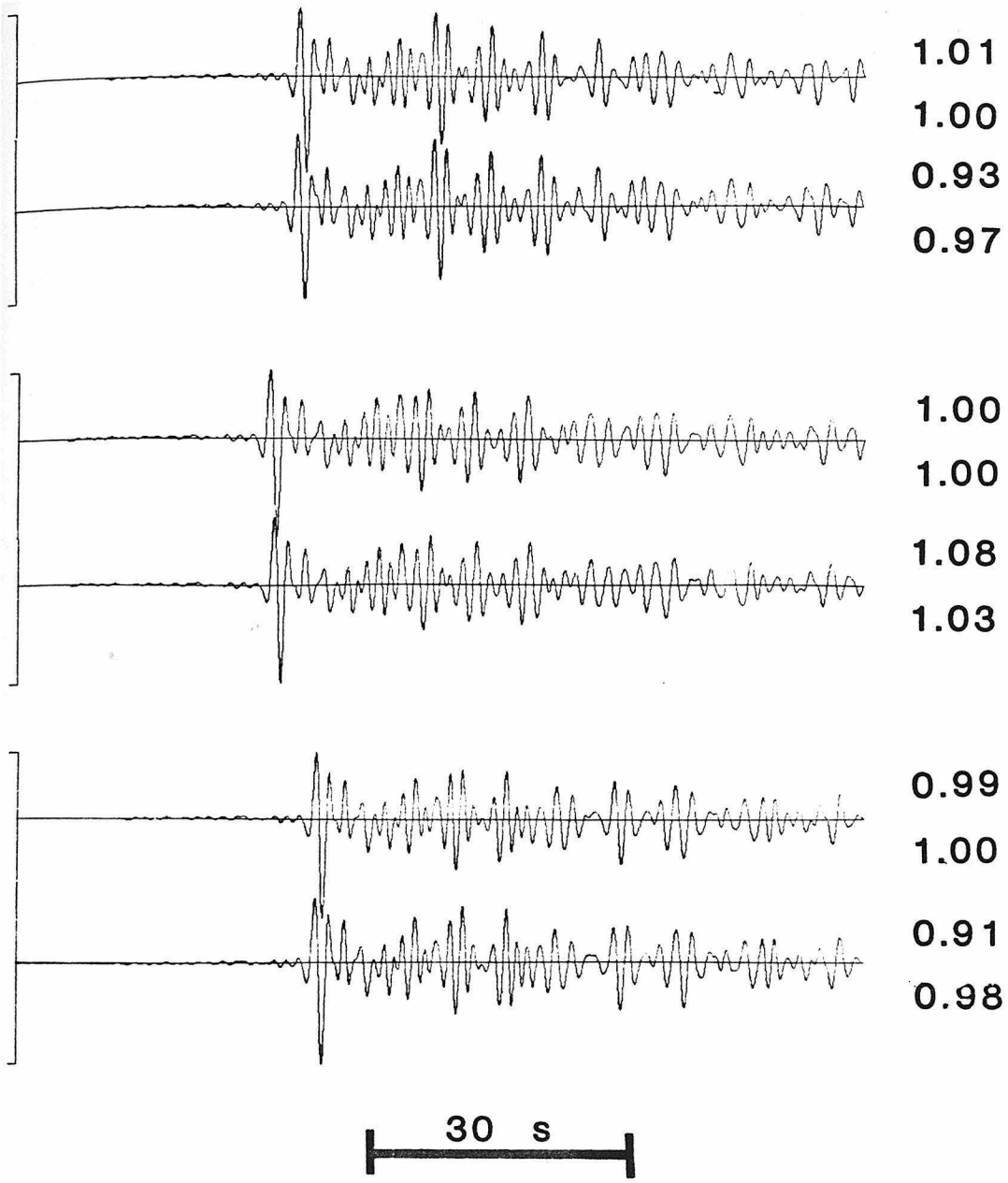

Figure 4: Waveforms for hybrid seismograms calculated in a FE grid removed from the source by a distance of 1500 km. Seismograms are calculated for a line source in a layer over a half-space. Each pair of seismograms is recorded at a given node. The upper trace in each pair includes the hourglass restoring force terms. The lower trace in each pair does not. The number to the right of each trace are amplitude ratios. The amplitude of the illustrated seismogram is compared to that of a synthetic calculated for the same location. The upper number is a ratio for peak to peak amplitudes, the lower for RMS amplitudes. Seismograms are of duration 102 seconds.

seismograms at successive nodes along any row or down any column alternate between being larger and smaller than those of the corresponding synthetics. Introduction of the hourglass restoring force terms removes this oscillation in the amplitude. Clearly the presence of the oscillatory term caused by the hourglass instabilities superimposed on the correct solution is not desirable. Thus, it is necessary to apply the hourglass restoring force correction to obtain the correct solution.

With these additions the SWIS FE code produces accurate solutions. However, the calculations are extremely time consuming. An effort was made to increase the speed of the calculations for the Cartesian SH option used for the calculations in this study. First, the options for general curvilinear and cylindrical coordinates were removed. Some small subroutines were incorporated into higher level routines to reduce the number of subroutine calls. The system was defined to have two dimensions and one degree of freedom thus removing a number of decision statements and blocks of code necessary to the implementation of other options. These changes also allowed the removal of a number of do loops and their replacement with single statements. Other modifications were made where incorporation of analytic simplifications of the expression being evaluated by the code substantially reduced the number of necessary calculations. The overall effect of these modifications was an increase of between a factor of four and and factor of five in the speed of execution of the modified and accelerated SWIS code over the original SWIS code for case of the propagation of SH waves in Cartesian coordinates.

The FE and propagator matrix methods used in the studies have now been explained, and the components of each which must be understood to explain the Representation Theorem coupling methods have been described. The modifications made to the SWIS FE code have increased the speed of the code by more than a factor of five. They have also allowed the application of time dependent displacement

constraints to selected nodes in the grid, and the recording of time slices, or snapshots of the motion of each node in the grid at a given time. These additional capabilities are utilized to implement the propagator to FE coupling, to allow the use of larger FE grids, and to better understand the propagation of disturbances through complex structures. Next it is necessary to understand the Representation Theorem (RT) and how it can be applied to coupling these two methods to produce a hybrid method utilizing the strengths of each.

The Representation Theorem and Green's Functions

The basis of the method used to couple the propagator matrix calculation to the FE calculation, or to couple the FE calculation into the Propagator matrix calculation is the application of the Representation Theorem on the boundary between the regions in which each method is used. The Representation Theorem (RT) relates the displacement at a point in a volume V to the body forces f_i in the volume V and to the displacements u and the tractions T_i on the surface S of volume V. There are many equivalent ways of expressing the RT, for example (Aki and Richards; eq 2.41)

$$u_p(\vec{x},t) = \int_{-\infty}^{+\infty} d\tau \iiint_V f_i(\vec{\xi}\,,\tau)\, G_{ip}(\vec{x},t-\tau\,;\,\vec{\xi},0)\, dV(\vec{\xi}) \tag{26}$$

$$+ \int_{-\infty}^{+\infty} d\tau \iint_S \left\{ G_{ip}(\vec{x},t-\tau\,;\,\vec{\xi},0)\, T_i\left[\, \vec{u}(\vec{\xi},\tau),\, n_j \right] - c_{ijkl}\, \frac{\partial}{\partial x_l} G_{kp}(\vec{x},t-\tau\,;\,\vec{\xi},0)\, u_i(\vec{\xi}\,,\tau)\, n_j \right\} dS(\vec{\xi})$$

where $\vec{\xi}$ the location of a point of the surface S of volume V, $\vec{x}$ the location of a receiver in volume V, $u_p(\vec{x},t)$ is the p component of the displacement at time t at the receiver location, $\vec{x}$, t is the time at which the observation is made, τ is the source time, $T_i(\vec{\xi}\,,\tau)$ is the boundary condition specifying stress as a function of source time τ for all points on surface S, n_j is the j^{th} component of the outward unit normal to the surface S, $u_i(\vec{\xi}\,,\tau)$ is the boundary condition specifying displacement as a function of source time τ for all points $\vec{\xi}$ on the surface S, and G_{ip} is the Green's function which

represents the displacement in the i^{th} direction at $\vec{x}$ at time t due to a unit impulse applied in the p^{th} direction at position $\vec{\xi}$ at time τ. The desired Green's functions are obtained by solving the wave equation below in volume V, subject to the initial conditions that G_{ip} and $\frac{\partial}{\partial x} G_{ip}$ are zero for $t \leq \tau$.

$$\delta_{ip}\, \delta(\vec{x} - \vec{\xi})\, \delta(t - \tau) = \rho \frac{\partial^2}{\partial t^2} G_{ip}(\vec{x}\ ,\ t\ ;\ \vec{\xi}\ ,\ \tau) - \frac{\partial}{\partial x_j} \left\{ c_{ijkl} \frac{\partial}{\partial x_l} G_{kp}(\vec{x}\ ,\ t\ ;\ \vec{\xi}\ ,\ \tau) \right\} \quad (27)$$

The form of the RT given as equation (26) is not optimal to demonstrate how the coupling of the two methods is accomplished. To transform it to a more manageable form several conditions are applied. First, it is assumed that no body forces are present within volume V. Thus, the first term on the right hand side of equation (26) vanishes. Next, the medium is assumed to be isotropic. This reduces the number of independent c_{ijkl} terms to nine from eighty one. It allows them to be written as

$$c_{ijkl} = \lambda\, \delta_{ij}\, \delta_{k_L} + \mu\, (\delta_{ik}\, \delta_{jl} - \delta_{il}\, \delta_{jk}) \quad (28)$$

Using these values of c_{ijkl} the tractions T_i can be expressed as

$$T_j = \tau_{ij}\, n_i = c_{ijpq} \frac{\partial}{\partial \xi_q} u_p(\vec{\xi}\ ,\ \tau)\, n_j = \left\{ \lambda\, \delta_{ij}\, u_{l,l} + \mu\, (u_{i,j} + u_{j,i}) \right\} n_j \quad (29)$$

Substituting (28), and (29) into (26) a more useful form of the RT is found.

$$u_p(x,t) = \int_{-\infty}^{+\infty} d\tau \iint_S \left\{ G_{pi} \tau_{ij} + \lambda G_{pl,l}\, u_j + (G_{pi,j} + G_{pj,i})\, u_i \right\} n_j\, dS(\vec{\xi}) \quad (30)$$

Where all derivatives are with respect to $\vec{\xi}$. For the case of SH waves only, (30) can be further simplified by applying the conditions governing SH motion and by assuming all quantities are constant with respect to x_2, that is

$$u_1 = u_3 = 0 \tag{31}$$

$$\tau_{11} = \tau_{33} = \tau_{13} = \tau_{31} = 0$$

$$G_{j1} = G_{j3} = G_{3j} = G_{1j} = 0$$

$$-\frac{\partial}{\partial x_2} = \frac{\partial}{\partial \xi_2} = 0$$

Also, it is usual to assume that the motion and stress are everywhere zero for times less than τ=0. Applying this condition and the conditions given in (31) to (30) and integrating from $-\infty$ to ∞ over x_2 gives the form of RT appropriate for a 2-D SH line source.

$$u_2(\vec{x},t) = \int_0^\infty d\tau \int_C \mu \left\{ \Gamma_{22} u_{2,k} + \Gamma_{22,k} u_2 \right\} n_k dC(\xi_1,\xi_3,\tau) \tag{32}$$

where C is the curve defined by the intersection of the surface S with the x_1–x_3 plane, and following the notation of de Hoop (de Hoop 1958)

$$\Gamma_{ij} = \int_{-\infty}^{+\infty} G_{ij}(x_1,x_3,t)dx_2 \tag{33}$$

Omitting the integration over x_2 gives a SH RT appropriate for a 3-D analogue of the procedure described below. Further discussions in this chapter relate to the 2-D problem.

The form of the line source Green's function given by de Hoop (de Hoop 1958) is

$$\Gamma_{22} = \frac{1}{2\pi\rho\beta^2} K_0(sr/\beta) = \frac{1}{2\pi\mu} \int_{r/\beta}^{\infty} \frac{1}{\left[t^2 - r^2/\beta^2\right]^{1/2}} e^{-st}\, dt \tag{34}$$

$$= \frac{1}{4\pi\mu} \int_{-\infty}^{\infty} \exp \frac{\left[-(s/\beta)(\xi^2 + r^{2)^{1/2}}\right]}{(\xi^2 + r^{2)^{1/2}}} d\xi$$

where $r^2 = (x_1 - \xi_1)^2 + (x_3 - \xi_3)^2$. This form is valid for a whole space, and must be modified to satisfy the half-space problem. The whole space problem is a solution to equation (27) subject to the radiation condition that $\Gamma_{22} \rightarrow 0$ and $\frac{\partial \Gamma_{22}}{\partial r} \rightarrow 0$ as $r \rightarrow \infty$. For the half-space problem Γ_{22} must satisfy an additional BC as well as satisfying equation (27) and the radiation condition. The BC Γ_{22} must satisfy is that there be no stress, σ_{zy}, on the free surface. That is, the relation $\frac{\partial \Gamma_{22}}{\partial z} = 0$, must be satisfied on the free surface, at z=0. This is equivalent to specifying that volume V is a half-space rather than a whole space. Physically, the introduction of the free surface boundary at z=0 implies that energy that would otherwise continue to radiate towards infinity will instead be reflected back toward the depth of the receiver. This implies that the addition of a term of the same form as the whole space solution, so that it will satisfy the original equation, but with the propagation distance r equal to the propagation path length of a surface reflection rather than a direct arrival, will satisfy the zero stress BC at the surface. The half-space Green's function for a SH line source given below is based on this reasoning and can be shown to satisfy the BC, the radiation condition, and the initial equation.

$$\Gamma_{22}(\vec{x}: \vec{\xi}) = \frac{1}{2\pi\mu} \left[K_0(sr^-/\beta) + K_0(sr^+/\beta)\right] \tag{35}$$

where $r^{\pm} = \sqrt{(x_1-\xi_1)^2 + (z\pm\xi_3)^2}$. To compare this form for the Green's functions to the forms of the displacements used in the rest of this discussion it is first necessary to transform the equation from the Laplace transform domain to the Fourier transform domain, and to express the modified Bessel function, K_0, in terms of Hankel functions or of exponentials. Examining the second expression in the first line of equation (34) indicates that it is the Laplace transform of a quantity, f(r,z), where f(r,z) is the first term in the integrand. Applying the change of variables, $\xi^2 = (vt)^2-r^2$, changes the lower limit of integration to zero and the integration variable to ξ. Then, noticing the symmetry of the resulting integrand allows the lower limit of the integral to be changed to $-\infty$ if a factor of one half is introduced. This gives the form of the equation in the second line of equation (34). Finally, introducing an additional change of variables, $s = i\omega$, changes the Laplace transform to a Fourier transform. The resulting expression for the Green's function is

$$\Gamma_{22} = \frac{1}{2\pi\mu}\left[K_0(ik_\beta r^+) + K_0(ik_\beta r^-)\right] \qquad k_\beta = \frac{\omega}{\beta} \tag{36}$$

Next, it is useful to transform the modified Bessel functions, K_0, into Hankel functions to make direct comparison with the displacement solution for the line source in a layered half-space possible. The modified Bessel function can be expressed in terms of Hankel functions (Abramowitz and Stegun, eq 9.6.4)

$$K_\nu(z) = \frac{-i\pi}{2} e^{-\frac{i\pi}{2}\nu} H_\nu^{(2)}\left(ze^{-i\pi/2}\right) \qquad -\frac{\pi}{2} < \arg(z) \leq \pi \tag{37}$$

The argument of the modified Bessel function, $ik_\beta r$, is of the form ix where x is a positive real number. Thus, $\arg(z)=\frac{\pi}{2}$, and the expression (37), is applicable. Substituting equation (37), with $\nu=0$, into equation (36) gives the first expression in the next group of equalities. It is in the form that it can be directly compared to a line source displacement expression for a homogeneous half-space that is used in the propagator

technique to develop the expression for the layered half-space. This expression is

$$\overline{v}(r,\phi,z) = \frac{i\pi}{2}\left[H_0^{(2)}(k_\beta r^+) + H_0^{(2)}(k_\beta r^-)\right] \tag{38}$$

Alternately, the equation (36) can be written in terms of integrals of exponentials and then be compared directly to the solution for a line source in a homogeneous half-space. The exponential form of the equation is the result of substituting the appropriately transformed version of the integral expression in equation (34) for each modified Bessel function in equation (36). This representation of the Green's function is given as the second equality in the next group of equations.

$$\Gamma_{22} = \frac{-i}{4\mu}\left[H_0^2(k_\beta r^+) + H_0^2(k_\beta r^-)\right] \tag{39}$$

$$= \frac{1}{2\pi\mu}\left[\int_{r_1/\beta}^{\infty} \frac{1}{\left[t^2 - r_1^2/\beta^2\right]^{1/2}} e^{-i\omega t} dt + \int_{r_2/\beta}^{\infty} \frac{1}{\left[t^2 - r_2^2/\beta^2\right]^{1/2}} e^{-i\omega t} dt\right]$$

Comparing the second equality in equation (39) to equation (25) for the line source in a homogeneous half space, and comparing the first equality in (38) to the alternate expression for the line source in the homogeneous half-space, equation (38), shows that

$$\overline{u_y}(x,z) = \frac{1}{2\pi\mu}\Gamma_{22}(\vec{x};\vec{\xi}) \tag{40}$$

Thus, the displacement Green's function can be calculated in a manner identical to the displacement solution, in either a layered half-space or a homogeneous half space. However, one must be careful to include the multiplicative factor of $\frac{1}{2\pi\mu}$ when determining the Green's functions for use in the Representation Theorem expressions.

The form of the Representation Theorem (RT) given in equation (32) has been used to determine approximate analytic solutions to the problems of propagation across a surface step (Knopoff and Hudson 1964), and of propagation in a layered elastic wedge (Hudson and Knopoff 1964). This is also the form used in this study to develop procedures for the coupling of FE and Propagator Matrix solutions.

Figures 5 and 6 show geometries useful for developing and explaining the methods to be used for coupling FE and propagator matrix methods. The purpose of developing these methods is to allow the propagation of wavefields from a source to a receiver through a series of plane layered media separated by complex regions that cannot be modeled using a plane layered structure, or by changes in the layered structure. For example, the complex regions that will be considered in chapter 2 are continent to ocean and ocean to continent boundaries. A simple geometry, consisting of a layer over a half-space, is used as a test case to show how the methods work, and how they can be applied in both this simple case and in more complicated cases. Figure 5 can be used to illustrate the geometry used to couple energy traveling through a layered medium, into a FE grid which may contain structures of arbitrary complexity. Figure 6 can be used to illustrate the coupling from such a FE grid into a layered structure where propagator matrix methods are used to transmit the energy further. Each of these figures will be discussed in detail later.

Propagator to Finite Element Coupling

In a layered medium the wavefield can be mathematically constructed at any point receiver within the layered half-space using the propagator matrix technique and an appropriate form of a source representation. The resulting seismogram at any point in the layered half-space will include not only a direct arrival and a surface reflection but also the superposition of many multiple reflections which produce the surface waves in the wavetrain. Although the seismograms are produced as modal

sums, in the limit of using all possible modes, they are equivalent to summing over all possible multiple reflections in terms of rays. Thus, they can be conceptualized in terms of rays. To simplify the graphical representation used in Figures 5 and 6 the seismogram at a source point in the layered half-space is represented by a single direct line from the source to the receiver. This line also implicitly represents all the reflected and multiply reflected rays in that seismogram which would hopelessly clutter the diagrams if they were included.

Figure 5 shows a graphical representation of a layer over a half-space. The source is represented by a large asterisk, and each receiver by a large point. The origin of the coordinate axes is also shown as a large point. The coordinate axes $x_1 = x$, and $x_2 = z$, are labeled at the origin of the Cartesian coordinate system used in this discussion. The arrows show the directions in which the values of each coordinate increase. The distance x increases to the right, the depth z increases downwards, and the coordinate $y = x_2$ increases out of the page. All motion occurs in the y direction since this is an SH wave problem. The free surface of the half-space is located at z=0, and the source is located at x=0 at depth h. The second long horizontal line is located at z=D, where D is the thickness of the layer above the half-space. The points denoting the receivers, also illustrate the locations of the nodes in two columns of a FE grid. The intervening columns of nodes are not illustrated to avoid cluttering the diagram. The short horizontal line that connects the lowermost nodes is at $z = D_{FE}$, and denotes the bottom of the FE grid. The FE grid is assumed to extend off the page toward the right. The vertical line connecting the leftmost column of receivers shows the lefthand edge of the FE grid. For the sake of simplicity and clarity the structure illustrated within the FE grid is the same layer over the same half-space as that used in the region traversed using the propagator matrix calculation.

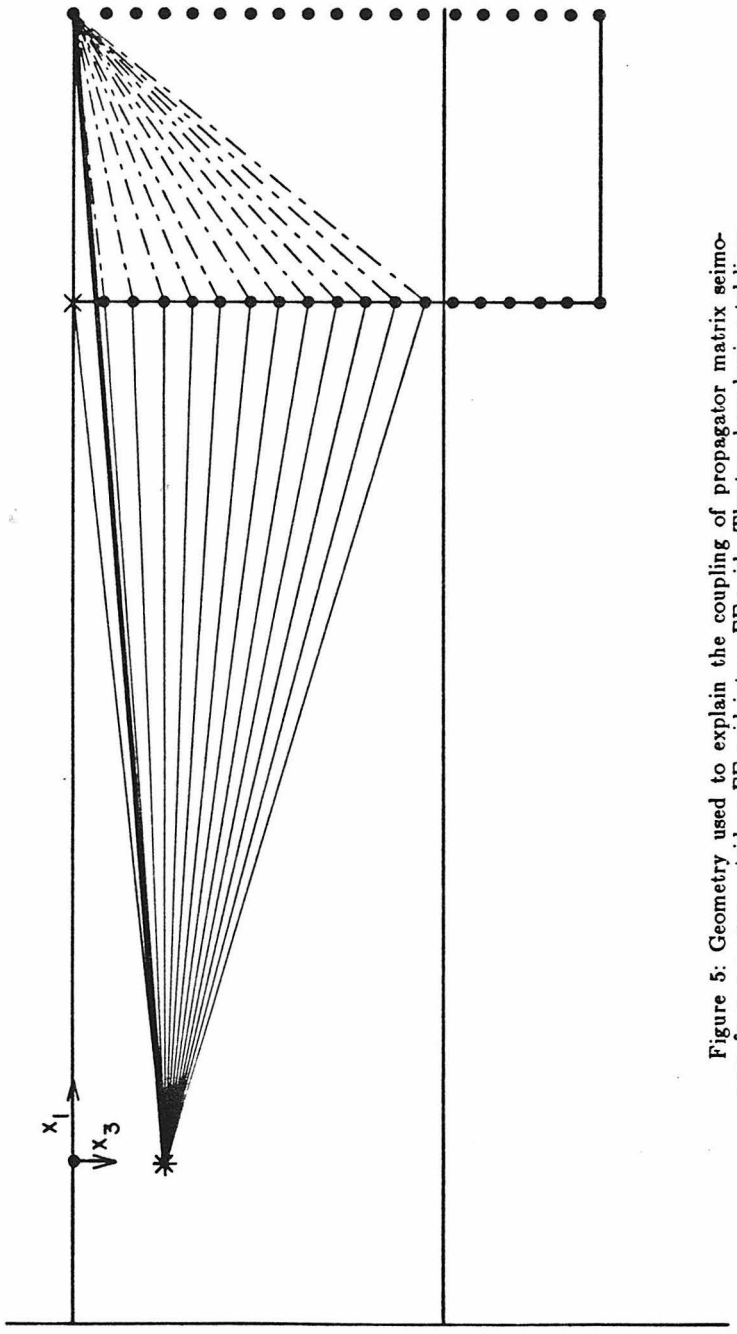

Figure 5: Geometry used to explain the coupling of propagator matrix seismograms from a source outside a FE grid into a FE grid. The two long horizontal lines show the free surface and the boundary between the layer and the half-space. The source is shown as an asterisk. Two columns of FE nodes are shown as dots. The vertical line connecting the dots and the short horizontal line perpendicular to it are the grid edges. The heavy solid line from the source to the surface reciever in the grid denotes the direct analytic seismogram, the solid lines between the source and the grid edge nodes denote the direct forcing functions, and the dotted lines indicate the source to reciever paths, for the sources created by the application of the forcing functions at the grid edge, that integrate to give the hybrid seismogram.

The coupling of a wavefield defined by the discrete sampling of seismograms along the leftmost edge of a FE grid, into that FE grid is straightforward. The seismograms, for a specified source function, are generated at a group of receivers equally spaced in z located a horizontal distance X from the source. The depth spacing Δz between the receivers is the node spacing in the FE grid into which the wavefield is to be coupled. The distance X is the minimum separation between the source and the lefthand edge of the grid. The solid lines connecting the source to the receivers along the left edge of the grid illustrates these seismograms. They are calculated by transmitting the appropriate source functions through the layer over a half-space structure from the source to the leftmost edge of the FE grid by using the propagator matrix method. The seismograms are then applied as displacement time history constraints on the leftmost column of nodes in the FE grid. The application of this type of constraints to a column of nodes in the FE grid completely specifies the subsequent motion at all points in that FE grid. Thus, a hybrid seismogram can be recorded at any node in the FE grid provided a FE calculation of suitable duration is completed. Consider, as an example, that the receiver at which the hybrid and analytic seismograms are to be compared is the surface receiver at a distance X2 from the source. The minimum distance from the source to the second column of nodes illustrated in Figure 5 is X2. The heavy solid line in Figure 5 represents the analytic seismogram, calculated using only the propagator matrix method and the appropriate source functions. The hybrid seismogram is represented by the integration over all the dashed paths connecting the edge nodes and the receiver. Each dashed path represents a seismogram for which the appropriate forcing function is a time dependent source.

Figure 5 shows the layer over a half-space structure extending into the FE grid. A series of calculations completed using such a homogeneous structure provides a

useful test of the procedures used. It allows the comparison of the hybrid solutions, those solutions propagated from the source to the receiver using a combination of methods, to analytic synthetics, those calculated entirely with the source functions and the propagator matrix technique, for receivers in locations identical with respect to the source. Hybrid and analytic synthetics calculated by using the layer over a half-space structure in both portions of the path will be shown later. These seismograms will be used to demonstrate the validity of the coupling method by comparing the hybrid results to the analytic results. Although, in this example, the FE grid contains the same layer over a half-space structure as that used for the propagator matrix calculations, any other arbitrary structure can be put into the FE grid without altering the coupling method. However, the calculation of analytic synthetics to which the resulting hybrid synthetics can be compared may be difficult or impossible. Thus, although we wish to address the effects of complex structures within the FE portion of the path the simple case where the FE grid contains the same layered structure as used for the propagator matrix calculation will be discussed here as it is the best test of the method.

In the examples discussed in later sections the seismograms used as forcing functions are generated using more than one type of source. The first types of sources used are line sources, for a single point force in a homogeneous half-space or a layered half-space. For these cases the applied forcing functions are $u_y(x,y,z)$. However, the balance of the sources used are double couple point sources. The propagator matrix solutions for these sources are of the form $\overline{v}(r,\phi,z)$. The displacements are expressed in cylindrical coordinates rather than in the Cartesian coordinates appropriate to the RT integral or the Cartesian FE representation. Thus it must be demonstrated that these cylindrical displacements can be used in place of the Cartesian ones expected without adversely affecting the results. This will be demonstrated in the following paragraphs.

The expressions for $\bar{v}(r,\phi,z)$ for the dip slip and strike slip faults, equations (6), are in cylindrical coordinates (r,ϕ,z), where $r = \sqrt{(x^2+y^2)}$. Displacement time histories of a series of locations corresponding to the first column of nodes in a FE grid a distance r_1 from the source were evaluated using these expressions. When these displacement seismograms are used as input forcing functions then they are used as if $\bar{v}(r,\phi,z)$ was an expression for $\bar{u}_y(x,y,z)$ rather than for $\bar{u}_\phi(r,\phi,z)$. No transformation from cylindrical to Cartesian coordinates is performed. The displacement field defined by the imposition of displacement time history constraints down the FE grid edge is then propagated an additional distance, Δr, through the FE grid to give the hybrid seismograms that approximate $\bar{u}_\phi$ at the receiver. The validity of using $\bar{v}(r,\phi,z)$ rather than $\bar{u}_y(x,y,z)$ will now be demonstrated. It will be shown that for $r_1 >> \Delta r$ substituting u_ϕ for u_y gives a good approximation of u_ϕ at the receiver despite the fact that the FE method produces 2-D rather than 3-D propagation effects.

Consider a FE grid with its leftmost edge a distance r_1 from a source, and a receiver, where hybrid and analytic synthetic results are recorded, a distance r_2 from the source. Define the distance propagated within the FE grid as $\Delta r = r_2 - r_1$. Consider, also, the expressions (6) for the displacements from a point dip slip or strike slip source. Only variations in the r coordinate need to be discussed to establish the validity of this procedure so, for clarity, (6a) or (6b) will be reduced to,

$$\left\{\bar{v}(r,\phi,z)\right\} = \bar{v}_\nu(\phi,z)\,\frac{\partial H_\nu^{(2)}(k_L r)}{\partial r} \tag{41}$$

where $\nu = 2$ for a strike slip source and $\nu = 1$ for a dip slip source. The derivative of the Hankel function can be expanded in terms of undifferentiated Hankel functions using (Abramowitz and Stegun, eq 9.1.29)

$$\frac{1}{k_L}\,H_\nu^{(2)}(k_L r) = -\,H_{\nu+1}^{(2)}(k_L r) + \frac{\nu}{k_L r} H_\nu^{(2)}(k_L r) \tag{42}$$

Each resulting Hankel function can be expanded in terms of the asymptotic expansion of H_ν for large r (Abramowitz, Stegun, eq 9.2.4)

$$H_\nu^{(2)}(k_L r) = \sqrt{\frac{2}{\pi k_L r}}\, e^{-i(k_L r - \frac{1}{2}\nu\pi - \frac{1}{4}\pi)} \qquad -2\pi < \arg(k_L r) < \pi \tag{43}$$

Replacing the derivative of the Hankel function in equation (41) with the product of k_L and the right side of expression (42), gives an expression for $\left\{\overline{v}(r,\phi,z)\right\}$ including only undifferentiated Hankel functions. Substituting the asymptotic expansion, equation (43), for each of these Hankel functions gives an alternate expression for $\left\{\overline{v}(r,\phi,z)\right\}$. It is

$$\left\{\overline{v}(r,\phi,z)\right\} = \overline{v}_\nu(\phi,z)\sqrt{\frac{2}{\pi k_L r}}\left[k_L - \frac{\nu}{r}\right] e^{i\pi\frac{(2\nu-1)}{4}}\, e^{-ik_L r} \tag{44}$$

Since we are considering the case of r large, $k_L >> \frac{\nu}{r}$, and the second term in the square brackets can be ignored, $\left\{\overline{v}(r_2,\phi,z)\right\}$ can be expressed in terms of ϕ, z, r_1, and Δr as

$$\left\{\overline{v}(r_2,\phi,z)\right\} = \overline{v}_\nu(\phi,z)\sqrt{\frac{2k_L}{\pi(r_1+\Delta r)}}\, e^{i\pi\frac{(2\nu-1)}{4}}\, e^{-ik_L r_1}\, e^{-ik_L \Delta r} \tag{45}$$

$$= \left\{\overline{v}(r_1,\phi,z)\right\}\sqrt{\frac{r_1+\Delta r}{r_1}}\, e^{-ik_L\Delta r}$$

$$\approx \left\{\overline{v}(r_1,\phi,z)\right\}\, e^{-ik_L\Delta r} \qquad \Delta r << r_1 \qquad k_L r_1 >> 1$$

Now, for a line source in a half space, equation (25), or for a line source in a vertically inhomogeneous half-space, the modal relation analogous to equation (45) is,

$$u_\phi(x2,z) = u_\phi(x1,z)\, e^{-ik_L x2-x1} = u_\phi(x1,z)\, e^{-ik_L \Delta x} \tag{46}$$

Comparing (46) and (45) shows that both expressions have the same form. In each case the displacement at r_2 can be expressed as the displacement at r_1 multiplied by a propagation factor. A FE or RT calculation will give the same propagation factor for each mode as the analytic expression, (46), above. If the displacements at r_1, $\overline{v}(r_1,\phi,z)$ or $u_y(x,z)$, and the propagation factors, $e^{-ik_L \Delta r}$ or $e^{-ik_L \Delta x}$, are correlated by considering $x1=r_1$ and $\Delta x=\Delta r$, then $\overline{v}(r_1,\phi,z)$, the 3-D solution, will be given by $u_y(x,z)$, the result of the 2-D FE or RT calculation, so long as the source is many wavelengths, $k_L r$, from the boundary and r is normal to the FE grid edge or the RT integration surface.

Finite Element to Propagator Coupling

The coupling of FE seismograms into a layered media through which they are transmitted by the propagator matrix technique and the application of the RT, is accomplished by direct evaluation of the RT integral as given in equation (32) using propagator matrix generated line source Green's functions. The geometry of the problem is illustrated in Figure 6. The geometry will be explained, then the coupling procedure will be discussed.

Figure 6 shows the geometry used to evaluate the RT integral, equation (32). Again, the layer above a half-space model is illustrated in both the FE and propagator matrix regions for clarity. In practice any structure can be used in the FE grid. The two long horizontal lines show the free surface and the boundary between the layer and the half-space. The solid vertical line which does not have dots superimposed upon it is the righthand edge of the FE grid. The FE grid is assumed to continue off the figure to the left. The source can be assumed to be either in the FE grid itself or on the far side of the FE grid. The short horizontal line shows the bottom of the FE grid. The x's shown within the grid and on its bottom boundary represent nodes in

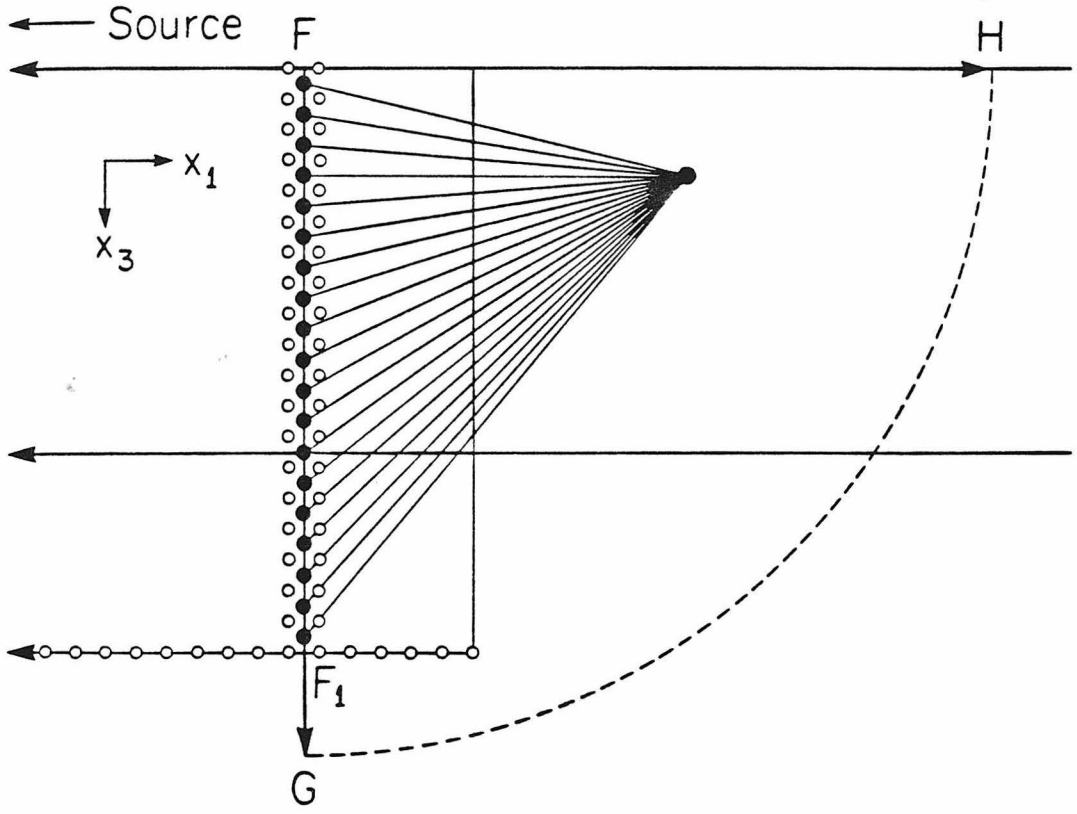

Figure 6: Geometry used to explain the coupling of FE stress and displacement time histories into propagator matrix calculations. The RT integration path, C, is shown as the closed curve FGHF. Finite element nodes are shown as open circles. The short vertical and horizontal lines are the boundaries of the FE grid. The two long horizontal lines show the free surface and the boundary between the layer and the half-space. The filled circles superimposed on the FG section of the integration path are element centers within the FE grid where stress and displacement time histories are recorded. The dot within the integration path denotes the receiver. The lines connecting the element centers and the receiver represent the line source Green's functions.

the FE grid. The two illustrated columns of nodes define the corners of a column of elements. The center of each of these elements is shown as a dot. The integration path, C, for the RT integral is illustrated as the closed curve FGHF. The arrows at G and H indicate that the integral is evaluated on the contour, C, where the x coordinate at G, and the z coordinate at H both tend to infinity. An example of a possible receiver inside the contour C is illustrated as a large dot outside the FE grid. The lines connecting the dots showing the column of element centers within the FE grid to the receiver represent the line source Green's functions for propagation from a source at the location of the element center to the receiver.

The evaluation of the RT integral on the contour, C, will be discussed in three parts. First the quantities used in the evaluation of the RT integral on the segment FG of the contour, C, will be discussed. Then, the procedure used to estimate the value of this integral will be explained. Finally, it will be shown that the contributions to the RT integral from integration along segments GH and HF of the contour, C, do not contribute to the solution.

Before the particulars of the integration procedure can be discussed, each of the quantities in equation (32) must be defined. The integration surface for the segment GH is a line with the x coordinate held constant, only the terms generated by setting k=1 in equation (32) need to be considered. Thus, the quantities of interest are, μ, u_y, σ_{xy}, Γ_{22}, and $\Gamma_{22,2}$. The displacement and stress time histories at the element centers, illustrated as dots in Figure 6, are recorded during the FE calculation. The element center displacement u_y, and the element center stress, σ_{xy}, are used as the u_2 and $\mu u_{2,1}$ terms respectively, in the RT integral (32). Line source Green's functions are calculated for the transmission of a unit line displacement, applied at each of the nodes illustrated as dots in Figure 6 at time t, to the receiver point. These Green's functions are calculated using the propagator matrix method. These displacement

Green's functions are the Γ_{22} terms in equation (32). The evaluation of the $\Gamma_{22,2}$ terms is analogous to the calculation of the displacement Green's functions. The details of this calculation will be discussed later when the evaluation of stress seismograms is discussed. Now, all the necessary time dependent quantities in the RT integral have been defined. It remains to note that the rigidity, μ, in equation (32) is the rigidity at the depth of the source.

The next step is to explain how the RT integral is numerically integrated. Consider the displacement and stress seismograms, and the displacement and stress Green's functions as time series. Each time series gives the amplitude of a displacement or a stress as a function of time. The time spacing between successive points in each time series is the time step duration, Δt, used in the FE calculation. It should be remembered that the terms $\Gamma_{22}u_{2,k}$ and $\Gamma_{22,k}u_2$, in the RT integral, equation (32), are convolutions. Thus, the evaluation of the integrand at each integration point is a four step process. First, each of the displacement and stress seismograms is Fourier transformed into the frequency domain. Then, the products of the Green's functions and FE results, $\overline{\Gamma}_{22}\overline{u}_{2,k}$ and $\overline{\Gamma}_{22,k}\overline{u}_2$, are calculated. In these expressions a bar denotes a Fourier transform. Next, the resulting products are inverse Fourier transformed back into the time domain. Finally, the sum of the two convolutions is determined and multiplied by the rigidity. Now, the value of the integrand at each element center on the integration surface is known. Integration along the segment FG or the contour, C, is approximated by taking the sum over the values of the integrand at each element center along the subsegment FF_1 of the segment FG times the segment length, and applying the assumption that the contributions to the integral from the remainder of segment FG are negligible. The assumption that no significant contribution is made by integration along segment F_1G can be justified for the case where F_1 is chosen so that the earliest possible arrival of energy from a source at depth F_1 is later

than the last arrival in the seismogram being considered. For the remainder of this discussion we will assume that the depth F_1 illustrated in Figure 6 satisfies this criterion. Thus, the integration of the RT integral on the segment FG of the contour, C, is expressed as a sum over the value of the integrand at each of the element centers along subsegment FF_1 times the segment length. This is equivalent to applying a trapezoidal rule numerical integration to the equation (32) along segment FF_1.

Next, the integration over the remaining two segments of the contour, C, will be shown to give no contribution to the RT integral. The segment of the contour FH, along the free surface will be considered first. The integration surface for the segment FH of the contour, C, is a line with the z coordinate held constant. Thus, only terms generated by setting k=3 in equation (32) need to be considered. The free surface boundary condition applied on this surface states that the is zero stress on this surface. Thus, at z=0 the stress, $\mu u_{2,3}$, is zero. Since the Green's function, Γ_{22}, used in all the calculations also satisfies the free surface BC, the Green's function stress, $\mu\Gamma_{22,3}$, is also zero at z=0. Therefore, one term in each product in the integrand of equation (32) is zero, causing the value of the integral along this portion of the contour, C, to be zero. Next, the segment GH of the contour, C, will be considered. As $r\rightarrow\infty$ the displacements Γ_{22} and u_2 must approach zero. The radiation BC used in deriving the expressions for these values imposes such a condition. Substituting the asymptotic expansion for H_ν into equation (38) and (39) and taking the limit as $r\rightarrow\infty$ also verifies this statement. Again, one component of each product in the integrand of equation (32) is zero. Clearly, this makes the integrand zero and verifies that the section GH of contour, C, makes no contribution to the RT integral.

In summary, the mechanics of the methods used to couple propagator matrix solutions into FE calculations and to couple FE results into the RT integral using line source Green's functions generated with the propagator matrix method are described

briefly. To couple propagator matrix solutions into a FE calculation three basic steps are necessary.

(1) Generate seismograms at an appropriate set of receivers using the desired source functions and the propagator matrix technique. An appropriate set of receivers consists of receivers at a fixed horizontal distance from the source, at depths corresponding to the nodes in the first column of the FE grid to be used in the FE calculation.

(2) Use this set of seismograms as displacement time history constraints on the left-most column of nodes in that FE grid.

(3) Record hybrid seismograms at the desired locations within the FE grid as the constrained FE calculation proceeds.

To couple results from a FE calculation back into a simple layered structure across which they can be transmitted using propagator matrix Green's functions and the RT integral five steps are needed.

(1) Record element center displacement and stress time histories from the FE calculation.

(2) Calculate line source displacement and stress Green's functions that will transmit a disturbance from each element center to the desired receiver.

(3) Fourier transform the displacement and stress time histories and the displacement and stress line source Green's functions into the frequency domain. Perform the multiplication of the displacement time history with the stress Green's function and the stress time histories with the displacement Green's functions. Inverse Fourier transform the products back into the time domain.

(4) Add the appropriate pairs of products and multiply by the rigidity to give the values of the integrand at each of the element centers.

(5) Sum the values of the integrands multiplied by their respective interval lengths along the integration surface to give the hybrid seismogram.

Tests of Accuracy: SH Pulse Input

The first, and the most basic, test of the validity of the RT formulation is the coupling of two successive FE calculations. This type coupling can in itself be used to advantage under some conditions, and will be referred to as grid extension in later discussions. For example, propagation through successive FE grids can be useful in some cases to deal with unwanted boundary reflections. As will be demonstrated later the transmitting BC used is angularly dependent, and removes little of the reflection at grazing or near grazing incidence. For FE calculations with large aspect ratios, that is nx $>>$ nz, wide angle reflections from the grid bottom can contaminate the results. When seismograms of short duration are required these wide angle reflections can be avoided by using a series of small aspect ratio grids. For example, if a series of two small aspect ratio FE calculations are used to model a long aspect ratio problem then it should be possible to shift at least half the width of the grid without worrying about wide angle reflections. In that case two small grid runs of the FE would be faster than one run with an expanded grid. Thus, the grid extension would be worthwhile.

In Figure 7 a pair of fifty by fifty node grids are illustrated. A line force source, which is a point force when it is projected onto the x-z plane defined by the FE grid, is applied to the first node in the n^{th} row of nodes in the first, or upper grid. It is shown in the figure as an crossed circle on the left edge of the upper grid. The wide vertical line within this grid represent the sixteenth column of elements, where intermediate seismograms are recorded for later use as forcing functions input to the second step of the procedure. The narrow vertical line in the upper grid represents the thirty first column of nodes where direct seismograms representing results for a

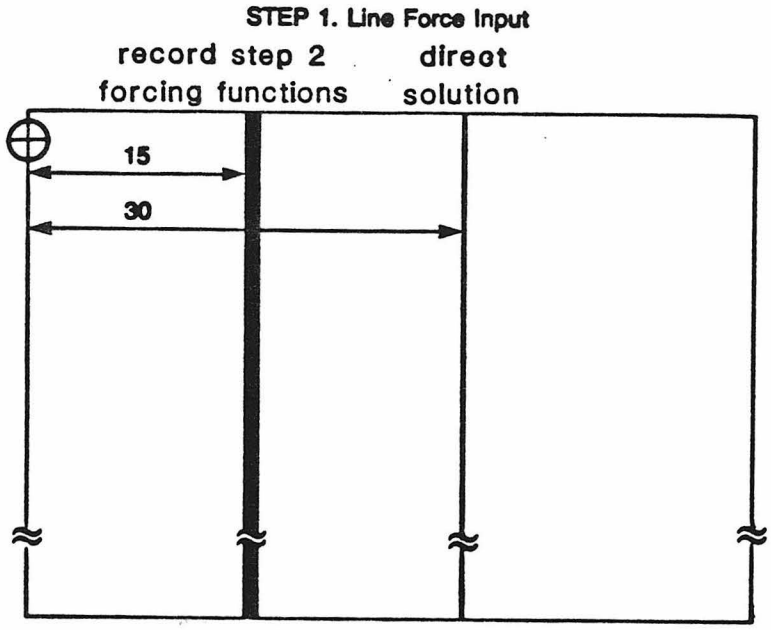

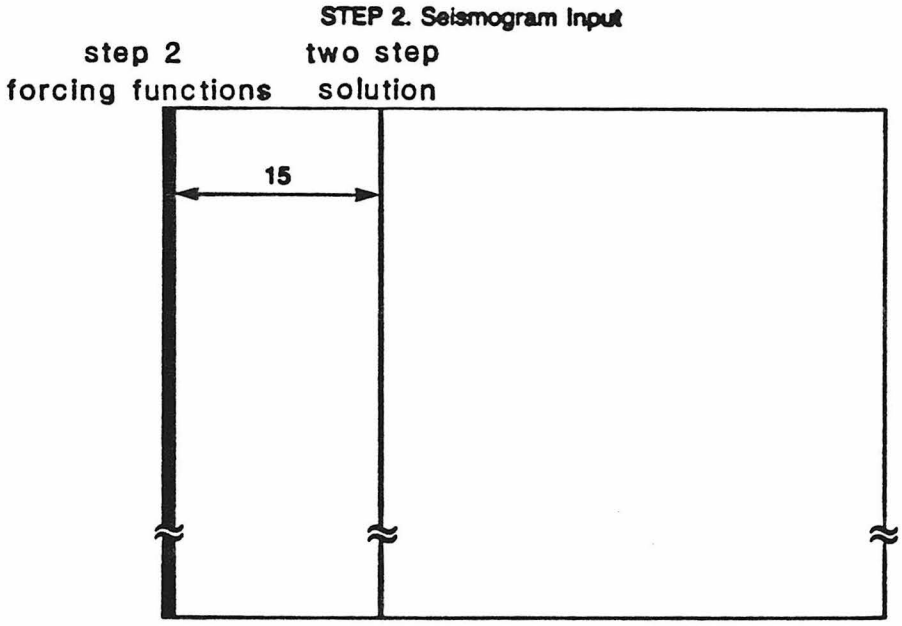

Figure 7: Grids used to test coupling of two successive FE calculations. Both grids are illustrated to scale. The horizontal lines ending in arrows are labeled with the number of element widths they span. The vertical lines within the grids show the locations of the depth sections where results were recorded. The crossed circle on the left side of the first grid represents the line source. Both grids have dimensions 50x50. The horizontal shift of the second grid with respect to the first grid is 15 element widths.

single FE calculation in a fifty by fifty grid are recorded. Figure 7 also shows the spatial relationship of the grid used for the second step of the procedure to the grid used to calculate the direct results and the forcing functions. The first column of nodes in the second grid is shifted to the right to coincide with the location of the sixteenth column of nodes in the first grid. The vertical position of the free surface in each grid is identical. For the second step the intermediate seismograms recorded in step one are used as forcing functions on the first column of nodes in the second grid. The single vertical line within the second grid represents column sixteen, where 'two step' seismograms are recorded. The total propagation distance for the 'two step' procedure, summed over both steps, is equal to the distance propagated in the direct calculation. The application of the displacement time histories used as forcing functions to the left hand edge, or the first column of nodes, of the second grid demonstrates that specifying the the displacements as a function of time due to a given source, for each of the nodes in the leftmost column of a FE grid constrains the motions of all points in the grid to be consistent with that source. When any column other than that closest to the source, in this case the leftmost column, is used as the input column, all nodes more distant from the source than the input column are consistent with the source. The nodes sourceward of the input column form a mirror image of the distant nodes with the symmetry line being the input column. Any energy incident upon the boundary formed by the input column is reflected as it would be from a rigid boundary.

Figure 8 shows a comparison of the seismograms generated by a direct calculation and by the 'two step' procedure. The top seismogram in each column is recorded at the surface. The vertical spacing between the nodes at which the remaining seismograms are recorded is 0.4 km or two element widths, depth increases as one moves down each column. The first column shows the direct results recorded at column

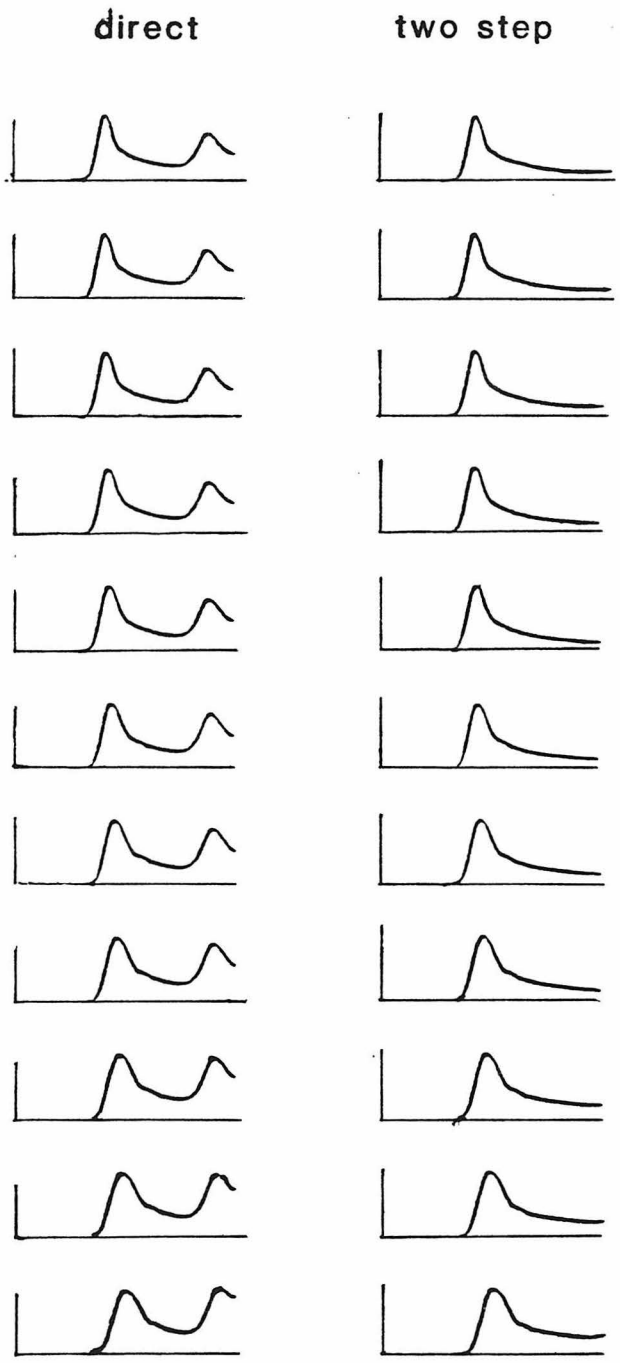

Figure 8: Sample waveforms recorded along the depth section thirty element widths from the source that is illustrated in figure 1.2d. The first column shows the direct seismograms, those recorded in the grid containing the source. The second column shows the two step results recorded at the same distance from the source but in the grid shifted away from the source. The vertical spacing between nodes where seismograms are illustrated is 2 element widths. The uppermost pair of seismograms are recorded at the surface. Depth increases as one moves down each column.

thirty two in the first grid. The second column shows the corresponding 'two step' results recorded at column sixteen of the second grid. The initial waveforms in each column are almost identical, the only discernible difference being a second pulse resulting from reflection from the right hand end of the grid which is seen for the direct calculation only. The reflection is not seen for the 'two step' procedure because the right hand end of the grid is fifteen element widths farther to the right, moving the reflection to a time later than the end of the seismogram. The amplitudes, measured as the height of the first peak, are equivalent. The amplitude variations between methods are less the 0.1%. These results demonstrate the validity of coupling two successive FE calculations by applying forcing functions as BC's on the edge of the second FE grid.

Figure 9 shows the grid geometry used to illustrate how forcing functions can be used to couple energy from a distant source into a FE grid. Seismograms for a line source 2.5 km below the free surface in a half-space, at a horizontal distance of fifteen kilometers from the edge of the grid, were determined using a numerical evaluation of the analytic solution for the direct ray and the ray reflected from the free surface (eq 25). The seismograms form a complete set of forcing functions including a seismogram for each node in the first column of the grid. Analytic seismograms determined by evaluation of the expressions for a line source in a half-space (eq 25) were calculated at horizontal distances from the source corresponding to rows sixteen and thirty-one of the grid. Rows sixteen, thirty one, and forty six are shown in Figure 9 as the three vertical lines within the grid. Using the forcing functions as input to a FE calculation hybrid solutions were calculated for all nodes in columns sixteen and thirty-one. Thus, the analytic solutions can be used as a reference against which the hybrid solutions can be compared.

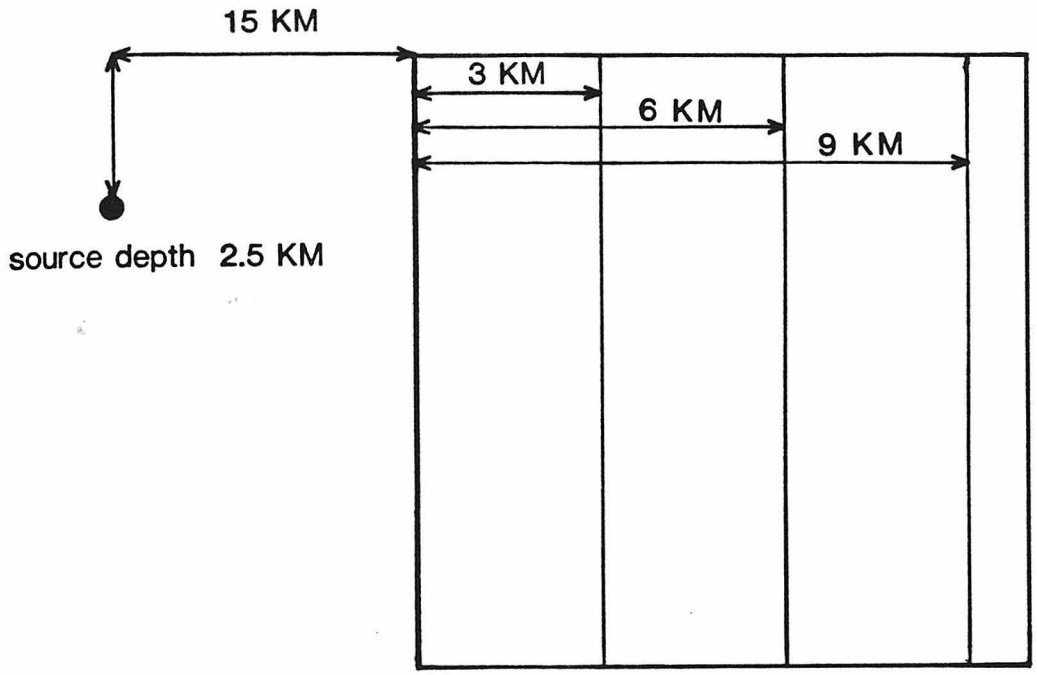

Figure 9: Geometry used to show the validity of coupling energy from a distant source into a FE calculation. The grid illustrated is 50x50 nodes, and is shown to scale. The source is illustrated as the filled circle outside the grid. The source to grid distance is not to scale. The vertical lines in the grid show the depth sections where seismograms were recorded. These seismograms are illustrated in **Figure 10** The horizontal lines ending in arrows are labeled with their lengths.

Figure 10 shows the results of the test of the validity of the RT coupling of energy from a distant source into a FE calculation. The first two columns show the results for column sixteen of the grid, which is three kilometers into the grid. The second two columns show analogous results at column thirty two, six kilometers into the grid. The first column in each group shows analytic seismograms for reference. The second column in each group shows the hybrid seismograms at the corresponding locations. The first seismogram in each column is recorded at the free surface. Successive seismograms moving down each column are recorded with one kilometer depth spacing. The waveforms of the analytic and the hybrid results agree extremely well. However, the 'hybrid' results for column thirty two include a reflection from the end boundary of the grid, not present in the analytic calculations. The illustrated seismograms are scaled so that the maximum peak has unit height. Thus, the apparent amplitude differences in the initial peaks at six kilometers is an artifact of the scaling. The correspondence in amplitude between the two methods is excellent. At three kilometers the agreement deteriorates below the fortieth of fifty grid points from better than 0.5% to as much as 10-20%. At six kilometers the departure from the correct amplitudes begins at a shallower depth, after about thirty five grid points. The variations of the quality of fit with distance from the grid edge and with depth from the free surface, can easily be explained. The truncation of the RT integration at the bottom of the grid causes artifacts which are largest as the depth of truncation is approached or surpassed. To be more specific, it is useful to extend the test discussed above to more clearly delineate the nature of these variations, and the restrictions they place on the use of this method of coupling a distant source into a FE calculation. A more extensive test will be discussed below.

To minimize the calculation needed to obtain the forcing functions, it is useful to investigate the effect of reducing the number of forcing functions used, that is limiting

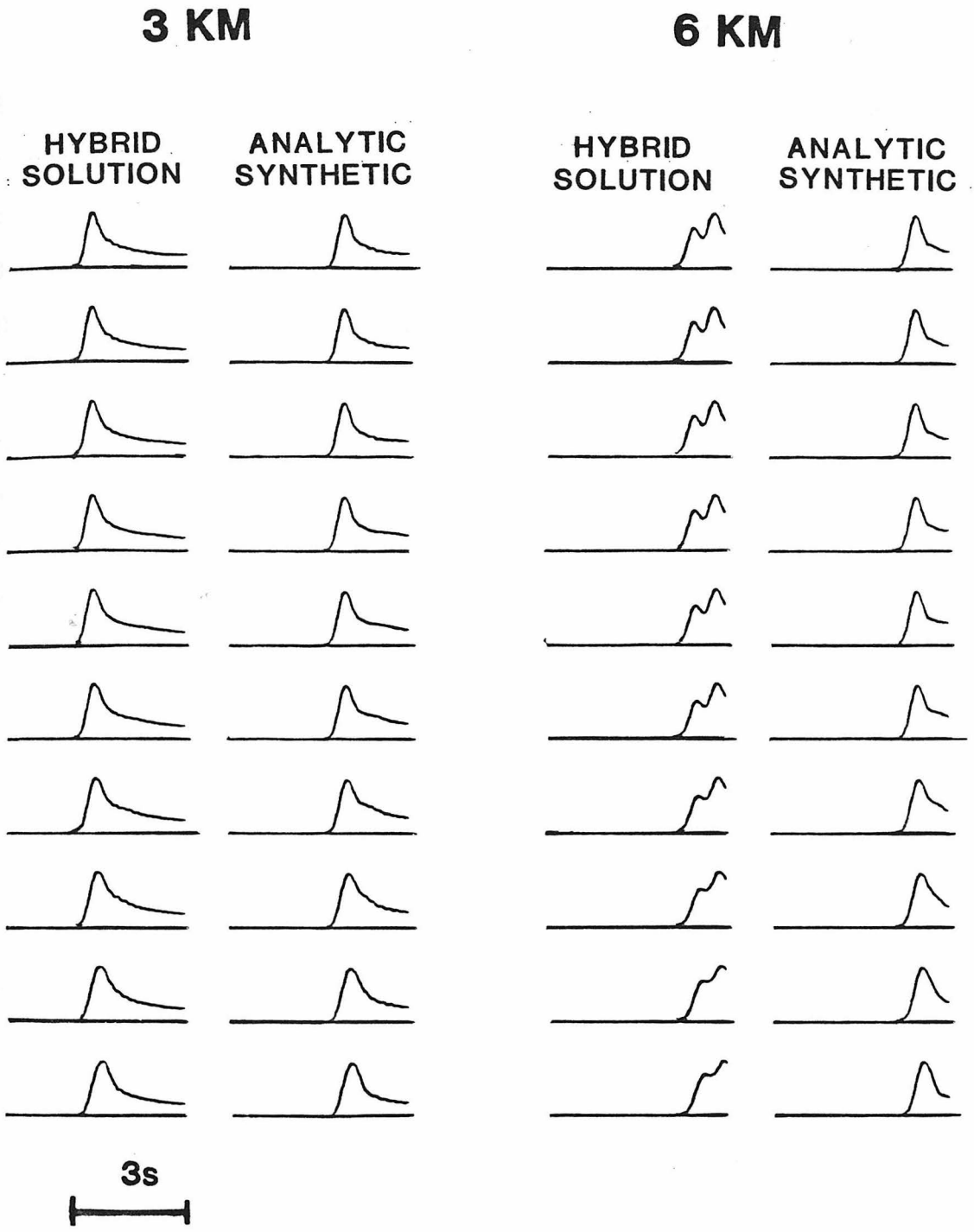

Figure 10: Demonstration of the coupling of a distance source into a FE calculation. Two pairs of columns showing seismograms recorded at the depth sections three and six kilometers from the grid edge. The first column in each pair shows the results of the FE step of the hybrid calculation, the second column shows the half-space synthetics at the same locations. The first row of seismograms are recorded at the surface, successive rows are separated by one kilometer in depth. Peak amplitudes are normalized to one.

the depth extent over which forcing functions are applied to the left hand grid edge. The exact solution of the RT coupling problem requires integration to infinite depth. However, energy arriving after the time of the last sample in the modeled seismogram can be ignored. Thus, the maximum depth which needs to be considered is twice the depth of the deepest receiver plus the distance over which the travel time is equal to the seismogram duration. It is clear that prohibitively large FE grids would be required to produce records of reasonable length or at large distances. However, solution of acceptable accuracy can be produced by integrating over a comparatively small number of forcing functions. The previous example, of coupling energy from a distance source into a FE grid illustrates that this is the case. For a fifty by fifty grid, discrepancies of less than 0.3% for the uppermost forty grid points are observed. A complete solution at the depth of the fortieth row of receivers would require nz to be larger than one hundred fifty, three times the size used in the example. This observation implies that fewer forcing functions are needed if some differences at depth, near the bottom of the grid, are permissible. An experiment to investigate the effects of applying forcing functions to only the top n nodes in the input column has been performed. A geometry and procedure analogous to that used to demonstrate the validity of the RT coupling of a distant source into a FE calculation was used.

The geometry of the grids used to investigate the effects of changing the number of the applied forcing functions and thus, the depth where the deepest forcing function is applied, on the accuracy of the resulting seismograms is shown in Figure 11. A line source embedded in a half-space at a depth of 2.5 km was used and is shown as a large solid dot on the vertical dotted line denoting the x coordinate origin. The horizontal distance from the source to the left hand edge of the grid is fifty kilometers. The first column of nodes in the grids used are shown as a pair of vertical solid lines. The two single solid vertical lines within the grids are the locations where the analytic

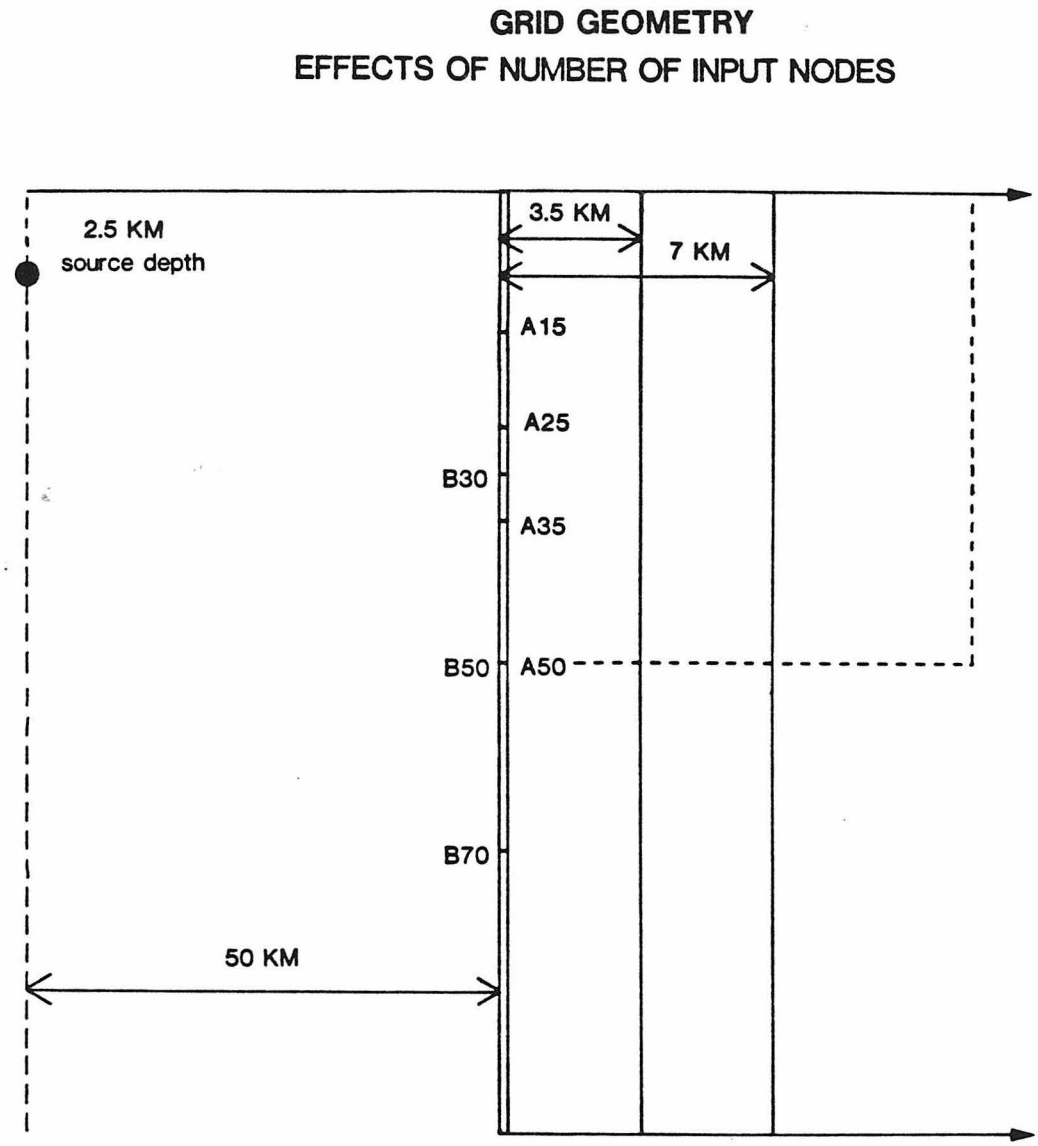

Figure 11: Grids used to test the effect of varying the number of forcing functions. Double vertical lines show the left edge of the grids. Horizontal lines crossing these vertical lines show the bottommost forcing function for each test. Tests A15, A25, A35, and A50 are completed in the 50x50 grid whose extent is marked by the dotted boundaries. Tests B30, B50, B70, and B100 are done in the large grid whose bottom is shown as a horizontal line ending in a solid arrow. The solid vertical lines within the grid show the depth sections where results are recorded. Solid horizontal lines ending in arrows are labeled with their lengths.

synthetic seismograms are compared with the hybrid seismograms from the FE calculations. They are at distances of 53.5 km and 57.0 km from the source, corresponding to columns sixteen and thirty one in the FE grids. Two grids are used for these tests. The dotted lines within the large 100x100 grid are the bottom and right hand edges of the smaller fifty by fifty grid used for the first four tests. The solid horizontal lines ending in solid arrows show the free surface and the bottom edge of the large FE grid used for the remaining tests. For both FE grids hybrid seismograms were calculated for four cases. Each of these cases used a different number of forcing functions. For the small FE grid fifteen, twenty five, thirty five, or fifty forcing functions were used. For the large FE grid thirty, fifty, seventy, or one hundred forcing functions were used. The vertical extents of the input forcing functions are illustrated to scale in Figure 11. The locations of the bottommost input forcing function for the small grid tests are shown by the horizontal lines labeled A15, A25, A35, and A50 which cross the first column of elements in the illustrated grid. For the large grid the bottommost forcing functions are shown as the lines labeled B30, B50, B70, and the bottom of the large grid, B100. Results from each of these eight tests were examined to determine the effects of grid size and vertical extent of the input forcing functions.

Figure 12 shows examples of the seismograms observed at column sixteen in the four small grid tests. The surface seismograms are illustrated in the first row of the figure. Each row is recorded at nodes about 0.9 km deeper, that is four element widths deeper than the previous row. The column of numbers in the middle of the figure give the node row at which that row of seismograms was recorded. The first column shows results from test A50. These waveforms are very similar to the analytic seismograms recorded for the same locations. The agreement is best at the surface, at depths below the thirty fifth node the decay of the pulse becomes less rapid than that seen on the analytic synthetic and the maximum amplitude of the pulse increases with

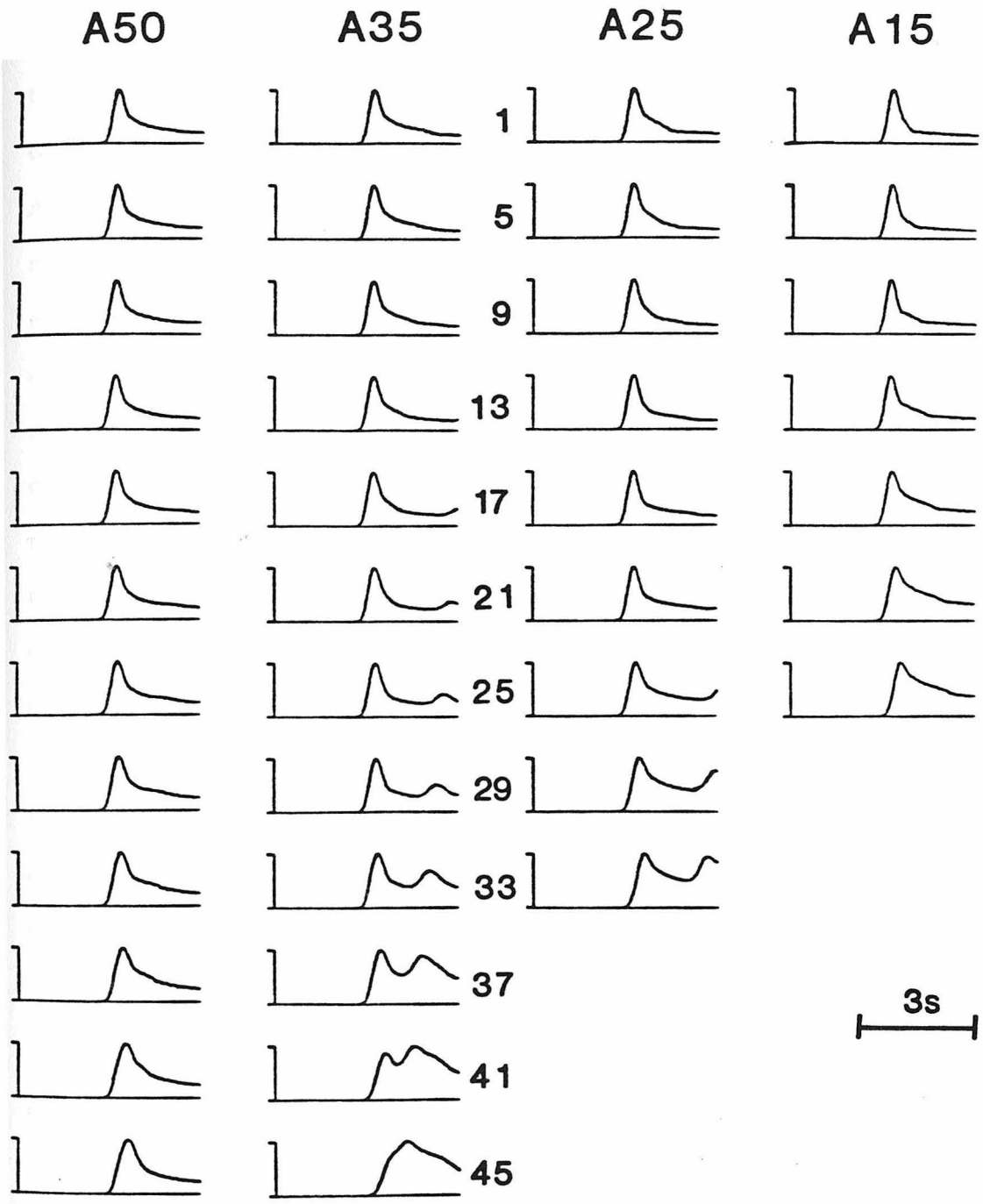

Figure 12: Seismograms for four cases using different numbers of forcing functions. Each column shows seismograms on a depth section at 53.5 km from the source. The first row is recorded at the surface. Vertical spacing between rows is about 0.9 km. The first column uses 50 forcing functions, the second 35, the third 25, and the fourth 15. The column of numbers in the center of the figure gives the node row number for each row of seismograms.

respect to the analytic synthetic. For this test the difference in waveform shape is small. The second column shows results from test A35. A second pulse not visible for the A50 test is present. This pulse is a reflection from the grid bottom of energy not canceled by the disturbances input in the bottommost fifteen forcing functions in test A50. The pulse is most prominent for traces recorded at depths below the bottommost forcing function applied in this test. This is predictable since it could not be expected that results for receivers below the input nodes would be reliable. If the reflection can be removed, as with an absorbing BC then the correspondence of A35 results to direct synthetics is good down to node row thirty or thirty five. The third column shows results of test A25. Again a reflected pulse contaminates the deeper receivers. Results compare well with the analytic synthetics down to about node row twenty. The fourth column shows results of test A15. Here, the same trend already observed continues. The correspondence between A15 results and analytic synthetics is good down to about node row ten. It appears that acceptable waveforms can be calculated for depths such that at least five to ten input forcing functions are applied at rows below the receiver. Similar results are observed for these tests at seven kilometers from the grid edge, and for the large grid tests at both distances. Some indication that calculation of accurate seismograms at longer distances may require a larger vertical extent of input forcing functions has been observed.

Figure 13 gives a more complete analysis of the amplitudes of the seismograms recorded in these eight tests in relation to the amplitudes of analytic synthetics. At both distances the maximum amplitudes of the seismograms from each test were tabulated. These amplitudes were used to calculate amplitude ratios. The amplitude ratio, A, is defined as

$$\text{A(node i)} = \frac{\text{AMPLITUDE OF DEPTH EXTENT TEST (node i)}}{\text{AMPLITUDE OF DIRECT CALCULATION (node i)}} \qquad (47)$$

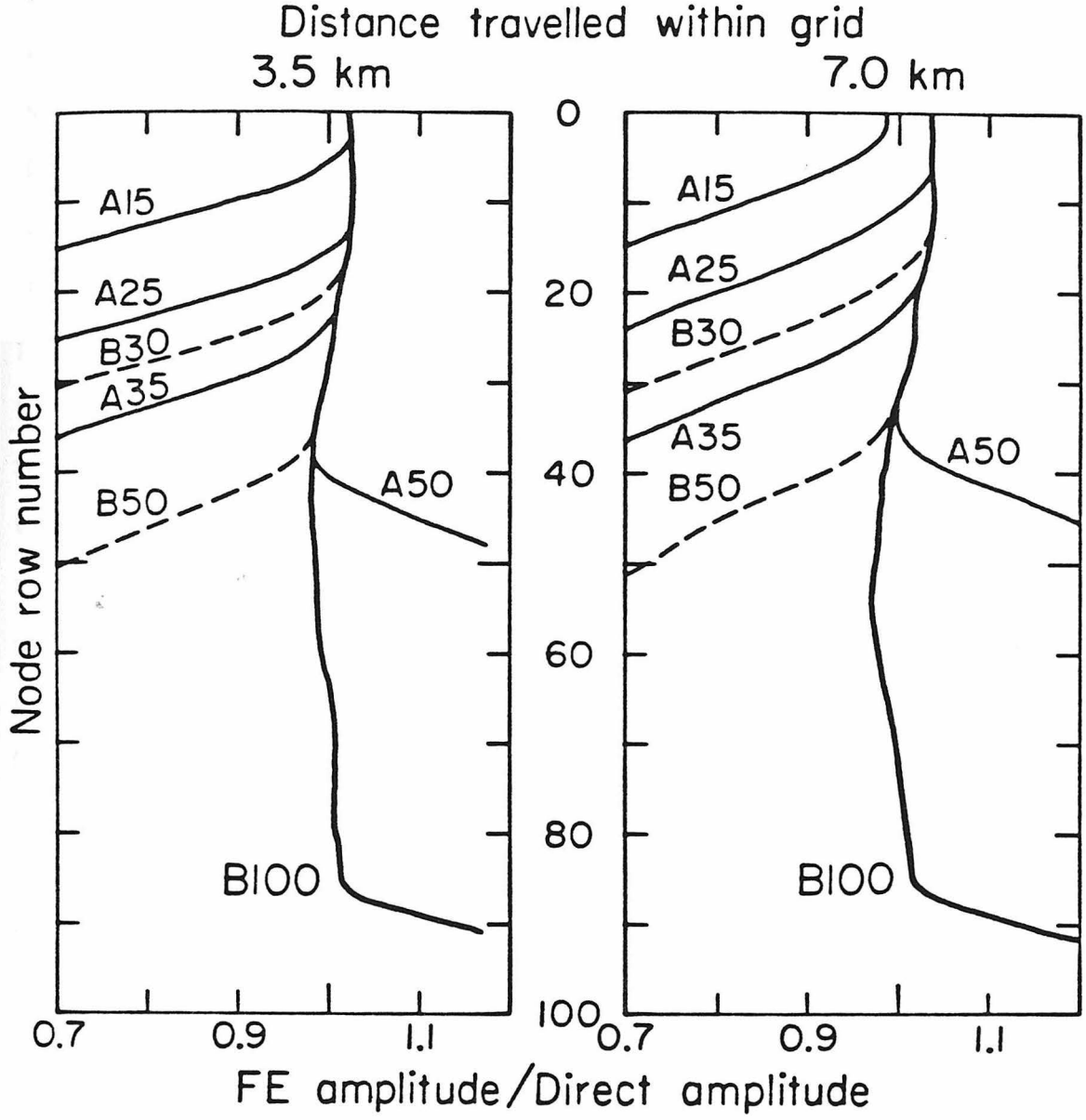

Figure 13: Relative amplitudes of synthetic and two step seismograms at the same locations, as a function of the number of input forcing functions. The left hand graph shows results recorded at a depth section 3.5 km from the grid edge, the right hand graph results recorded at 7 km. Heavy lines show tests for which all node rows in the grid have forcing functions applied. Lighter solid lines show results of tests in the 50x50 grid. Dotted line show result of tests in the 100x100 grid. The number in the label above each line indicated the number of forcing functions used in that test.

These amplitude ratios were then plotted as a function of depth, measured as a number of node rows. The resulting plots are shown in Figure 13. The left hand plot is for a distance of 3.5 km, and the right hand plot for a distance of seven kilometers. The heavy lines in each plot indicate the amplitude ratios for the two tests in which all nodes in column one of the grid have forcing functions applied to them, A50 and B100. These tests are used as a reference against which the other tests can be compared. The dotted lines labeled A15, A25, and A35 show where the amplitude ratios for the three tests in the small grid, using partial sets of forcing function input, depart from those of test A50. The amplitude ratios agree well with those of the A50 test for the near surface nodes in each test. The depth at which they depart from the A50 results increases as the number of input forcing functions increases. As expected the amplitude correspondence is better when more complete input is used. Examining these results at a distance of 3.5 km shows that if results for n rows are desired, input forcing functions should be applied to n+5 nodes. At seven kilometers similar results are observed but the departure from acceptable amplitude ratios occurs four or five nodes shallower. Thus, as distance increases a larger depth extent of input forcing functions is needed to produce amplitude correspondence within acceptable bounds. The results for the tests using the larger grid are show in Figure 13 as the light lines labeled B30 and B50. The results show the same trends as the results for the small grid indicating that the artifacts in the tests using truncated input sets are due to interaction with the grid bottom of incompletely integrated signals in the seismograms.

If one wishes the analytic solutions to correspond well to the FE solutions the frequency content of the forcing functions used to drive the FE calculation becomes important. To investigate the effects of the frequency content of the input, sets of forcing functions for a source distant from the FE grid were calculated for two cases.

Each of these sets consists of seismograms calculated along a depth section fifty kilometers from the source, with a vertical node spacing of 0.2 km. Both sets of seismograms were determined for a line source, with a triangular time function, in a half-space (eq 25). The first case used a time function with a duration of .15 seconds, the second used a time function with a duration of .45 seconds.

The results of these tests are illustrated in Figures 14 15, and 16. The first two of these figures show the seismograms recorded on a depth section 53.5 km from the source. The vertical spacing between successive rows of seismograms is about one kilometer. The amplitudes in all traces in these figures have been normalized such that the peak amplitudes of each trace appear the same size. The first column in each figure shows the analytic solutions. The second column shows the same seismograms band pass filtered between one and one hundred seconds. The third column shows the bandpass filtered hybrid solutions. Figure 14 shows the results using the 0.15s time function, and Figure 15 shows the results for the 0.45s time function. Figure 16 addresses the amplitude correspondence for both cases. In Figure 14 it is possible to see both the direct arrival and the arrival reflected from the free surface in the direct seismograms recorded at depth. These arrivals are clearly higher frequency than the minimum period of one second transmittable by the FE grid. The hybrid solutions for this case contain unwanted oscillations. However, when the hybrid solutions, and the direct solutions are both band pass filtered their waveforms are in excellent agreement. Alternatively, band pass filtering the forcing functions before they are input to the FE calculation will produce unfiltered hybrid solutions almost indistinguishable from the filtered hybrid solutions calculated using the unfiltered forcing functions. Aliasing of energy traveling in waves of frequency higher than can be propagated by the grid into lower frequency bands does not seem to be a problem for these tests. Figure 15 shows that waveforms of the direct and hybrid solutions correspond well when the input has

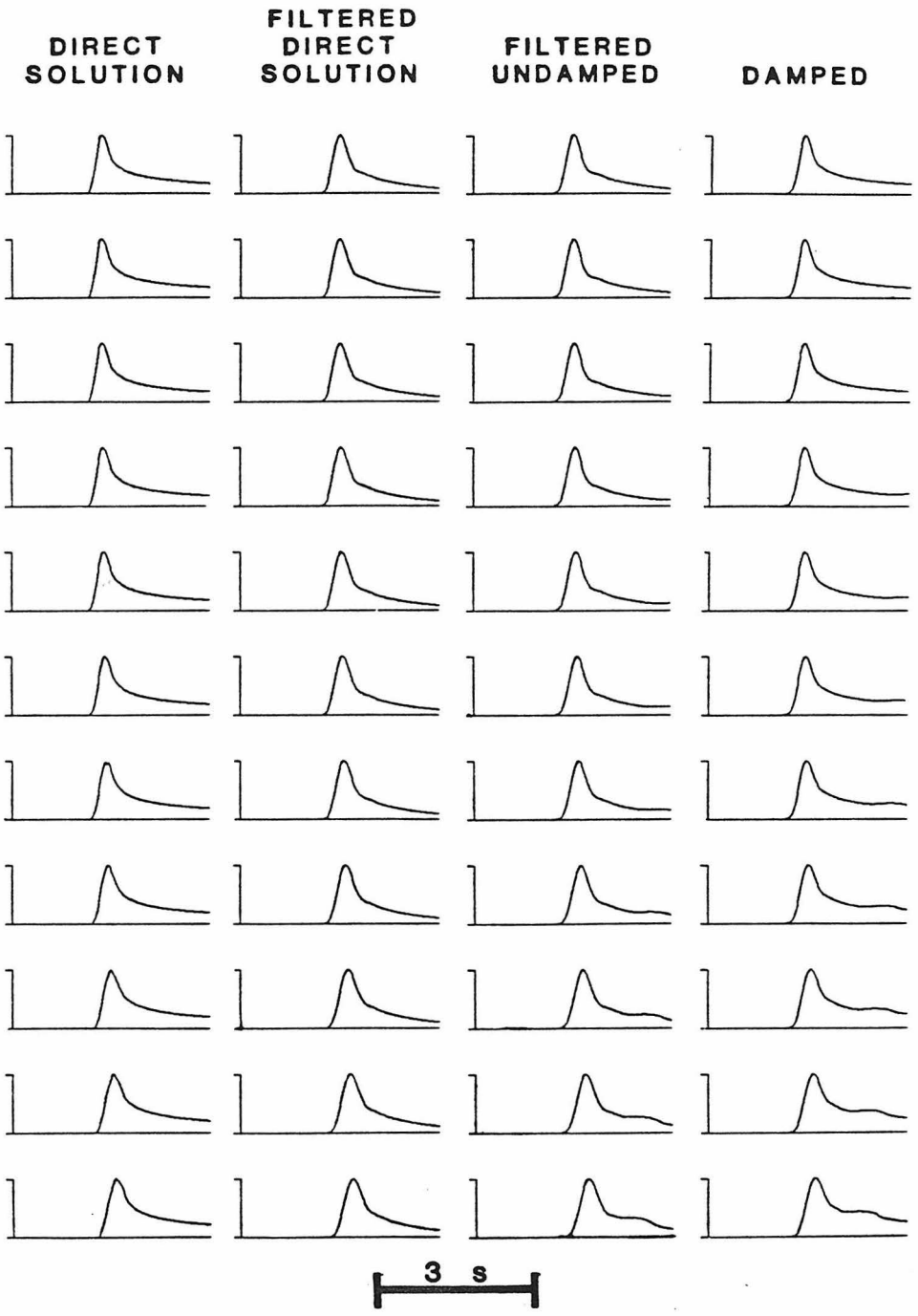

Figure 14: Effects of filtering and internal damping on FE solutions. Column one shows a depth section of line source half-space synthetics with a triangular time function of .15s duration. Column two shows the same seismograms band pass filtered between 1s and 100s period. Column three shows the hybrid solutions without internal damping and with the same bandpass filter applied. The fourth column shows the hybrid solution with internal damping. No filter is applied. Amplitudes of each trace are normalized to give unit peak amplitude.

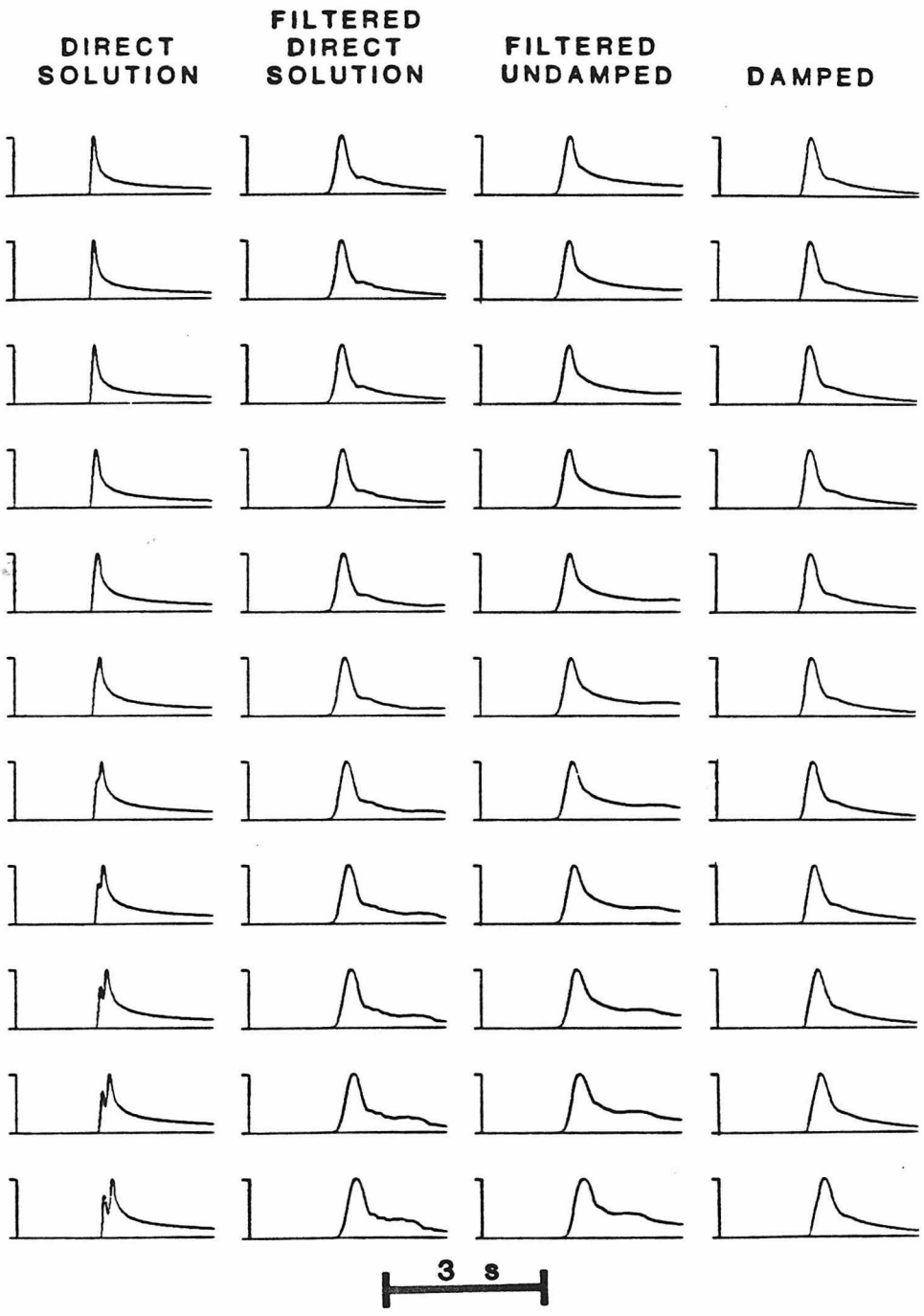

Figure 15: Effects of filtering and internal damping on FE solutions. As for figure 14 but using a triangular time function of .45s duration.

no significant high frequency component. In this case the bandpass filtering makes little or no additional improvement to the correspondence of the two sets of results.

The spurious oscillations seen in the unfiltered hybrid solutions can be removed by filtering as discussed above, or by the introduction of a damping coefficient within the FE calculations. For each of the sets of forcing functions used in the tests discussed in the previous paragraph FE solutions were determined both with and without damping. The damping coefficient used in the FE code is dependent on distance. Therefore, a single damping coefficient cannot produce correct amplitudes at a variety of distances. At the distance for which the coefficient is calculated, and within a few grid spacings of that distance, the coefficient produces FE results that correspond very well with the direct solution. If the direct solution contains high frequencies the results correspond to the filtered direct results. This can be seen by examining Figures 14 and 15. In each of these figures column two shows the filtered direct solutions, and column four shows the hybrid solution using internal damping with the FE calculation. The damping coefficient is chosen to be optimal at the illustrated distance. The correspondence in waveform between these two columns is very good.

Figure 16 shows the amplitude ratios for the tests of filtering and damping efficiency. It illustrates the relative accuracy of using the damped FE and the filtered undamped FE approaches. The damped FE calculation shows more variation with depth of the amplitude ratios. The ratios are calculated at the distance for which the damping coefficient was optimal. However, for the calculation which includes damping, as distance from this point increases the amplitude ratios rapidly depart from one and show even larger variations with depth. On the other hand the ratios for the filtered undamped FE calculation remain quite stable.

The results of these tests can be summarized by noting the following important observations. If the input seismograms contain frequencies higher than those that can

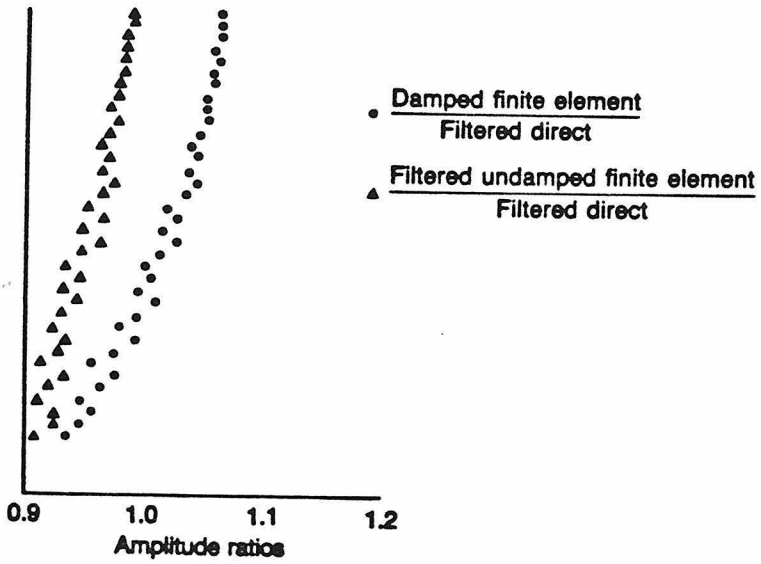

Figure 16: Amplitude ratios as a function of depth for seismograms recorded on a depth section 57 km from the source.

be propagated through the FE grid, as in the case of the rapid rise observed for the forcing functions and analytic seismograms with the 0.15s time function, then the grid acts as a filter. The amplitude of the FE solutions are significantly reduced with respect to the analytic solutions and spurious oscillations are introduced near the end of the waveform. The correspondence of amplitudes and waveforms between the analytic solution and the hybrid solution for this situation is poor because the analytic solution contains higher frequencies than the hybrid solution, and the hybrid solution contains numerical artifacts. Low pass filtering the analytic solution and the hybrid solution will improve the waveform fit enormously, and bring the amplitude ratios much closer to one. The cutoff frequency of the low pass filter should be at most the highest frequency that the grid can propagate. It is not important whether the input forcing functions or the output hybrid solutions are filtered. Both approaches produce equivalent results. When input forcing functions contain no frequencies too high for propagation, filtering of hybrid solutions or analytic synthetics is not necessary as it does not change the goodness of fit. The use of internal damping in the FE calculation is distance dependent and introduces addition variation in the goodness of fit of amplitude and waveform as a function of depth. Considering all these observations the best combination of filtering and damping when a range of distances is to be used is to filter an undamped FE solution. If theoretical results are available the filtered undamped solutions should be compared directly to them. If the theoretical results contain high frequencies they should be low pass filtered before being compared to the filtered undamped solutions. This approach should give the best correspondence to the theoretical results.

Tests of Accuracy: SH Lg Mode Sum Input

The accuracy of coupling a 2-D SH pulse from a source outside a FE grid into that grid have now been thoroughly discussed. The limitations of such an approach

have also been defined. However, generalizing these results, which have been demonstrated only for a line source in a half-space, to a line source or a point source in a layered media or even in a layer over a half-space can be misleading. Some of the tests discussed below illustrate cases for which results do not generalize. The physical model used in all of these tests is a layer over a half-space. The addition of the layer above the half-space allows for the existence of Love waves. This changes the behavior of the accuracy of coupling a distant source to a FE calculation. In these tests the layer has a thickness of thirty two kilometers, an S wave velocity of 3.5 km/s, and a density of 2.7 g/cc. The underlying half-space has an S wave velocity of 4.5 km/s, and a density of 3.5 g/cc. The initial calculation demonstrating the validity of coupling a distant source into a FE grid for the case of a layer over a half-space used a grid spacing of 0.53 km in both x and z. All subsequent tests used a grid spacing of 0.5 km in both x and z. All tests use a time step of 0.05 s. Each test uses the same set of ninety forcing functions, or a subset of that same set, applied to the leftmost column of nodes. Forcing functions are calculated for a strike slip point double couple source at a depth of eight kilometers. The source to grid edge horizontal distance is 1500 km.

The seismograms used as forcing functions in the tests discussed below are calculated as mode sums over modes with periods between 0.5 s and 100 s. The fundamental mode and the first five higher modes are included in each calculation. This is not a complete representation, but produces a seismogram that shows the overall character of the arrivals seen in data in the L_g group velocity range of between 2.8 and 3.5 km/s. A complete representation would require as much as five times the amount of calculation to produce the forcing functions or the synthetics used for comparison to the hybrid results. To assure the inclusion of all energy down to a period of 0.5 s twenty two higher modes would be necessary, for all energy down to a period of one

second eleven higher modes need to be included. The cutoff frequency of the sixth higher mode is 1.9 s. The forcing functions used are complete to that period and contain a significant portion of the energy at the shorter periods considered. For waveform modeling of data the use of a more complete mode set would be advisable, but for the tests discussed here it is an unnecessary expenditure of effort. An example of a forcing function or direct seismogram, recorded at the surface at a distance of 1500 km from the source is shown in Figure 17. The group velocities of the arrivals are shown along the horizontal axis. The heavy rectangle enclosing the largest portion of the seismogram delimits the portion of the trace used as a displacement time history to drive the surface node on the depth section at 1500 km from the source. The seismogram shown in this figure is not the actual trace used as a forcing function. It has been band pass filtered between 0.01 and 1.0 Hz and has had the WWSSN short period receiver function applied to it. The traces used as forcing functions have been band pass filtered but do not have the instrument applied. Examples of such traces at different source receiver separations are shown in Figure 18. In this figure these traces are labeled synthetic.

At this point it is useful to digress and to more precisely define the RMS amplitude measure used in subsequent discussions and the method used to calculate it. The form of the relation used to determine the RMS amplitude is

$$\mathrm{RMS} = \frac{\sqrt{\sum_{n=1}^{m} \left[\mathrm{amp}(n)^2\right]}}{\sqrt{m}} \qquad m = \frac{T_{RMS}}{\Delta t} \tag{48}$$

where m is the number of points in a sampling window or duration T_{RMS} seconds. The location of the sampling window with respect to the arrivals of maximum amplitude and the duration of the trace contained within the sampling window have a significant effect on the value of the RMS amplitude. Care must be taken to choose

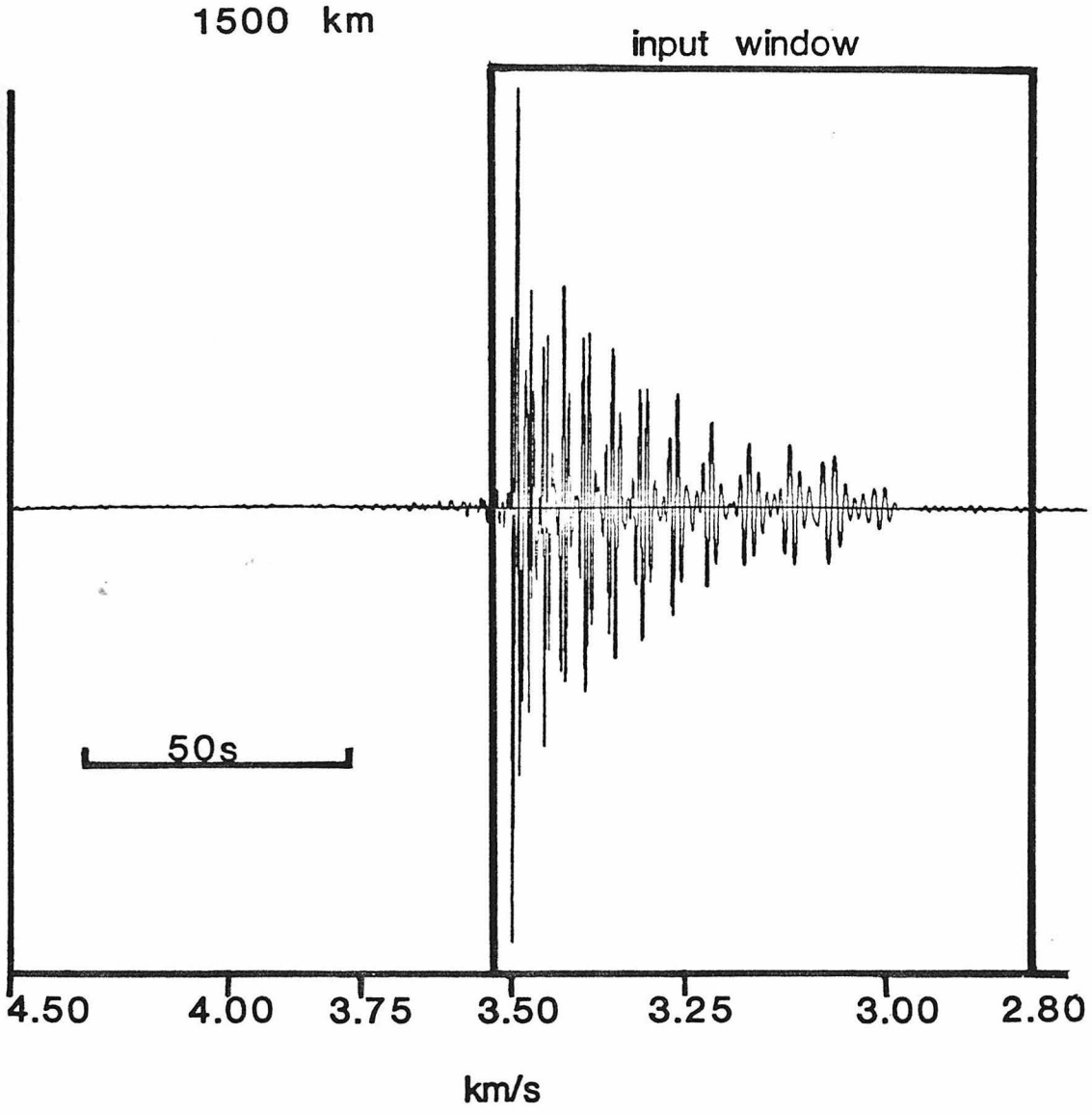

Figure 17: Sample forcing function for SH L_g wave FE calculation. The seismogram includes modes with periods between 0.5s and 1000s. Only the fundamental and the first five higher modes are used. The mode sum synthetic has been transmitted 1500 km from the source using the propagator matrix technique. The resulting seismogram has been band pass filtered between 0.01 and 1 hz, and has the WWSSN short period instrument has been convolved with it. The portion of the seismogram within the box labeled input window is used as a forcing function. The numbers along the axis indicate the group velocities of the arrivals.

windows for two sets of results that are compatible with each other and produce meaningful comparisons. For example, choosing the beginning of the seismogram being considered as the first point in the sampling window can cause difficulties when comparing different calculations or when comparing successive seismograms along a depth or distance section. When different calculations are being compared extreme care must be taken to insure that both seismograms begin at the same absolute time. When successive seismograms in a depth or distance section are being compared, the duration of the portion of the trace with negligible amplitude that occurs before the first arrival increases with distance from the source. This creates an artifact that makes RMS amplitudes appear to decrease with distance. To avoid these and other problems some other method of determining the beginning of the sampling window must be devised. It would be possible to correct for the distance term by ignoring enough points at the beginning of the seismogram to compensate for the difference in arrival time. However, when models became more complicated the choice of the first arrival, and the determination of its travel time from the source becomes more complicated due to the possible presence of strong refracted or diffracted phases. Thus, a more general approach which does not require the use of theoretical travel times has been chosen. Two different methods of selecting the first point in the sampling window have been used. The selection of one of these two methods was based on the characteristics of the waveform as discussed below.

The first method, which was used in the majority of cases, selects the first point to be included in the sampling window and the last point to be included in the seismogram by bracketing the portion of the seismogram whose RMS amplitude is to be measured. This piece of the seismogram is bracketed with sections of seismogram with sustained low amplitude persisting for at least a defined minimum duration. This method is used when the oscillations in the waveform are very small until the first

large and impulsive arrival occurs, when no periods of sustained low amplitude occur during the duration of the trace, and when the amplitude of the seismogram decays to a sustained low amplitude at its end. Given that all three of these conditions are satisfied the following algorithm produces stable and accurate RMS amplitude measures. The algorithm consists of five steps:

(1) Determine the size of the maximum absolute value of amplitude in the seismogram

(2) Set a cutoff value for the amplitude at some fraction of the maximum (usually .01 or .05)

(3) Beginning at the location of the maximum absolute value scan toward the beginning of the seismogram until a series of samples two seconds in duration all have amplitudes smaller than the cutoff amplitude. The first point in this series is defined to be the first point in the sampling window used to determine the RMS amplitude.

(4) Beginning at the location of the maximum absolute value scan toward the end of the seismogram until a series of samples two seconds in duration all have amplitudes less than the cutoff amplitude. The first sample in that series of samples defines the last point in the seismogram.

(5) Calculate the RMS amplitude for sampling windows with durations 15, 20, 25, .., 85s. If the duration of the sampling window exceeds the duration of the seismogram then the longest sampling window used is the duration of the seismogram, and that duration is recorded.

The second method is used when small arrivals precede the main arrival on only a subset of the traces being considered, when the small arrivals preceding the main arrival contain sustained periods of low amplitude on some subset of the traces, and when sustained periods of low amplitude occur elsewhere within any of the

seismograms. This method is not used when the arrival with maximum absolute amplitude is preceded by a lower amplitude arrival of long (>10s) duration, or when the maximum amplitude occurs within the first 10s of the seismogram. This method is also useful when slight wraparound occurs as a result of convolving the instrument with the seismogram producing small spurious arrivals before the main peak. If significant wraparound occurs, the convolution length is extended to remove it. The determination of RMS amplitude is not expected to correct it. The basics for the algorithm used for the second method are identical to those used in the first method. The only differences lie in the method used to select the first point in the sampling window, and in the duration (5s) of sustained low amplitude that defines the end of the seismogram. When using the second method the first point in the sampling window is defined to be the point in the time series for a time ten seconds before the time of the peak of maximum absolute amplitude. Clearly, if the maximum amplitude occurs late in the seismogram this method is not useful. However, when periods of sustained low amplitude occur early in the seismogram, or when small amplitude early arrivals are detected on only a subset of the seismograms then this method gives stable RMS amplitudes whereas the amplitudes using the first method will not be stable.

These algorithms yield a series of RMS amplitude values that can be used to compare results derived using different methods. If RMS amplitudes agree within all period ranges, and waveforms are similar the fit is considered to be excellent. If discrepancies occur or increase with the length of the sample window, then there is probably a problem modeling the later arrivals, that is, the representation of later arrivals is probably incomplete. If the shortest time windows show discrepancies that decrease rapidly as the window length increases then the amplitudes of the initial arrivals are unstable or incorrect. Examining the behavior of the RMS amplitude as a function of sample window length can give insight into the nature of and the

underlying reasons for misfit between methods. In most of the discussions that follow, the method used to obtain RMS amplitudes will not be specified. Both methods described above give consistent interpretations if they are applied to all seismograms in a given example. While the actual amplitude measures may vary between the two methods the changes seen in amplitude within a given example are the same regardless of the method used so long as the same method is consistently applied. The variation of RMS amplitude with the length of the sample window will be discussed only when such variation have direct impact upon the results of the comparisons.

Now I will return to the discussion of the RT coupling of a distant line source in a model consisting of a layer over a half-space into a FE calculation. First, it is useful to establish that the coupling of energy from a distant source into a FE grid is valid for a layered structure more complicated than a half-space. The seismograms illustrated in Figures 18 and 19 verify that the method of coupling does generalize as the theory implies it should. The seismograms in Figure 18 are recorded at two distances from the grid edge, and at five depths for each of these distances. A pair of seismograms is shown for each of these ten locations. The upper seismogram in each pair is the direct synthetic determined as a mode sum and transmitted to the receiver using the propagator technique. The lower seismogram in each pair is the hybrid synthetic for which the first portion of the path is traversed using the propagator matrix technique and the remainder of the path is traversed in a FE grid. For this test a 100x100 node grid was used and sixty forcing functions were applied to the FE grid edge. All seismograms in Figure 18 have a duration of fifty five seconds and have been band pass filtered between .01 and 1 Hz. The amplitudes of all traces are normalized so the maximum peak to peak amplitude of each trace appears to have the same value. Within each pair the variation in peak to peak amplitude is less than five percent. The peak to peak amplitude ratios of the hybrid synthetic to the analytic synthetic

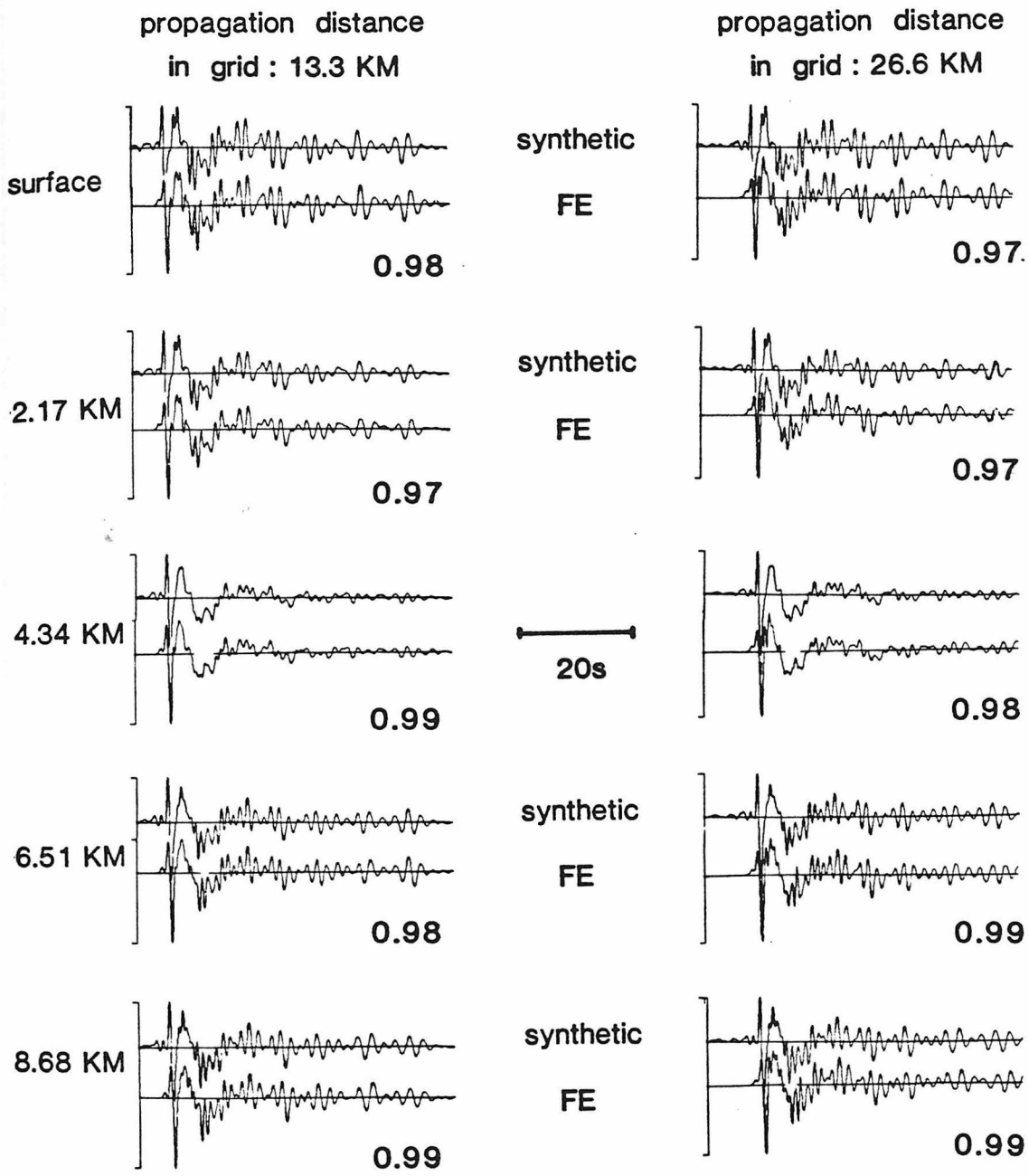

Figure 18: Comparison of hybrid solution to mode sum synthetics. The upper trace in each pair is a mode sum synthetic transmitted using only propagator matrices. The lower seismogram in each pair is the hybrid solution. The depths for each row and the horizontal propagation distances in the FE grid for each column are shown. The ratio of the FE to synthetic peak to peak amplitudes is given as the number below each pair of traces. Each trace has been band pass filtered between .01 and 1.0 Hz, and its maximum peak to peak excursion has been normalized to one.

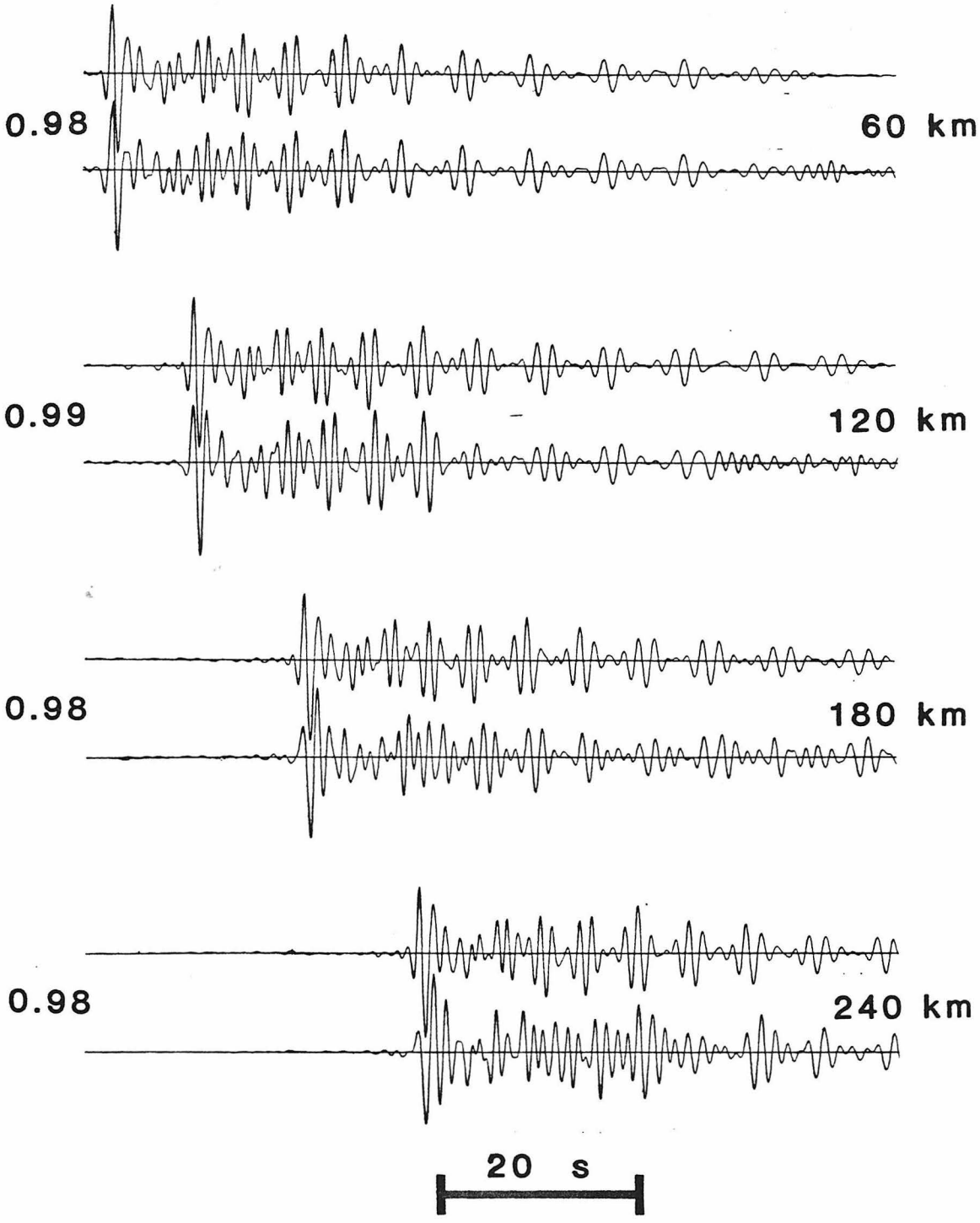

Figure 19: Comparison of hybrid solutions and 3-D mode sum synthetics. The forcing functions used are 3-D mode sum synthetics. The upper trace in each pair is the mode sum synthetic, the lower trace is the hybrid solution. Numbers at the left above each pair of seismograms indicates distance from source to receiver at the surface. Numbers at the right give the ratio of RMS amplitude of the hybrid solution to the RMS amplitude of the direct synthetic.

are shown below the right end of each pair of traces. The major differences in the synthetic and hybrid solutions are seen in the amplitude of the first large positive and negative peaks. The amplitude of these peaks is not stable since they are the result of sampling a very high frequency arrival not resolved at the time spacing used. These peaks yield the maximum peak to peak amplitude so the peak to peak amplitude is not stable. This makes the peak to peak amplitude a poor measure of the amplitude fit between models. A far more stable measure of amplitude correspondence between seismograms of this type is the RMS amplitude calculated over some time window appropriate to the seismograms being compared. The RMS amplitudes calculated with window lengths of as much as 45s agree to better than one percent for all pairs of seismograms shown in Figure 18. RMS amplitudes calculated with window lengths greater than 45 seconds show discrepancies in the amplitude correspondence between each pair due to the finite length of the seismogram. Some discrepancies are seen between the detailed waveforms of the direct and hybrid synthetics. These discrepancies are of at least two types. First, and most easily explained, are the small arrivals seen at the beginning of the seismogram in the direct synthetics only. The lack of these arrivals on the hybrid synthetics is due to the exclusion of the very low amplitude initial portion of each seismogram used as forcing function. These portions lie outside the input window as illustrated in Figure 17. Second, are the small discrepancies seen in the higher frequency component of the seismograms, particularly within the first twenty seconds of the trace. To better quantify these shorter period differences, and to enable one to view the record as one would see data from an event, the WWSSN short period instrument response is convolved with seismograms of the type shown in Figure 18 to give seismograms of the type shown in Figure 19.

Figure 19 shows comparisons between direct and hybrid synthetics for a selection of horizontal distances along the free surface. Above each pair of seismograms the

horizontal distance from the source to the receiver is shown. For this test a FE grid of dimensions 150x300 nodes was used. Beside each pair of traces the ratio of hybrid to direct RMS amplitudes is given. In each pair, the upper seismogram is the direct synthetic and the lower trace is the hybrid synthetic. The duration of all seismograms is 102s and the peak to peak amplitude of each trace is scaled to the same value. Each seismogram shown is bandpass filtered between 0.01 and 1.00 Hz and includes the WWSSN instrument. The bandpass filter is applied to the forcing functions and to the resulting FE seismograms. It is applied twice in succession to the direct synthetics. The waveform correspondence between the two types of synthetics is excellent for short horizontal distances, but worsens as horizontal distance increases. The most striking changes occur in the maximum peak to peak amplitudes, and in the amplitudes of successive peaks relative to each other in the first ten to twenty seconds of the record. It appears that the waveform correspondence between the two types of synthetics is excellent if the first ten to twenty seconds of the record is omitted. The discrepancies early in the seismogram could have several sources such as, truncation errors due to the use of too few input forcing functions, the comparison of hybrid seismograms which experience 2-D spreading in the portion of their paths in the FE grid to direct seismograms which experience 3-D propagation along the entire path, reflections from the bottom of the FE grid, and possible intrinsic errors due to the accuracy of the numerical codes or completeness of the chosen representation for the forcing functions and direct seismograms. Some of these possible sources for differences in waveform will be discussed in detail below or in later chapters. It is important to note that despite the small variations in the waveform the RMS amplitude correspondence is excellent and stable as propagation distance increases.

Next the necessary vertical extent of input forcing functions needed to produce an accurate mode sum hybrid seismogram and the truncation error associated with

that vertical extent will be discussed. For the case of the SH pulse from a line source discussed earlier it was found that accurate results required a vertical extent of forcing functions greater than the depth of the receiver by an amount that increased as the horizontal propagation distance increased. This meant that the coupling of an SH pulse from a distant source into a grid with a high aspect ratio necessarily produced results that became very poor at large distances. Fortunately, this behavior does not directly generalize to the case of a layer over a half-space. For a layer over a half-space the results are compatible with and can be explained by considering the Love waves to be modeled in terms of constructive interference of post critical multiple reflections trapped within the crustal layer. This interpretation of Love waves suggests that the most critical nodes at which forcing functions need to be applied are the initial nodes in each row of the grid located in the crustal layer. The results of the calculations illustrated in Figures 20 and 21 show large changes in the waveforms and amplitudes of hybrid synthetics occur as the number of input forcing functions increases, until all nodes in the first column of the grid that lie within the crustal layer have forcing functions applied to them. Further increases in the depth extent of applied forcing functions produce only small changes in waveform in the first thirty seconds of the trace and almost no changes in RMS amplitudes. This remains true of the hybrid synthetics after propagation distances of more than five to ten layer thicknesses of the crustal layer.

All results shown in Figures 20 and 21 were calculated in a FE grid of dimension 150x300 nodes. Five FE calculations were completed, each using a different number of applied forcing functions. These tests use fifteen, thirty, forty five, sixty, and ninety applied forcing functions. In Figures 20 and 21 a number or numbers appear below and at the right end of each seismogram. This number n indicates that n forcing functions are applied to the topmost n nodes in the first column of the FE grid in the

calculation that produced the illustrated seismogram. The pairs of numbers at the left end of each seismogram are peak to peak and fifty five second RMS amplitude ratios. For each seismogram the ratio shown is the ratio of the amplitude of the seismogram being considered to the amplitude of the seismogram at the same location for the example using sixty forcing functions. The uppermost number is the peak to peak ratio, the number below it is the RMS ratio. The layer thickness of thirty two kilometers is equivalent to sixty four rows of nodes. The sixty fifth row of nodes is the first row describing the half-space. The calculation using sixty applied forcing functions is used as a reference since the behavior of the discrepancies due to truncation of the vertical extent of input forcing functions changes when forcing functions are applied outside the layer.

Figure 20 shows three groups of seismograms. Each group is recorded at the surface at a given horizontal distance. That distance is shown on the figure above each group of traces. The first group consists of a single seismogram recorded five kilometers or ten elements from the grid edge. This seismogram represents the identical results observed in the five test cases. The second group of seismograms are recorded twenty five kilometers from the grid edge. The first seismogram in this group represents the almost identical results for the three test cases using the largest numbers of applied forcing functions. Amplitude discrepancies between these cases were less that 0.2%, and no differences in waveform could be seen when the seismograms for each case were overlaid. However, the second two seismograms in the group, representing the tests with thirty and fifteen applied forcing functions respectively show significant differences in waveform and amplitude. The most striking effect of using fewer applied forcing functions is the reduction in the amplitudes of the later arrivals in the seismograms with respect to the early arrivals. The peak to peak amplitudes and the RMS amplitudes with longer window lengths were also reduced as

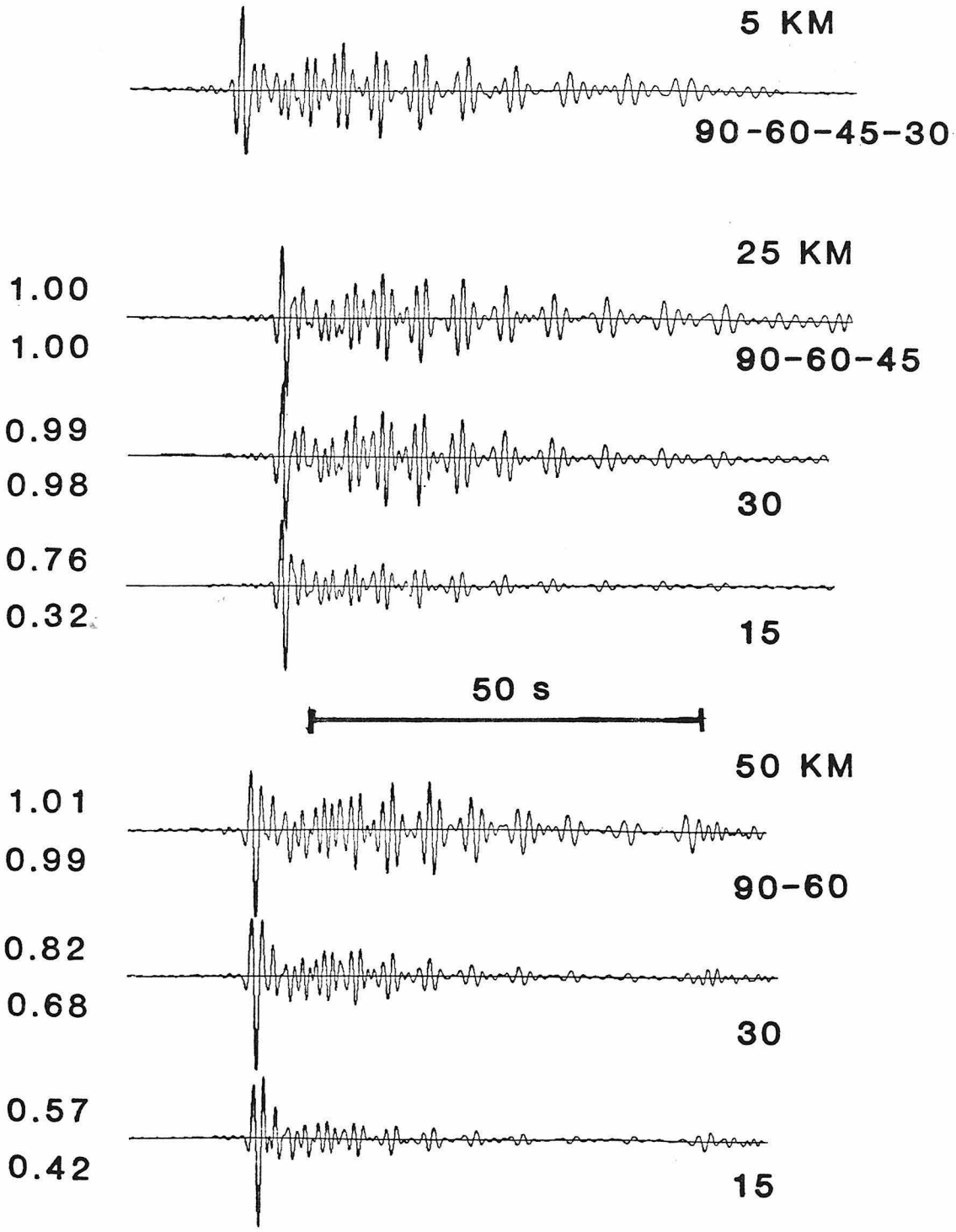

Figure 20: Comparison of hybrid results using different numbers of input forcing functions. Each group of seismograms shows results at a given horizontal distance, as labeled above that group. The number or numbers below and to the right of each seismogram indicate the number of nodes where forcing functions are applied. The pairs of numbers to the left of each seismogram are amplitude ratios. The upper number in each pair is the ratio of the peak to peak amplitudes of that trace to the trace using 60 forcing functions recorded at that distance. The lower number in each pair is the corresponding ratio for RMS amplitudes.

the number of applied forcing functions decreased. In particular, for the seismogram generated using thirty applied forcing functions the RMS amplitude measure corresponds well with the examples using more forcing functions until the window length of the RMS operator exceeds sixty seconds, then the discrepancy increases as the window length increases. For the example using fifteen forcing functions the trend seen in the RMS amplitudes follows the same pattern but the differences in peak to peak amplitude mean that agreement is not good even at a window length of fifteen seconds. If results of the calculation using fifteen forcing functions are examined at locations between the two distances illustrated it is found that the behavior seen in the thirty forcing function example is seen at distances around twelve kilometers in the fifteen forcing function calculation. The third group of seismograms is recorded at a distance of fifty kilometers. The second two seismograms in that group also show the rapid decline in RMS amplitude as the RMS window length increases. However, the example using thirty forcing functions now also shows poor agreement even in the fifteen second window. The example using forty five forcing functions is not illustrated at this distance. The RMS amplitude of the forty five forcing function seismogram corresponds well with the more complete examples for RMS windows as long as sixty five seconds. It was not considered necessary to illustrate this seismogram as it was so similar to the first seismogram in the group. From examining the seismograms at these three distances patterns are beginning to emerge, that will be clarified by the additional distances illustrated in the next figure.

Figure 21 is a continuation of Figure 20 for seismograms recorded at greater distances along the free surface. The amplitude ratios of the two examples using fifteen and thirty forcing functions continue to decrease with distance, although the RMS amplitudes have almost stablized by the time the horizontal distance has reach 150 km. The disturbances visible in the trace have become larger with respect to the

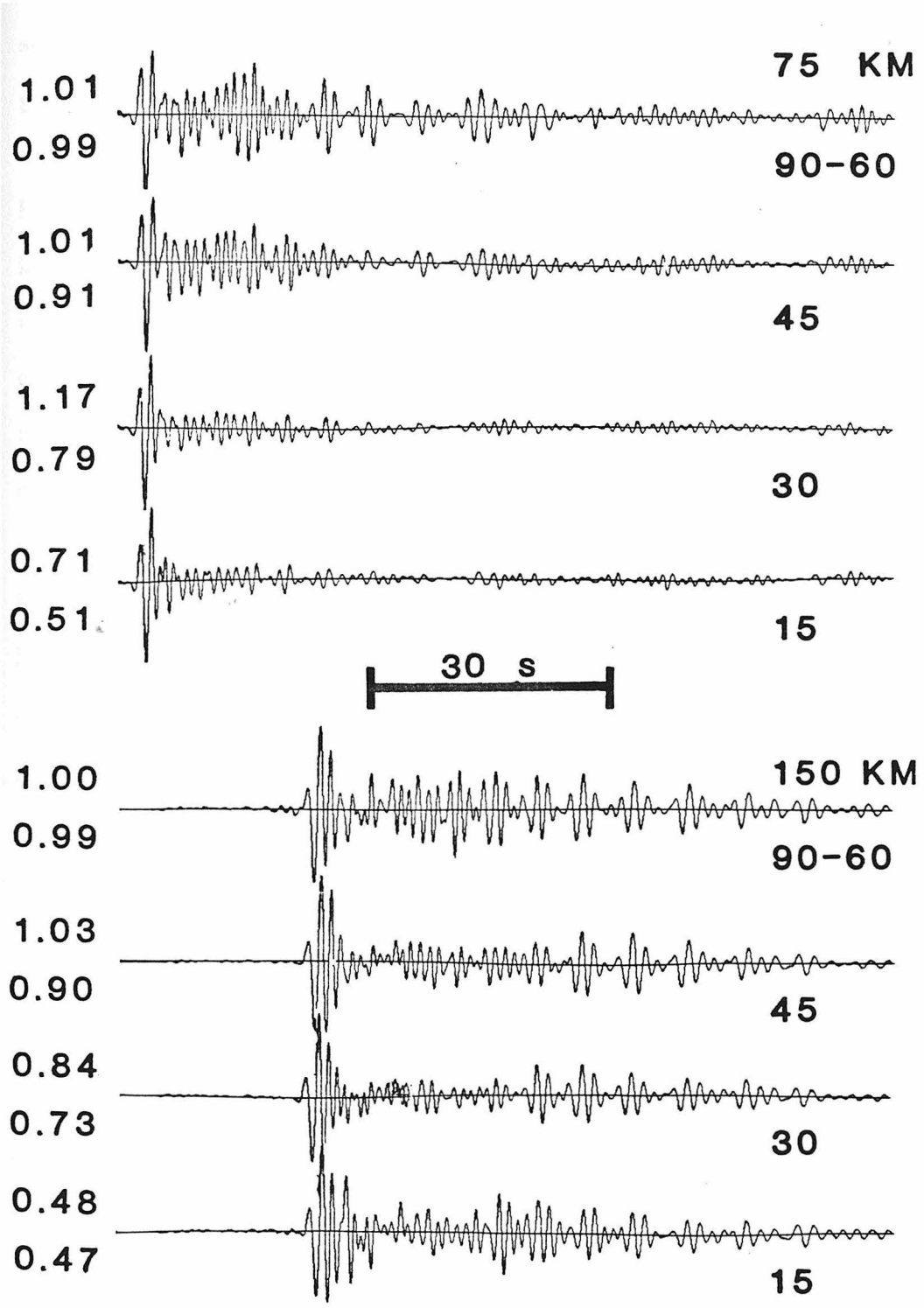

Figure 21: Comparison of hybrid results using different numbers of input forcing functions. Details are the same as figure 20.

shrinking arrival that determines the maximum peak to peak amplitude of the seismogram. For the example using forty five forcing functions the later arrivals continue to shrink with respect to the earlier arrivals as horizontal distance increases, reducing the RMS amplitude in successively shorter time windows. At distances between seventy five and one hundred kilometers the RMS amplitude stabilizes at about 90% of the values seen for the examples using more forcing functions. However, the waveforms correspondence continues to decay. Generalizing the results seen in the examples using a depth extent of forcing functions considerably less than the thickness of the crustal layer leads to several observations. Seismograms along the surface are identical regardless of the number of forcing functions used provided that the propagation distance in the FE grid is less than or equal to the depth extent of the forcing functions. Beyond that distance range the amplitude of the waveform begins to decay. The amplitudes of the latest arrivals are the first to be reduced. As the distance increases progressively earlier arrivals are reduced in amplitude while amplitudes of the later arrivals continue to decay further. As the number of forcing functions increases the rate of amplitude decay decreases and the RMS amplitude value at which the amplitude eventually stabilizes increases. When the depth extent of forcing functions exceeds the crustal layer thickness this behavior changes. At a distance of three hundred kilometers the two examples using sixty and ninety forcing functions continue to agree very well. They show some differences in waveform, barely perceptible when the waveforms are overlaid, in the relative amplitudes of successive peaks during the first twenty to thirty seconds of the seismogram. At larger distances this discrepancy increases slightly, but the amplitude ratios remain very stable and the waveform differences remain small and confined to the first thirty seconds of the seismograms. Thus, truncation error can explain at least a part of the waveform discrepancies seen in the early portions of the seismograms illustrated in the surface section shown in Figure 19.

Figures 22 and 23 illustrate the effects of using different numbers of row of nodes, that is varying the vertical extent of the FE grid, on the resulting SH L_g mode sum seismograms. In each of these figures two groups of three seismograms are shown. Each group is labeled with its propagation distance in the FE grid. The same forcing functions, for a source 1500 km distant at a depth of eight kilometers, are used for each calculation. All seismograms in these figures are plotted at the same scale. The uppermost seismogram in each group was calculated in a FE grid with ninety rows, the center seismogram in a FE grid with one hundred fifty rows and the lower seismogram in a FE grid with three hundred rows. An additional difference between the grids used in these tests is that the grid in which the uppermost seismogram in each group is calculated has a length of five hundred nodes and the other two grids have a length of three hundred nodes. Consequently, differences seen in the last ten to twelve seconds of the upper two records can be attributed to reflections from the righthand edge of the grid. All other differences seen between these seismograms can be attributed to reflections from the bottom edge of the grid. Since the travel time to the bottom of the grid is increased as the number of rows in the grid is increased, any reflections from the bottom of the grid should be seen at different points in the seismogram for each grid. The length of the seismogram is chosen so that reflections from the bottom of the three hundred row grid should arrive after the end of the seismogram. The reflections from the righthand edge of the grid are small but clearly visible, and are, as expected, identical on both of the lower two seismograms in each group. Examining the group of seismograms for a propagation distance of fifty kilometers within the FE grid shows essentially no differences between the seismograms recorded in grids with ninety and three hundred rows. When compared carefully to these seismograms the seismogram calculated in the grid with one hundred fifty rows shows some small differences in the amplitudes of some of the peaks. The RMS amplitudes agree to within less than 0.1%. This implies that reflections from the bottom of the

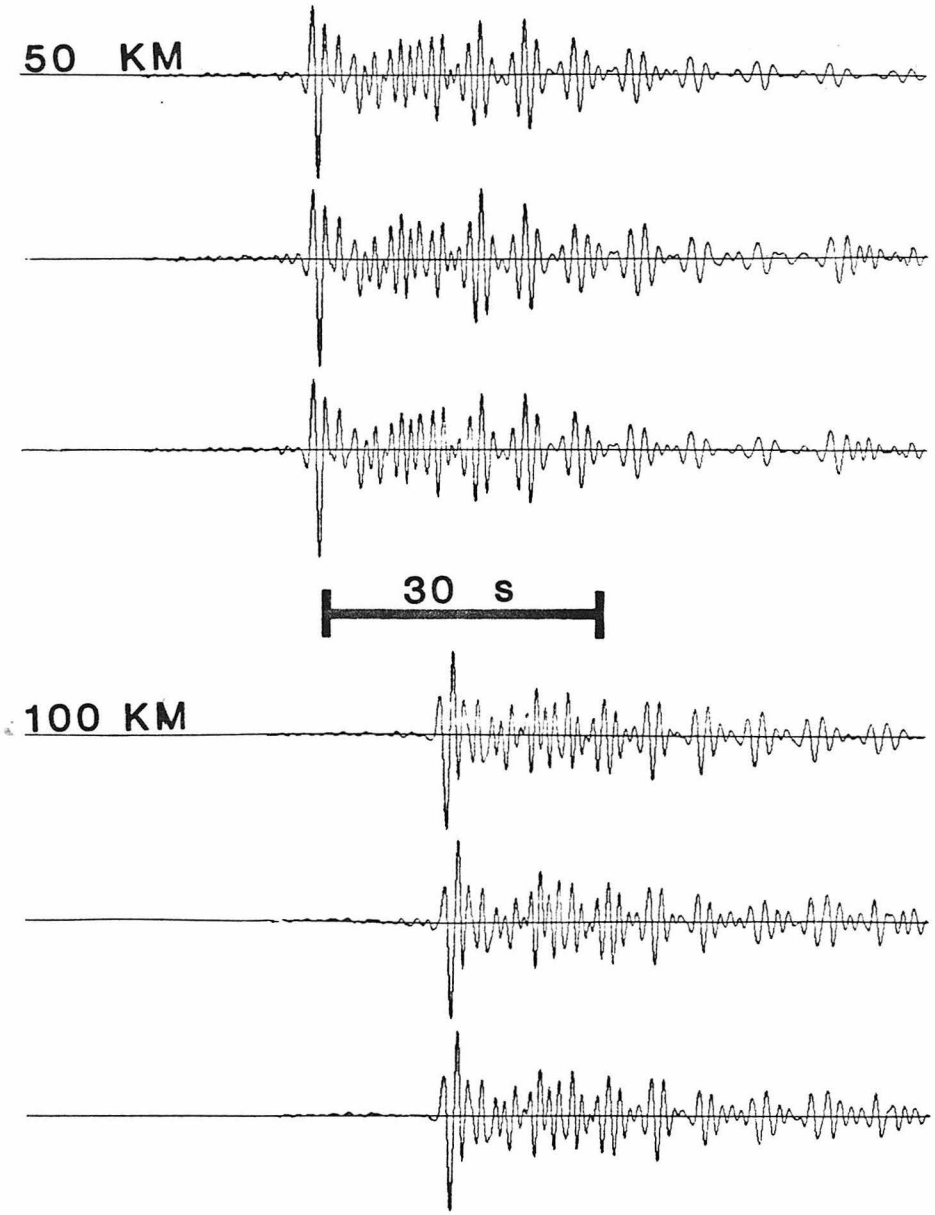

Figure 22: Comparison of hybrid solutions for cases using different numbers of rows of nodes. Results show wide angle reflections are not important. Each group of three seismograms is recorded at the free surface at the indicated distance from the grid edge. The upper trace in each group uses 90 rows of nodes, the center trace 150 rows of nodes and the bottom trace 300 rows. The peak to peak amplitudes of each trace are normalized to one. Differences in peak to peak amplitudes are so small that all peak to peak and RMS amplitude ratios are 1.00. Duration of each seismogram is 102 seconds.

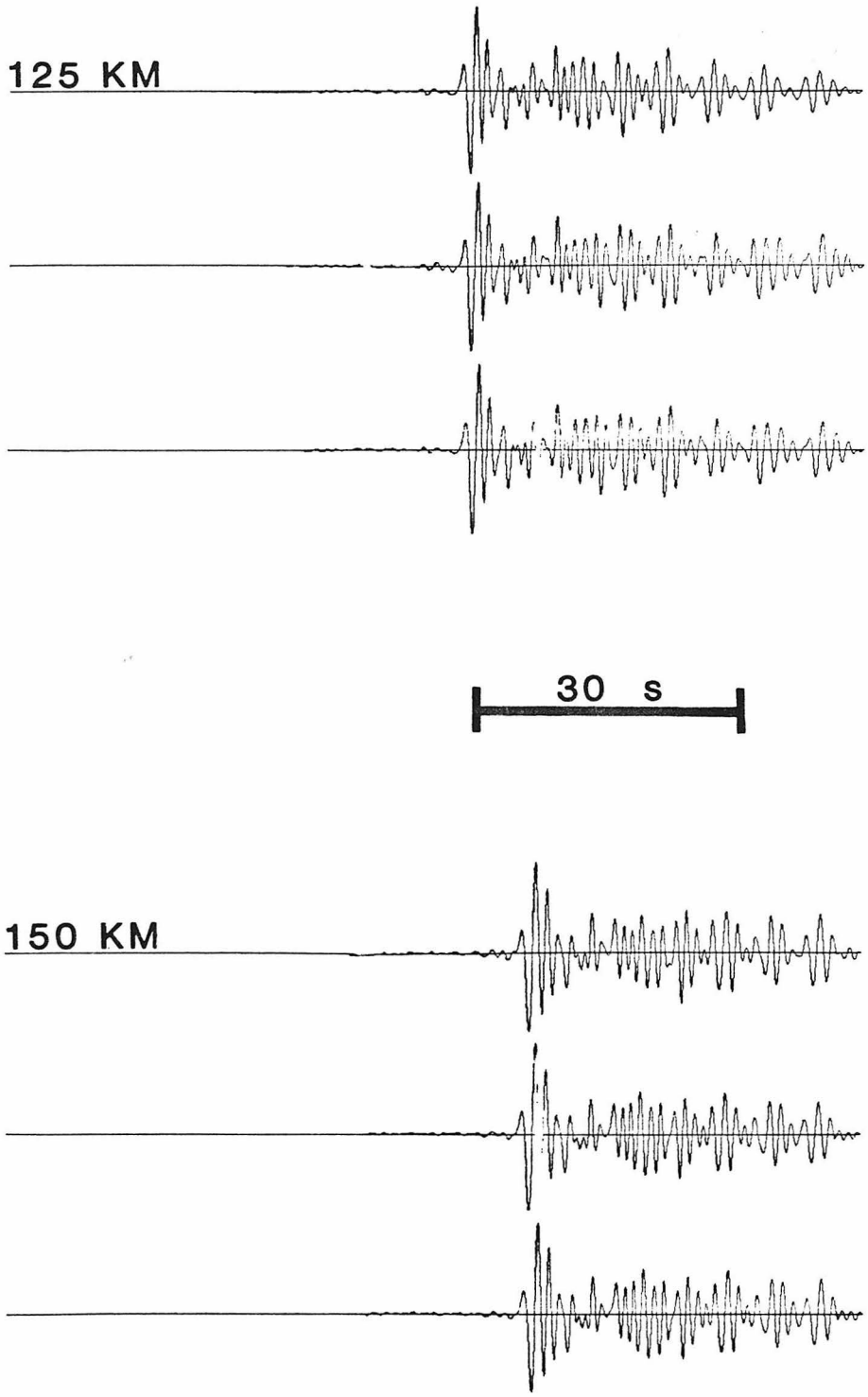

Figure 23 Comparison of hybrid solutions for cases using different numbers of rows of nodes. Details are the same as for figure 22.

grid are insignificant with short path lengths in the grid. For a path length of one hundred kilometers within the FE grid the reflections from the bottom of the grid remain insignificant, as illustrated in the second group of seismograms in figure 22. The two groups of seismograms in Figure 23 show that the reflections from the bottom of the grid remain insignificant to distances of at least one hundred fifty kilometers. Thus, even for aspect ratios as high as three the reflections from the bottom of the grid are not significant when the propagation of SH type L_g mode sum seismograms in a layer over a half-space is being considered. This conclusion will be further supported when the transparent boundary conditions are considered in the following chapter. It will be demonstrated that reflections from the bottom of the grid are significant only when structures are not plane layered.

Summary

In this chapter the basics of the modal propagator matrix method and the FE method were discussed, including the modifications made to the existing implementations of these methods. An approach to apply the Representation Theorem to combine these techniques into a hybrid method was explained. The particulars of the implementiation of the coupling technique differ depending on whether the propagator results are to be passed into the FE calculation or the the FE results are to be transmitted further using the propagator matrix technique. The coupling from modal propagator matrix results to the FE method was demonstrated for the simple example of a layer over a half-space. This simple structure allowed the calculation of analytic synthetics to which the hybrid synthetics could be directly compared to give estimates of the accuracy of the coupling technique.

Chapter 2

Application of Modal Propagator Matrix to Finite Element Coupling to Investigation of L_g Propagation across Ocean Continent Boundaries

Introduction

In this chapter the effects of a thinning or thickening of the crustal layer on the propagation of L_g mode sum seismograms will be examined. The thinning or thickening of the crustal layer is used as a simple model of ocean to continent or continent to ocean transitions. The L_g phase is of particular interest since it is used in several important applications such as mapping the extent of continental crust, magnitude determination, and discrimination between explosive and earthquake sources. The understanding of the observations that L_g wave is attenuated completely when the propagation path includes an oceanic portion of length greater than one hundred to two hundred kilometers or a region of complex crustal structure is not complete, and a clear explanation of this phenomenon could have important consequences for all these types of studies.

The transition model calculations presented in this chapter show that passage through a region of thinning crustal thickness, the model for a continent to ocean transition, increases the amplitude and coda length of the L_g wave at the surface, and allows much of the modal energy trapped in the crust, which forms the L_g phase, to escape into the subcrustal layers as body waves or other downgoing phases. The magnitude of both these effects increases as the length of the transition increases or the slope of the layer boundaries decrease. The passage of the wavefront exiting the continent to ocean transition region through the oceanic structure allows further energy to escape from the crustal layer, and produces a decrease in L_g amplitude at the

surface as the length of the oceanic path increases. The amplitude decrease is maximum near the transition region and decreases with distance from it. Passage through a region of thickening crust, the model of a ocean to continent transition, causes a rapid decrease in the L_g amplitude at the surface of the crust. The energy previously trapped in the oceanic crustal layer spreads throughout the thickening crustal layer, and any amplitude which has been traveling through the subcrustal layer but has not reached depths below the base of the continental crust is transmitted back into the continental crust. The attenuation of L_g at the crustal surface along a partially oceanic path occurs in the oceanic structure and in the ocean to continent transition region. The attenuation at the surface depends in part on the escape of energy at depth through the continent to ocean transition region into the underlaying half-space.

Designing FE Grids and Sampling FE Solutions

A study of the effects of the length of simple transition regions on the attenuation of SH type L_g mode sum seismograms passing through them has yielded some interesting results. Two classes of transition models were considered. An example of each class is illustrated in Figure 1. Calculations were performed for four individual models from each class, for a continental crustal layer over a mantle half-space, and for an ocean layer and an oceanic crustal layer over a mantle half-space. The difference between individual transition models was the length of the transition region, or the horizontal distance between points B and D shown in Figure 1. As discussed earlier, real ocean to continent type transitions occur over lengths of order one hundred kilometers. However, an upper limit on the length of the transition of one hundred kilometers was imposed by limiting FE computation time per model to approximately one cpu day. Thus, the lengths used for this investigation were a step transition (0 km), twenty five , fifty, and one hundred kilometers. In order to discuss the results of the FE calculations using these models one must first describe the models.

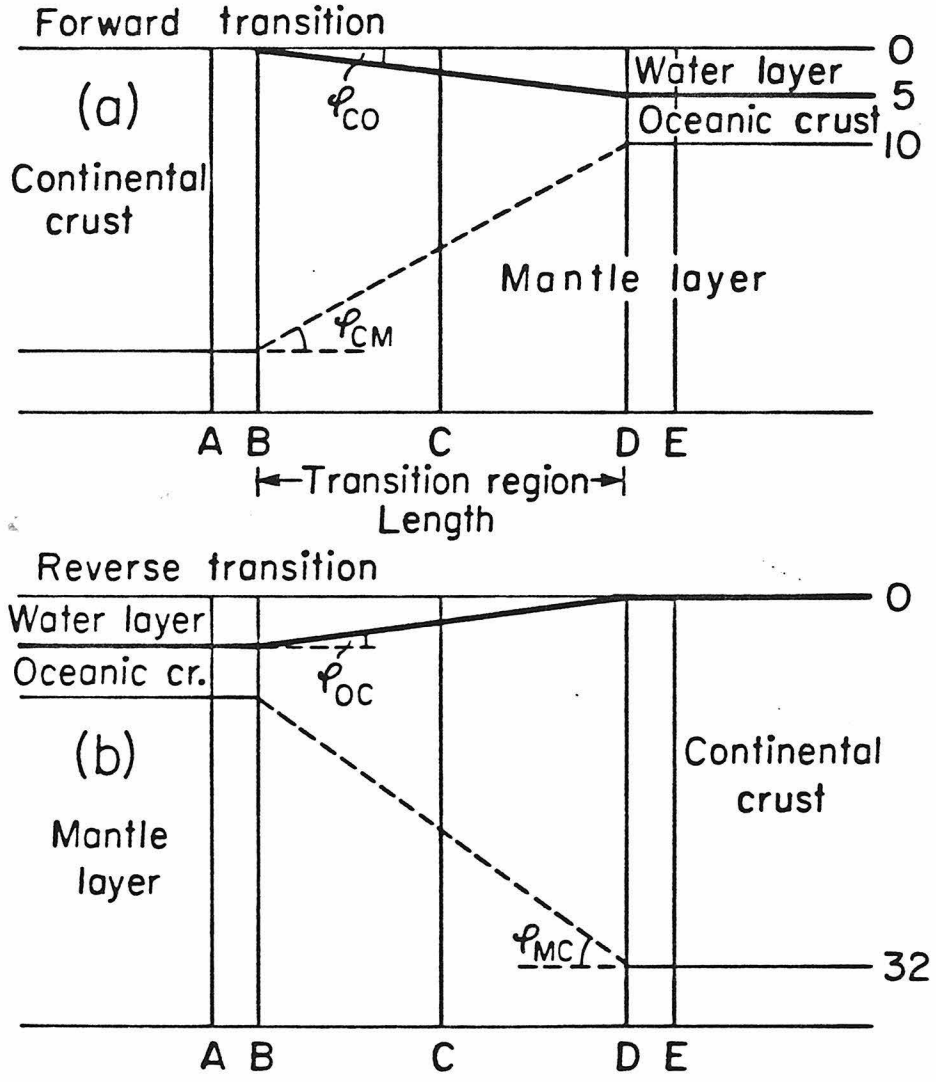

Figure 1: Explanation of terms and illustration of the model classes used to describe the behavior on passage through a transition region. The heavy line (——) between the water layer and the crustal layer is the surface. The sloping portion of this surface is the continent to ocean boundary for the forward transition model and the ocean to continent boundary for the reverse transition model. Similarly, the sloping dashed line (----) between the crust and mantle layers is the crust to mantle boundary for the forward transition and the mantle to crust boundary for the reverse case. The length of the transition is the distance from B to D, B is referred to as the beginning of the transition , D as the end of the transition, C as the center of the transition. A is 5 km from B, E is 5 km from D.

Also, the methods used to obtain and display the results of the calculations using those models must be considered.

Analysis of the effects of various transitions on the waveforms and amplitudes of L_g waves using FE techniques requires that the motions of the nodes of the FE grid be sampled so that the progress of the L_g waves across the transition can be observed. Two methods of sampling are used in this study. Complete displacement time histories are recorded for selected nodes, and the displacements of all nodes in the grid are recorded at given time intervals. The first approach produces seismograms which can be used to illustrate variations of amplitude and waveform with distance or depth, the second approach produces time slices and is a clear way to illustrate the propagation and distortion of wavefronts caused by passage through the inhomogeneous structure. For each model seismograms were recorded at intervals of approximately five kilometers along the surface. Groups of seismograms at the same horizontal distance, Δ, from the edge of the grid, were recorded at each of several different Δ' s. At each of these Δ' s the surface seismogram and seismograms equally spaced in depth below it were recorded. Such depth sections, with a vertical spacing of 2.5 km, were recorded at distances including those corresponding to positions A through E (Figure 1) for each model. For each one hundred kilometer transition additional depth sections were recorded midway between B and C and midway between C and D. For the fifty kilometer forward transition an additional depth section with vertical spacing of 0.5 km was recorded twenty five kilometers beyond the end of the transition region. This section was used as input for later reverse transition calculations. For the continental layer over a half-space model, or the forward reference model, depth sections were recorded at distances corresponding to positions A though E in each forward transition calculation. Thus, each depth section in a forward transition model corresponds to a depth section in the forward reference model whose component seismograms have

propagated the same distance, both as mode sum synthetics in the same plane layered medium, and as waves in their respective FE grids. Similarly, depth sections at distances corresponding to positions A through E in each reverse transition model are recorded in the reverse reference model calculation. For each model time slices were recorded once or twice every twenty five seconds, that is, every two hundred fifty or five hundred time steps.

At this point it is useful to digress and explain the time slices used in these studies. A time slice records the displacement at each point in the FE grid. These displacements are graphically represented by centered symbols plotted at an array of points depicting the nodes in the FE grid. The size of the symbol plotted at the node is increased as the absolute value of the displacement increases, producing darker areas where larger displacements are occurring. Each of the time slices is self scaled, that is the largest value of the absolute value of amplitude in the grid sets the symbol size to 1.5 element widths at the node where it occurs. At all other nodes the product of two quantities, the ratio of the amplitude at that point to the maximum amplitude, and the size of the largest symbol (1.5 element widths), is the size of the symbol plotted. The symbols also have a minimum size set by the resolution of the plotter. Therefore, to avoid plotting points whose amplitudes vary by orders of magnitude at the same minimum size, a cutoff must be defined below which no symbol is plotted. For the illustrated layer over a half-space time slices this cutoff is one percent of the maximum amplitude. For the illustrated forward and reverse time slices the cutoff is two percent of the maximum amplitude. Setting the cutoff this low means that the smallest symbols cover a range of amplitudes between one or two percent and about eight to ten percent of the maximum amplitude. The self scaling of the time slices means that successive time slices may show the same absolute amplitude as a different symbol size. Thus, the same region of the waveform will appear darker on a time slice

with a given maximum amplitude than on another time slice with a larger maximum amplitude. This difference must be remembered when interpreting the time slices. At any depth within the grid the pattern of displacements seen in a time slice, as a function of distance, can be understood by comparing it to a seismogram recorded at that same depth. The oscillations in amplitude with distance at a given time are similar to those seen as a function of time at a given distance. Thus, the seismogram can be considered to be a recording of the passage of successive points of the coherent wavefield seen in the time slice past a fixed recorder. Conversely, the time slice can be viewed as showing the location in space of the energy that forms each peak in the seismogram, at a given instant of time.

Now, returning to the definition of the model classes used in this study, the two classes of transition models and the two classes of reference models used will be discussed. An example of each transition model class is shown in Figure 1. The difference between individual transition models within each class is the length of the transition region, or the horizontal distance between points B and D shown in Figure 1. The first class of models are used to describe continent to ocean transition regions. In further discussions these models will be referred to as forward models, and the transitions they represent as forward transitions. The second class of models are used to describe ocean to continent transition regions. In further discussions these models will be referred to as reverse models and the transitions they represent as reverse transitions. As the length of the transition region increases in either class of transition model, the angle that the the ocean to crust boundary or crust to ocean boundary makes with the horizontal (ϕ_{OC} or ϕ_{CO} in Figure 1) varies between 3° and 90° , and the angle the the crust to mantle boundary or the mantle to crust boundary makes with the horizontal (ϕ_{MC} or ϕ_{CM} in Figure 1) varies from 12° to 90°. The differences in slope of the boundaries and the different elastic properties of the layers they separate

indicate that different behavior should be expected along those two boundaries. The first type of reference model consists of a thirty two kilometer thick layer over a half-space. This will be referred to as the continental reference model. The second type of reference model consists of two five kilometer thick layers, one water and one of the same material as the layer in the continental reference model, and a half-space of the same material as the half-space in the continental reference model. This model will be referred to as the oceanic reference model. All of these models will be described in detail below. Then the design of the FE grids to represent these models will then be discussed.

The first class of models are models of forward transitions. In each forward model the transition region is characterized by a continuous rate of thinning of the crustal layer between the thirty two kilometer thick continental crust at the beginning of the transition region and the five kilometer thick oceanic crust, overlain by five kilometers of water, at the end of the transition region. The crustal layer has a SH wave velocity, v_C, of 3.5 km/s and a density of 2.7 g/cc, while the half-space has an SH wave velocity, v_M, of 4.5 km/s and a density of 3.4 g/cc. Each transition model has the same boundary conditions (BC's) applied to it. Thus, the same set of forcing functions are used to drive the FE calculation performed on each forward model. In each case the leftmost column of nodes of the forward transition FE grid are constrained to move with the displacement time histories specified by the forcing functions. The forcing functions are a vertical section of sixty mode sum seismograms, calculated at depth intervals of 0.5 km beginning at the surface, for a source at eight kilometers depth at a distance of Δ=1500 km. The same mode sum forcing functions are also used as input to the continental reference model.

The second class of models are models of reverse transitions. Each reverse transition is modeled as a smooth increase in thickness of the crustal layer between a five

kilometer thick oceanic crust, overlain by five kilometers of ocean, at the beginning of the transition and a thirty two kilometer thick continental crust at the end of the transition. The forcing functions for the reverse transition tests are recorded during the fifty kilometer forward transition calculation. They consist of a depth section of hybrid seismograms recorded twenty five kilometers past the oceanic end of the fifty kilometer forward transition transition region, which corresponds to a distance of 1755 km from the source. The vertical spacing within the depth section is 0.5 km. The reverse transition forcing functions are also used as input to a reverse reference or oceanic model of a five kilometer thick ocean layer and a five kilometer thick oceanic crustal layer over a mantle half-space. An additional series of calculations using the reverse transition models were done to investigate the effects of ocean to continent transitions on mode sum seismograms from an oceanic source. The forcing functions used for these calculations were determined as a sum of the fundamental and the first ten higher modes for a source 1500 km from the grid edge at a depth of eight kilometers below the ocean surface in an oceanic structure. These oceanic mode sum seismograms are also used as input for the reverse reference model.

Finite Element calculations are computationally intensive, consuming many hours of computer time. In order to maximize the information yielded by a calculation using a particular amount of cpu time, the model grids must be carefully designed. It is important to minimize the number of grid points, and the time spacing, and to maximize the spacing between nodes. Other considerations are also important, most notably, the removal of reflections created by the boundaries of the grid from the portion of the waveform to be studied.

The first step in designing a grid for FE calculations is to determine grid size, grid spacing, and the time step duration. These quantities are chosen so that the FE calculation remains stable but executes as rapidly as possible. The highest frequency

of the waveform to be modeled and the S velocity of the material through which it propagates determine the smallest allowable grid spacing. At least six nodes per wavelength are needed to avoid numerical dispersion problems. Therefore, to propagate a wave with a maximum frequency of f through a medium with velocity V, the grid spacing required is

$$dx \leq \frac{V}{6f} \tag{1}$$

It should be noted that in a structure containing regions of different velocities the slowest velocity should be used to determine dx to insure stability of the calculations. Given the minimum grid spacing dx, the maximum time step duration follows directly. To maintain numerical stability in the code the wavefront can travel no more that half the grid spacing per time step.

$$dt \leq \frac{dx}{2V} \tag{2}$$

In this case the minimum velocity, V, within a complicated model should be used to insure stability within the whole model. In this study, we are considering L_g waves with a predominant period of approximately one second propagating through a layer of 3.5 km/s over a half-space of 4.5 km/s. Thus, we have chosen dx=.5 km and dt=.05s. This will allow the inclusion of frequencies as high as 1.17 Hz.

The next step in designing the grid is determining the number of grid points that will be needed, the dimensions of the grid, the location of the transition region within the grid, and the duration of the input forcing functions. The dimensions of the grid are expressed as the number of grid points in the horizontal direction, nx, and in the depth direction, nz. The location of the transition region within the grid is defined in terms of the distances from the leftmost grid edge to positions A, B, C, D, E, in Figure 1. The values of these parameters were chosen to satisfy two criteria. First, that a

seismogram of duration D_s seconds could be recorded at A (Figure 1) before the multiple reflection of the input wave from the beginning of the transition, B, to the leftmost grid boundary then back to A reaches A. Second, that a seismogram uncontaminated by the multiple reflection with duration D_s seconds could be recorded at the receiver closest to the rightmost edge of the grid. This receiver is defined to be at a distance x_f from the leftmost grid edge. For the calculations in this study x_f was chosen to be twenty five kilometers past the end of the transition. These two criteria concern themselves only with reflections from the leftmost edge of the grid. Nonphysical reflections can also occur from the bottom and the rightmost edge of the grid. These latter reflections are removed using transparent BC's which are explained and verified in a later section. Using the present code it is not possible to apply these BC's to a node which is constrained to a given displacement time history. Applying such a constraint makes the boundary appear rigid to any wave incident upon it from the grid. Since the leftmost column of nodes must be so constrained to couple the source into the FE grid, the left hand edge of the grid is considered to be reflecting. The duration D_s was chosen to be fifty five seconds because it was observed to be the coda length for a SH L_g mode sum seismogram, including the fundamental and the first five higher modes, at a distance of one thousand kilometers from the source. Although the input seismograms finally used were calculated at 1500 km and have a coda of at least seventy seconds, the amplitudes in the coda are reduced by an order or magnitude at fifty five seconds with respect to the beginning of the trace, and are rapidly decreasing. Thus, extending the grids and the number of time steps was considered to be an unnecessary expenditure of computer time. For all the models used in this study the values of parameters defining the size of the grid and the location of the transition region within it are given in table 1. In this table all quantities except nt and T_{mcalc} are given as the number of nodes in the horizontal direction from the left edge of the

grid to the depth section or boundary indicated. For the corresponding distances in kilometers divide the numbers by two. The quantity nt is given as a number of time steps, and the value of T_{mcalc} is in seconds.

TABLE 1
GRID CHARACTERISTICS FOR TRANSITION MODELS

	nx	nz	nt	T_{mcalc}	A	B	C	D	E
model	# nodes		# Δt	s	# nodes				
0f	310	90	1921	96	230	240	240	240	250
25f	365	90	2101	105	240	250	275	300	310
50f	525	90	3101	155	350	360	410	460	470
100f	500	90	2441	122	250	260	360	460	470
0r	350	90	2561	128	275	285	285	285	295
25r	400	90	2501	125	275	285	310	335	345
50r	450	90	2601	130	275	285	335	385	395
100r	525	90	2941	147	275	285	385	485	495
31f	575	90	2701	135	255	265	315	365	375
31r	575	90	2701	135	417	427	477	527	537
69f	675	90	3001	150	265	275	325	375	385
69r	675	90	3001	150	523	533	583	633	643
fref	530	90	3201	160					
rref	525	90	3201	160					

To calculate the duration of the displacement time histories used to drive the calculation, T_{mi}, the distance from the leftmost side of the grid to the beginning of the transition region, A (see Figure 1), and the number of time steps the calculation must run to produce the desired seismograms, T_{mcalc}, a simple series of calculations was performed. The duration of the forcing functions, T_{mi}, must be long enough that a seismogram of duration D_s can be recorded at both x_f and A. In a layered medium the first arrival at a distance x will occur between the arrival times of a wave traveling entirely in the slowest medium, $T_{slow}=r/V_{min}$, and the wave traveling entirely in the fastest medium, $T_{fast}=r/V_{max}$. In these expressions $r = \sqrt{x^2 + (h-z)^2}$ where h is source depth and z is receiver depth. To allow the possible arrival time of the first significant energy to be anywhere between T_{slow} and T_{fast}, T_{mi} is chosen to be D_s plus

the travel time difference $\Delta T = T_{slow} - T_{fast}$. Since ΔT will be largest for the longest distance, providing a long enough seismogram at x_f will automatically provide one at A. So T_{mi} becomes

$$T_{mi} = D_s + x_f \frac{V_{max} - V_{min}}{V_{max} V_{min}} \tag{3}$$

In this expression r has been replaced by x. This is a valid substitution for distances $x >> x_c$, the critical reflection distance. For the examples considered here the source to receiver distance is larger than 1500 km, well in excess of the critical reflection distance. This would seen to imply that this substitution is valid for these calculations. However, the coupling of the energy from the distant source into the FE grid requires the specification of displacement time histories on a column of nodes. This is equivalent to applying a time variable source at each of the nodes constrained by a forcing function. The distance from these sources to the receivers within the FE grid is less than or of the same order as x_c. It can still be show that the substitution of x for r is valid, although, it may give an overestimate of the necessary duration, T_{mi}. To demonstrate this consider a receiver at depth z. The first significant energy at that receiver arrives from the nearest source, that at depth h=z. Thus, substituting x for r in the expression for T_{slow} is correct. Substituting x for r in the expression for T_{fast} will either make no difference or decrease the value of T_{fast}. Thus the travel time distance, ΔT, can be larger that the exact value but not smaller. This guarantees that portions of the seismogram that should not be contaminated with reflections will not be.

To determine a numerical value for T_{mi}, the distance x_f must be known. The value of x_f follows directly when the distance to the beginning of the transition, B, is known. To assure a seismogram at A of duration D_s which is not contaminated by reflections from the leftmost edge of the grid it is sufficient to specify that the two

way travel time from A to the leftmost edge of the grid be T_{mi}. Then the unknown value of x_f cancels and A can be expressed as

$$A = \frac{D_s V_{min} V_{max} + (T_l + x_f)(V_{max} - V_{min})}{(V_{max} + V_{min})} \tag{4}$$

where V_{min} is the velocity in the oceanic and continental crustal layers (3.5 km/s), V_{max} is the velocity in the mantle layer (4.5 km/s), and T_l is the length of transition region, (0, 25, 50, 100 km), x_l is the distance from the end of the transition to the last receiver (25 km) plus the distance from A to B (5 km). Once the distance to A is determined the distances to B, C, D, E, and x_f are known. This allows T_{mi} to be determined from (3), and the duration of the calculation follows directly.

$$T_{mcalc} = D_s + \frac{x_f}{V_{min}} \tag{5}$$

These calculations are modified slightly when the output at x_f is to be used as the input to a subsequent FE calculation. The necessary duration of uncontaminated seismogram at x_f becomes the duration of the input forcing functions needed for the second FE calculation. This is why the values of A, T_{mi}, and T_{mcalc}, for the fifty kilometer forward transition are larger than the values given by the above relations. The seismograms from the fifty kilometer forward transition at x_f are used as the forcing functions for all the reverse transition calculations. When a series of more than two FE calculations are performed, the values of the parameters above should first be determined for the final calculation. The value of T_{mi} for this calculation will give the value of D_s for the penultimate calculation. In this way the values of the parameters for each FE calculation from the last to the first can be determined.

Understanding the Accuracy and Efficiency of the Transparent BC

Transparent boundary conditions (BC's) are applied at two boundaries, both the rightmost edge and the bottom edge of each transition model FE grid. These, BC's

are introduced to remove the nonphysical reflections created by the interaction of the wavefronts with those two boundaries. Their introduction removes the requirement that those boundaries be far enough from the receivers that no reflections from them contaminate the desired results. However, the BC's do not remove all of the reflected energy, thus for detailed waveform modeling it is preferable to enlarge the grid rather than using the BC's, if such an enlargement is feasible. In all other cases, where small discrepancies in waveform can be tolerated, the interference on the small reflection with the incoming seismogram produces changes of less than 1% in the RMS amplitudes. For seismograms of fifty five seconds duration, removing the reflection from the right end of the grid by extending the grid would require increasing nx by almost two hundred grid points. This increases execution time by thirty to sixty percent. If reflections from the bottom edge of the grid must also be removed, nz must also be increased by two hundred grid points. The increase in execution time to remove both types of reflection by extending the grid is a factor of three to five. Clearly, a more efficient way to remove the reflections is desirable.

The transparent BC used in the calculations discussed in this study is implemented by averaging a rigid boundary solution with a free boundary solution for the displacement at the edge nodes. If no boundary condition is applied the boundary nodes form a free surface. When a wavefront interacts with a free surface a complete reflection of the incident wavefront occurs. If the edge nodes are constrained to have zero displacement, that is to produce a rigid boundary, the incident wavefront is completely reflected, but a change in the sign of the amplitude is introduced. This suggests that one way to remove contamination due to reflections is to add a solution with a rigid right edge boundary to a solution with a free right edge boundary (Smith 1974). Adding the corresponding seismograms from these two separate calculations is, however, a poor solution. Such an approach takes more computer time than simply

extending the grid in nx, and it also removes only the primary reflections, leaving multiple reflections to contaminate the results. The situation for removing reflections due to both bottom and edge boundaries is little better since four separate calculations are required to remove the primary reflections in this case. A better solution, suggested by Frazier, Alexander, and Petersen (1973), is to calculate displacements for the rigid boundary and for the free boundary cases, for each edge node at each time step. Those two displacements can then be averaged to give a displacement closer to that observed if the boundary was not present. For a normally incident plane wave this average exactly represents the transparent boundary. However in practice the incident wavefront is neither normally incident nor a plane wave. This means that the actual value at the transmitting boundary is a linear combination of the rigid boundary and free boundary solutions whose coefficients depend upon the angle of incidence of the energy. The boundary condition used here assumes that the average of the two solutions will in most cases be the best approximation to the transparent boundary that can be simply implemented. To implement the transparent BC's about twice as many calculations are necessary at each node on the transparent boundary. This increases the overall execution time of a transition type run by less than two percent.

The efficiency of the transparent BC's must be demonstrated and their limitations must be understood. The validity of the BC's for L_g mode sum input will be discussed later, but to more clearly illustrate their limitations it is useful to examine their effects on a simple SH pulse traveling in a homogeneous 2-D half-space. Two different situations are examined, first reflections from the rightmost edge of the grid are considered, then reflections from the bottom of the grid. The grids used for each of these tests are shown in Figure 2. The heavy lines within the grid show the nodes where hybrid seismograms are recorded. The time step used was of 0.05 seconds duration,

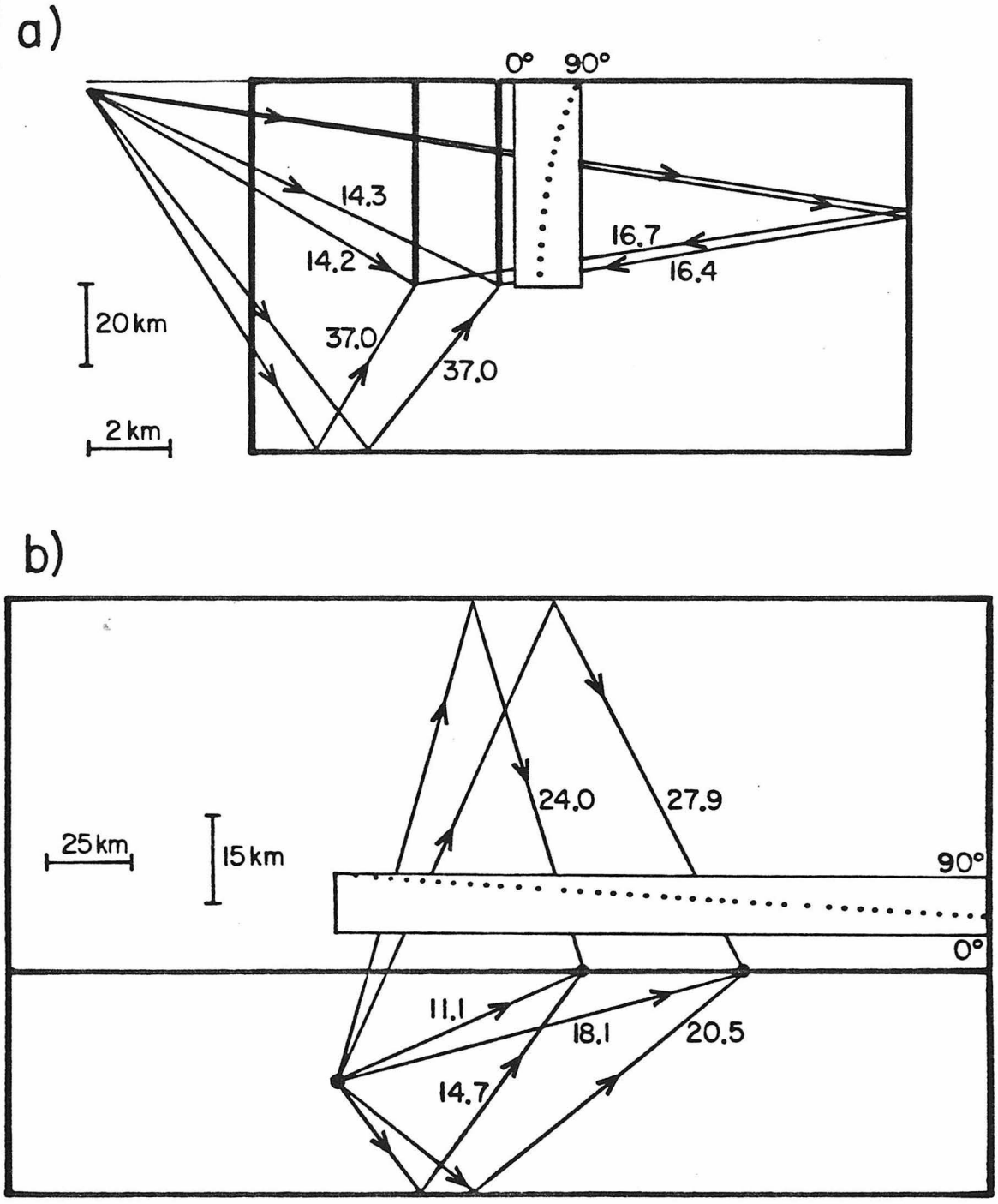

Figure 2: Grid geometries for the tests of the boundary condition for a 2-D SH pulse. Part a) shows the grid used to investigate reflections from the right end of the grid, part b) the grid used to study reflections from the bottom of the grid. Sample source to receiver ray paths are shown in both grids for the direct path, and for the path reflected from the grid bottom. Sample ray paths including a reflection from the right grid edge in a), or a free surface reflection in b) are also shown. Each ray path is labeled with its travel time. The sets of receivers are indicated by the solid lines within the grids. The dotted lines in the inset boxes show the variation of incident angle as a function of receiver depth or range.

and the grid spacing was 0.5 km. The dotted line in the inset rectangle shows the variation of the angle between the incident SH ray and the boundary being investigated along that boundary. In each grid the important SH ray paths are illustrated for sample receivers, and labeled with their travel times.

The geometry of the grid used to examine edge reflections is illustrated in Figure 2a). The size of this grid, 80x450 nodes. Examining the illustrated travel times shows that no contamination from bottom reflections reaches the receivers during the thirty five second duration or the seismograms. The horizontal distance from the source to the left edge of the FE grid is four kilometers. The horizontal distances from the source to the depth sections where results are recorded are eight and ten kilometers. The vertical range of receivers is between the surface and fifty kilometers depth. Thus, angles of incidence at the right end boundary of the FE grid are between thirty and ninety degrees.

The geometry of the grid used to study reflections from the bottom of the FE grid is shown in Figure 2b). The dimensions of the grid are 350x110 nodes. For this series of calculations the source used is a line source applied at a single point within the grid. The source was located within the grid to allow for a large range of angles of incidence at the bottom boundary. The time history of the force applied at the source is triangular with a rise time of ten time steps and a total width of twenty time steps. The small higher frequency oscillations superimposed on the decaying portion of the pulse in both calculations is due to finiteness of the embedded source. The illustrated travel times indicate that the reflection from the free surface arrives at a time well separated from the reflection from the bottom of the grid.

Figure 3 illustrates the effect of introducing the transparent BC's at the rightmost grid edge of the grid shown in Figure 2a). Each pair of seismograms represents one of the receivers on the depth section eight kilometers from the source. Figure 4

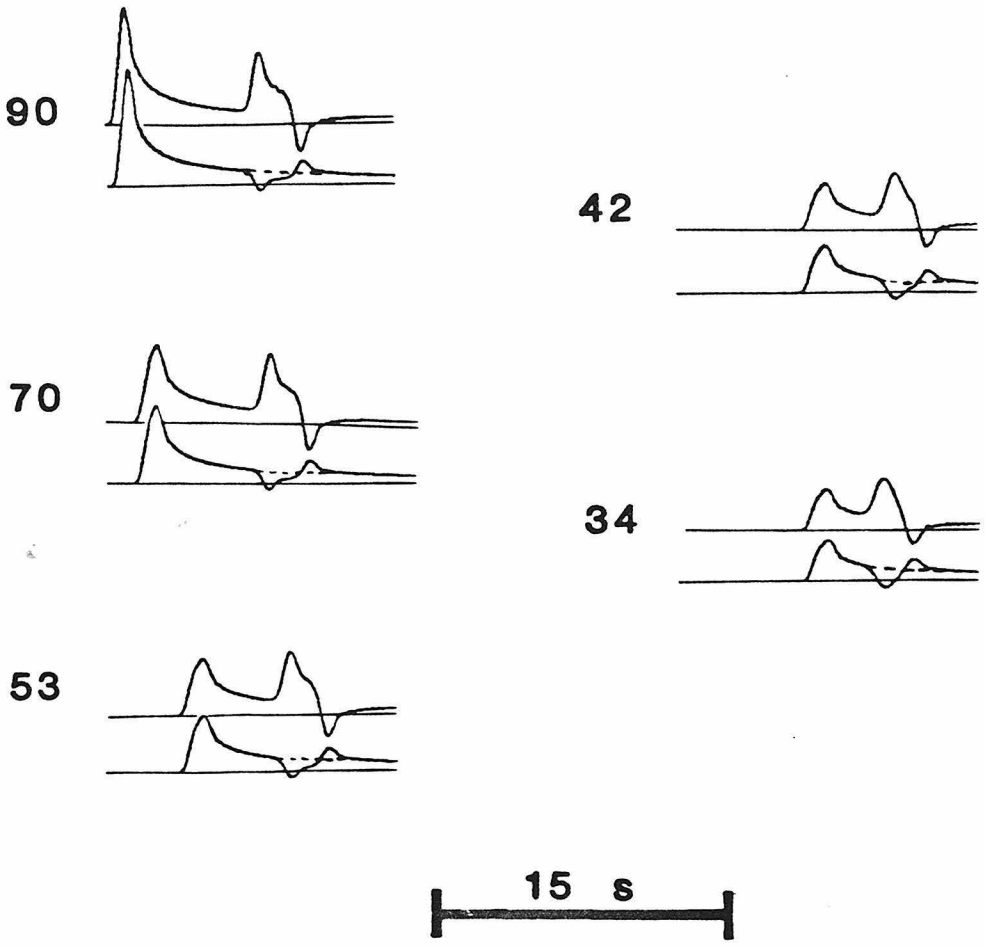

Figure 3: Efficiency of the absorbing BC demonstrated by results from calculations in the grid illustrated in Figure 2a. The uppermost seismogram in each pair is the hybrid solution with no BC's applied. The lower seismogram of each pair shows the hybrid solution with the BC applied to the appropriate boundary as a solid trace and the direct synthetic solution as a dotted line. The numbers beside each pair indicate the angle of incidence of the arrival at the reflecting boundary.

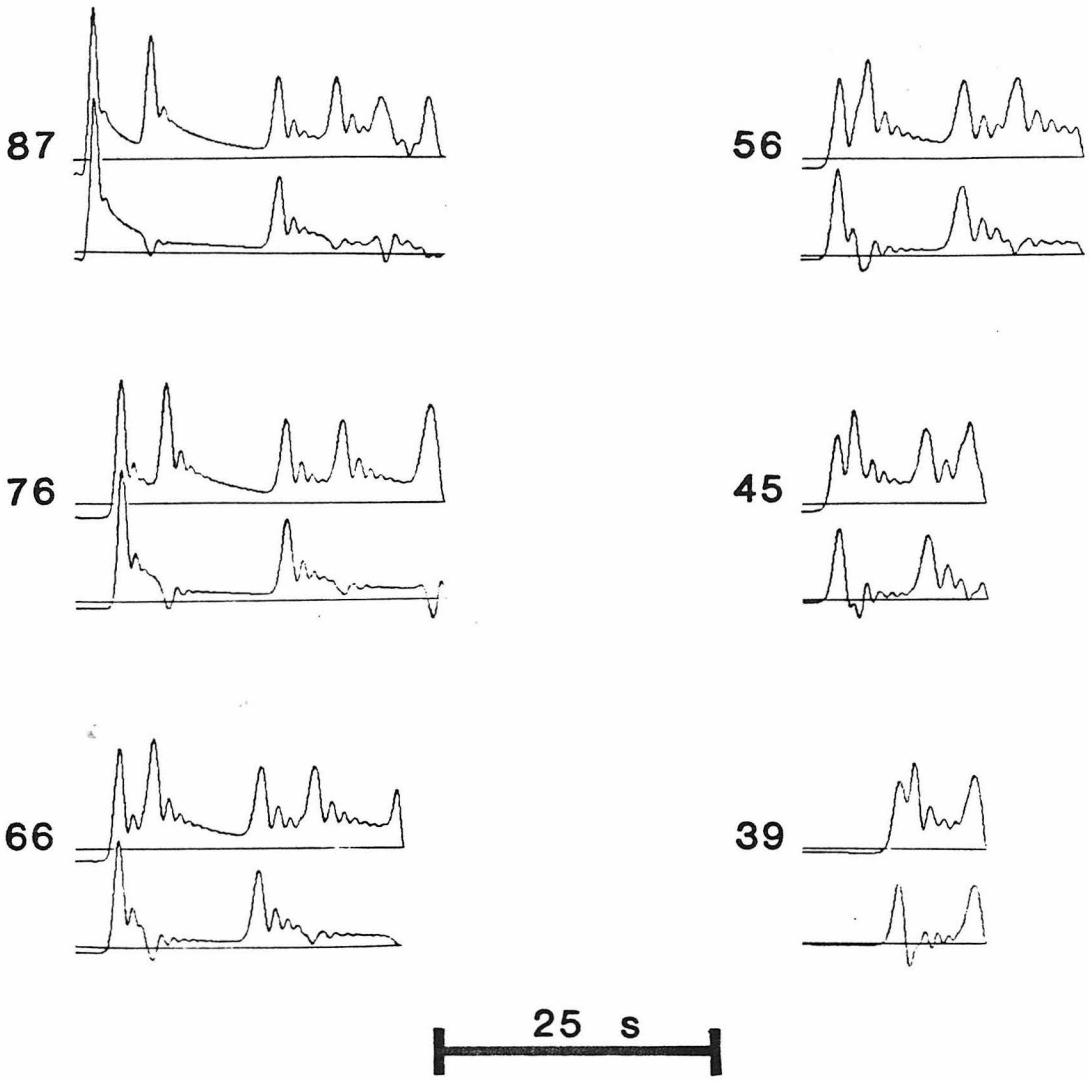

Figure 4. Efficiency of the absorbing BC demonstrated by results from calculations in the grid illustrated in Figure 2b. Details are identical to those explained in Figure 4.

illustrates the effect of introducing the them at the bottom grid edge of the grid shown in Figure 2b). Each pair of seismograms represents one of the receivers along the plane at thirty five kilometers depth. The uppermost trace in each pair shows the hybrid synthetic with no BC applied. The lowermost trace of each group shows both the analytic synthetic and the hybrid synthetic calculated using the BC. on the rightmost edge of the grid. The dotted portion of this trace shows where the analytic synthetic departs from the hybrid solution. The number to the left of each pair of traces indicates the angle of incidence, in degrees, at the rightmost edge of the grid in Figure 3 or the bottom edge of the grid in Figure 4. A second reflection, whose amplitude is inverted with respect to the first, is seen in Figure 3 only. This is the multiple reflection from the rightmost grid edge then from the rightmost grid edge. It illustrates that a boundary, such as the rightmost grid edge, with displacement time history constraints applied to it acts as a rigid boundary when considering energy incident upon it from the FE grid. In Figure 4 the upper trace in each group shows two pairs of almost equivalent sized peaks. The first pair of peaks are the direct arrival and its reflection from the bottom edge boundary of the grid, the second smaller pair of peaks shows the free surface reflection followed by its multiple reflection from the bottom grid edge.

For normal incidence the BC is very efficient, removing 93% of the reflected amplitude. The reflected pulse prominent when no BC is applied is very small when it is applied. For near normal incidence, the BC continues to be efficient, reflecting at most thirty percent of the incident amplitude for angles of incidence as small as fifty degrees. The BC is equally efficient for the same angle of incidence on either boundary. The two grids used to investigate the two boundaries separately illustrate some difficulties that occur when using such an angularly dependent transmitting BC. Most geometries of interest here involve a distant source, so the angles of incidence at the

bottom boundary are much smaller than at the rightmost edge boundary. When the angle of incidence is small less than half the incident energy is removed. Thus, although the reflections from the rightmost grid edge are uniformly small and produce on the order of a one percent change in RMS amplitude for a distant source, the reflections from the bottom of the grid are only slightly reduced in amplitude and contribute significant unwanted components to the resulting seismograms. Conversely, a nearby source was chosen for the test of the BC at the rightmost edge of the grid and a source in the grid was chosen for the bottom grid boundary test. In both cases these choices were made to give a large range of incident angles in the calculations.

Next the validity of the BC's for L_g mode sum seismogram input will be discussed. Figure 5 shows the layer over a half-space (L/HS) grid models used to verify the accuracy and efficiency of the BC's as applied to SH L_g wave propagation. All FE calculations discussed for the test use the forward transition forcing functions as input. The results of these calculations are illustrated in Figure 6 and Figure 7. Both figures show seismograms that have been band pass filtered between .01 and 1.0 Hz. The seismograms shown in Figure 6 have also been convolved with the WWSSN short period instrument response. Four separate calculations were performed. First, an L_g mode sum synthetic seismogram for the same source used to generate the forward transition forcing functions was calculated for surface nodes at distances corresponding to R1 and R2 in Figure 5. These are the uppermost traces in each group in Figure 6. Next, seismograms were generated using the hybrid method and the long grid, in Figure 5. No BC's were applied when the seismograms were propagated through the FE portion of the path. The length of the long grid, nx=200, was chosen so that fifty five seconds of seismogram could be recorded at R1 and R2 without contamination from end reflections. Sample results from this calculation are shown as the second seismogram in each group in Figure 6 and the uppermost seismogram in each group in

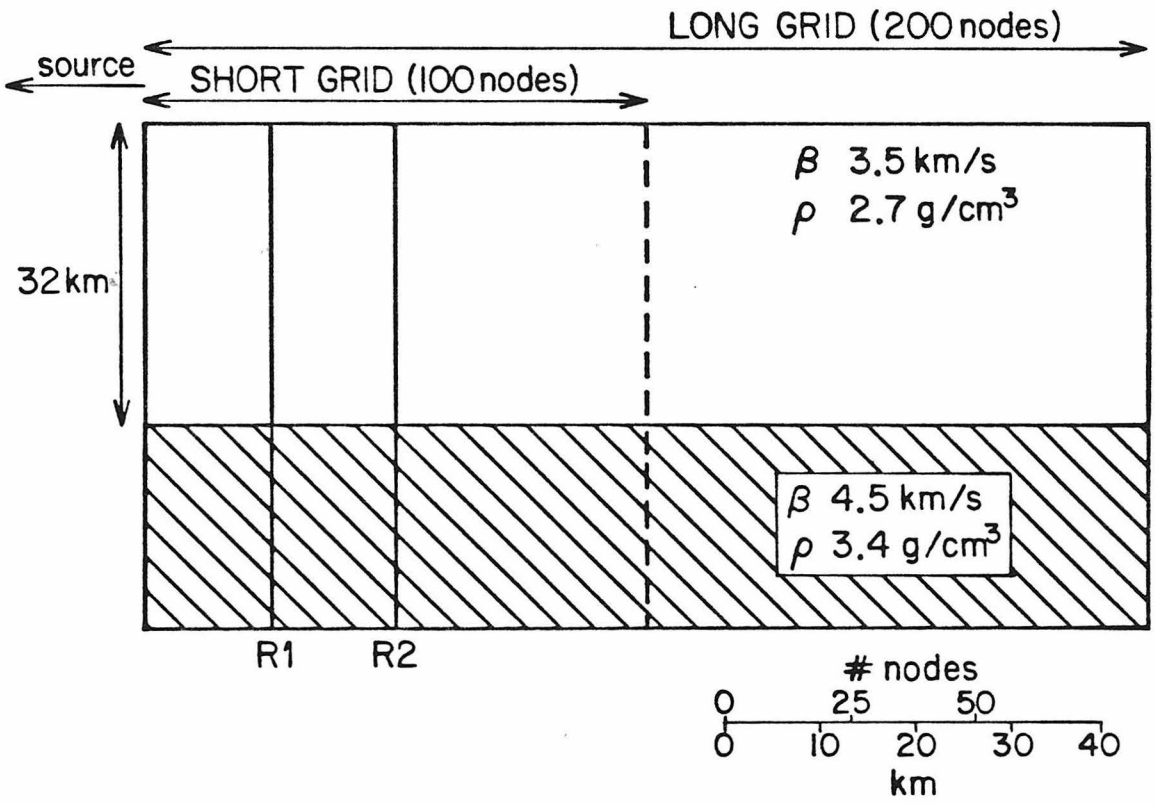

Figure 5: Grid configuration for test of absorbing BC's for the case of incident L_g mode sum waves. The solid vertical lines within the grid shown the locations of the depth sections of receivers where results are recorded. The dotted vertical line indicates the end of the short grid.

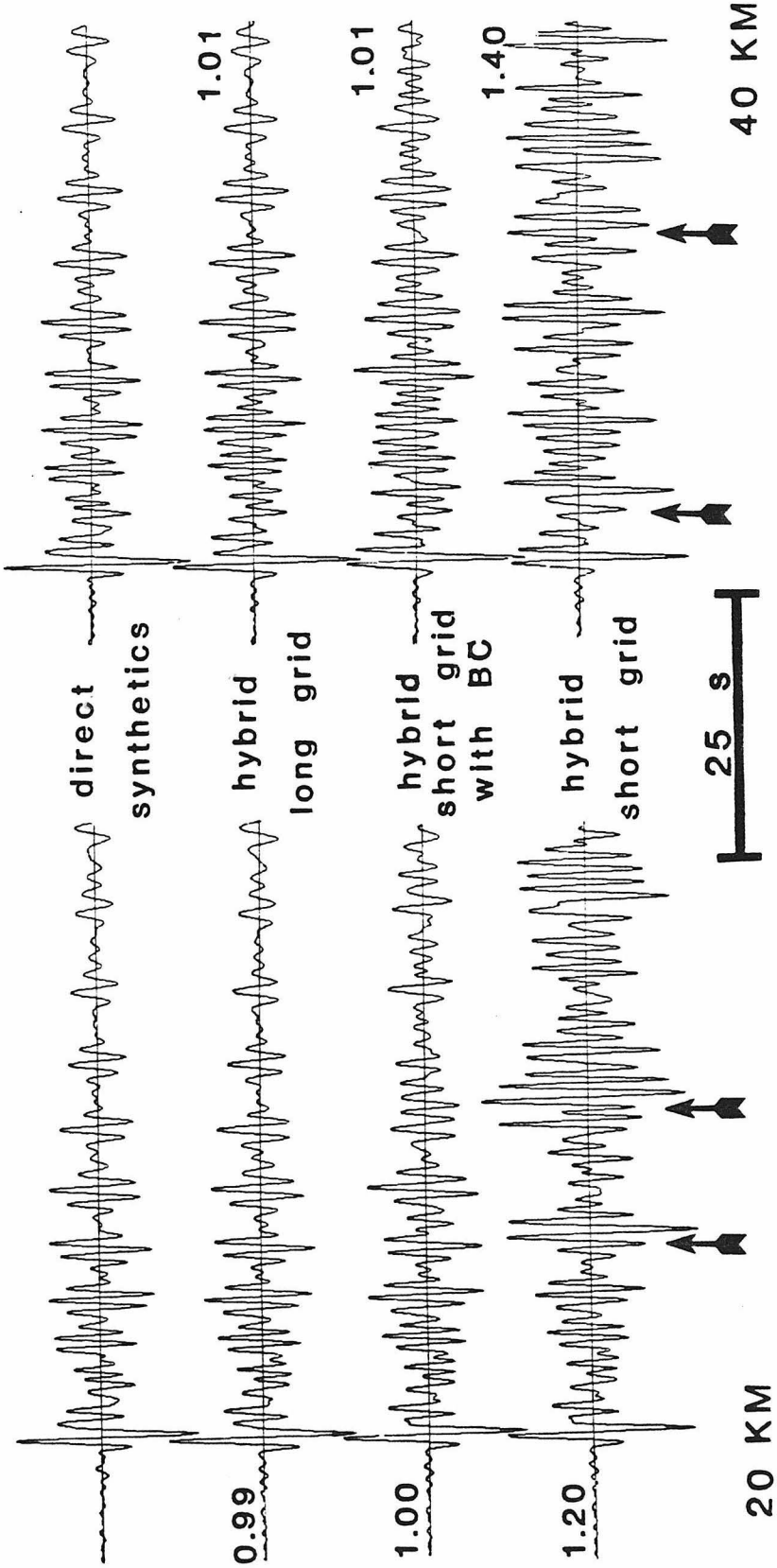

Figure 6: Seismograms recorded at the surface for the distances R1 and R2 in Figure 5. The first seismogram in each group is a direct synthetic, the second is a hybrid synthetic determined using the long grid shown in Figure 5, the third and fourth are hybrid synthetics determined using the short grid in Figure 5 with and without the applied BC respectively. The number beside each of the hybrid synthetics is the RMS amplitude ratio. The amplitude ratio is taken with the direct synthetic as a reference. Seismograms are plotted at the same scale after they have been band pass filtered between .01 and 1 Hz and have been convolved with the short period WWSSN instrument.

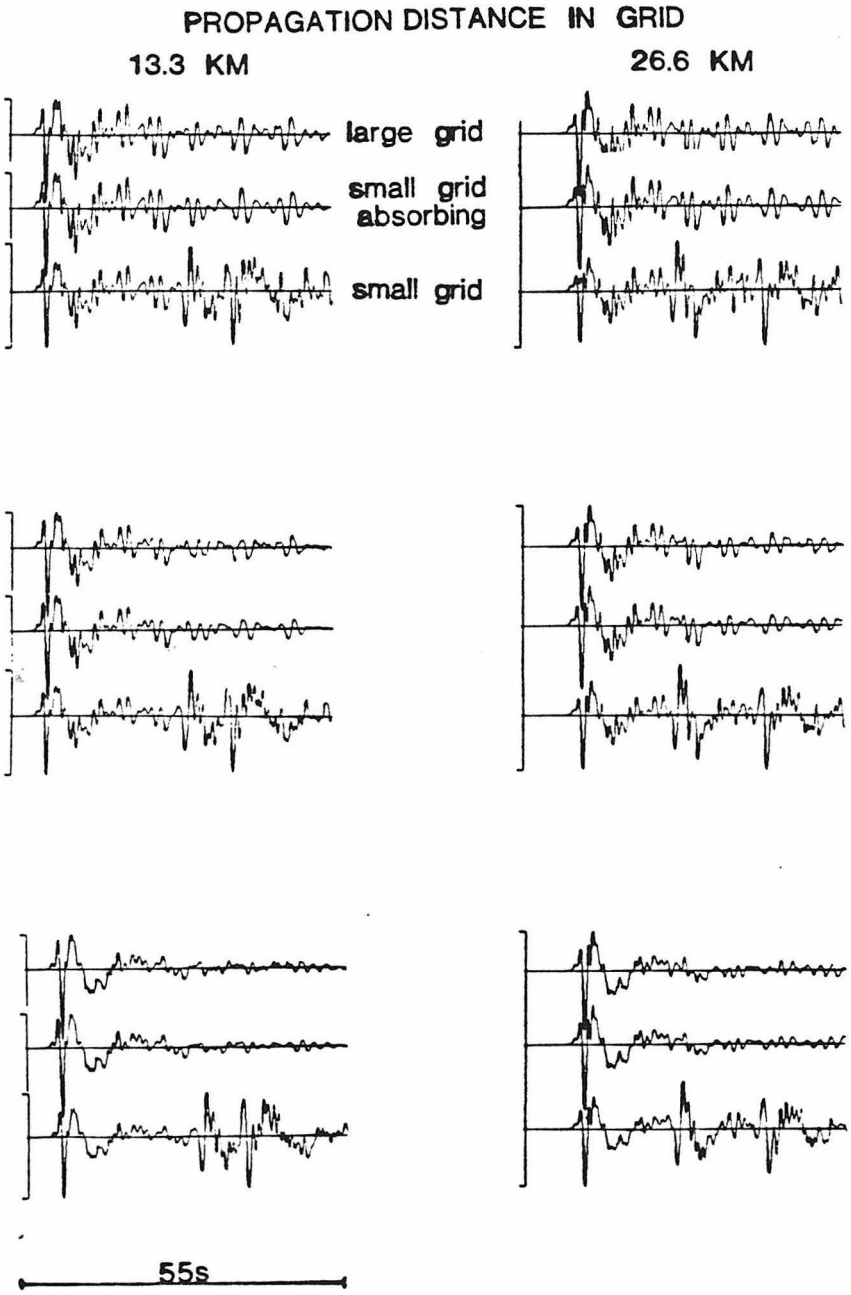

Figure 7: Seismograms recorded at the surface and at depth at the distances R1 and R2 in Figure 5. The first seismogram in each group is a hybrid synthetic determined using the long grid shown in Figure 5. The second and third are hybrid synthetics determined using the short grid with and without BC's respectively. Seismograms are normalized so the peak to peak amplitude of each trace appears identical. RMS amplitudes of each group of traces agree to within 1% before the arrival of the reflection. The seismograms have been band pass filtered between .01 and 1.0 Hz.

Figure 7. Third, seismograms were generated using the hybrid method and the short grid illustrated in Figure 5. The short grid is terminated at its rightmost edge by the vertical dotted line. Along this edge the transparent BC was applied at each node at each time step in the calculation which propagated the input seismograms through the FE portion of the path. Seismograms resulting from this calculation are shown as the third trace in each group in Figure 6 and as the center trace in each group in Figure 7. Finally, the previous FE calculation was repeated without the transparent BC's, and the results are illustrated as the fourth and final trace in each group in Figure 6 and as the bottom trace in each group in Figure 7.

When the final three traces in each group in Figure 6 are compared to each other or the three traces in each group in Figure 7 are compared to each other it becomes clear that the transparent BC's are removing most of the reflected energy. In the last trace the reflection from the grid edge is clearly visible, and the multiple reflection is also clear. Arrival times of the two large peaks marking these reflections are consistent with their identification as reflections. The arrival time of the two reflections are shown on Figure 6 as arrows below the bottom seismogram in each group. Comparison of the long grid and the short grid with transparent BC's shows that most of the reflected amplitude has been removed by the BC's. Comparing the results show in Figures 6 and 7 shows that the BC's are also somewhat frequency dependent for L_g mode sum seismogram type input. Very little difference is seen between the hybrid long grid solutions and the hybrid short grid solutions with the BC's applied when the results in Figure 7 are examined, and the changes that are seen appear to be in the higher frequency component of the traces. This observation is corroborated by the results shown in Figure 6. These results have had the WWSSN short period instrument applied to them, and thus, have had their higher frequency component enhanced and their lower frequency component attenuated. They show larger differences

between the hybrid long grid solutions and the hybrid short grid solutions with the BC's applied than are visible in the results before the instrument is applied. The increased differences are coincident with reflections obvious on the seismogram showing the hybrid short grid results without BC's. The differences are largest for the multiple reflections. Despite easily visible differences in waveform the seismograms shown in Figure 6 have RMS amplitudes that agree to within less than two percent for all RMS window lengths. This indicates that small changes in waveform may be expected but the amplitudes of the seismograms should be stable and not significantly contaminated by reflections from the grid edges. The increased discrepancies in both waveform and amplitude introduced by the multiple reflections will be avoided in the transition FE grids described below. This reduces the discrepancies in RMS amplitude to less than one percent.

Reflections from the bottom edge of the grid should also be considered. As previously discussed, the transparent BC can be very inefficient for the case of an SH pulse incident at the bottom of the grid. Due to the small angle between the SH ray and the grid bottom for any source which is not in the grid or in close proximity to the grid the BC will remove only a small portion of the reflected amplitude. Fortunately, this behavior does not generalize to modal displacement in a layered half-space. For the case of L_g mode sums propagating in a layer over a half-space, the L_g wave input to the grid is constructed as a superposition of Love wave modes. These Love wave modes can be thought of as the superposition of the constructive interference between multiply reflected post-critical SH waves in the crust. This suggests that much of the energy in the SH type L_g waves for a layer over a half-space should be contained in the layer, interacting predominantly with the real boundary between the layer and the half-space, and with the free surface. The waveforms of the hybrid seismograms with and without the transparent BC's on the grid bottom are almost identical. Amplitude

comparisons show differences of less the 0.1%. This can be seen by examining the first two seismograms in each group in Figure 6. The analytic synthetics and the hybrid results with no BC's are in excellent agreement indicating that reflections from the bottom boundary in the FE portion of the hybrid calculation are not significant. Thus, it appears that, for a layer over a half-space, reflections from the grid bottom are not important when modal displacements are being propagated. This argument applies to the forward and reverse reference models when mode sum SH L_g seismograms generated for the forward or reverse reference modes respectively are used. This argument cannot, however, be generalized to imply that little energy reaches the bottom boundary for the transition model calculations, or for the reverse reference model using the depth section recorded at x_f in the fifty kilometer forward transition model as forcing functions. It will be shown that in these models significant energy escapes from the crustal layer into the mantle half-space.

The properties discussed above are also observed in the time slices from the layer over a half-space calculation shown in Figure 8. At the upper right corner of each time slice a number indicating the time, in seconds, since the beginning of the FE calculation is shown. The arrows pointing to the surfaces of the bottom three time slices show the location that the slowest traveling energy seen at the leftmost edge of the wavefield of the previous time slice has moved to in the time elapsed between the two sections. The first striking feature of the time slices are that the SH type L_g waves are, in the most part, confined within the layer. The bottom of the layer in the illustrated depth sections is easily visible as the bottom of the high amplitude portion of the wavefield. This delineation is clear even though forcing functions are applied to all illustrated rows of nodes. Thus, the time slices show that a negligible portion of the energy interacts with the bottom of the grid. Thus, introducing transparent BC's on the bottom of the grid where little energy reaches makes no perceptible difference in

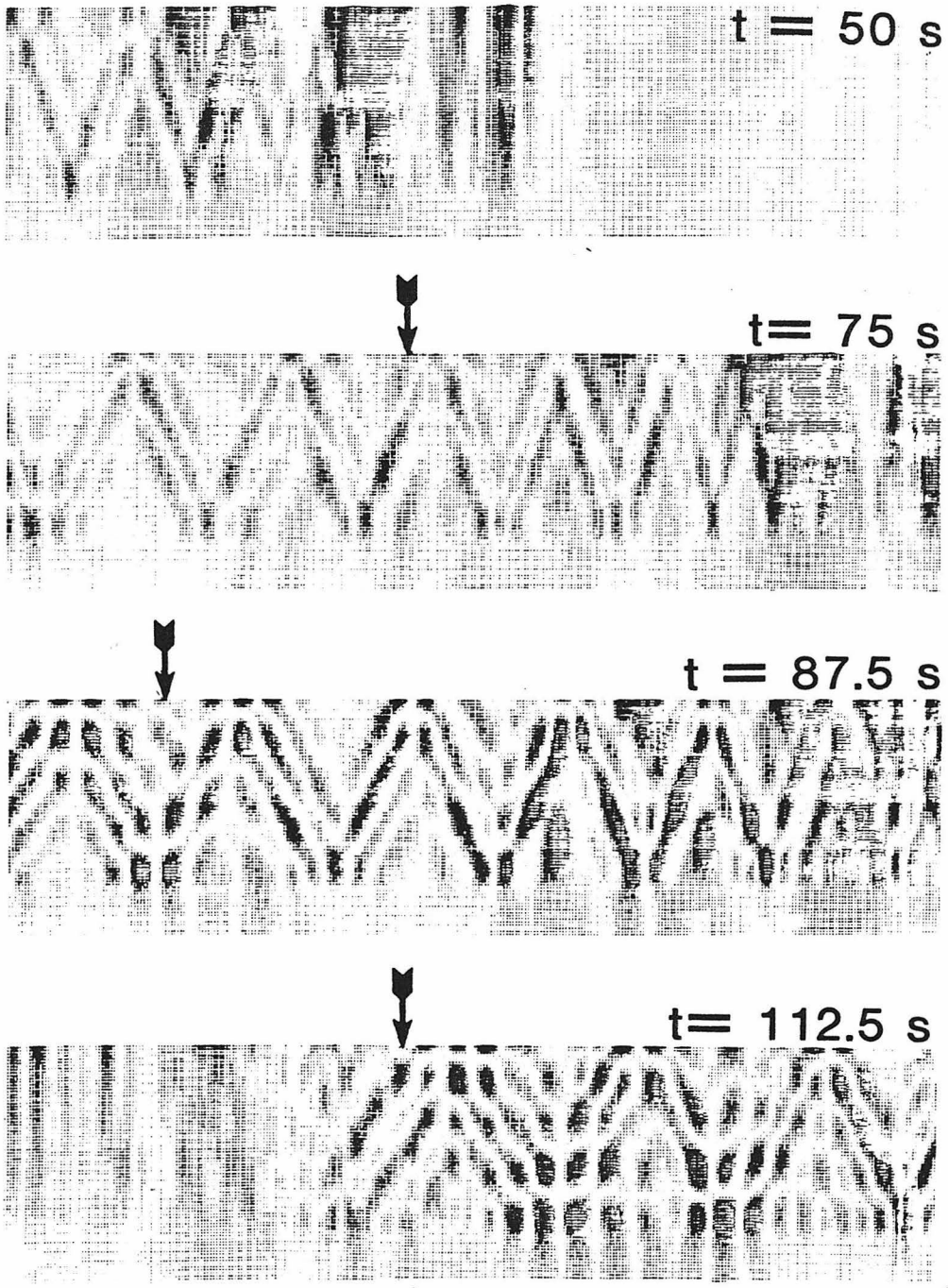

Figure 8: Time slices showing the propagation of an SH type L_g wavefield through a layer over a half-space structure. The bottom of the layer can be seen as the lower termination of the darker regions. The dark triangular regions show the wavefronts. The arrows above the lower three time slices show the location of the slowest traveling energy visible at the lefthand edge of the previous time-slice at the time of the present time slice. The time since the initiation of the FE calculation is show at the upper right corner of each time slice.

the results. The second striking feature is that the high amplitude portions of the wavefield resemble the wavefronts for multiply reflected SH waves of a collection of different phase velocities superimposed upon one another.

Another feature clearly visible in these time slices is the energy reflected back toward the source from the rightmost edge of the grid. The upper two time slices both show the maximum amplitude portion of the waveform propagating through the grid. In the first time slice the large peaks at the beginning of the waveform, seen as the darkest regions, have propagated about halfway across the grid. In the second time slice they have reached the right end of the grid. In the third time slice these high amplitude regions have propagated beyond the rightmost edge of the grid. Thus, the maximum amplitude in the third time slice is smaller than that in the first two time slices. The same regions of wavefield in the third time slice appear darker than in the second time slice. The reflection from the grid edge is also visible if the time slice is carefully examined. In the fourth time slice, the maximum amplitude has again been reduced and the end of the applied wavefield is accentuated. The amplification also makes the reflected wavefield clearly visible particularly in the portion of the grid which the incident wavefield has completely passed through. The end of the incident wavefield is clearly visible in this time slice as the end of the portion of the wavefield showing superimposed triangular regions of high amplitude. To the left of this area an attenuated mirror image of the beginning of the incident wavefield can be seen. This is the beginning of the reflected wavefield. Examining seismograms shows that actual amplitudes of this reflection are between five and eight percent of the incident amplitudes.

This discussion has established that the transmitting BC at the grid bottom boundary is not important for SH type L_g mode sum seismograms traveling through the same layered structure in which the source is located. However, the purpose of

this study is to examine the effects of continental oceanic boundaries on the transmission of L_g mode sum seismograms. When the crustal layer is thinned or thickened with distance, the modes are no longer completely trapped within the layer. Energy can be converted to modes compatible with the local layer thickness and to other forms including forms such as body waves that can propagate into the half-space and away from the layer. When the wavefield reaches the second layered structure, modes incompatible with that new layer thickness will leak out of the layer, rapidly at first, then at a steadily decreasing rate. These phenomena are observed and will be discussed and explained in detail later as the results are presented. They imply that reflections of energy escaping from the crustal layer towards the bottom boundary of the grid could possible seriously contaminate transition calculation results. The grids are designed to minimize these problems. Consider a node on one of the dotted boundaries shown in Figure 1. At this node energy is converted into modes consistent with the local layer thickness and into forms that will propagate into the half-space. Thus, it can be considered as a source for a wavefield propagating into the half-space. Wide angle reflections, of the energy escaping from the thinning crustal layer, from the grid bottom require long distances, Δ, to travel from this source to the grid bottom to the receiver. In almost all cases the model grids do not extend far enough, in the x direction, beyond the transition for this to be a problem. The energy will encounter the rightmost end of the grid, either on the downgoing or the upgoing portion of its path, rather than reaching a receiver at or near the surface as a wide angle reflection. Since a wavefront which has a small angle of incidence with the bottom boundary has a large angle of incidence with respect to the end boundary, most of the amplitude of the wavefront from the conversion source incident on the rightmost end boundary, will be transmitted rather than reflected. Therefore, it is removed from the grid. Careful grid design will prevent significant contamination from wide angle bottom reflections.

The results from the forward and reverse transition calculations will now be discussed. First the effects of a forward transition on the incoming SH L_g mode sum seismograms will be explained. Then, the further effects due to continued propagation of this energy through a reverse transition will be considered. Next, the variation in the effects introduced by the forward transition as a function of transition length will be discussed. Finally, the variations in the effects observed as the wavefront passes through the reverse transition, as a function of the length of that transition will be explained. The consideration of the effects due to varying the length of the oceanic path between the two transition regions will be discussed briefly. A more complete discussion of this problem will be given in the next chapter.

Changes to L_g Wavetrains on Passage through a Forward Transition Region

The passage of a wavefield consisting of SH type L_g mode sum energy contained mainly in the layer above the half-space through a forward transition such as that illustrated in Figure 1a) has several effects on that wavefield. These effects are illustrated in Figures 9 to 15. These figures show several important tendencies. As expected the behavior along the continent ocean boundary shows distinct differences when compared to the behavior at the crust mantle boundary. Along the continent ocean boundary amplitudes are seen to increase with distance, Δ. No energy is propagated into the ocean layer. Energy which is not reflected back from the crust ocean boundary toward the source appears to be concentrated near this boundary and propagated along it to produce an amplification of amplitude which is maximum at the surface of the crust. Along the crust mantle boundary a similar but smaller concentration effect is seen. However, this effect is dominated by the conversion and/or escape of energy across the boundary into the mantle layer. The propagation of the energy remaining in the crustal layer when the wavefront leaves the transition region

through the oceanic layered model shows that energy is leaking out of the bottom of the oceanic crustal layer, particularly at the beginning of the oceanic layer near the end of the transition region. Each of these observations will be discussed in detail below and supporting results will be shown in the figures.

First the results of a sample calculation with a transition length of twenty kilometers will be discussed. The geometry of the grid is illustrated, to scale, in Figure 9. The upper hatched region is the ocean layer, the unhatched region the crustal layer, and the lower hatched region is the mantle layer. The heavy vertical line at the left-most edge of the grid represents the column of nodes constrained to move with the input L_g displacement histories. The heavy vertical line labeled A is the column of nodes for which displacement time histories are recorded to use as input to the reverse transition. The two vertical lines labeled Fc1 and Fc2 show receiver sections used to illustrate the effect of the transition on the distribution of amplitude with depth. Dots on Fc1, and Fc2 indicate positions of receivers for which displacement time histories are illustrated in Figure 10. Open circles, and dots located at the surface of the crustal layer, refer to nodes for which displacement histories are plotted in Figure 11. In both Figures 10 and 12 all seismograms are band pass filtered between .01 and 1.0 Hz, but no instrument is applied. The numbers above and to the right of each seismogram are the maximum peak to peak amplitudes of each seismogram.

Figure 10 shows seismograms recorded at the positions shown as dots in Figure 11. The first column of seismograms in this figure shows the changes seen with depth at distance Fc1. The second column shows the seismograms on depth section Fc2. The seismogram at the surface of the oceanic crustal layer in the depth section at Fc2 shows a substantial increase in amplitude over the seismogram at the same depth in depth section Fc1. These seismograms are shown as the second row in this figure. Not only is the peak to peak amplitude fifty percent larger but the average amplitude

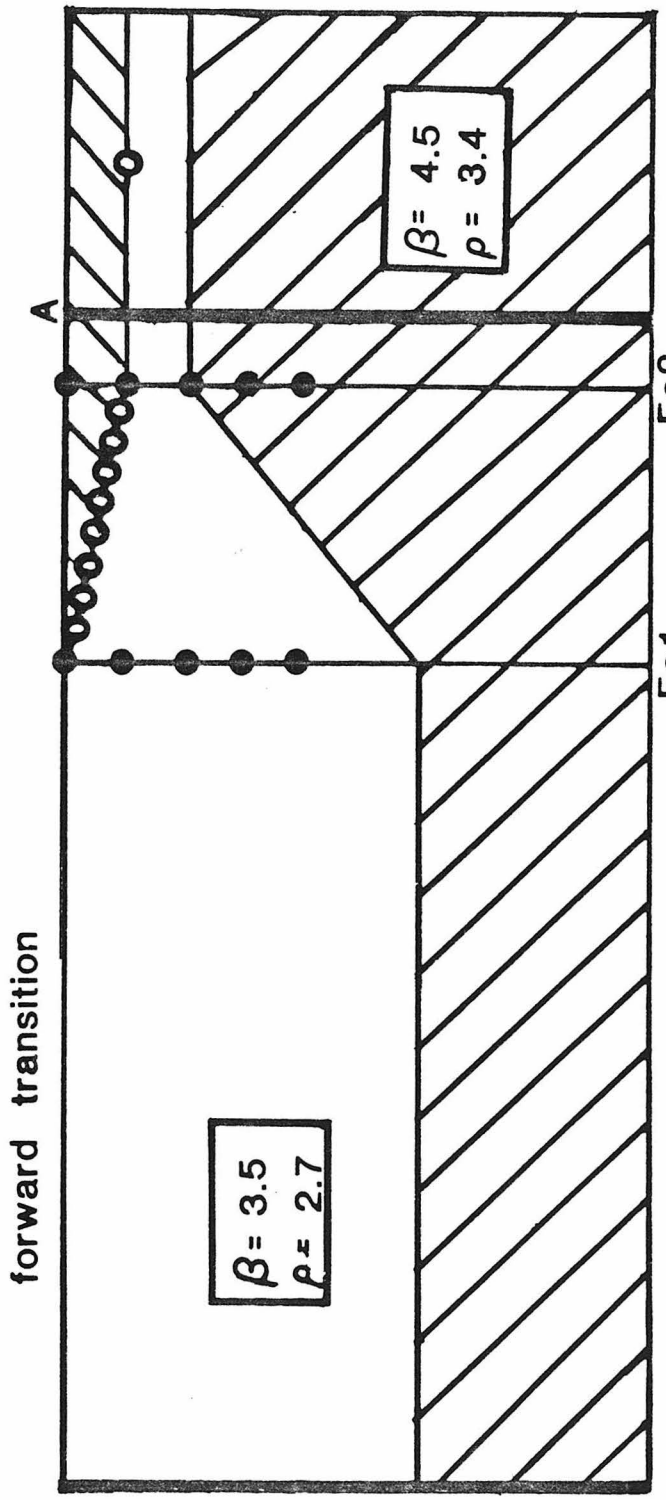

Figure 9: Grid geometry for the twenty kilometer forward transition used to illustrate the effects of a forward transition on the waveforms and amplitudes of seismograms as a function of distance, Δ, and depth. The upper hatched region is the oceanic layer, the lower hatched region the mantle layer, and the unhatched region the crustal layer. The heavy vertical line labeled A shows where seismograms are recorded for use as forcing functions in the reverse transition calculation. The heavy line at the left end of the grid is the column of receivers to which SH L_g seismograms are applied as forcing functions. The vertical lines labeled Fc1 and Fc2 show depth sections of receivers. The dots on Fc1 and Fc2 show receivers for which seismograms are illustrated in Figure 10. The open circles along the surface of the crustal layer show the receivers for which seismograms are shown in Figure 11.

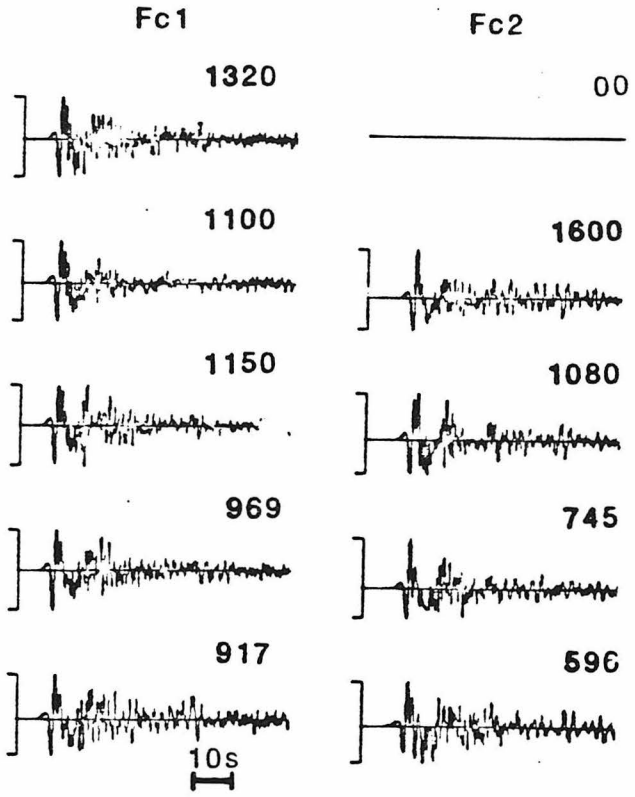

Figure 10: Seismograms recorded at receivers shown as dots on depth sections Fc1 and Fc2 in Figure 9. The first column shows the seismograms recorded at Fc1, the second the seismograms recorded at Fc2. The numbers above the right end of each seismogram show the peak to peak amplitude. The first row of seismograms show receivers at the depth of the surface of the continental crust. Successive rows show pairs of receivers at increasing depths. The second row is at the depth of the surface of the oceanic crust, the third at the depth of the base of the oceanic crust. All receivers illustrated are above the base of the continental crust.

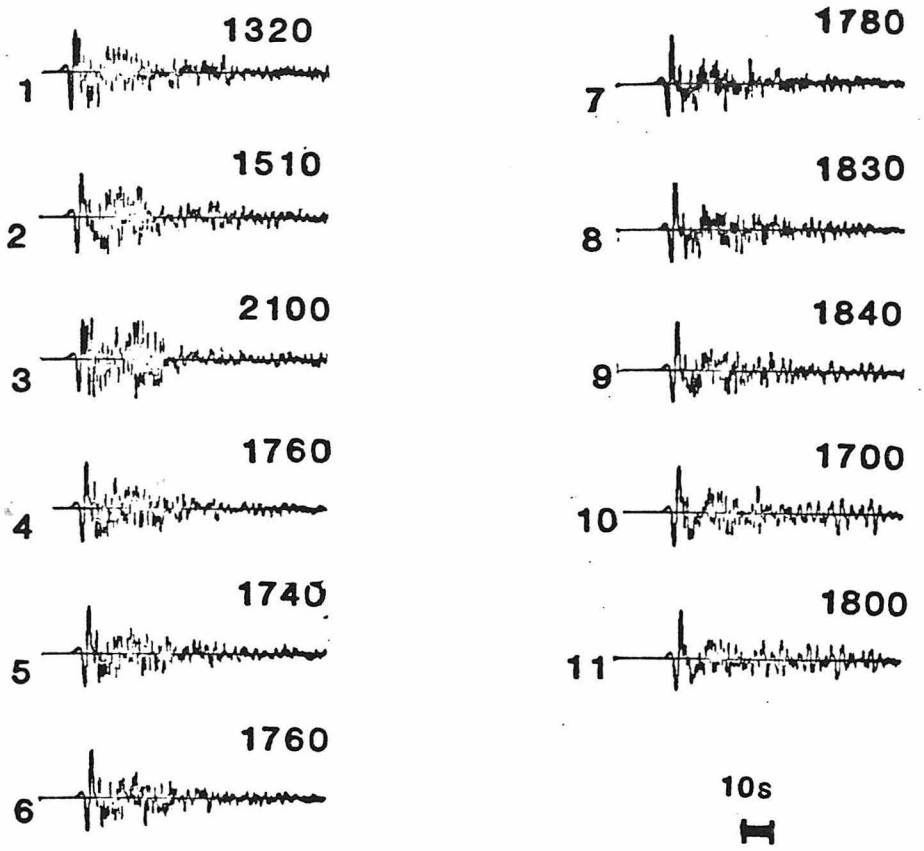

Figure 11: Seismograms recorded at receivers along the surface of the crustal layer in a forward transition calculation. These seismograms are recorded at the receivers shown as open circles and dots on the surface of the crustal layer in Figure 10. The numbers to the left of each seismogram indicate the location of the node at which that seismogram is recorded. The leftmost open circle is receiver 1. The numbers increase as one moves to the left along the surface of the crustal layer. The numbers above the right end of each seismogram give the peak to peak amplitude of that seismogram.

of the coda has increased by a factor of approximately two with respect to the maximum peak to peak amplitude. Thus, the increase in RMS amplitude is considerably larger. The nodes at the depth of the bottom of the oceanic crustal layer, the third row of seismograms in this figure, show a small decrease in peak to peak amplitude and a relatively constant RMS amplitude across the transition. Examination of the nodes on Fc1 and Fc2 with depths between these pairs shows that the increase in amplitude is largest at the surface of the crust and decreases rapidly toward the base of the crust. The amplitudes of the seismograms transmitted across the crust mantle boundary, rows four and five in this figure, are decreased by passage through the transition region. The transmitted waveforms are similar to the incident waveforms and show an increasing reduction in transmitted peak to peak amplitude as depth increases. Amplitude is seen at depths below the depth of the bottom of the continental crustal layer. These results support the statements that energy is concentrated at and then travels along the crust ocean boundary, and that energy escapes from the crustal waveguide when the wavefield crosses the transition. They also indicate that some of the energy escaping from the transition region into the half-space is traveling down towards the bottom boundary of the grid. This figure helps quantify the magnitudes of these effects. The actual distortions of the wavefield will be clearer when the time slices, Figures 12 to 14, are discussed.

Figure 11 shows seismograms recorded at the receivers along the surface of the crust. These receivers are shown in Figure 9 as open circles and as the dots on crustal surface on depth sections Fc1 and Fc2. The numbers to the left of each seismogram show the sequence, in space, at which the seismograms were recorded. Seismogram one was recorded at the leftmost surface receiver shown in Figure 9. The number used as the label increases as one moves towards the right across Figure 9. A clear increase in peak to peak amplitude is seen as one moves down the crust ocean boundary

towards the oceanic portion of the model. This increase is not necessarily monotonic, as will be shown later when the properties of the transition response to an incident wavefield as a function of transition length are discussed. Not only is the amplitude increasing but the length of the coda with amplitudes above one third of the maximum peak to peak amplitude is also increasing. These seismograms are some of the strongest evidence for the concentration of amplitude at the surface of the crust as the wavefield passes through the transition. They also illustrate how the nature of the waveforms change as the wavefield passes through the transition.

A series of time slices is shown in Figures 12 through 14. These time slices were recorded during the FE calculation for the twenty five kilometer long forward transition discussed earlier. The time slices are recorded at intervals of twenty five seconds beginning twenty five seconds after the initiation of the FE calculation. The time elapsed since the start of the FE calculation is shown for each time slice above and at the right end of that time slice. The dimensions of the illustrated grid are 365x90 nodes. The heavy lines outlining the grid show the bounds of the crustal layer, the bottom edge, and both end edges of the grid. The water layer is not outlined as no displacements take place within it. For this calculation sixty forcing functions were used. Thus all displacement input to the grid through the leftmost grid edge is within the crustal layer. The cutoff for minimum amplitude to be plotted on each time slice is two percent of the maximum amplitude within that time slice. The arrow above each time slice except the first shows the location to which the component of the wavefield with velocity 2.8 km/s, seen at the leftmost edge of the grid in the previous time slice, has moved in the time elapsed since the previous time slice.

Figure 12 shows the first two time slices, which illustrate the wavefield approaching the transition region within the grid through the plane layered continental structure. In the first time slice the displacements which are seen entering the grid are

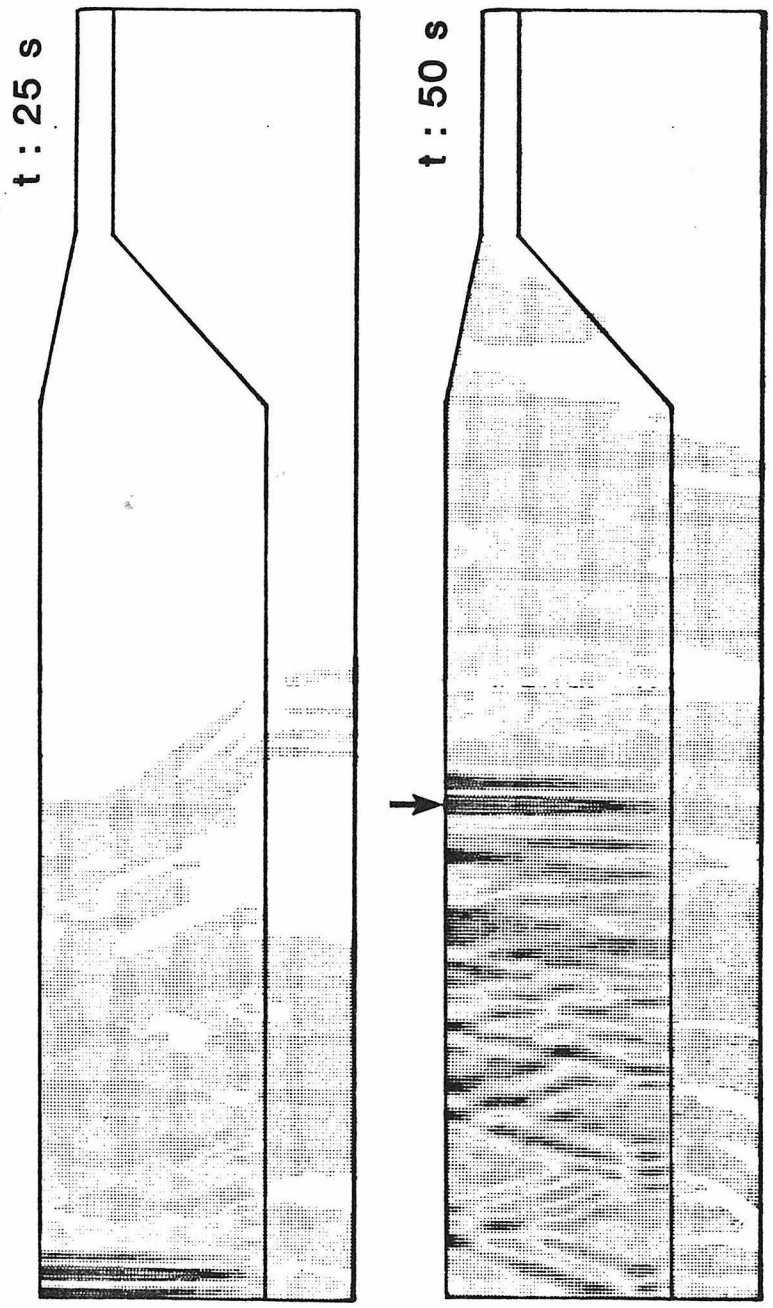

Figure 12: Time slices recorded during the 25 km forward transition calculation. The crustal layer and the ends and bottom of the FE grid which contain it are outlined. Within these outlines the displacements at each grid point at the indicated instant of time are plotted at the location of that point. A larger displacement produces a larger point. Thus, high displacement areas appear darker. The maximum amplitude in each time slice produces a point of maximum size. An amplitude of less than 2% of this maximum produces no point. The time since the initiation of the FE calculation is shown above the right end of each grid. The arrow above a time slice shows the location to which the disturbances moving at 2.8 km/s, seen at the left end of the previous time slice, have moved in the intervening duration.

equivalent to the largest peak to peak amplitudes in the seismograms. The dark, almost vertical lines show the same displacements seen in the seismograms as the highest amplitude initial peaks. The light grey areas seen to the right of the dark vertical linear areas are very low amplitude disturbances that precede the large arrivals in the seismograms. The second time slice shows the same high frequency arrivals after they have propagated about halfway through the plane layered portion of the transition grid. In this time slice more of the wavefield can be seen. As more of the wavefield enters the grid triangular regions of maximum amplitude become visible.

Figure 13 shows the next two time slices in the sequence which illustrate the passage of the highest amplitude portions of the wavefield through the transition region. In the third time slice, the first shown in this figure, the dark linear vertical region at the beginning of the wavefield has passed about halfway through the transition region. Comparing the portion of the wavefield visible within the grid in the second time slice with the same portion in the third time slice shows that the normalized amplitudes of all the displacements have been reduced in the third time slice with respect to the first two. This is evidence that the maximum amplitudes seen within the transition region are considerably larger than the displacements in the unperturbed layer over a half-space wavefield. As the high amplitude disturbance passes through the transition the maximum amplitude along the crust ocean boundary is most strongly amplified, and the dependence of amplitude on depth becomes more pronounced, since the amplitude near the depth of the base of the continental crustal layer is reduced. The sections of the wavefield present in both the third and fourth time slices are much more prominent in the fourth time slice. This is because the highest amplitude region of the wavefield, seen within the transition in the third time slice, has propagated past the rightmost edge of the grid. Thus, the maximum amplitude in the fourth time slice is much smaller than in the third. Figure 14 shows an additional time slice. Again the

amplitude has been reduced with respect to the previous time slice and the portion of the wavefield visible in both slices is amplified in the fifth time slice. The wavefield continues to show triangular regions of maximum amplitude. The extent of each triangular region, in the x direction, increases for regions of the wavefield incident on the left end of the grid at a later time.

The triangular pattern of maximum amplitudes in the wavefields can easily be explained. Let the SH L_g energy in the crustal layer be interpreted in terms of being the superposition of the constructive interference of post-critically reflected multiple SH wave reflections. The critical angle, the minimum angle between the ray and the normal to the boundary for which total internal reflection occurs, is about fifty one degrees. Since the wavefront can be considered to be perpendicular to the ray, the wavefronts that are visible as the triangular regions of maximum amplitudes can be expected to show angles of incidence with the boundary of between 0° and 39°. In the first two time slices the angles of incidence range between 0° and 25°. In the third time slice the angles of incidence of the wavefronts at the layer boundary reach 35°, in the fourth time slice they reach 38°. The superimposed triangular regions of maximum amplitude are seen to increase in average width as the left edge of the grid is approached in any given time slice, that is, as portions of the wavefield incident on the left grid edge at later times are considered. This increase in width of the triangular maxima corresponds to an increase in phase velocity which can be translated to a increase in period and/or a larger contribution from higher modes. Thus, the higher frequency content at the beginning of the seismogram is also clearly visible in the time slices. The later parts of the seismogram are predominantly of longer periods and contain more higher mode energy.

It can be seen that some energy is leaking into the half-space even in the plane layered region, this leakage is small and cannot be seen in the seismograms in this

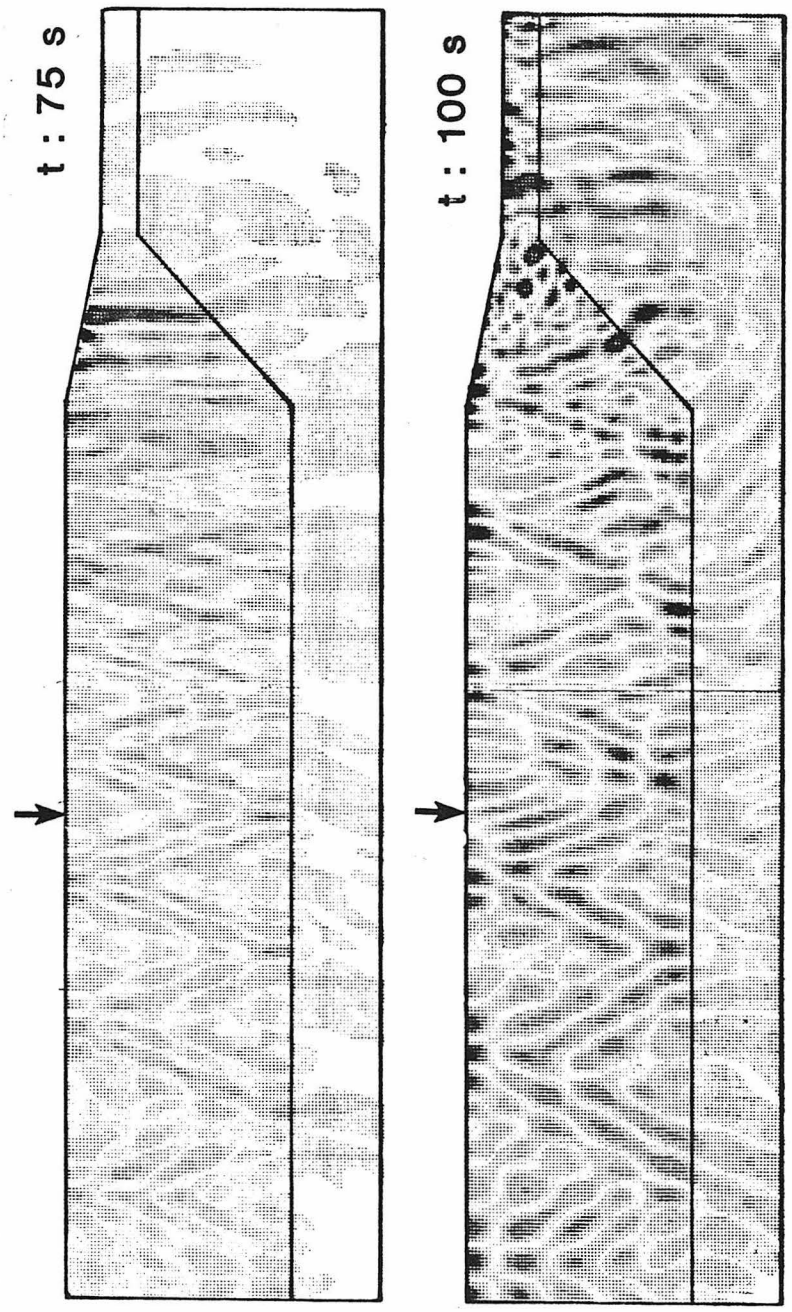

Figure 13: Time slices recorded during the 25 km forward transition calculation. Details of the form of these time slices are the same as for Figure 12. The time slices in this figure are recorded after the completion of additional time steps in the same FE calculation that produced the time slices in Figure 12.

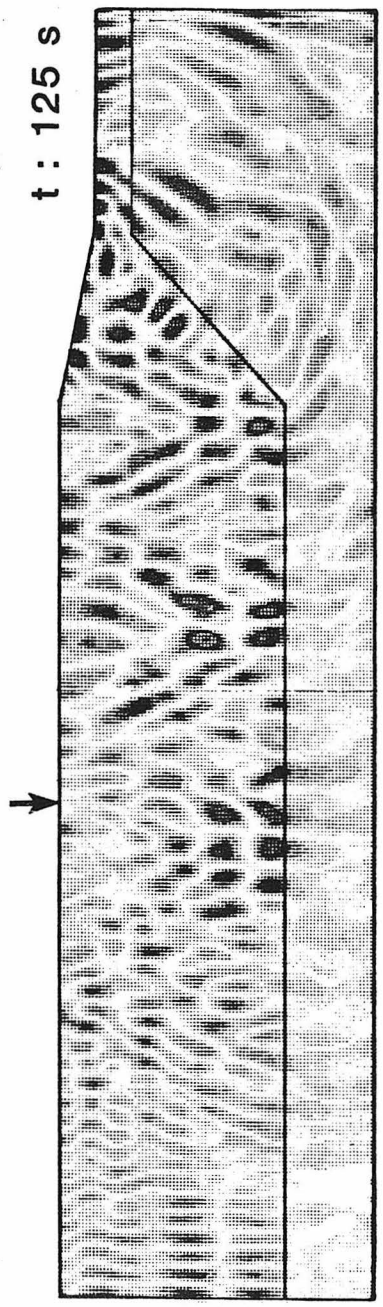

Figure 14: Time slice recorded during the 25 km forward transition calculation. Details of the form of these time slices are the same as for Figure 12. The time slices in this figure are recorded after the completion of additional time steps in the same FE calculation that produced the time slices in Figure 12 and 14.

example. However, in the layer over a half-space reference model the time slices show this leakage is largest closely following the maximum amplitude regions, seen as the dark vertical lines in the first two time slices. The extent of the low amplitude disturbance produced by this leakage increases with distance propagated through the grid. The region of the seismogram corresponding to this region of the wavefield where leakage is maximum is the region in which small discrepancies are seen between synthetics and FE results for large propagation distances in the grid. The observation of amplitude passing into the half-space helps explain why some small waveform changes can be seen.

When regions of the wavefield with large amplitudes pass through the transition region, amplitude can be seen crossing the crust mantle boundary particularly adjacent to the high amplitude regions within the crustal layer of the transition region. The energy crossing the boundary produces regions of significant amplitudes that are visible in the oceanic half-space both in the transition region and in the region of oceanic structure. In the region of this oceanic half-space corresponding in depth to the continental crust two main effects on the propagating amplitudes can be seen. First, as x increases, the highest amplitude regions in the half-space which form at the intersections of the wavefronts with the crust mantle boundary in the transition region, are propagating at some angle away from the crustal layer toward the bottom boundary of the grid. The component of the motion towards the bottom boundary increases as the width of the triangular regions of maxima in the incident wavefield increases. Thus, as the angle between the wavefront and the crust mantle boundary in the continental crustal layer decreases the maximum amplitude regions crossing the crust mantle boundary in the transition region propagate to the grid bottom while traveling a shorter horizontal distance. The high amplitude regions in the half-space of the oceanic structure propagate towards the bottom boundary of the grid more rapidly for

the energy later in the incident wavefield. Second, energy is escaping from the high amplitude regions in the crustal layer as they propagate through the oceanic crustal layer. This energy forms a forward bending arc in the mantle half-space, due to the higher velocity in that half-space, that connects to the energy which escaped from the same portion of the wavefield when the wavefield passed through the transition to the bottom of the half-space. As the high amplitude regions of the wavefieldpropagate more directly towards the grid bottom the tails forming due to leakage from the oceanic crustal layer become fainter and detach from the high amplitude downward traveling portions of the wavefield.

To explain the observations made of the time slices the ray diagrams shown in Figure 15 are useful. This figure shows two transition structure outlines identical to those used to accentuate the structure on the time slices. The lines within these outlines show three multiply reflected rays, for angles of incidence, i, at the crust mantle interface of the continental structure of 55°, 65°, and 75° respectively, and the effect of the forward transition region on each. The angles chosen give a good sampling of the possible post-critical range of incident angles ($>51^{o}$). The arrows on the rays show the directions of propagation. The triangular regions of high amplitude in the time slices show the wavefronts which are perpendicular to the rays shown in Figure 15.

The upper transition shows the ray paths when the rays encounter the crust mantle boundary of the transition before the crust water boundary. When these rays pass into the transition region their incident angles, i, at the crust mantle interface in the continental structure are reduced by the angle, ϕ_{CM}, to give their incident angles, $j=i-\phi_{CM}$, at the crust mantle boundary. This angle of incidence, j, allows transmission into the mantle layer when $j<51°$. The angle between the transmitted ray and the normal to the crust mantle boundary, shown in the figure as a dashed line, is j'.

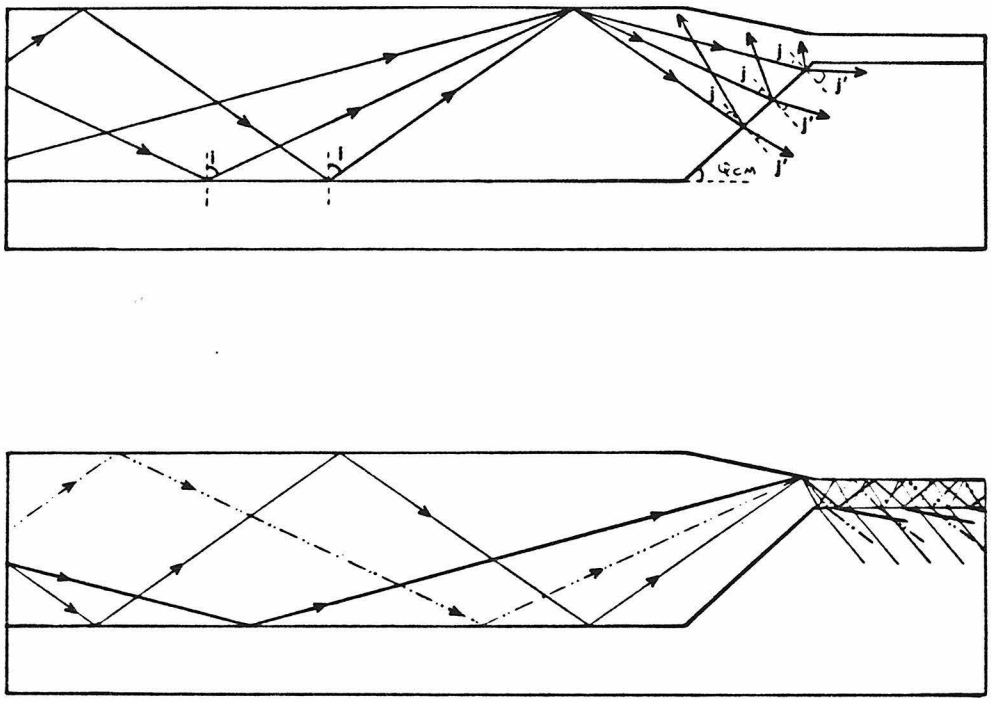

Figure 15: Illustration of ray paths within a forward transition structure. Each diagram shows rays with angles of incidence, i, 55°, 65°, and 75°, at the free surface and crust mantle interface in the continental portion of the model. The transition structure within which the rays are traveling is a 25 km forward transition drawn to scale. The upper diagram shows propagation paths for rays that encounter the crust mantle boundary before the crust water boundary. The lower diagram shows propagation paths for rays that encounter the crust ocean boundary only as they pass through the transition region. The arrows indicate the direction of propagation of the wavefront along the ray.

The angle, $j' = \sin^{-1}\left(\sin j \frac{V_M}{V_C}\right)$, increases as the angle, j, increases and the portion of the incident amplitude transmitted across the crust mantle boundary decreases. Thus, as the angle i increases the fraction of the incident amplitude transmitted into the half-space decreases and the resulting regions of high amplitude in the half-space travel across the crust mantle boundary more horizontally. It follows that as the angle of incidence of the wavefront at the crust mantle interface of the continental structure increases the wavefield propagates more directly towards the base of the grid as it crosses the crust mantle boundary. This explains the increase in z component of propagation in the half-space as the calculation proceeds and the incident energy is of higher phase velocity and period. The rays reflected from the crust mantle boundary are reflected back toward the source for angles of incidence at the crust mantle boundary less than twice ϕ_{CM}. For reflections points immediately preceding the beginning of the transition region rays can propagate through the transition region without interacting with either boundary within the transition and then propagate with unchanged angles of incidence through the oceanic crustal layer.

The lower transition shows the ray paths when the rays encounter the crust ocean boundary before they encounter the crust mantle boundary. For reflection points close to the end of the transition reflected rays are transmitted directly into the oceanic crustal layer. The same angles of incidence at the crust mantle interface in the continental structure are used as in the previous example. These angles of incidence in the continental crustal layer yield angles of incidence $j = i - \phi_{CO}$ in the oceanic crustal layer. The illustrated paths show one way modes which are not of appropriate frequencies to be trapped within the oceanic crustal layer enter that layer. They produce multiply reflected rays at pre-critical angles within the oceanic crust and demonstrate why amplitude is seen crossing the crust mantle boundary in the oceanic structure following the transition. They also explain why this leakage is

maximum near the transition and decreases as the distance from the transition increases. If, at each successive reflection at the crust mantle interface the transmission coefficient is T, then the amount of transmitted amplitude for the n^{the} bounce is $(1-T)^{n-1}TA$, where A is the original amplitude, and T is less than one. Clearly, the amount of escaping energy decreases with distance. Rays that pass through the transition without encountering any boundary can be directly converted to oceanic modes and continue to bounce with the same post-critical angles of incidence at the crust mantle interface and the free surface as they did in the continental structure. Rays that reflect from the crust ocean boundary then from the crust mantle boundary have angles of incidence of $i-\phi_{CM}-2\phi_{CO}$ at the crust mantle boundary. If this angle is less than twice ϕ_{CM} then the ray is reflected back towards the source. If the angle is larger than this value then pre-critically reflected rays in the oceanic crustal layer, with angles of incidence $i-2\phi_{CM}-3\phi_{CO}$ are produced.

Changes to L_g Wavetrains on Passage through a Reverse Transition Region

The passage of a wavefield consisting of SH type L_g mode sum energy for a continental layer over a half-space model, which has passed through a forward transition of fifty kilometers length, through a reverse transition such as that illustrated in Figure 1b) has several effects on the wavefield. These effects are illustrated in Figures 16 through 21. The figures show several important properties. Again, behavior along the ocean continent boundary shows distinct differences when compared to the behavior along the mantle crust boundary. Along the surface of the oceanic crustal layer amplitudes decrease with distance, Δ. Along the surface of the crustal layer in the transition region amplitudes are seen to decrease with distance, Δ, even more rapidly than along the oceanic crustal surface. No energy is propagated from the ocean layer into the continental crustal layer. Energy incident from the oceanic crustal layer travels

up the surface the ocean crust transition while the distribution with depth of amplitude changes considerably. The concentrations of amplitude within the oceanic crust distribute themselves throughout the entire continental crustal layer. Amplitude seems to travel up the ocean crust boundary more readily than it spreads into the lower section of the continental crust. Amplitude incident on the mantle crust boundary appears to be primarily transmitted into the continental crustal layer. As the wavefield exiting the transition propagates through the continental structure the distribution of amplitude with depth continues to readjust thus reducing the surface amplitudes. Each of these observations will be discussed in detail below and supporting results will be shown in the figures.

First, the results of a sample calculation with a transition length of twenty five kilometers will be discussed. The geometry of the grid containing this transition region is illustrated, to scale, in Figure 16. The heavy line labeled A at the left end of the grid represents the column of nodes constrained to move according to the time histories recorded twenty five kilometers beyond the right end of the forward transition region shown in Figure 9. These time histories result from recording the wavefield after passage through the forward transition due to SH L_g mode sum seismogram forcing function applied to the right end of that transition. The two vertical lines labeled Rc1 and Rc2 show receiver depth sections used to illustrate the effects of the transition on the distribution of amplitude with depth. The upper hatch region shows the ocean layer, the lower hatched region shows the mantle layer, and the unhatched region shows the crustal layer. Dots on Rc1 and Rc2 indicate positions of receivers for which displacement time histories are illustrated in Figure 17. Open circles and dots located on the surface of the crustal layer refer to a surface section of nodes for which displacement time histories are illustrated in Figure 18.

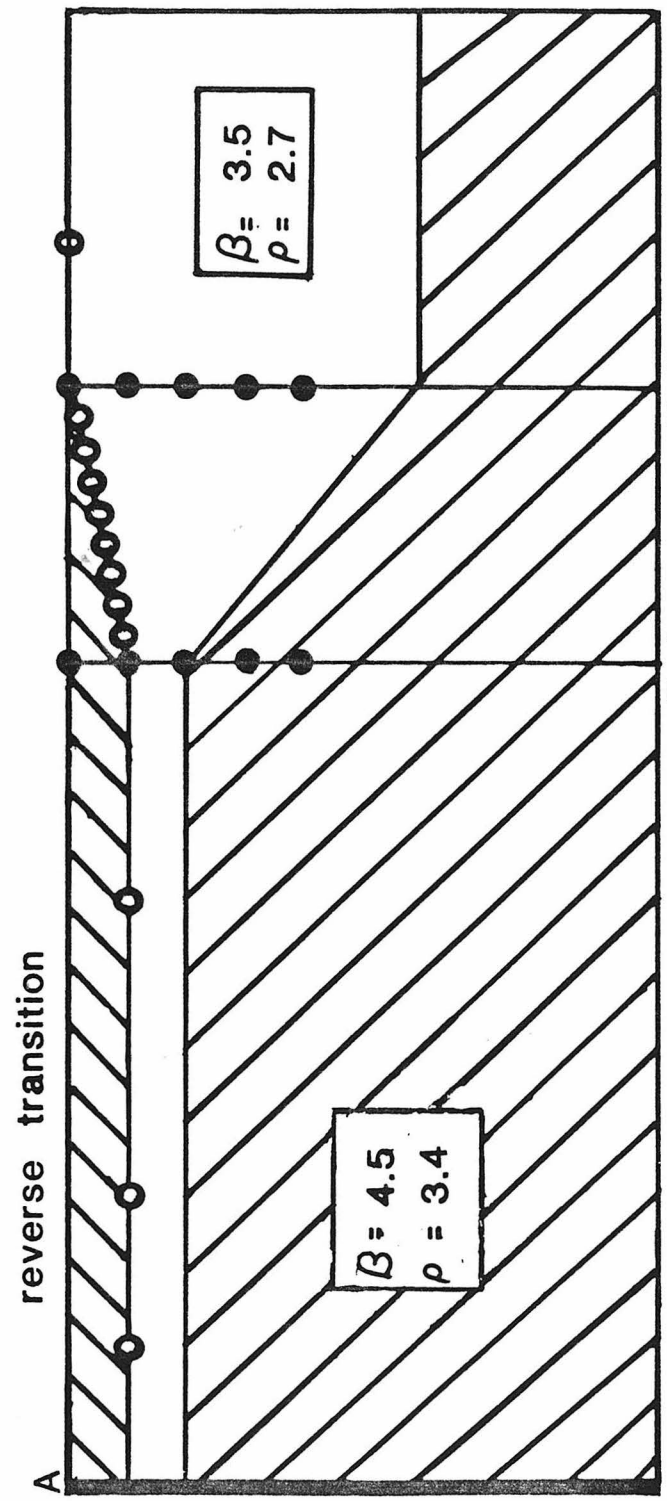

Figure 16: Grid geometry for the 20 km reverse transition used to illustrate the effects of a forward transition on the waveforms and amplitudes of seismograms as a function of distance, Δ, and depth. The upper hatched region is the oceanic layer, the lower hatched region the mantle layer, and the unhatched region the crustal layer. The heavy vertical line labeled A shows where seismograms recorded in the forward transition calculation are applied as forcing functions. The vertical lines labeled Rc1 and Rc2 show depth sections of receivers. The dots on Rc1 and Rc2 show receivers for which seismograms are illustrated in Figure 17. The open circles along the surface of the crustal layer show the receivers for which seismograms are shown in Figure 18.

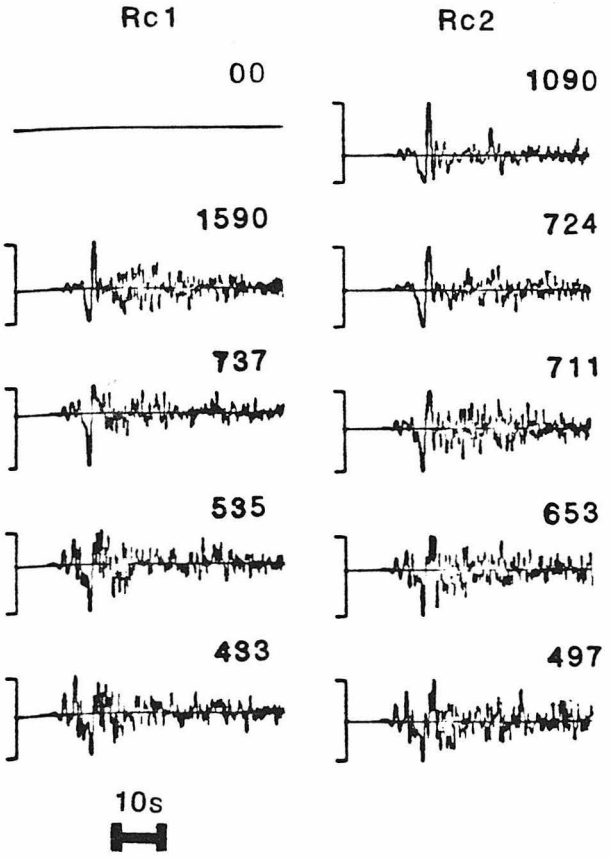

Figure 17: Seismograms recorded at receivers shown as dots on depth sections Rc1 and Rc2 in Figure 16. The first column shows the seismograms recorded at Rc1, the second the seismograms recorded at Rc2. The numbers above the right end of each seismogram show the peak to peak amplitude. The first row of seismograms show receivers at the depth of the surface of the continental crust. Successive rows show pairs of receivers at increasing depths. The second row is at the depth of the surface of the oceanic crust, the third at the depth of the base of the oceanic crust. All receivers illustrated are above the base of the continental crust.

Figure 17 shows seismograms recorded at positions shown as dots in Figure 16. All seismograms are band pass filtered between .01 and 1.0 Hz. No instrument is applied. The first column of seismograms in this figure shows the changes to waveform and amplitude as a function of depth at distance Rc1. The second column shows the seismograms illustrating the same type of variations on depth section Rc2. The numbers above and to the right of each seismogram show the maximum peak to peak amplitude of each seismogram. The surface seismogram on section Rc2, the first seismogram in the second column, shows a 25% decrease in peak to peak amplitude when compared to the surface seismogram in column Fc1 of Figure 10. Thus, even without considering attenuation, transmission of L_g type waves from continental to oceanic to continental structures can reduce the surface amplitudes by twenty five percent. At the depth of the surface of the oceanic crustal layer, the second row in this figure, propagation through the transition reduces the peak to peak amplitude by more than a factor of two. At depths between the surface of the continental crust and the depth of the surface of the oceanic crust the decay of amplitude with depth decreases with depth. The amplitude concentrated in the oceanic crust also spreads into the continental crustal layer below the oceanic crustal layer. The last two pairs of seismograms in this figure are recorded at depth below the bottom of the oceanic crust and above the bottom of the continental crust. Propagation across the transition at these depths produces an increase of about twenty percent in peak to peak amplitude. An increase in the amplitudes of the coda with respect to the maximum amplitude is also observed, giving an increase in RMS amplitude of about thirty five percent. Clearly, most or all of the amplitude incident on the mantle crust boundary is transmitted into the continental crustal layer, and the increase in amplitude is due to energy previously concentrated in the oceanic crust spreading throughout the continental crust within the transition region. These results support the statements that

energy incident from the oceanic crustal layer travels up the surface of the ocean crust transition, and that the concentrations of amplitude within the oceanic crust distribute themselves throughout the continental crustal layer on passage through the reverse transition and the first kilometers of the continental structure. It is also clear that amplitudes incident on the mantle crust boundary are largely transmitted across it into the crustal layer. The actual distortions of the wavefield will be cleared when the time slices, Figures 19 through 21, are discussed.

Figure 18 shows seismograms recorded along the surface of the crust, shown in Figure 16 as open circles and as dots on the crustal surface at distances Rc1 and Rc2. The numbers to the left of each seismogram show the sequence, in space, in which the seismograms were recorded. Seismogram 1 was recorded at the leftmost surface receiver, the leftmost open circle on the oceanic crustal surface in Figure 16. The number used as a label increases as one moves to the right across Figure 16. Peak to peak amplitudes are shown as the numbers above and to the right of each seismogram. A clear decrease in peak to peak amplitudes is seen as one moves along the surface of the oceanic crustal layer approaching the transition region. The amount of this reduction in amplitude is becoming smaller per unit distance as the wavefront travels through the oceanic portion of the model. Not only are the peak to peak amplitudes being reduced, but the portion of the coda with amplitudes comparable to the maximum amplitude is being reduced in length. Thus, the RMS amplitude decreases faster than the peak to peak amplitude. As the wavefront enters the transition region the decay of amplitude as a function of the distance, Δ, is accelerated. Although the decrements in amplitude appear to be smaller in the transition region than in the crustal layer of the oceanic structure, examining Figure 16 shows that the distance between the receivers in the transition region is one eighth of the distance between those on the surface of the oceanic layer. Thus, the decay per unit distance in the

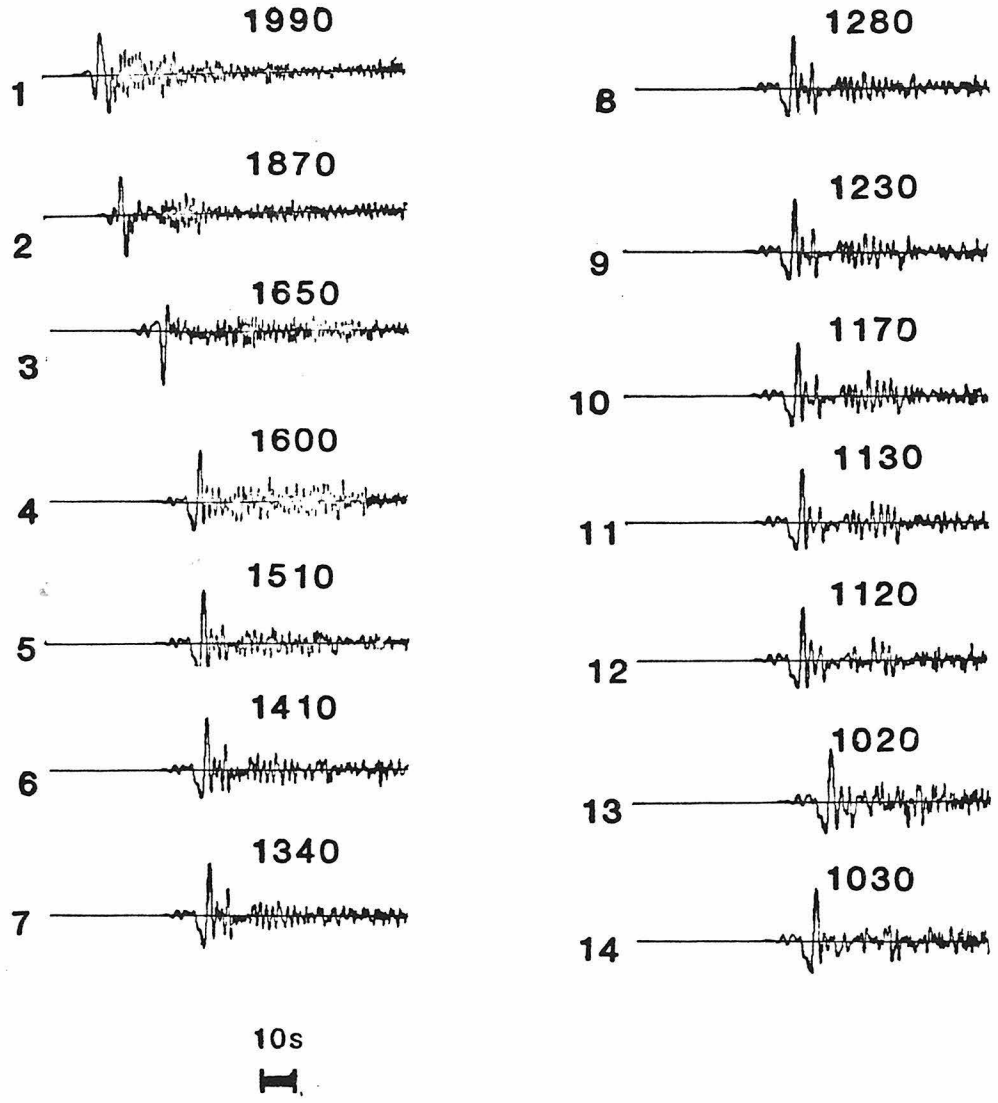

Figure 18: Seismograms recorded at receivers along the surface of the crustal layer in a reverse transition calculation. These seismograms are recorded at the receivers shown as open circles and dots on the surface of the crustal layer in Figure 16. The numbers to the left of each seismogram indicate the location of the node at which that seismogram is recorded. The leftmost open circle is receiver 1. The numbers increase as one moves to the left along the surface of the crustal layer. The numbers above the right end of each seismogram give the peak to peak amplitude of that seismogram.

transition is a factor of two to eight larger than in the oceanic structure. The amplitude decay within the transition is monotonic. The rate of decay is not necessarily constant showing some tendency to become smaller towards the end of the transition. A slight peak to peak amplitude increase is seen as the wave travels through the first kilometers of the continental structure. However, the RMS amplitude continues to decrease slowly until the wavefield readjusts to the new structure.

It should be noted that the continuation of the forward transition calculation by coupling results recorded during that calculation into the reverse transition grid calculation does introduce some uncertainties in the results. First, sixty of ninety nodes at the leftmost edge of the reverse transition grid have forcing functions applied to them. This vertical truncation of the incoming wavefield will have some effect. Also, any reflections included in the seismograms recorded to use as forcing functions will be added to the forward propagating wavefield in the reverse calculation. These effects tend to increase the amplitudes at the surface of the oceanic layer near the left end of the grid. In this region results are available at the same physical locations in both forward and reverse transition grids. An example of a seismogram recorded at the same physical position but at different nodes in the two transition grids the first seismogram in Figure 18 and the eleventh seismogram in Figure 9 can be compared. The latter portion of the seismogram shown in Figure 9 is contaminated with reflections and should be ignored. Comparing the first twenty seconds of these two seismograms shows that the amplitude is increased when the coupling procedure is used. Examining other common results shows that the discrepancy seen in this example is much larger than average, but agrees in sign with other points. Thus, the uncertainties introduced by the coupling process appear to increase the amplitudes in the second grid by about three percent. Therefore, they could possibly lead to a slight underestimate of the magnitude of the attenuation effect, but should not lead to an

overestimate. Propagation through a fifty kilometer forward transition followed by 120 km of oceanic structure followed by a fifty kilometer reverse transition reduces the amplitudes at the surface by at least twenty five percent.

A series of time slices is shown in Figures 19 through 21. These time slices were recorded during the FE calculation for the fifty kilometer long reverse transition discussed earlier. The time slices are recorded at intervals of 12.5 seconds beginning 37.5 seconds after the initiation of the FE calculation. The time elapsed since the start of the FE calculation is shown for each time slice above and at the rightmost end of that time slice. The dimensions of the illustrated grid are 450x90 nodes. The heavy lines outlining the grid show the bounds of the crustal layer, and the horizontal and vertical extent of the grid. The water layer is not outlined. No displacements take place within it. Again, sixty forcing functions, this time recorded in the fifty kilometer forward transition calculation, are applied to the left end of the grid. Thus input forcing functions extend to three times the depth of the bottom of the crustal layer, or to six crustal layer thicknesses below the water surface. The cutoff for minimum amplitude to be plotted on each time slice is two percent of the maximum amplitude in that time slice. The arrow above each time slice except the first shows the location to which the component of the wavefield traveling at 3.5 km/s seen at the leftmost edge of the grid for the previous time slice has moved in the time elapsed since the previous time slice.

Figure 19 shows the first two time slices, which illustrate the wavefield traveling through the oceanic layer over a half-space structure. In the first time slice the leading edge of the wavefield has propagated about halfway through the oceanic structure, in the second the leading edge of the wavefield is about to enter the reverse transition. The high amplitude concentrations in the oceanic crust travel slower than the lower amplitude disturbances in the half-space. Triangular regions of maxima can be seen but they are not nearly so clear as in the case of the wavefield seen in the forward

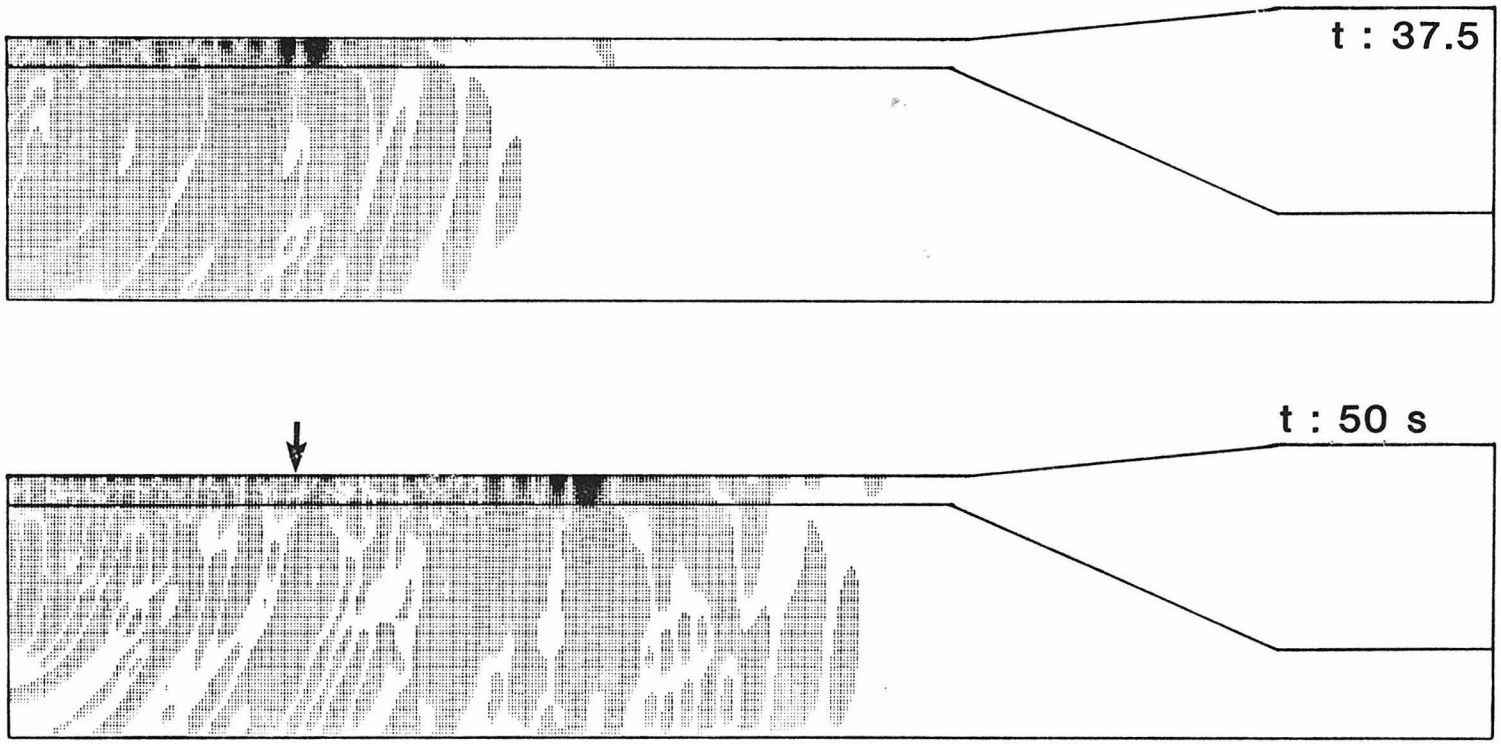

Figure 19: Time slices recorded during the 50 km reverse transition calculation. The crustal layer and the ends and bottom of the FE grid which contain it are outlined. Within these outlines the displacements at each grid point at the indicated instant of time are plotted at the location of that point. A larger displacement produces a larger point. Thus, high displacement areas appear darker. The maximum amplitude in each time slice produces a point of maximum size. An amplitude of less than 2% of this maximum produces no point. The time since the initiation of the FE calculation is shown above the right end of each grid. The arrow above a time slice shows the location to which the disturbances moving at 3.5 km/s, seen at the left end of the previous time slice, have moved in the intervening time.

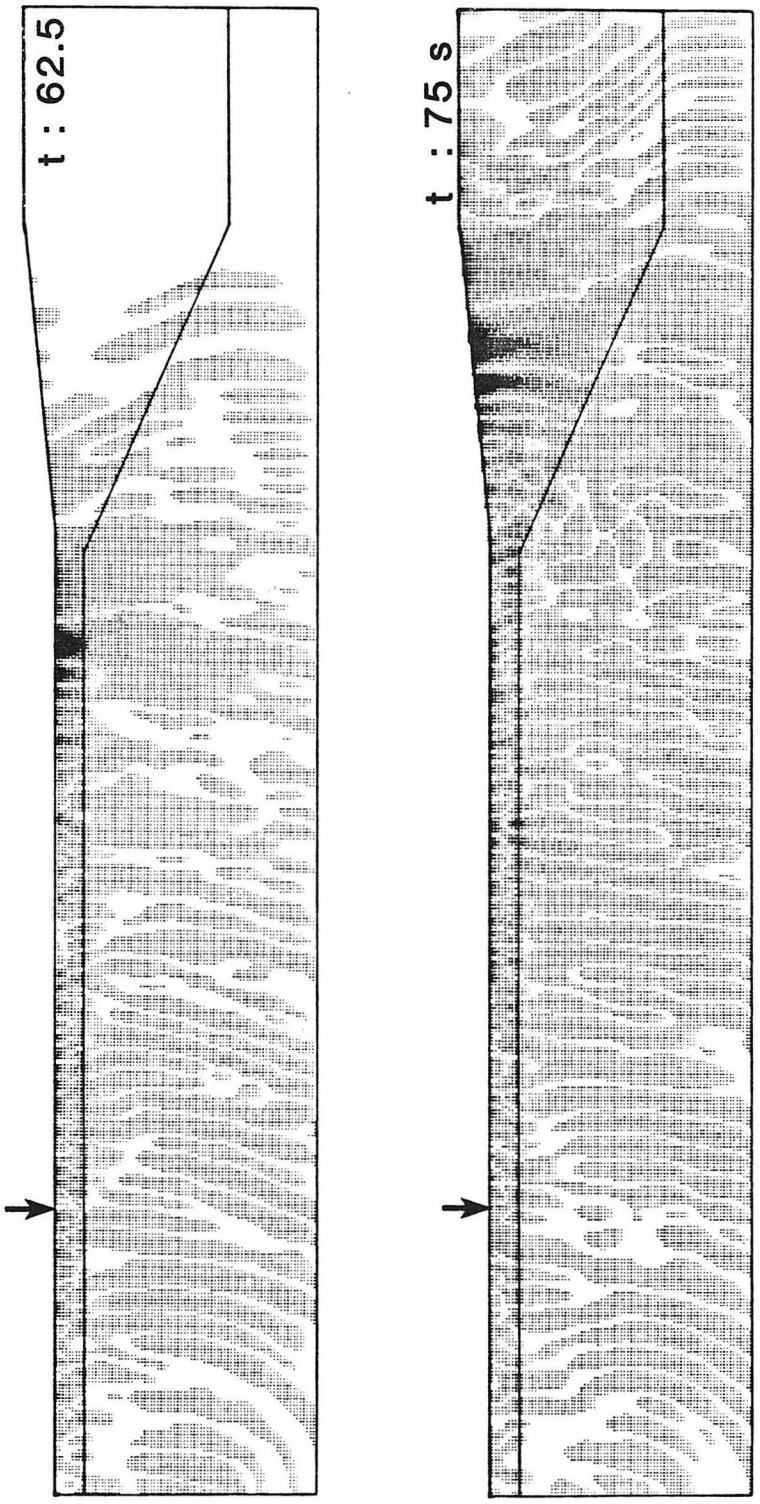

Figure 20: Time slices recorded during the 25 km forward transition calculation. Details of the form of these time slices are the same as for Figure 19. The time slices in this figure are recorded after the completion of additional time steps in the same FE calculation that produced the time slices in Figure 19.

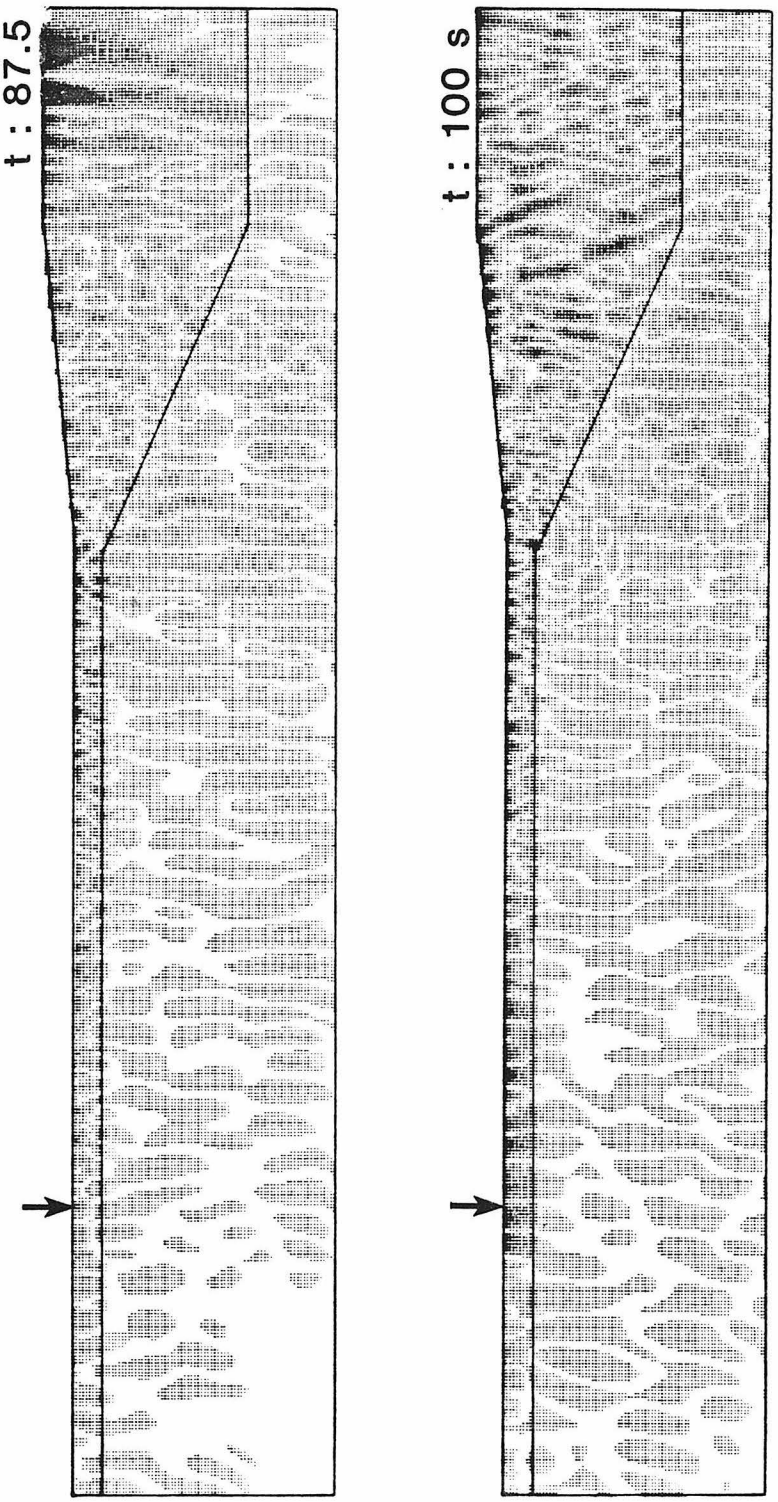

Figure 21: Time slice recorded during the 25 km forward transition calculation. Details of the form of these time slices are the same as for Figure 19. The time slices in this figure are recorded after the completion of additional time steps in the same FE calculation that produced the time slices in Figure 19 and 21.

transition. Some of the regions of displacement within the half-space are larger in the second time slice than in the first. This growth is due mainly to a reduction in the maximum amplitude. Some of the clear shape changes in these areas are due to propagation effects.

Figure 20 shows the next two time slices in the sequence. Figure 21 shows the two time slices following those shown in Figure 20. The time slices in Figure 20 illustrate the passage of the highest amplitude portions of the wavefield through the transition region. The time slices in Figure 21 show the propagation of the highest amplitude portions of the wavefield through the continental structure at the end of the grid, and the propagation of later portions of the wavefield through the transition region. In the third time slice, the uppermost in Figure 20, the maximum amplitude has been slightly reduced with respect to the second time slice, but the differences in the wavefield due to this amplitude reduction is small. In the fourth time slice, however, the maximum amplitude has been significantly reduced. Thus, the remainder of the wavefield has been amplified. This reduction of maximum amplitude illustrates that the regions of maximum amplitude passing through the transition region are spreading to include all depths in the continental crustal layer and are thus being reduced in amplitude at any particular node. This decrease in maximum amplitude in the fourth time slice accounts for many of the enlargements of the disturbances seen in the oceanic half-space when the third and fourth time sections are compared. The fifth time slice, the uppermost in Figure 21, has maximum amplitude somewhat smaller than the fourth time slice. The differences do not produce significant changes in the lower amplitude portions of the wavefield. However, the sixth time slice shows a substantially amplified wavefield since the initial maximum amplitude disturbances have propagated out of the grid. The triangular regions of maxima are beginning to appear in the continental structure. Addition propagation in x in the continental structure may

be needed to stabilize the wavefield in the region of the grid with continental structure . Examining these time slices verifies that very different kinds of effects occur along the ocean crust boundary and along the mantle crust boundary. It also shows that due to propagation into the half-space at an angle to the crust mantle boundary in the forward transition some energy in the reverse transition calculation is propagating out of the bottom of the grid. These different effects will be discussed separately below.

Regions of significant amplitude incident on the mantle crust boundary are transmitted across it. In the third and fourth time slices the reflection from this boundary are too small to be seen. The pattern of the displacements seen in the oceanic half-space is significantly distorted by transmission across the mantle crust boundary. The uppermost portion of a disturbance crosses the boundary first and begins to move more slowly. The remainder of the disturbance, still in the mantle layer continues to move with the mantles faster velocity. As the disturbance moves through the length of the transition, an increasing section of it moves into the crustal layer. This results in a slope being superimposed on the portion of the disturbance which has propagated back into the crustal layer. This slope is dependent of the length of the transition, l, the velocity in the crustal layer, v_c, and the velocity in the mantle slope clearly visible in both the third and the fourth time slices ahead of the layer, v_M, $\text{Slope} = \tan^{-1}\left[\frac{l\,(v_M - v_c)}{v_M}\right]$. In this case the angle is about fifty two degrees. This region of the wavefield with largest amplitudes. This pattern is also seen in the fifth and sixth time slices shown in Figure 21. In these time slices the amplitude incident from the oceanic crustal layer dominates that transmitted from the oceanic mantle layer.

The effect of the reverse transition region on the energy previously traveling in the oceanic crustal layer is very different. A concentration of amplitude leaving the oceanic crustal layer propagates along the ocean crust boundary. While it propagates along this boundary the lower edge of the amplitude concentration is no longer constrained as trapped modes by the lower edge of the oceanic crustal layer. Consequently, amplitude can migrate downwards within the crustal layer of the transition and in the crustal layer of the continental structure following the transition region. The small concentrations in amplitude traveling along the ocean continent boundary in the third time slice show little change in form. The amount of amplitude escaping from them is smaller that the low amplitude cutoff imposed on the plot. In the fourth time slice the maximum amplitude regions have propagated to the center of the transition region and spread throughout the depth range above the depth of the bottom of the oceanic crust. Some evidence is visible that some amplitude has been translated to depths below the oceanic crust. In the fifth time slice, shown in Figure 21, The maximum amplitude regions have propagated to the rightmost end of the grid. In this time slice it is clear that the amplitude previously confined to the oceanic crustal layer has distributed itself throughout the entire depth range of the continental crust. Some transmission of amplitudes, spreading down from concentrations of amplitude originally trapped in the oceanic crustal layer, across the the crust mantle interface is also seen. The amplitudes are still much larger near the surface, and decay rapidly with depth.

The disturbances seen in the half-space of the oceanic region of the reverse transition grid contain significant energy but the amplified surface amplitudes make them appear small. Comparing the first two time slices shows that for a subset of these disturbances the component of motion in the z direction in the half-space is increasing for successive groups or disturbances. This tendency continues in the later sections.

These packets of amplitude propagate rapidly enough in z that some will pass across the bottom boundary of the grid before they reach the reverse transition region. The amount of energy that passes out of the grid in this way as the wavefield travels between the two transition regions is related to the angles of incidence of the wavefronts at the crust ocean and crust mantle boundaries in the forward transition region. For the case of a single reflection within the transition region the angle of incidence for a wavefront which first encounters the crust mantle boundary is $i-\phi_{CM}$, for a wavefront which first encounters the crust ocean boundary it is $i-\phi_{CO}$, where the angles mentioned are illustrated in Figures 1 and 16. When discussing the time slices for the forward transition these waves were also visible and were seen to travel at angles dependent on the phase velocity of the incoming waves. Adding the results seen in these time slices to those observed in the forward transition time slices to help interpret the problem shows that the direction is also a function of the length of the transition, and the amount of escaping energy is clearly dependent on the length of the intervening oceanic structure. Results supporting the existence of these effects will be discussed in detail and explained later.

The Dependence of Changes to L_g Wavetrains Passing through a Forward Transition Region on Transition Length

The forward transition tests using a variety of transition lengths illustrate several properties that change with the length the transition model or the slopes of the crust ocean and the crust mantle boundaries. At depths corresponding to the crust water boundary the amplitude of the reflected component of the seismograms traveling back into the continental crustal layer, that is back toward the source, decreases as the length of the transition increases. A similar reflected component is observed at depths corresponding to the crust to mantle boundary. The reflected amplitudes are much smaller with respect to the incident amplitudes for depths coincident with the crust

mantle boundary than at depths coincident with the crust ocean boundary. The difference in the magnitudes of the effects in these two depth ranges will be explained by the difference in velocity contrast across the two boundaries in the transition region and the difference in the angles ϕ_{CM} and ϕ_{CO} shown in Figure 1. Although no energy in transmitted into the water layer, not all energy impinging on the water layer is reflected back toward the source. Instead some of the energy is concentrated by the transition into the oceanic crustal layer. The amount of concentrated energy, increases as the length of the transition increases. Quantification of a similar concentrating effect associated with the crust mantle boundary is difficult because this effect is dominated by transmission of energy across that boundary. The amplitudes in the mantle layer within the transition region are maximum immediately below the crust mantle boundary, and decay nearly exponentially with depth below that boundary. The amplitude of the transmitted seismograms recorded at nodes below the oceanic crustal layer, at the end of the forward transition, decrease as the length of the transition increases. Despite this observation the time slices show that the amount of amplitude transmitted across the boundary increases as the length of the transition increases. The amplitudes of seismograms recorded at nodes along the surface of the crustal layer show a general increase as one passes through the transition. However, this increase does not appear to be monotonic. The variation in surface amplitude within the transition zone has similar pattern for all lengths of transitions, but the width of the oscillations are proportional to the width of the transition region. Each of these effects will be discussed and explained below.

The effects discussed above will be explained with the aid of Figures 15 and 22. Figure 22 illustrates two forward transition structure outlines for a one hundred kilometer transition region, at the same scale as the twenty five kilometer forward transition outlines used in Figure 15. The lines within each of these four outlines

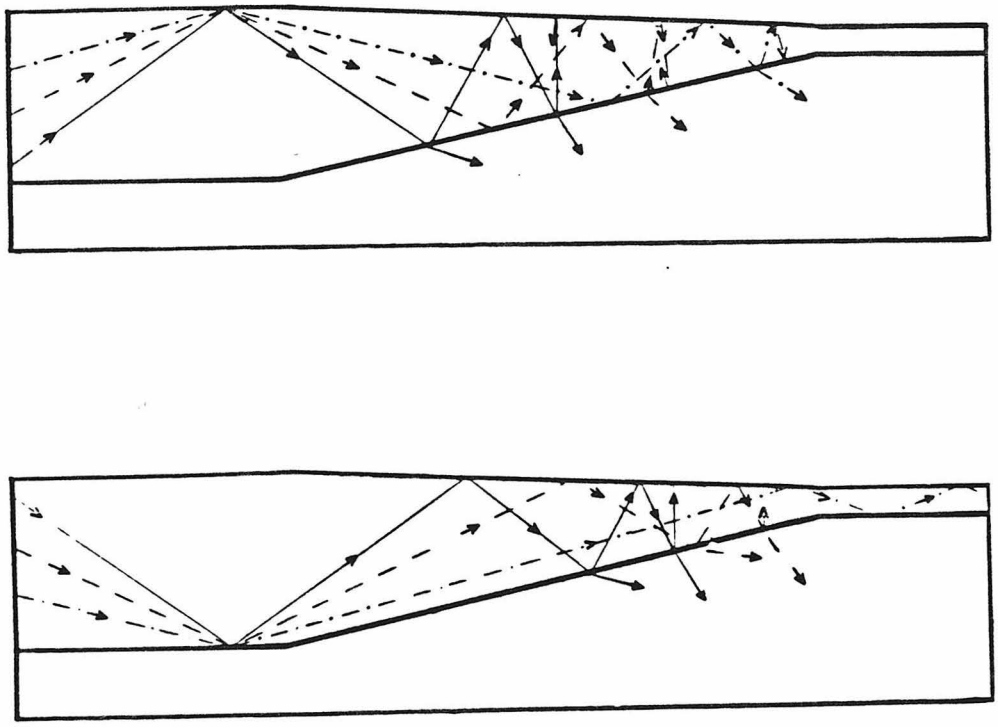

Figure 22: Illustration of ray paths within a forward transition structure. Each diagram shows rays with angles of incidence, i, 55°, 65°, and 75°, at the free surface and crust mantle interface in the continental portion of the model. The transition structure within which the rays are traveling is a 100 km forward transition drawn to scale. The upper diagram shows propagation paths for rays that encounter the crust mantle boundary before the crust water boundary. The lower diagram shows propagation paths for rays that encounter the crust ocean boundary before the crust mantle boundary. The arrows indicate the direction of propagation of the wavefront along the ray.

show the same three multiply reflected rays. These rays are for sample angles of incidence, i = 55°, 65°, and 75°, at the crust mantle interface of the continental structure. The angles chosen give a good sampling of the possible range of post-critical incident angles, $> 51°$. The arrows on the rays show the direction of propagation. To avoid cluttering the ray diagrams the incident angles, i, at the crust mantle interface in the continental structure, j, at the crust mantle boundary in the transition, and j', the angle between the transmitted ray and the normal to the boundary are illustrated only in the first diagram in Figure 15. To explain some of the above effects multiple reflections within the transition region will be considered. To differentiate the angles of incidence for the later reflections within the transition region from j, the angle of incidence at the first boundary encountered in the transition region, an addition to the notation will be made. In further discussions the incident angle j, will become j_1, and the incident angle for subsequent reflections within and following the transition will be denoted j_n, where n denotes the n^{th} reflection of the ray after it enters the transition region. Similarly, the transmitted rays for the n^{th} reflection of a ray after entering the transition region, will be denoted j_n'. Also useful in the following discussions is the transmission coefficient as a function of the incident angle, j_n. For the examples discussed here the displacement transmission coefficient, $T = \frac{2\cos(j)}{\cos(j)+1.62\cos(j')}$, varies monotonically between zero for the critical angle j=51°, and .76 for normal incidence, j=0.

Most of the properties of the wavefield that vary with the length of the forward transition are illustrated in the FE results shown in Figures 23 and 24. The amplitudes represented in these figures are RMS amplitudes calculated using a window length of sixty seconds or less. Figure 23a illustrates the variation in the RMS amplitudes with distance along the surface of the crustal layer for each forward transition model. Figure 24 shows the variation in the RMS amplitudes with depth at distances

corresponding to depth sections A, B, C, D, and E shown in Figure 1, and at an additional depth section ten kilometers further from the source than depth section E. These figures will be used to demonstrate the changes in the properties of the wavefield as it propagates through different forward transitions.

Figure 23a shows the variation of 60s RMS amplitude with distance, Δ, from the source for each of the forward transition FE calculation. The results of the FE calculations for each forward transition region are represented by a line labeled with the length of that transition region. The lines were determined by measuring RMS amplitudes at grid points along the surface of the crustal layer, at intervals of five kilometers, and drawing a line through the resulting points. The vertical axis shows the RMS amplitudes. Since the relative amplitudes produced using the different forward transition amplitudes are being compared the absolute values of the amplitudes are not shown. These absolute values will change according to the moment of the source. The horizontal axis shows the distance, Δ, from the source. The vertical lines labeled B and D are at distances from the source corresponding to the beginnings and the ends of the transitions respectively. The horizontal axis does not have the same scale for all transitions. The scales are identical for all transitions within the region of continental structure to the left of the transition region and within the region of oceanic structure to the right of the the transition region. However, within the transition region, between B and D, the horizontal scale is different for each calculation. Amplitudes recorded within each transition region are plotted with respect to an origin at B, the beginning of the transition region. Consider that the distance between B and D on the plot is BD centimeters. If the horizontal distance from B to the node at which the amplitude is recorded, for a transition of length L kilometers, is x kilometers, then the observation is plotted at a point a distance (x/L)BD centimeters to the right of B. This method of plotting shows the changes in amplitude through the transitions of

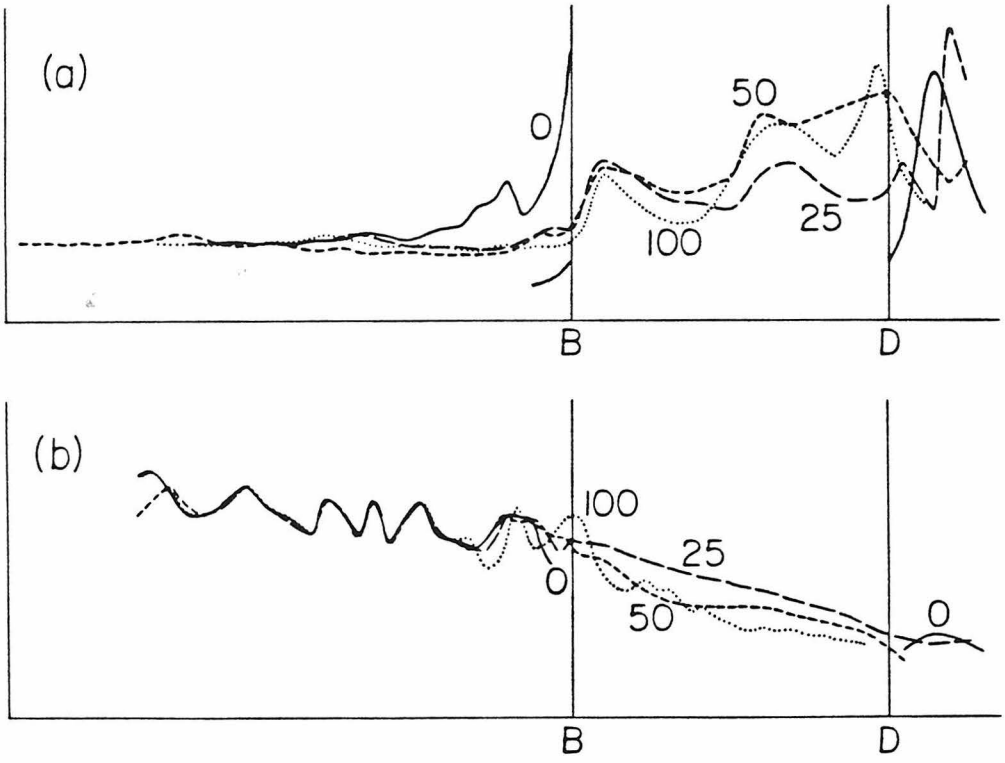

Figure 23: Variation of surface amplitude along the surface of each transition. The upper sketch shows the variation in RMS amplitude (60s) along the surface of each forward transition model. The lower sketch shows the amplitude (50s RMS) distance relation of surface amplitudes for each reverse transition. Amplitude is recorded as the y coordinate. The distance scale is not uniform along the whole x axis. The two vertical lines indicate the limits of the transition region. Outside the transition region the scale is uniform. Within the transition region distances are plotted, with respect to an origin at the beginning of the transition region, as fractions of the transition length. All data points lie on the indicated lines except for some scatter in the 100 km transition results.

various lengths within the same region of the plot. The amplitudes recorded at nodes along the surface of the crustal layer within each transition region show a general increase as one moves from B towards D. The size of this increase is smallest for the step transition and increases as the length of the transition increases. Superimposed on the general increase of amplitude is an oscillatory term. The method of scaling the distance coordinate within the transition region makes the coincidence of maxima and minima at approximately the same fraction of the transition length for all transitions considered very clear. Thus, the variations of amplitude along the surface of the crustal layer in the transition show similar patterns for all transition lengths, and the widths of the fluctuations in amplitude along the surface of the crustal layer within the transition region are approximately proportional to the width of the transition region. If no transition region is present in the grid the increases in amplitude before reaching distance B would not be seen. These increases are due to the presence of energy reflected from the transition back towards the source. The increase is largest for a step transition and decreases as the length of the transition increases. The fluctuations in amplitude following the transition region shows that the wavefield has not stablized in the few kilometers beyond the transition regions illustrated in this figure.

Figure 24 shows the variation of 50s RMS amplitude with depth recorded at distances corresponding to depth sections A, B, C, D, and E in Figure 1a, and an additional depth section ten kilometers to the right of depth section E. Six individual graphs are shown to illustrate the variation of amplitude with depth in the forward transition models. Each depth section is represented by one graph . Each of these graphs is labeled in the upper left corner with the letter that identifies the depth section on which the illustrated amplitudes were recorded. The unlabeled plot is for the sixth depth section. The vertical axis of each plot shows the depth. The upper end of

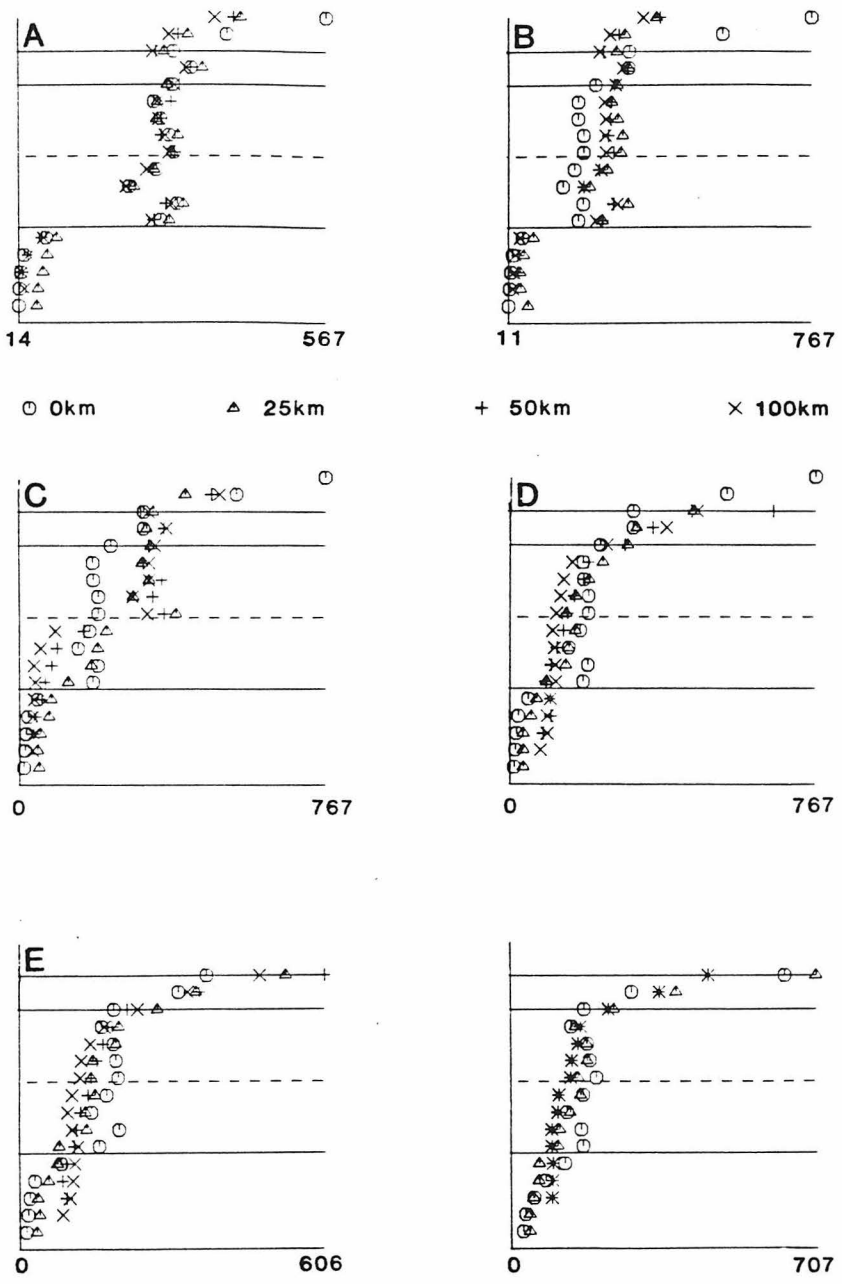

Figure 24: Variation of 55s RMS amplitude with depth on depth sections A, B, C, D, E, of Figure 1 for each forward transition model. An additional depth section 10 km to the right of depth section E is also illustrated. Each plot illustrates results for one depth section. The letter at the upper left of each plot identifies the location of the depth section as illustrated in Figure 1. The three solid horizontal lines are, from top to bottom, the surface and base of the oceanic crustal layer, and the base of the continental crustal layer. The dashed horizontal line shows the depth of the base of the crustal layer in depth section C, at the center of the transition region.

the vertical axis corresponds to the surface of the continental crust. The uppermost solid horizontal line corresponds to the depth of the surface of the oceanic crustal layer. The central solid horizontal line is at a depth corresponding to the bottom of the oceanic crustal layer. The lowermost solid horizontal line shows the depth of the bottom of the continental crustal layer. The dotted horizontal line shows the depth of the bottom of the crustal layer in the transition region at the distance of depth section C. The horizontal axis shows the amplitude of the seismograms. The labels on the horizontal axes show the values of amplitudes at the ends of these axes. Although the length of the horizontal axis is fixed the scale on it is determined by the points with the largest and smallest amplitudes so the scales of each graph differ. The values of amplitude at the ends of the horizontal axis are given to facilitate comparison between results at different distances. Each symbol on any of these graphs represents the RMS amplitude of a seismogram. Each transition length is plotted using a different symbol. A legend defining which symbol represents each transition length is shown below the first row of graphs. A subset of nodes on each depth section was chosen to be included in the appropriate graph. The surface node and nodes equally spaced down the depth section with a separation of 2.5 km were included in this subset.

The increase in amplitude for seismograms at crustal surface nodes at distances ranging from B to D can be explained in terms of amplitude concentrated at the surface of the crustal layer in the transition. Concentrated amplitude is observed as an increase in amplitude of seismograms in the oceanic crustal layer of the transition region, at depths between the surface and ten kilometers, with respect to the amplitudes of seismograms at the same distance from the source and depth, calculated using the forward reference model and the same input forcing functions. In Figure 23a the magnitude of the energy concentrated at the surface of the crustal layer in the transition is seen to increase as the length of the transition increases. In Figure 24 this

tendency is seen to apply within the crustal layer of the transition region. This behavior can be explained using the Figures 15 and 22 and observing the differences between them. In a transition region of any length greater than zero the angles of incidence, j, are less than the angles of incidence, i. Decreasing this angle j will cause the reflection points at the boundaries in the transition region to become closer together. This implies that the density of rays will increase in the transition producing higher amplitudes there. As the length of the transition increases the number of bounces within the transition increases and the angle of incidence in reduced producing increases concentration of amplitude. These effects would be equally efficient at a crust mantle boundary with the same slope if transmission of amplitude across that boundary was not a factor. However, the amplitude concentrated at the crust mantle boundary is partially transmitted across it. Thus the concentration of amplitude near the crust mantle boundary is offset by the escape of energy across it.

At depths corresponding to the crust water boundary the amplitude of the component of the seismogram reflected back into the continental layer, that is back toward the source, decreases as the length of the transition increases. This is also true for the amplitude of the component of the seismograms reflected back into the continental layer at depths corresponding to the depth of the crust mantle boundary. The reflected component of the seismogram is defined to be that component which remains when a hybrid seismograms recorded on depth section A (Figure 1) in a forward transition calculation have the hybrid seismogram at the same depth and distance from the source, recorded during the forward reference calculation, subtracted from it. The amplitudes referred to in this discussion are the RMS amplitudes of seismograms taken using a fifty five second window. The amplitude of the reflected components of the seismograms is much smaller below the bottom of the oceanic crustal layer than above it regardless of the length of the transition.

The reduction in the reflected amplitude as the length of the transition increases is easily explained by observing important differences between Figures 15 and 22. Two different effects contribute. First, as the length of the transition region increases the amount of amplitude concentrated at the crust ocean boundary and thus transmitted into the oceanic crustal layer increases. This reduces the amount of amplitude reflected back toward the source. Second, in the longer transition regions more energy is able to escape into the half-space across the crust mantle boundary. This effect also decreases the amount of amplitude available to be reflected. The cause of the increase in transmission across the crust mantle boundary as the length of the transition increases can be explained by considering the angles ϕ_{CM}, and ϕ_{CO} as shown in Figure 1. Reducing these angles, that is increasing the length of the transition, allows more reflections of a given ray within the transition region before it reaches the oceanic crustal layer or is reflected back toward the continental structure. For each of these reflections the angle of incidence is $j_n = j_1 - (n-1)\,(\phi_{CM}+\phi_{CO})$. When this angle becomes negative the ray returns toward the source. Clearly, for smaller values of the angles ϕ_{CM}, and ϕ_{CO} more bounces can occur before the ray turns back toward the source or enters the oceanic structure. Each time the ray bounces the angle j_n is smaller, so the angle j_n' is smaller. Thus, the amount of amplitude transmitted across the transition increases, and the angle of incidence of the disturbance transmitted into the half-space with the grid bottom boundary increases. The transmission of additional energy across the transition leaves less energy within the crustal layer to be reflected back towards the source.

The Dependence of Changes to L_g Wavetrains Passing through a Reverse Transition Region on Transition Length

The reverse transition tests also illustrate the behavior of properties dependent on the length of the transition region. A longer transition is more effective at reducing

surface amplitudes. Examination of Figure 23b shows that the surface amplitude decay across the transition is monotonic for the shorter reverse transitions and shows a small oscillatory component for calculations using longer reverse transition models. The figure also shows the surface amplitude vs. distance relation along the oceanic portion of the path is oscillatory. This oscillatory behavior is also observed for the oceanic reference model calculation, where it is superimposed upon a slow decrease in amplitude. The amplitude distributions with depth indicate that energy is traveling down from the crustal surface, spreading throughout the crustal layer. Some of the energy eventually escapes across the crust mantle boundary in the region of continental structure. The amplitudes in the crustal layer of the transition distribute themselves over a larger depth range in a longer transition. Thus the amplitude originally traveling in the oceanic crustal layer has time to distribute itself over a larger depth range when it is traveling through a longer transition. The amount of amplitude incident on the reverse transition from the half space is transmitted into the crustal layer. The amplitudes below the crustal layer of the transition region do not die off as strongly with depth as they do in the forward transition case, in fact the amplitudes may even increase with depth below the crustal layer as seen in Figure 25. The increase with depth below the crustal layer indicates that amplitude is traveling down toward the grid bottom and out of the system being considered. It appears that it is in the reverse transition and the propagation through the intermediate oceanic layer that causes the attenuation of L_g type waves when they travel across a mixed path containing an oceanic region.

Figure 23b shows the variation of 50s RMS amplitude with distance from the source, Δ, for each of the reverse transition FE calculations. The RMS amplitudes determined during a reverse transition calculation are depicted in this figure by a line labeled with the length of the forward transition region model in which they are

determined. The vertical axis shows the RMS amplitudes. Since the amplitudes produced using the different reverse transition models are dependent on the moment of the source and the effects being investigated are the amplitude variations caused by modifying the transition models numerical values on the amplitude axis are unnecessary. The horizontal axis shows the distance, Δ, from the source. The vertical lines labeled B and D show the locations of the ends of the transitions. The scale on the horizontal axis between B and D is different for each transition length and is defined in the same manner as the scales within the forward transition region shown in Figure 23a. This method of scaling shows the changes in amplitude through the reverse transition regions of various lengths within the same region of the plot. The amplitudes recorded at nodes along the surface of the crustal layer within each reverse transition region show a general decrease as one moves from B towards D. The size of this decrease is smallest for the step transition and increases as the length of the transition increases. Superimposed on the general increase of amplitude is an oscillatory term. The sizes of the oscillations seen in the reverse transition results are much smaller than those seen in the forward transition results. The fluctuations appear to be confined near the beginning of the transition region for the reverse transition case as opposed to distributed throughout the transition for the forward transition case. The amplitudes of the fluctuations in the reverse transition case are approximately proportional to the width of the transition region. The curve for the 25km reverse transition shows no visible fluctuations. For the 100km reverse transition the fluctuations begin smaller than those seen in the oceanic structure and are rapidly reduced as the wavefield passes through the transition. The oscillation in amplitude following the transition region shows that the wavefield has not stablized in the few kilometers beyond the transition regions illustrated in this figure. The differences between the results for the different transition lengths immediately preceding the transition region

suggests that some type of reflection, diffraction, or scattering from the transition region is affecting the wavefield immediately adjacent to the start of the transition region.

Figure 25 shows the variation of 50s RMS amplitude with depth on depth sections A, B, C, D, and E in Figure 1b, and an additional depth section ten kilometers to the right of depth section E. Each of these depth sections is represented by one of the six individual graphs shown in the figure. Each of these graphs is labeled in the upper left corner with the letter that identifies the depth section on which the illustrated amplitudes were recorded. The unlabeled plot is for the sixth depth section. The vertical axis of each plot shows the depth. The upper end of the vertical axis corresponds to the surface of the continental crust. The horizontal lines within each graph, from the uppermost to the lowermost, are at the depths of the surface, the surface of the oceanic crustal layer, the base of the oceanic crustal layer, the base of the crustal layer at depth section C, and the base of the continental crustal layer respectively. The labels on the horizontal axes show the values of amplitudes at the ends of these axes. These values of amplitude are given to facilitate comparison between the individual graphs, each of which has a different horizontal scale. The RMS amplitudes of seismograms at the surface and equal intervals of length 2.5 km down each depth section are shown as centered symbols on the graph for that depth section. Each transition length is plotted using a different symbol. A legend defining which symbol represents each transition length is shown below the first row of graphs.

The length of the intermediate oceanic path between the continent to ocean and the ocean to continent transition is also being investigated. Calculations for two distances have been completed using single FE calculations. Calculations for an additional, longer, distance were done using multiple FE calculations to go from the edge of the first transition model to the receiver. Due to computational limits, the lengths

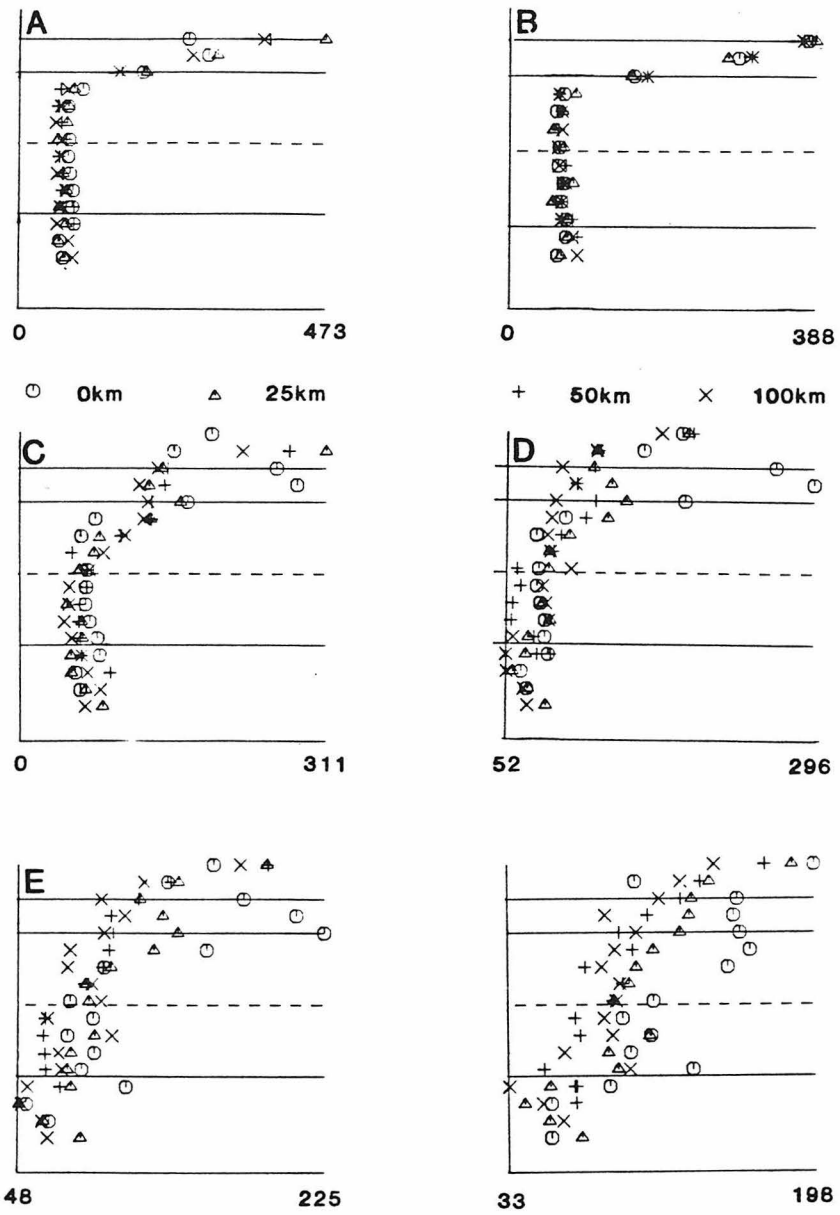

Figure 25: Variation of 55s RMS amplitude with depth on depth sections A, B, C, D, E, of Figure 1 for each reverse transition model. Each plot illustrates results for one depth section. The letter at the upper left of each plot identifies the location of the depth section as illustrated in Figure 1. The horizontal lines are at the same depths as in Figure 24.

of these intermediate paths are short, but definitely within the range of interest. Lengths of 30, 70, and 120 km, have been used. For the shortest paths energy transmitted in to the mantle layer has little time to travel towards the bottom of the grid and thus out of the region of consideration before much of it passes back into the crustal layer as it travels through the reverse transition. This implies that there may be a critical length of intermediate oceanic path beyond which enough of the energy has been propagated through the crust mantle boundary or leaked from the oceanic structure and subsequently escaped from the region of interest that amplitudes of the attenuated L_g recorded after the reverse transition would be reduced to the invisible level due to dilution caused by propagation through the reverse transition region. To completely analyze this assertion models using longer path lengths of intermediate oceanic structure should be considered. In order to investigate longer path lengths in the oceanic structure the RT coupling method for continuing FE calculations through a plane layered structure using RT integration and propagator matrix Green's functions must be used. The accuracy of the numerical implementation of this method must be established before such calculations can be presented. Therefore, the discussion of the numerical implementation of this method and of the results examining the effects of the intermediate path length in the oceanic structure will be left for the next chapter.

Conclusions

In conclusion, a summary of the important observations of the effects of regions of thinning or thickening of the crust on SH L_g type wavefields will be given. First the effects of a forward transition on the incoming SH L_g mode sum seismograms will be summarized. Then, the further effects due to continued propagation of this energy through a reverse transition will be stated in brief. Next, the variation in the effects introduced by the forward transition as a function of transition length will be summed up. Finally, the variations in the effects observed as the wavefront passes through the

reverse transition, as a function of the length of that transition will be summarized. The consideration of the effects due to varying the length of the oceanic path between the two transition regions has been mentioned, but, the detailed discussion of this problem and its summary is reserved for the next chapter.

Now, the effects produced when a SH L_g mode sum wavefield is propagated through a 20km forward transition region will be summarized. First, amplitudes at the surface of the crust are amplified by about fifty percent as the wavefield passes through the transition region. These amplitude increases decrease in magnitude with depth becoming net decreases at the bottom of the oceanic crustal layer. These increases and their behavior with depth can be understood by noticing that as a ray travels through a transition region the distance between successive reflection points decreases thus amplitude concentrated at the surfaces of the crustal layer. However, amplitude is transmitted across the crust mantle boundary and not across the crust ocean boundary. Thus, the concentration at the crust ocean boundary is maximum at the surface and decays with depth. The concentration effect at the crust mantle boundary is masked by the transfer of amplitude across that boundary. The amplitudes in the mantle layer are largest directly below the crust and decay rapidly with depth. The amplitude transmitted across the crust mantle boundary in the transition region propagates at some angle toward the grid bottom as x is increases. The angle that the wavefront formed by this amplitude makes with the grid bottom boundary increases as the width, in x, of the triangular regions of maxima incident from the continental structure increase. Thus, as the phase velocity decreases later in the record this angle increases. The actual size of that angle is dependent on the angle the crust mantle boundary makes with the horizontal, ϕ_{CM}, and is the complement of the difference between the incident angle in the continental structure and the angle ϕ_{CM}. Amplitude crosses the crust mantle transition into the oceanic structure. This leakage

is largest near the end of the transition region and decreases with distance away from it.

Next, a summary of the important observations for the reverse transition will be given. First, amplitudes at the surface of the crustal layer decrease as the wavefield travels through the oceanic layer. The size of this change in amplitude decreases as the propagation distance in the oceanic crustal layer increases. The size of the decrease in amplitude is controlled by the amplitude of wavefronts propagating through the oceanic crustal layer with pre-critical angles of incidence. At each successive reflection of such a wavefront from the crust mantle interface in the oceanic structure, the same fraction of a remaining total amplitude is transmitted across the boundary. Thus, the total amplitude of this component decays most rapidly in the first kilometers of transmission through the oceanic structure while the incident wave still has higher amplitudes. As the wavefield travels through the reverse transition region the surface amplitude reduces rapidly as the concentrations of amplitude previously trapped in the oceanic crustal layer travel up the ocean crust boundary while spreading themselves throughout the depth extent of the crustal layer. The maxima in these regions remain at the surface. At the end of the transition region the amplitude reduces rapidly with depth down to the crust mantle interface. The amplitude incident upon the mantle crust boundary from the oceanic half-space is transmitted across it with a resulting distortion in the wavefield. The form of this distortion is the superposition of a slope, $\text{Slope} = \tan^{-1}\left[\frac{l\,(v_M - v_c)}{v_M}\right]$, onto the disturbance incident at the mantle crust boundary after it has passed into the continental crustal layer.

Now, the properties of the calculated amplitudes in a forward transition model which depend on the length of the forward transition model will be summarized. First, RMS amplitudes recorded at nodes along the surfaces of the crustal layers show

that amplitude in the transition region increases as the crustal layer thins. The size of the increase is largest for the longest transitions. This is explained by considering that the incident angles at the boundaries in the transitions decrease as the transition region thins, thus, increasing the density of rays and the amplitudes at the transition boundaries. As the crustal layer thins, a similar increase in amplitude at the crust mantle might be expected. However, the amount of amplitude concentrated at the boundary decreases as the angle ϕ_{CM} or ϕ_{CO} increases. The steeper angle of the crust mantle boundary should cause a much smaller concentration at the crust half-space boundary than that seen at the crust ocean boundary. In addition amplitude propagates across the crust mantle boundary and thus any energy concentration at that boundary immediately travels across it. The amount of energy transmitted across the crust mantle boundary increases as its length increases. The increase in transmission across the crust mantle boundary as the length of the transition region increases is explained by the increased number of reflections within a longer transition region. Since amplitude from each ray enters the mantle half-space at each reflection, more reflections produce more transmitted amplitude. The wavefield created by the transmitted energy propagates through the grid towards its base more rapidly as the phase velocity decreases. As discussed earlier, the wavefield also propagates downward more rapidly as the length of the transition region increases. The angle of incidence of the transmitted ray with the horizontal is, $i_h = j_n' + \phi_{CM}$. Clearly, for a longer transition with a smaller ϕ_{CM} the rays are more nearly normally incident at the grid bottom. Thus, for a gentle transition the path length in the oceanic structure that will allow the transmitted energy to escape the system and not reenter the reverse transition is shorter than for a steeper transition region.

Chapter 3

Finite Element to Modal Propagator Matrix Coupling: Tests of Accuracy and Applications to the Transmission of Lg along Partially Oceanic Paths

Introduction

In this chapter the effects of the length of the intermediate path between the continent ocean and ocean continent transition regions is investigated. First the results of two FE calculations with different intermediate path lengths are presented and compared. These examples are contrasted with the path length used in the previous chapter. Then the RT integration method is discussed and explained. First analytic expressions for the stress components of double couple and line sources are derived, then the expressions for displacement and stress line source Green's functions are determined. These expressions are used to illustrate the validity and determine the accuracy of the RT coupling method. The RT coupling method can be used to continue the propagation of FE results through a layered structure using the displacement and stress Green's functions for the remaining path length and the displacement and stress time histories recorded at a column of element centers within the FE grid.

FE Results: Effect of oceanic path length on the attenuation of Lg

Results of two FE calculations including both forward and reverse transition regions and an intermediate region of oceanic structure are presented here. Many of the details of transmission of wavefield through a forward transition region or a reverse transition region have previously been discussed and will not be repeated here. The vertical extent of the grid and thus that of each time slice illustrated for these calculations is larger than that for the results discussed in the previous chapter. This increase in vertical extent makes the disturbances moving down through the

underlying half-space easier to see. The change in the angle at which these disturbances travel down toward the base of the grid as the width of the triangular regions of maxima widen later in the wavefield is also more clearly visible in these examples.

In Figures 1 to 4 time slices recorded during a calculation using a grid which included fifty kilometer long forward and reverse transition regions separated by an intermediate path, whose length is thirty two kilometers, of oceanic structure. In Figures 5 to 7 the results of a calculation using a grid containing the same fifty kilometer forward and reverse transition regions separated by an intermediate path of seventy nine kilometers are illustrated. Figure 8 shows the RMS amplitude as a function of distance along the surface of each of these models. The upper plot shows the amplitudes for the thirty two kilometer oceanic path and the lower plot shows the amplitudes for the seventy nine kilometer long oceanic path. The amplitude, or vertical scale on each of these plots is identical, however, the horizontal scale, measuring distance along the surface of the crustal layer, is not uniform. The vertical bars on the plots indicate the ends of the regions of oceanic structure. The horizontal scales are uniform between these bars and uniform but different outside these bars. Between these bars the horizontal distance scale is defined so that the total length of the oceanic path in the illustrated model scales exactly to the distance between the bars. The scale outside the area defined by these bars is such that the distance between each point in the regions of equally spaced points is ten nodes.

Examining the time slices for the two examples with different oceanic path lengths shows that the major difference between them appears to be the amount of energy which is escaping out through the bottom of the grid. In the case of the shorter path length only the disturbances traveling through the half-space with the steepest angles are able to pass out of the system. All other disturbances are largely or completely transmitted back into the continental crustal layer since they have not

propagated downwards far enough to avoid being incident of the mantle crust boundary in the reverse transition. This observation provides an explanation of why there is a critical length of intermediate oceanic path beyond which the Lg wave does not travel. As the path length in the oceanic region increases, disturbances traveling through the crust mantle boundary in the forward transition region at progressively shallower angles are able to propagate downwards beyond the base of the continental crustal layer and escape into the mantle. This means that less energy is available to be transmitted back through the mantle crust boundary of the reverse transition and reconverted to Lg wave energy. This trend is seen, although less clearly, in the forward and reverse time slices in chapter 2. The intermediate oceanic path length for that example is one hundred sixty nine kilometers. Disturbances that are seen to propagate out of the grid in that long path example can be traced, even in the example with the longer path length presented here, across the oceanic path length back into the crust through the reverse transition region. This implies that as the path length increases more and more converted energy is able to leave the system.

There is another contribution of the oceanic path length to the attenuation of Lg passing through an oceanic structure. The energy that is transmitted into the oceanic crustal layer is not all in the form of modes compatible with trapped modes in the oceanic crust. Therefore, as the wavefront propagates through the oceanic structure further energy leaks from the crustal layer and propagates downward to eventually escape from the system.

Calculation of Stress Components

To test the RT algorithm for coupling FE results to propagator calculations it is first necessary to determine expressions for the stress seismograms and the stress and displacement Green's functions used in the convolution integral. These expressions are developed and demonstrated in this section. The use of these expressions in the RT

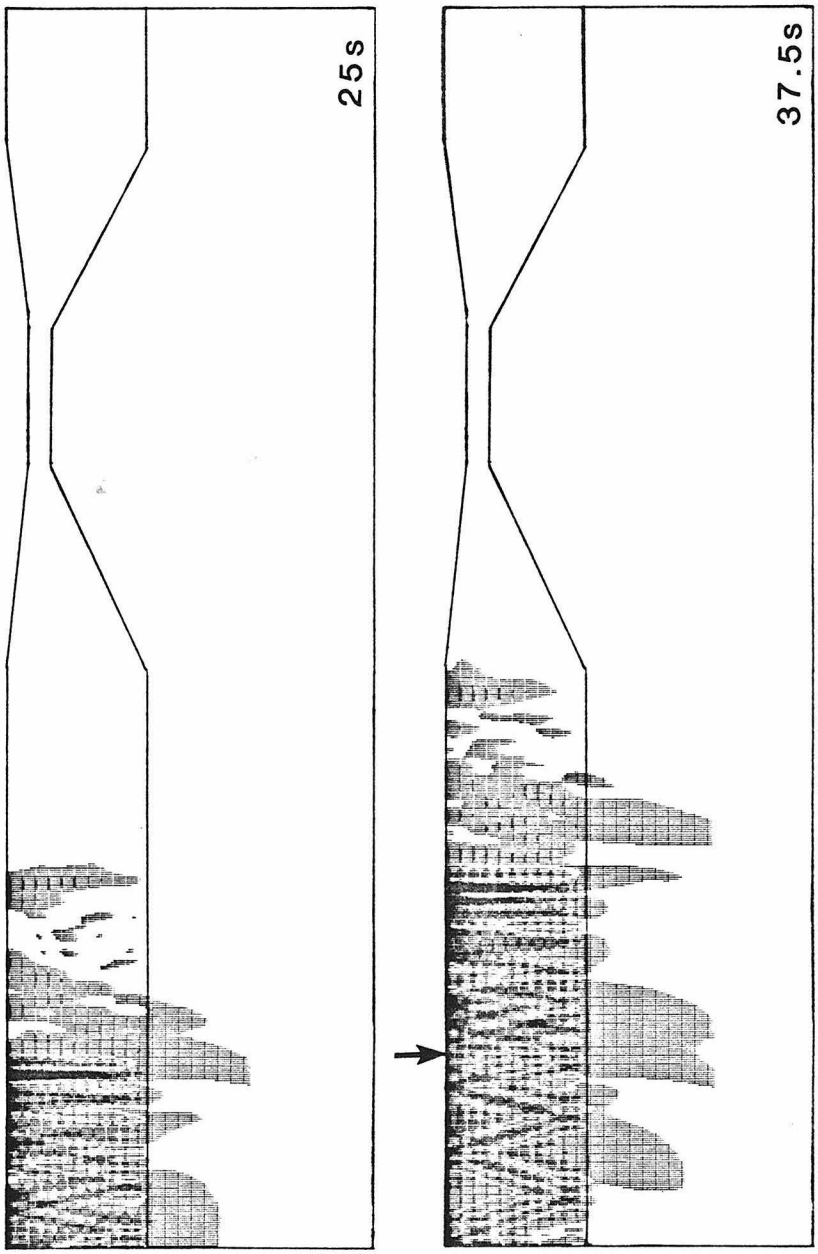

Figure 1: Time slices recorded during the calculation using an intermediate oceanic path length of 32 kilometers. The crustal layer and the ends and bottom of the FE grid which contain it and the underlying half-space are outlined. Within the outlines the displacements at each grid point at the indicated instant of time are plotted. A larger displacement produces a correspondingly larger point on the plot. Thus, high displacement areas appear darker. Each time slice is scaled so its maximum amplitude appears identical on the plot. The time since the initiation of the FE calculation is shown below the right end of each grid. The arrow above a time slice shows the location to which the disturbances, moving at 3.5 km/s, seen at the left end of the previous time slice, have moved in the intervening time.

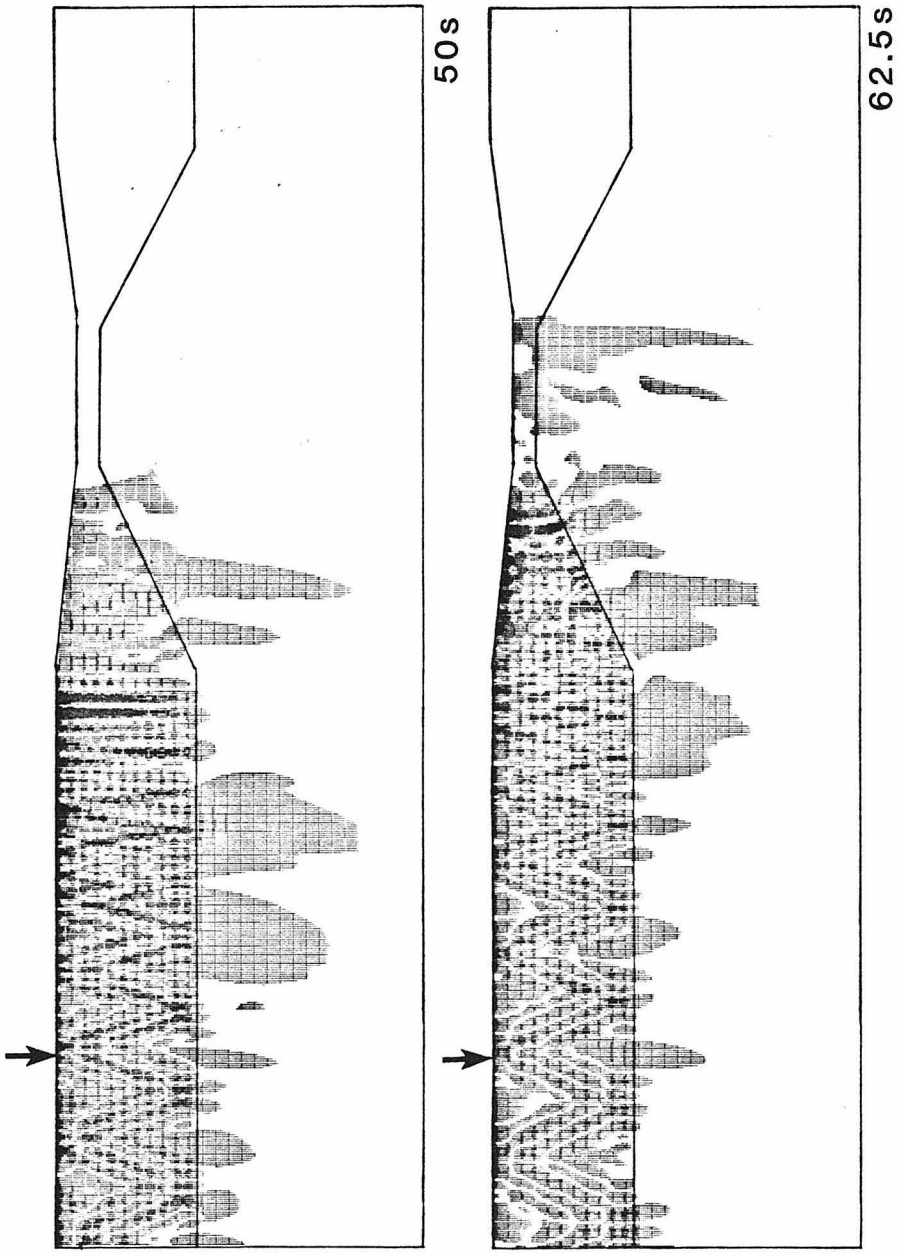

Figure 2: Time slices recorded during the calculation using an intermediate oceanic path length of 32 kilometers. Time slices for two later times illustrating the further propagation of the wavefield through the model. Details are the same as for Figure 1.

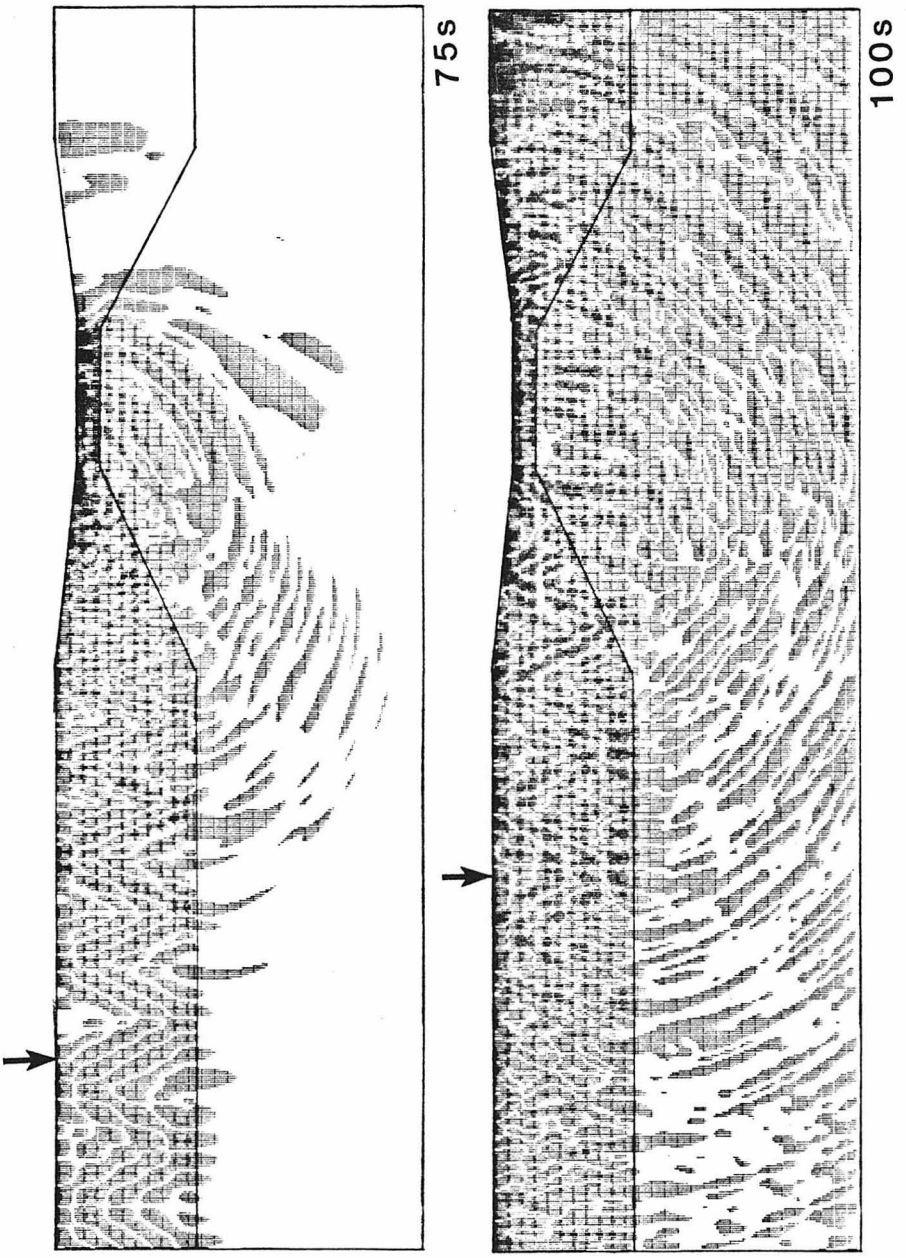

Figure 3: Time slices recorded during the calculation using an intermediate oceanic path length of 32 kilometers. Time slices for two later times illustrating the further propagation of the wavefield through the model. Details are the same as for Figure 1.

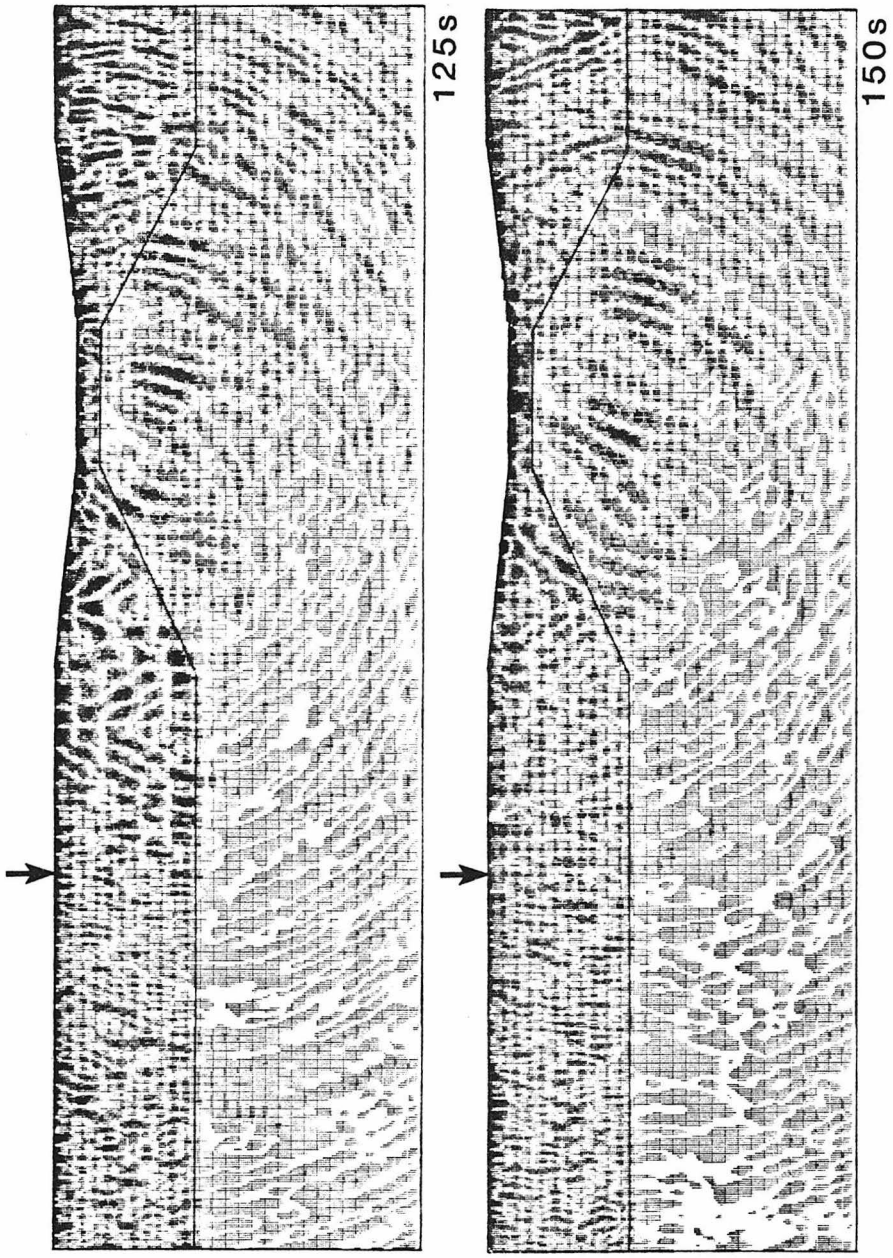

Figure 4: Time slices recorded during the calculation using an intermediate oceanic path length of 32 kilometers. Time slices for two later times illustrating the further propagation of the wavefield through the model. Details are the same as for Figure 1.

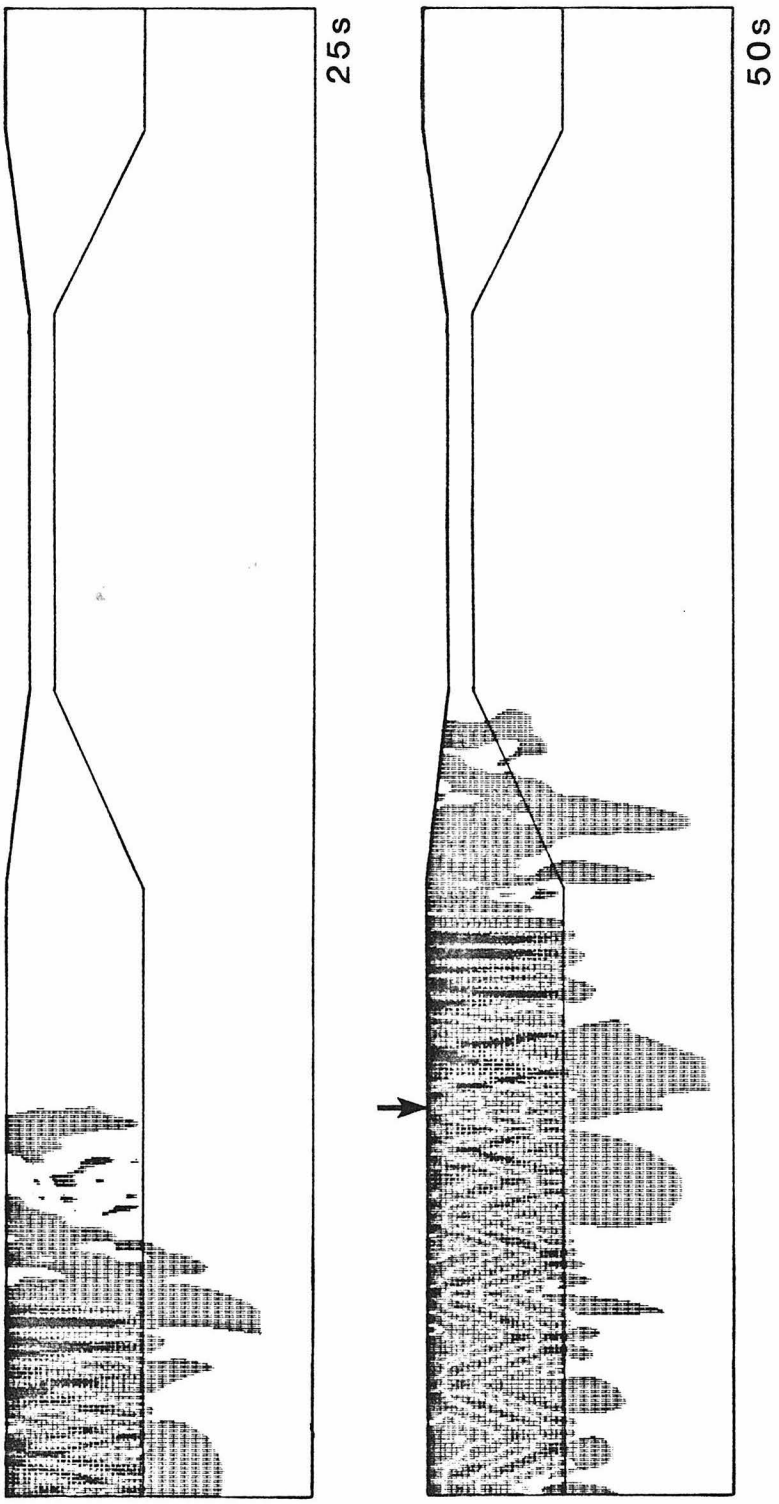

Figure 5: Time slices recorded during the calculation using an intermediate oceanic path length of 79 kilometers. Details are the same as for Figure 1.

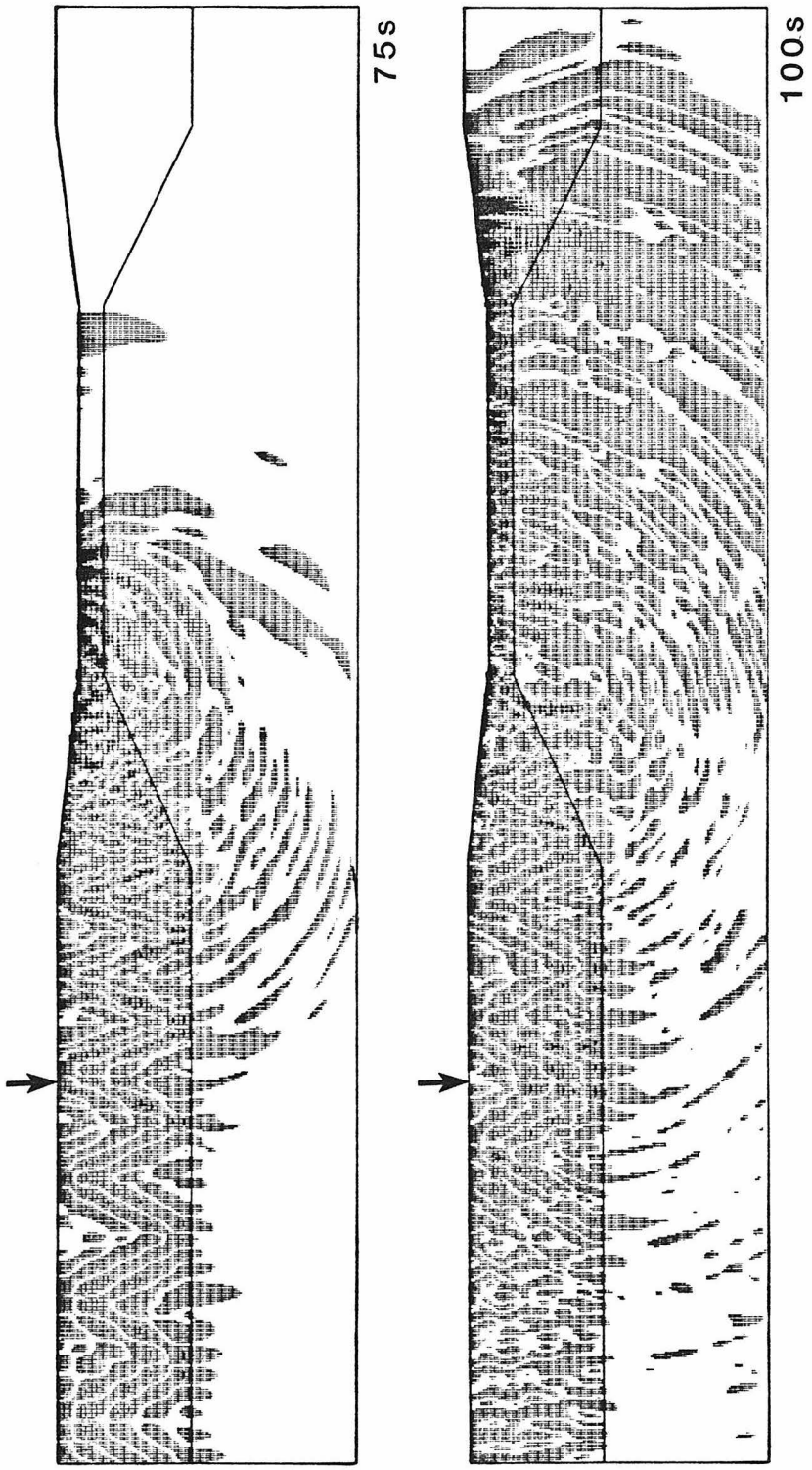

Figure 6: Time slices recorded during the calculation using an intermediate oceanic path length of 79 kilometers. Time slices for two later times illustrating the further propagation of the wavefield through the model. Details are the same as for Figure 1.

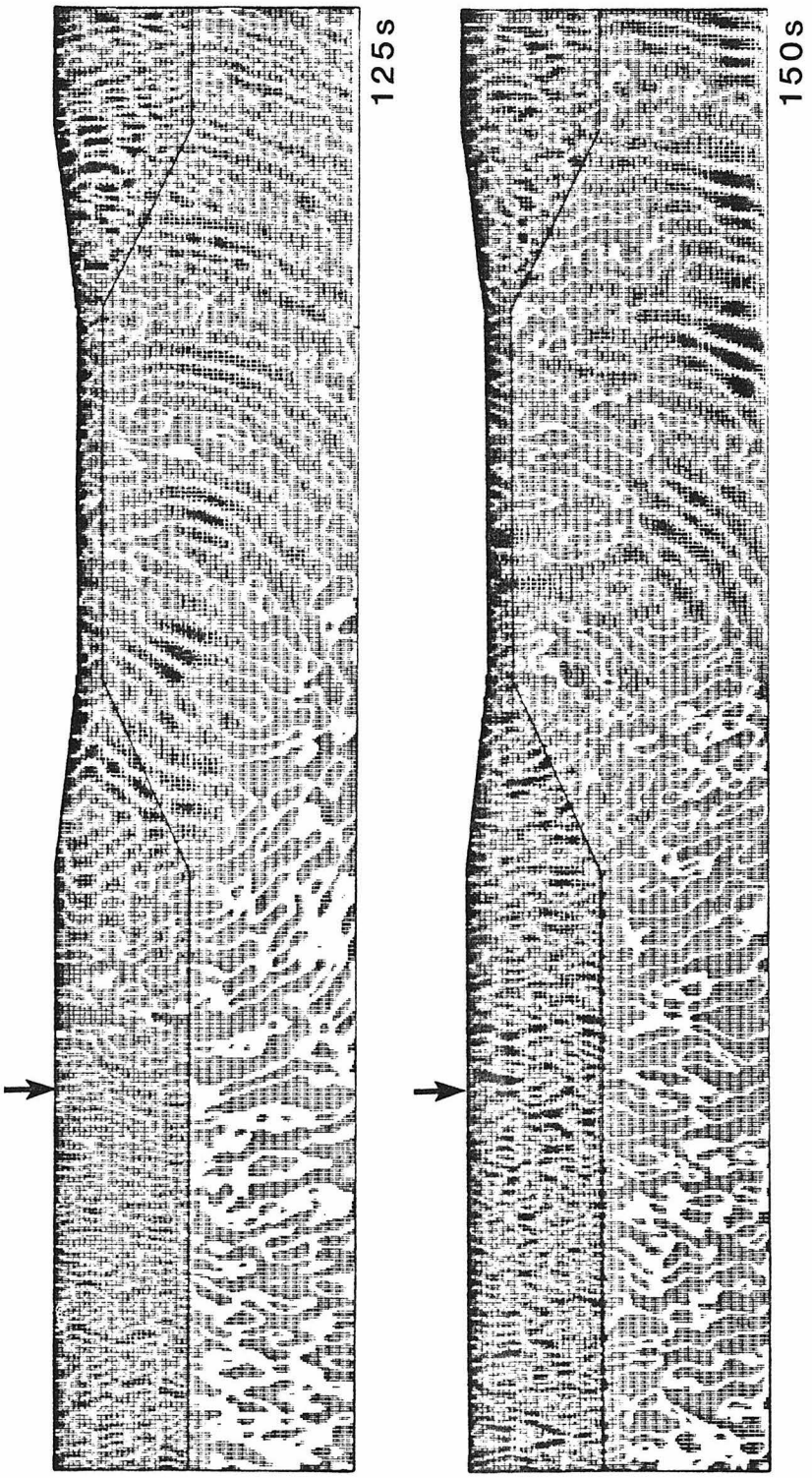

Figure 7: Time slices recorded during the calculation using an intermediate oceanic path length of 79 kilometers. Time slices for two later times illustrating the further propagation of the wavefield through the model. Details are the same as for Figure 1.

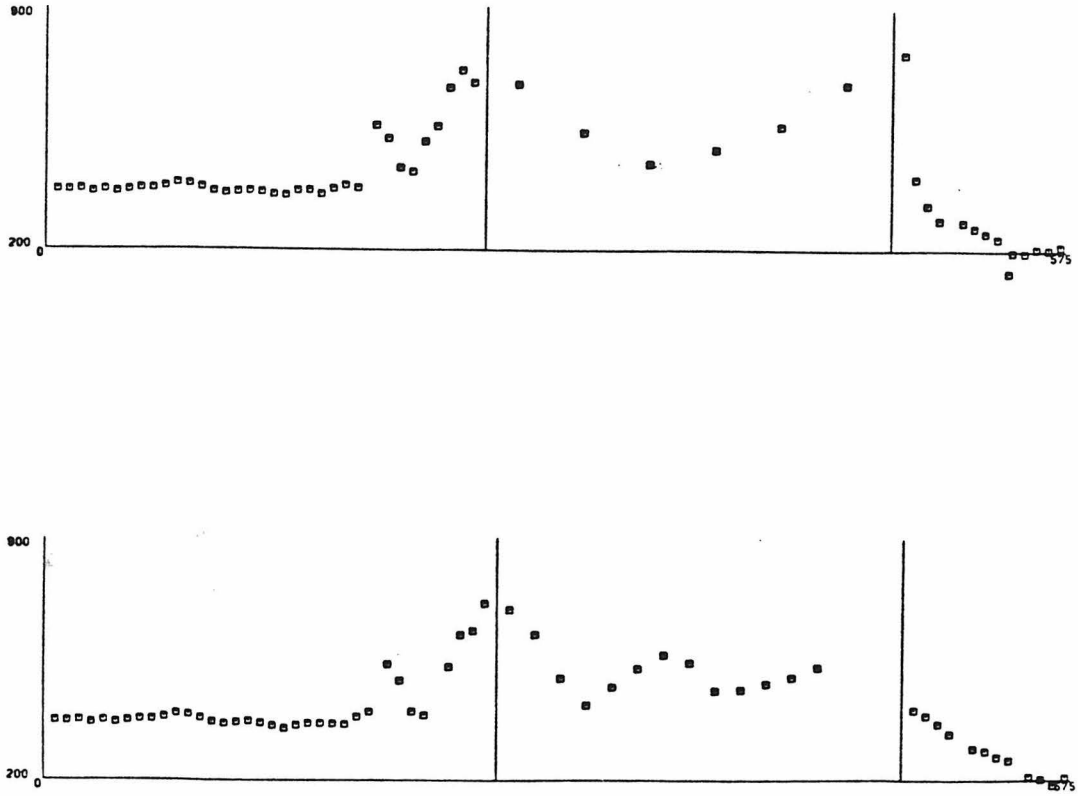

Figure 8:RMS surface amplitudes for the two FE models including both forward and reverse transitions. The upper plot shows the RMS surface amplitude for the model with an intermediate oceanic path of 31 km length. The lower plot shows the corresponding amplitude for the model with an intermediate oceanic path of 69 km length. The horizontal scale between the two vertical bars is different for each plot. This region represents the oceanic path. The scale between the vertical bars is chosen so that the shorter oceanic path plots with the same length as the longer one.

integral will be discussed in the next section. The determination of displacement and stress Green's functions is necessary in all applications of the RT integration method regardless of whether the forcing functions are FE results, analytic stress and displacement seismograms, or stresses and displacements from other sources. However, the stress seismograms are used in the following discussions only as an example of a well defined form of forcing functions. Using stress and displacement seismograms as forcing functions produces RT integration results which may be directly compared to purely analytic synthetics allowing one to verify the accuracy of the RT integration. For the SH problem in Cartesian coordinates the stresses that need to be considered are σ_{xy} and σ_{zy}. For the geometry used to couple surface waves from a FE grid into a layered medium through which the waves will be transmitted by convolution with propagator matrix generated Green's functions, only the stress σ_{xy} is used. However, σ_{zy} will also be derived for completeness. Should the geometry change so that it would be necessary to integrate over a horizontal surface such as the bottom of the grid then σ_{zy} would also be used.

The stresses, σ_{xy} and σ_{zy}, can be expressed in terms of spatial derivatives of displacements. One method of calculating values for these stresses is to express the derivative as a difference and evaluate the difference equation numerically. The expressions used to evaluate the stresses in the FE method are one such set of difference equations. They are

$$\sigma_{xy} = \mu \frac{\partial u_y}{\partial x} = \mu \frac{u_y(1)-u_y(2)-u_y(3)+u_y(4)}{4\Delta x} \tag{1a}$$

$$\sigma_{zy} = \mu \frac{\partial u_y}{\partial z} = \mu \frac{-u_y(1)-u_y(2)+u_y(3)+u_y(4)}{4\Delta z} \tag{1b}$$

In these expressions 1, 2, 3, 4, denote the positions of the nodes at the corners of the 2-D element (Figure 2, chapter 1) for which the element center stresses are σ_{xy} and

σ_{zy}. The displacement perpendicular to the FE grid is u_y, and the horizontal and vertical spacings of the nodes in the grid are Δx, and Δz respectively. Evaluating these relations gives a reasonable approximation to the desired stress values. A second, and more direct, method for determining the values of the stresses is to evaluate the analytic expression for each stress derived from the analytic displacement expressions. The derivations of analytic stress expressions are outlined below. Expressions for the stresses are determined for several different cases. First, dip slip and strike slip double couple sources are considered, then, a line source in a horizontally layered medium. Finally, the expressions for the line source Green's functions are derived.

The choice of evaluation of analytic expressions over the numerical calculation of derivatives is based on speed and accuracy. Evaluation of the analytic expressions for a stress component requires the same amount of calculation as the evaluation of a displacement. For a given depth section of n elements n element center stress components and n element center displacements need to be determined to evaluate the RT integral which propagates the wavefield from the RT surface through a layered structure to the receiver. Thus, if the calculation of each stress or displacement takes time t, the computation of the necessary displacement and stress components by evaluating the analytic expressions would take time 2nt. When the stress component is determined using numerical differentiation, time (2n+2)t is required to evaluate the displacements used in the difference equations, time nt is required to evaluate the element center displacements, and additional time is required to process the numerical difference equations. Clearly direct evaluation is faster. The calculation of numerical derivatives is known to be a potentially unstable numerical procedure since subtraction of almost equal numbers is possible. Thus, direct evaluation will be more reliable in cases where the numerical derivative becomes unstable. The analytic evaluation is also more accurate since it is equivalent to a numerical derivative with infinitesimal

spacing between the corners of the element. The accuracy of the numerical derivative increases as that spacing decreases. In practice, however, for the types of disturbances considered in this study, the increase in accuracy is small and both estimates are equally acceptable.

A numerical procedure is implemented to evaluate the analytic expressions for the stress components. The validity of the procedure is illustrated by comparing analytic stress time histories, determined by evaluation of equation (4) and (6) below, with corresponding results generated using the difference equations (1). The results of these comparisons are discussed after the analytic stress relations are developed.

The analytic expressions for the stress components for SH waves from a point double couple source are directly obtainable from the expressions used to determine the corresponding displacement seismograms. These expressions,

$$\left\{\overline{v}(x,z)\right\} = -\frac{M_0}{2\omega}\,\underline{A}_L\,\frac{\partial H_2^{(2)}(k_L r)}{\partial r}\left[\frac{v_S(h)}{v_0}\right]_H\left[\frac{v_R(z)}{v_0}\right]_H \tag{2a}$$

$$\left\{\overline{v}(x,z)\right\} = -\frac{M_0}{2\omega}\,\underline{A}_L\,\frac{1}{\mu_S}\,\frac{\partial H_1^{(2)}(k_L r)}{\partial r}\left[\frac{\tau^*(h)}{\dot{v}_0 / c_L}\right]_H\left[\frac{v_R(z)}{v_0}\right]_H \tag{2b}$$

where the variables are as defined in chapter 1, lead to expressions for the stress σ_{zy} when their derivatives with respect to z are calculated. Only the final term in each equation depends directly on z. From Harkrider (1964)

$$\frac{\partial}{\partial z}\left[\frac{v_R(z)}{v_0}\right]_H = -\frac{k_L}{\mu_R}\left[\frac{\tau^*(z)}{\dot{v}_0 / c_L}\right]_H \tag{3}$$

Substituting $\left\{\overline{v}(z)\right\}$ from (2) for u_y in (1) and replacing the derivative of $\left[\frac{v_S(h)}{v_0}\right]_H$ by (3) gives

$$\left\{\sigma_{zy}(x,z)\right\} = -k_L\frac{M_0}{2\omega}\,\underline{A}_L\,\frac{\partial H_2^{(2)}(k_L r)}{\partial r}\left[\frac{v_S(h)}{v_0}\right]_H\left[\frac{\tau^*(z)}{\dot{v}_0 / c_L}\right]_H \tag{4a}$$

$$\left\{\sigma_{zy}(x,z)\right\} = -k_L \frac{M_0}{2\omega} \underline{A}_L \frac{1}{\mu_S} \frac{\partial H_1^{(2)}(k_L r)}{\partial r} \left[\frac{\tau^*(h)}{\dot{v}_0 / c_L}\right]_H \left[\frac{\tau^*(z)}{\dot{v}_0 / c_L}\right]_H \tag{4b}$$

Expressions (2) also yield the expressions for stress σ_{xy} when their derivatives with respect to x are calculated. All terms except the Hankel function are constant with respect to x. By expanding the Hankel function term in an asymptotic series for large r, and ignoring terms of order $\frac{1}{r}$, it can be shown that

$$\frac{\partial}{\partial x}\left\{\frac{\partial H_2^{(2)}(k_L r)}{\partial r}\right\} \approx -ik_L \frac{\partial H_2^{(2)}(k_L r)}{\partial r} \tag{5}$$

Then combining (1), (2), and (5) gives

$$\left\{\sigma_{xy}(x,z)\right\} = ik_L \mu_R \frac{M_0}{2\omega} \underline{A}_L \frac{\partial H_2^{(2)}(k_L r)}{\partial r} \left[\frac{v_S(h)}{v_0}\right]_H \left[\frac{v_R(z)}{v_0}\right]_H \tag{6a}$$

$$\left\{\sigma_{xy}(x,z)\right\} = ik_L \frac{\mu_R}{\mu_S} \frac{M_0}{2\omega} \underline{A}_L \frac{\partial H_1^{(2)}(k_L r)}{\partial r} \left[\frac{\tau^*(h)}{\dot{v}_0 / c_L}\right]_H \left[\frac{v_R(z)}{v_0}\right]_H \tag{6b}$$

Equations (2) are the analytic expressions for displacement for the dip slip and strike slip faults, the corresponding expressions for the stresses are shown in (4) and (6).

The analytic expressions for a line source in a layered medium are derived by a procedure similar to that used in the previous section to obtain the stress expressions for the point double couple source. The same sequence of calculations is applied to the expression for the displacement produced by a 2-D line source as was applied to the expressions for the strike slip and dip slip displacements. These calculations yield the analytic 2-D line source stress equations. The displacement at depth z due to a line source at depth h is

$$\left\{\overline{u}_y(x,z)\right\} = 2\pi i \underline{A}_L \frac{\mu_S}{k_L} \left[\frac{v_S(h)}{v_0}\right]_H \left[\frac{v_R(z)}{v_0}\right]_H e^{-ik_L x} \tag{7}$$

In this case all terms in (7) except $\left[\frac{v_R(z)}{v_0}\right]_H$ are independent of z. Thus, the stress σ_{zy} has the same form as the displacement expression with $\left[\frac{v_R(z)}{v_0}\right]_H$ replaced by its derivative with respect to z, that is by the right hand expression of (3). Similarly, the stress σ_{xy} has the same form as the displacement with the exponential in x replaced by its derivative. Therefore, the stresses for the 2-D line source are

$$\left\{\sigma_{zy}(x,z)\right\} = -2\pi i \mu_S \underline{A}_L \left[\frac{v_S(h)}{v_0}\right]_H \left[\frac{\tau^*(z)}{\dot{v}_0 / c_L}\right]_H e^{-ik_L x} \tag{8a}$$

$$\left\{\sigma_{xy}(x,z)\right\} = 2\pi \mu_S \mu_R \underline{A}_L \left[\frac{v_S(h)}{v_0}\right]_H \left[\frac{v_R(z)}{v_0}\right]_H e^{-ik_L x} \tag{8b}$$

Next it is simple to extend the treatment used in the previous paragraph to the expression for the displacement Green's function for a line source in a layered half space. It has been previously shown that this Green's function is

$$\left\{\Gamma_{22}(x,z;\xi_1,h)\right\} = -\frac{i}{k_L} \underline{A}_L \left[\frac{v_S(h)}{v_0}\right]_H \left[\frac{v_R(z)}{v_0}\right]_H e^{-ik_L(x-\xi_1)} \tag{9}$$

In this case a stress source term rather than a stress receiver term is needed. Thus, the z derivative is taken with respect to the source term. All terms in (9) except $\left[\frac{v_S(h)}{v_0}\right]_H$ are independent of z, so the σ_{zy} term has the same form as the displacement equation with $\left[\frac{v_S(h)}{v_0}\right]_H$ replaced by its derivative with respect to z. The form of this derivative is identical to that in (3) except that the R subscript is replaced by an S subscript denoting the properties at the source at the RT surface rather than at the receiver. Similarly the stress σ_{xy} has the same form as the displacement equation with the exponential term replaced by its derivative with respect to x. Therefore the derivatives of the Green's function are

$$\left\{\Gamma_{22,3}(x,z;\xi_1,h)\right\} = \frac{i}{\mu_S}\underline{A}_L \left[\frac{\tau^*(h)}{\dot{v}_0 \,/\, c_L}\right]_H \left[\frac{v_R(z)}{v_0}\right]_H e^{-ik_L(x-\xi_1)} \tag{10a}$$

$$\left\{\Gamma_{22,1}(x,z;\xi_1,h)\right\} = -\underline{A}_L \left[\frac{v_S(h)}{v_0}\right]_H \left[\frac{v_R(z)}{v_0}\right]_H e^{-ik_L(x-\xi_1)} \tag{10b}$$

Now it is necessary to illustrate that expressions (4), (6), and (8), for the stress components give the correct results. The tests illustrated in Figures 9, 10, and 11 are analogous. In each case the upper trace in each pair is the displacement or stress as calculated using one of the sets of analytic expressions given above. The lower trace in each pair is the same displacement component, generated by averaging the surrounding four nodes, or the same stress component calculated using the difference equations (1) with $\Delta x = \Delta z = .5$km. The node spacings are chosen to correspond to those used in the FE calculations. The top pairs of traces are the V=u_y displacements at the surface. The second pairs of traces are the stress σ_{xy} at 0.25 km depth, and the third pairs of traces are σ_{zy} at 0.25 km depth. The ratio of the analytic peak to peak amplitude to the numerical peak to peak amplitude is given for each pair of traces by the upper number beside that pair. The same type of ratio, analytic to numerical, is calculated using the RMS amplitudes of the seismograms and is shown as the lower number beside each pair. The quality of the waveform correspondence and the amplitude ratios remain essentially constant as one moves down the depth section. Figure 9 shows the results for the case of the 2-D line source, equation (8). The pairs of displacement and stress time histories show excellent correspondence when their waveforms are compared. Numerical derivatives for σ_{xy} agree with the corresponding analytic derivatives to within $\approx$ 4% for peak to peak amplitude and to within $\approx$1% for RMS amplitude. The peak to peak differences between the two methods are about 2% for the average displacement $\overline{V}$ and the stress σ_{zy}. As expected, for all three cases, the correspondence improves as Δx and Δy are reduced. Figure 10 shows the results

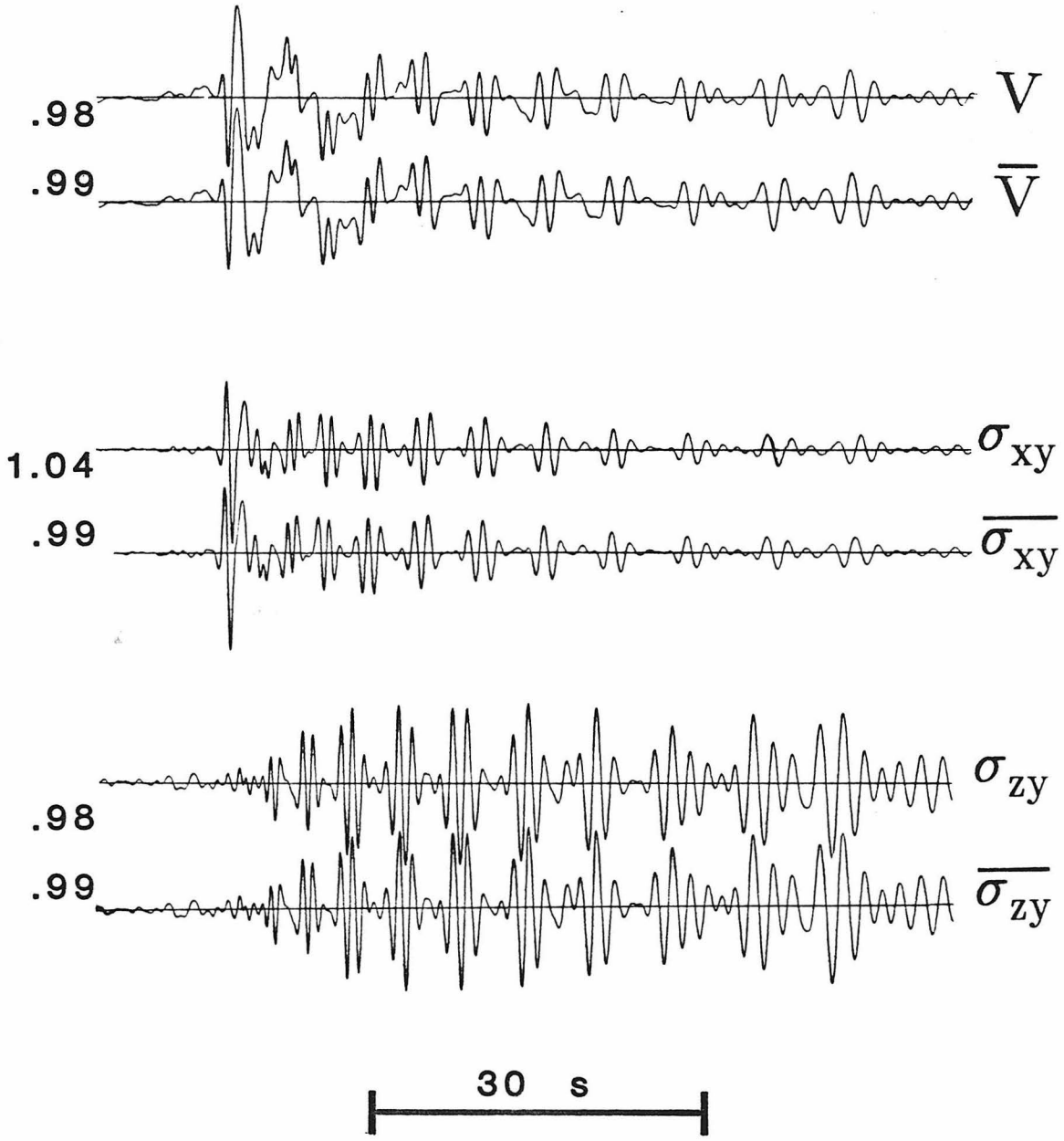

Figure 9: Comparison of element center displacement and stress time histories calculated for a 2-D line source using two methods. Upper traces in each pair are evaluations of the analytic expressions at the element centers. Lower traces are determined by using displacements calculated at the nodes surrounding the element center to evaluate the difference equations. For all traces Δ=1500 km, and source depth is 8 km. The fundamental and first five higher modes are included in the synthetics. The upper number to the left of each trace is the peak to peak amplitude ratio of the numerical to analytic calculations, the lower number is the corresponding RMS amplitude ratio.

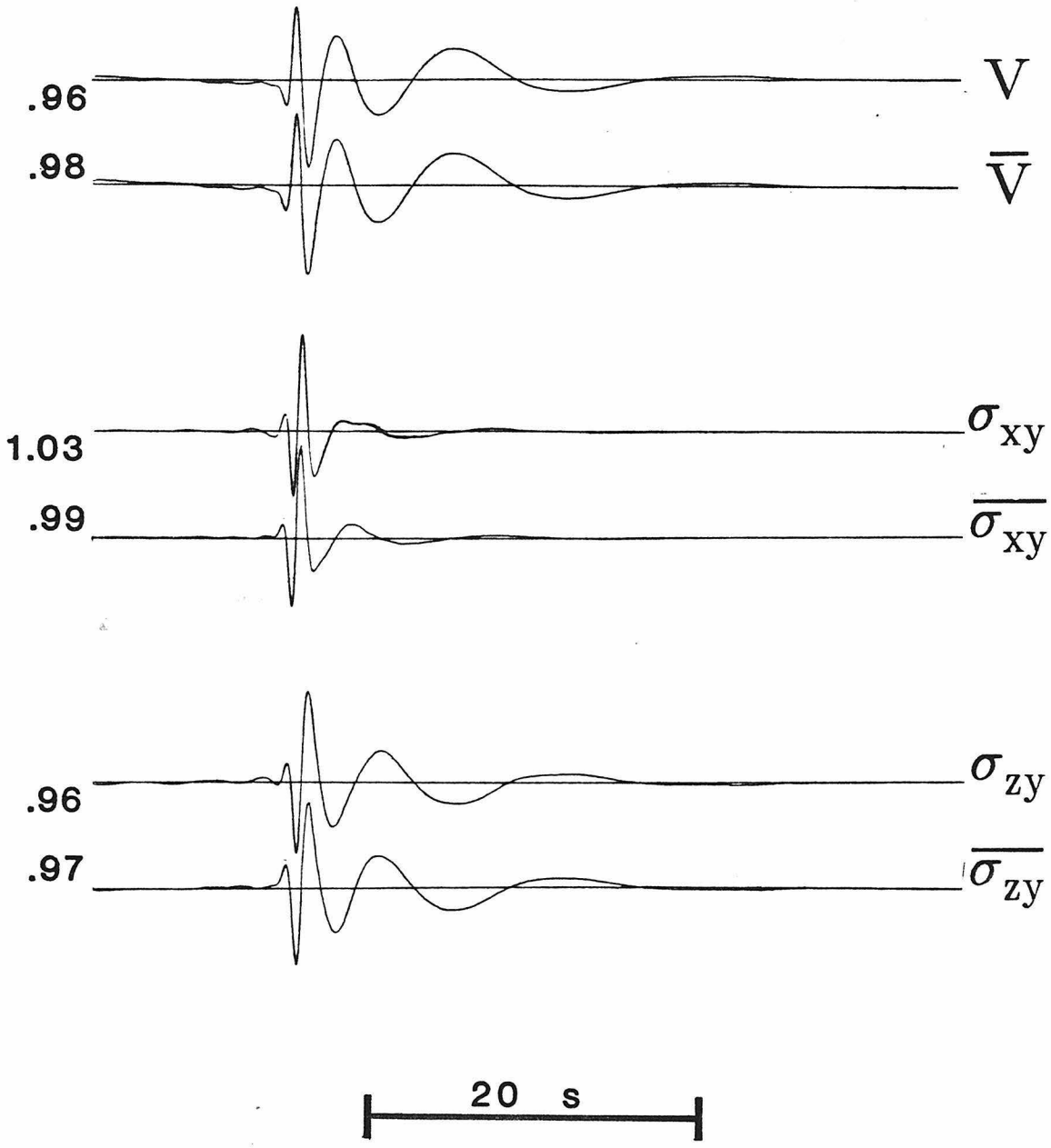

Figure 10: Comparison of element center displacement and stress time histories calculate for a strike slip type double couple source using two methods. Only the fundamental mode is illustrated. Other details are the same as for figure 9.

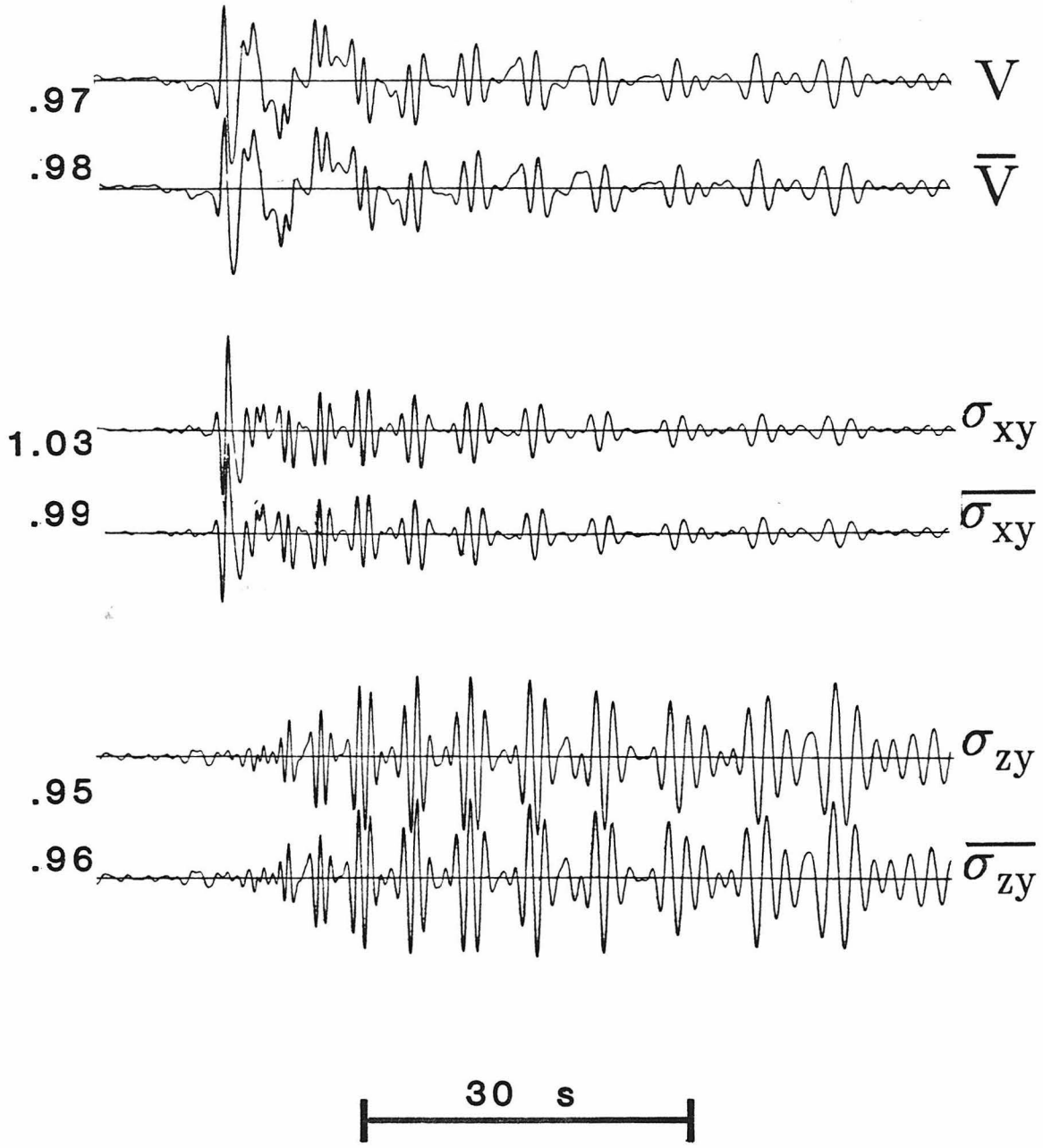

Figure 11: Comparison of element center displacement and stress time histories calculated for a strike slip type double couple source using two methods. Details are the same as for Figure 9.

for the case of a strike slip source, equations (4) and (6), using the fundamental mode only. Again, the waveform correspondence within each pair is excellent. The peak to peak amplitude ratios are close to one, showing less than 4% difference. Since the major variation between the two methods is the resolution of the magnitude of the high frequency peak near the onset of the trace the RMS amplitudes show a smaller variation of 2.5% or less. Figure 11 shows the results for the strike slip source, for a mode sum including the fundmental mode and the first five higher modes. The waveforms do not match as precisely as in the case of the fundamental mode alone, but the correspondence is still excellent. The amplitude ratios do not significantly change when the higher mode energy is added. Again, both for the fundamental mode alone and for the mode sum, correspondence between the analytic and numerical methods of evaluation improves rapidly as Δx and Δz are reduced. These tests not only indicate the validity of the analytic expressions above, they also give an estimate of the uncertainties present in the numerical differentiation used in the FE calculations.

RT Coupling of Analytic 2-D Seismograms and Green's Functions

In this section the validity and accuracy of the numerical implementation of the Representation Theorem coupling technique, used in the following section to pass FE results into a layered media, will be discussed in detail. The tests discussed below are designed to give RT integration results directly comparable with purely analytic results. First mode by mode results are presented to illustrated where the discrepancies between the RT results and the analytic results originate. Mode sum results are then presented. The form of the RT integral and its relation to the propagator matrix formulation is discussed and a method for mode by mode filtering of mode sum forcing function input is explained. The type of formulation used to explain the filtering method is also applied to derive more quantitative mode by mode analysis of the

origins of discrepancies between RT integration results and purely analytic solutions. These quantitative estimates of the sources of discrepancies explain the differences seen between the RT integration results and the purely analytic results quite well.

All the results discussed in this section are derived using a simple geometry. In all cases the model is a layer over a half-space. The layer has a thickness of thirty two kilometers, a SH wave velocity 3.5 km/s, and a density 2.7 g/cm^3. The half-space has SH wave velocity 4.5 km/s and density 3.4 g/cm^3. The same layer over a half space model is used for the entire path, making calculation of purely analytic synthetic for the entire path length of $\Delta = 1600$ km, or $\Delta = 1750$ km simple. Purely analytic synthetic seismograms were calculated at these distances for the mode sum and separately for each of the fundamental mode and the first five higher modes. The forcing functions used are the displacement and stress seismograms for a line source at at depth of ten kilometers and a distance of $\Delta = 1500$ km from the source. The forcing functions are evaluated at positions corresponding to the element centers of the rightmost column of elements in a FE grid with horizontal and vertical spacing of .5 km, whose right hand edge lies $\Delta = 1500.25$ km from the source. Thus, the seismograms are evaluated at points along a vertical surface, at depth intervals of 0.5 km, beginning at a depth of 0.25 km below the surface. All forcing functions are evaluated at a distance of $\Delta = 1500$ km. Separate sets of forcing functions were generated for each mode. A set of forcing functions which is a sum over the fundamental and the first five higher modes was also calculated. The displacement seismograms calculated using the RT integral are for distances of $\Delta = 1600$ km, or$\Delta = 1750$ km. Performing RT integrations to determine hybrid solutions at these distances requires Green's functions for propagation distances $\Delta = 100$, or $\Delta = 250$ km. At each of these distances a set of stress and displacement Green's functions was determined for each mode and an additional set was determined for a mode sum including the fundamental and the

first five higher modes. The Green's functions in each set were evaluated for a source at each of the locations where displacement and stress forcing functions were determined and a receiver at the surface. The RT integration surface for these examples extended to a depth of 37.5 km and included seventy five integration points. In the following discussions the seismogram resulting from a RT integration may be referred to as a hybrid seismogram, even though, for these tests of accuracy, the same method is being used to generate Green's functions and forcing functions.

The first group of tests using the sets of forcing functions and Green's functions discussed above produced mode by mode RT integration results to compare to the purely analytic synthetic single mode seismograms. The set of single mode forcing functions for each of the individual modes, was convolved with the single mode set of Green's functions for the same mode according to the RT integration relation. This produced a hybrid seismogram for that mode to compare to the corresponding purely analytic synthetic. Comparisons of the RT integration sums and the purely analytic synthetics for each individual mode are shown in Figures 11 and 12. In Figure 11 comparisons for the fundamental mode, the first higher mode, and the second higher mode are presented. Each of these pairs is illustrated at a distance of $\Delta = 1600$ km from the source. Figure 12 is a continuation of Figure 11 showing the results for the third through fifth higher modes. The upper two pairs of traces are also illustrated for a distance $\Delta = 1600$ km . The lowermost pair of traces, those for the fifth higher mode, are illustrated at a distance of $\Delta = 1750$ km from the source. The fifth higher mode results at 1500 km are equally well fit, but presenting an example for another distance helps verify the observation that the goodness of fit between the hybrid seismograms and the analytic synthetics does not depend significantly on distance propagated using the RT integration over stress and displacement seismograms and Green's functions. In each of these figures there are three pairs of seismograms. The

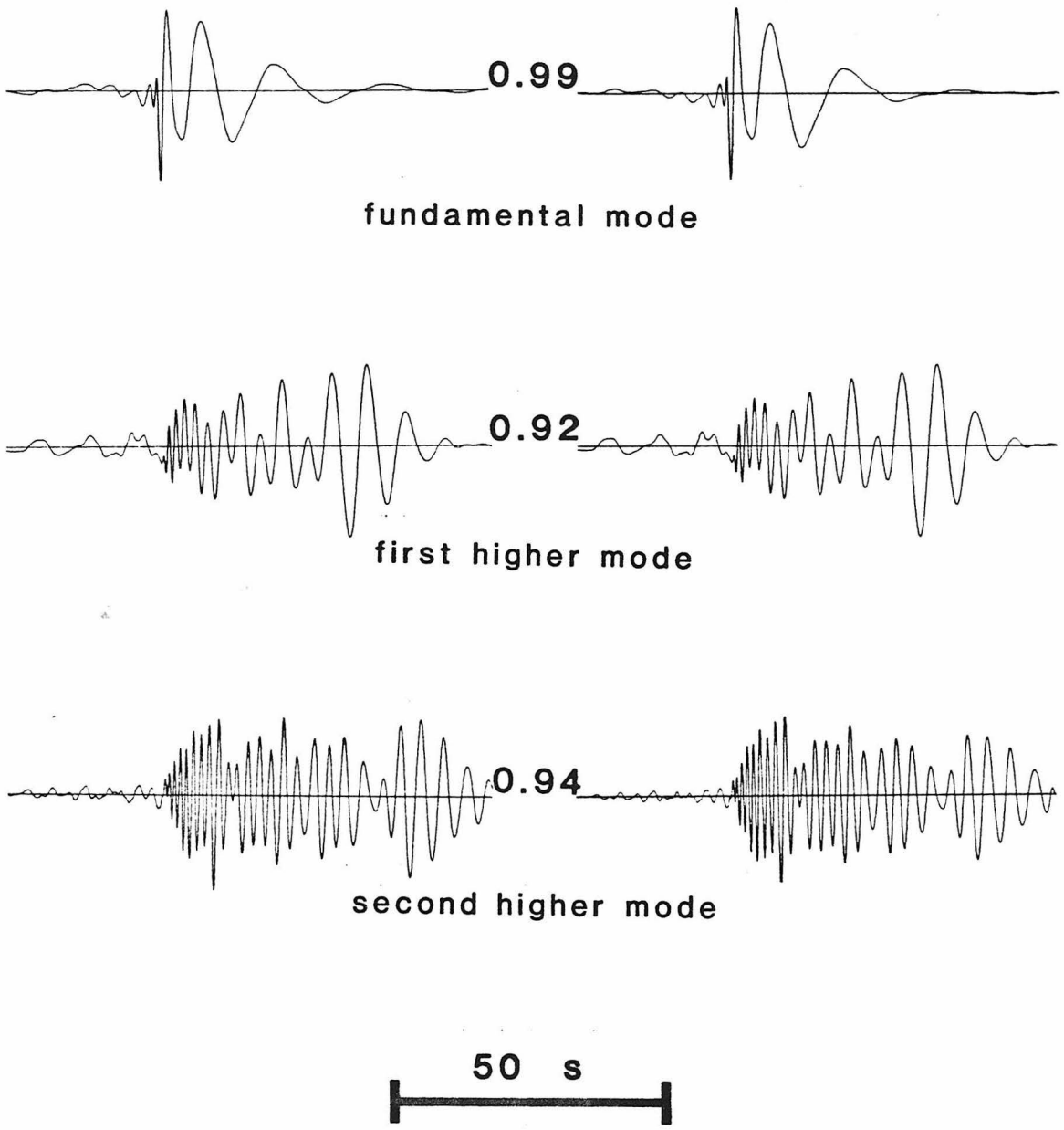

Figure 12: Comparison of analytic and hybrid synthetics at Δ=1600km. The hybrid synthetics are transmitted the first 1500 km using the propagator method, and the remaining 100 km using RT integration with propagator generated Green's functions. The left column of seismograms shows the analytic synthetics and the right column the hybrid synthetics. The results are presented mode by mode, and the mode is identified below each pair of traces. The number between each pair of traces is the ratio of the RMS amplitude of the hybrid trace to the RMS amplitude of the analytic trace.

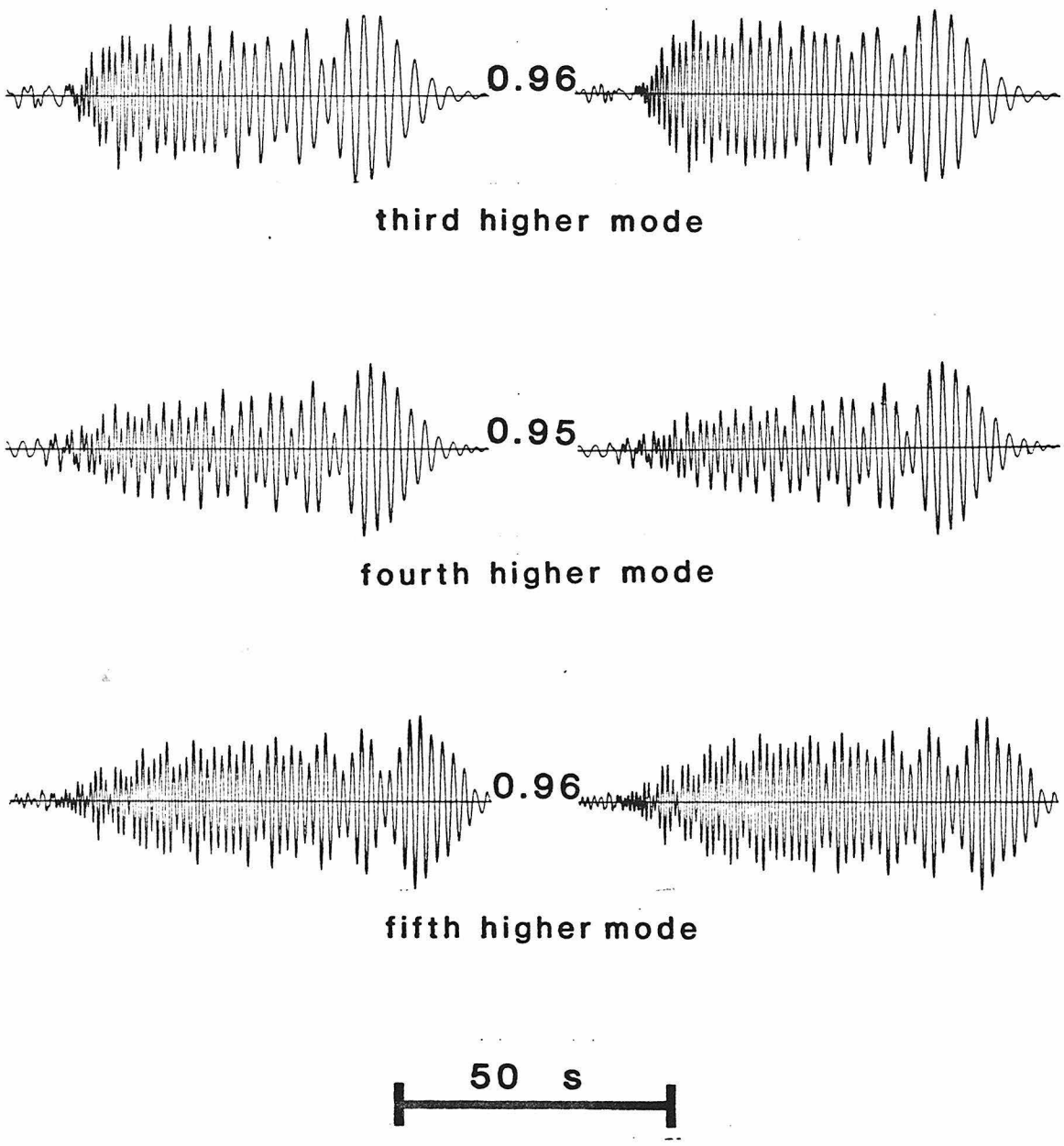

Figure 13: Comparison of analytic and hybrid synthetics at Δ=1600 km. This figure is a continuation of Figure 12 showing the remaining modes. Other details are the same as for Figure 12.

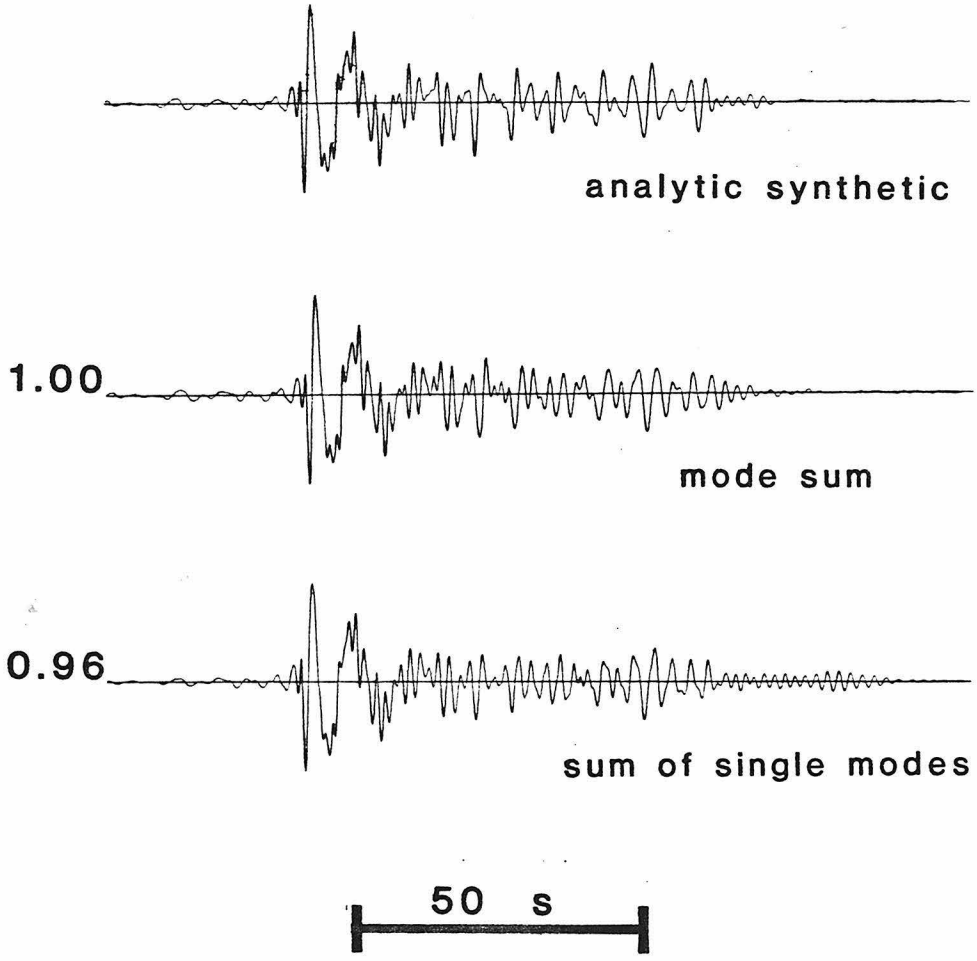

Figure 14: Comparison of analytic and hybrid mode sum seismograms. The upper seismogram, labeled analytic synthetic is a calculated using the propagator technique for the whole path. The center seismogram, labeled mode sum, is calculated using a RT integration of mode sum Green's functions and forcing functions. The lower seismogram, labeled sum of single modes, is the sum of the RT integration results for each individual mode.

leftmost seismogram in each pair shows the purely analytic synthetic, the rightmost seismogram shows the hybrid synthetic produced by RT integration. Between each pair of seismograms is a number indicating the ratio of the RMS amplitude of the hybrid synthetic to the RMS amplitude of the purely analytic synthetic. Below each pair of traces is a label indicating which mode is being illustrated. All the seismograms are bandpass filtered for periods between one and twenty-five seconds. The long period limit on the band pass filter was chosen to improve the correspondence between the waveform of the purely analytic synthetic and the RT integration result for the same mode. Longer periods seem to be poorly reconstructed by the RT integration, and are consequently filtered out of the displayed results. The filtering has the largest effect for the first two higher modes, and has a progressively smaller effect for each successive higher mode. Higher mode results depend less on the long periods and produce an increasingly good fit even before filtering. The increasing discrepancies between the purely analytic and the hybrid synthetics for successively lower higher modes is due to the larger proportion of long periods in those modes, and is a likely source of discrepancies in the mode sum calculations presented in the next paragraph and will be explained later in terms of the quantitative estimates of error yet to be derived.

The next test conducted was the RT integration using the mode sum forcing functions and Greens functions. The hybrid synthetic resulting from this integration is compared to the purely analytic mode sum synthetic in Figure 14. In this figure the hybrid synthetic is labeled mode sum and the purely analytic synthetic is labeled analytic. The seismogram labeled sum of single modes is calculated by summing the hybrid solutions for each individual mode to produce another estimate of the mode sum hybrid synthetic. Clearly the waveforms of all three seismograms are extremely similar. The numbers to the left of each of the lower two seismograms indicates the

ratio of the RMS amplitude of that seismogram to the RMS amplitude of the purely analytic mode sum seismogram. The agreement in amplitude between the purely analytic and hybrid mode sum results is better than the agreement seen for any single mode. This improvement in agreement is probably fortuitous. The mode sum synthetic calculated as a sum over the single mode hybrid results shows a more realistic amplitude measure consistent with the single mode results previously presented.

The RT integration is accomplished by the evaluation of the following expression based on integrating equation 32 of chapter 1 along a vertical surface.

$$u_2(\vec{x},t) = \int_0^\infty \left\{ \Gamma_{22}(x,z;\xi_1,\xi_3) u_{2,1}(\xi_1,\xi_3) + \Gamma_{22,1}(x,z;\xi_1,\xi_3) u_2(\xi_1,\xi_3) \right\} n_k d\xi_3 \qquad (11)$$

In this expression the displacement at time t at location $\vec{x}$ is determined as a RT integral. The forcing functions, $u_2(\xi_1,\xi_3)$ and $\mu_S u_{2,1}(\xi_1,\xi_3)$ are evaluated on the vertical surface perpendicular to the propagation direction at a distance ξ_1 from the origin for points with a range of values of ξ_3. Thus, the propagation distance for the forcing functions is ξ_1. The Green's functions, Γ_{22} and $\Gamma_{22,1}$ are evaluated by placing a source point in each position where a forcing function is evaluated. By substituting alternate expressions, in terms of the variables used in the Propagator matrix method, for the Green's functions and forcing functions in equation (11) the Representation Theorem can be expressed in terms of terms constant with respect to ξ_3 times a simple integral with ξ_3 as an integration variable. To derive this form of the RT equation (9) is substituted for $\Gamma_{22}(x,z;\xi_1,\xi_3)$, and equation (8b) is substituted for $\Gamma_{22,1}(x,z;\xi_1,\xi_3)$. Also, equation (7) is substituted for $u_2(\xi_1,\xi_3)$, and equation (10b) for $u_{2,1}(\xi_1,\xi_3)$. Performing these substitutions gives

$$u_2(\vec{x},t) = \int_0^\infty \mu(\xi_3) 4\pi \frac{\mu_S}{k_L} \left[\frac{v_S(h)}{v_0} \right]_H \left[\frac{v_R(z)}{v_0} \right]_H \underline{A}_L^2 e^{ik_L x} \left[\frac{v_R(\xi_3)}{v_0} \right]_H \left[\frac{v_R(\xi_3)}{v_0} \right]_H d\xi_3 \quad (12)$$

When the above mentioned substitutions into equation (11) ar performed it becomes evident that both convolutions in the integrand of equation (11) produce identical expressions. Therefore, it should be possible to accelerate the numerical evaluation of *11) by evaluation only one of the convolutions and then doubling the resulting solution. This approach had the additional advantage that it makes it unecessary to record both displacement and stress time histories in the FE calculations. Either one of these should be sufficient to calculate a 2-D SH RT integral. Even more useful is the fact that the equality of the two convolution terms allows determination of the value of the RT integral with the evaluation of half the number of Greens function. Tests have been conducted to investigate the validity of this approach. The waveforms of the solutions, for complete evaluation of the RT integral, and for evaluation of either term in the integral are indistinguishable when the resulting seismograms are examined. Thus, it was considered unnecessary to illustrate the results from these tests. The amplitudes of the sums of each term in the integral of (11), however, were ot necessarily identical. Using the term containing the displacement and the Green's function stress general yielded amplitudes a percent or two higher than using the other term. These amplitudes were usually in better agreement with the synthetic than the amplitudes determined by summing the two terms. The differences in amplitude agreement are small enough to be ignored. Further calculations of the RT integral may be done by doubling the value of the first term in (11) without significantly effecting the solution.

Returning to equation (12) it is clear that many of the terms do not depend upon the integration variable ξ_3. Taking these terms outside the integral and then comparing them to equation (7) allows equation (12) to be simplified to

$$u_2(\vec{x},t) = u_2(\vec{x},t) * 2\underline{A}_L \int_0^{\infty} \mu(\xi_3) \left[\frac{v_R(\xi_3)}{v_0}\right]_H \left[\frac{v_R(\xi_3)}{v_0}\right]_H d\xi_3 \qquad (13)$$

Defining I_1 to be the relation

$$I_1 = \int_0^\infty \mu(\xi_3) \left[\frac{v_R(\xi_3)}{v_0} \right]_H \left[\frac{v_R(\xi_3)}{v_0} \right]_H d\xi_3 \tag{14}$$

immediately leads to the relation

$$A_L = \frac{1}{2I_1} \tag{15}$$

Later the use of this last relation in the estimation of the minimum error for each mode will be discussed. First some consequences of equation (14) will be considered. It is well known that if i and j represent two different modes for a given period, that is $k_i \neq k_j$ for $\omega_i = \omega_j$, or for a given wave number $k_i = k_j$, $\omega_i \neq \omega_j$, then the orthogonality relation for Love waves states that

$$\int_0^\infty \rho(z) v_i(z) v_j(z) dz = 0 \qquad i \neq j \tag{16}$$

In this equation v_i is the equivalent of the component of u_2 in equation (14) due to the single mode i. Comparing (14) and (16) shows that equation (14) is a form of the orthogonality relation. At this point it is useful to notice that the two $\left[\frac{v_R(\xi_3)}{v_0} \right]_H$ terms in the equation (14) each have separate origins. One originates with the forcing functions and the other with the Green's functions. Thus, any single modes not common to both the $\left[\frac{v_R(\xi_3)}{v_0} \right]_H$ term from the forcing function and the $\left[\frac{v_R(\xi_3)}{v_0} \right]_H$ term from the Green's function will produce zero contribution to the resulting hybrid result. This implies that the only modes present in both the Green's functions and the forcing functions will be present in the RT integration results. Thus, choosing Green's functions with a subset of the modes present in the forcing function will produce a filter that gives RT integration results that contain only that subset of modes. This is

demonstrated in the next set of numerical experiments.

A series of calculations investigating the accuracy and efficiency of the use of a Green's functions, containing only a subset of the modes present in the forcing functions, as a filter to extract only those modes from the forcing functions has been completed. In particular, the single mode sets of Green's functions were used in the RT integral along with the mode sum set of forcing functions. A RT integration was completed for each single mode set of Green's functions. Figure 15 presents results of the RT integration of the mode sum forcing functions and the fundamental mode Green's functions. Figure 16 is analogous to figure 15 but uses the third higher mode Green's function set. In each of these figures two columns of five seismograms are illustrated. The left column shows results of the single mode Green's functions integrated with the mode sum forcing functions. The right column shows the results of integrating single mode Green's functions with single mode forcing functions. The RT integration is numerically evaluated by summing the convolutions at discrete points along the RT surface. The sum begins with the point nearest the surface and then adds points at steadily increasing depth. In Figures 15 and 16 the first row of seismograms is a single convolution, the sum down to a depth of 0.25 km. The second row is the sum of 15 convolutions, and includes all integration points to a depth of 7.25 km. This pattern continues with the depth of the deepest point included in the integration indicated to the right of each pair of seismograms. The numbers between each pair of seismograms indicate the ratio of the RMS amplitude of the left trace to the RMS amplitude of the right trace. For the fundamental mode case this amplitude ratio varies only slightly with depth and shows a trend of increasing with depth only in the upper eight kilometers. However, as illustrated by the third higher mode, the higher mode ratios continue increasing with depth to much larger depths. This implies that the integration must proceed to a reasonable depth for the amplitude of the filtered mode sum

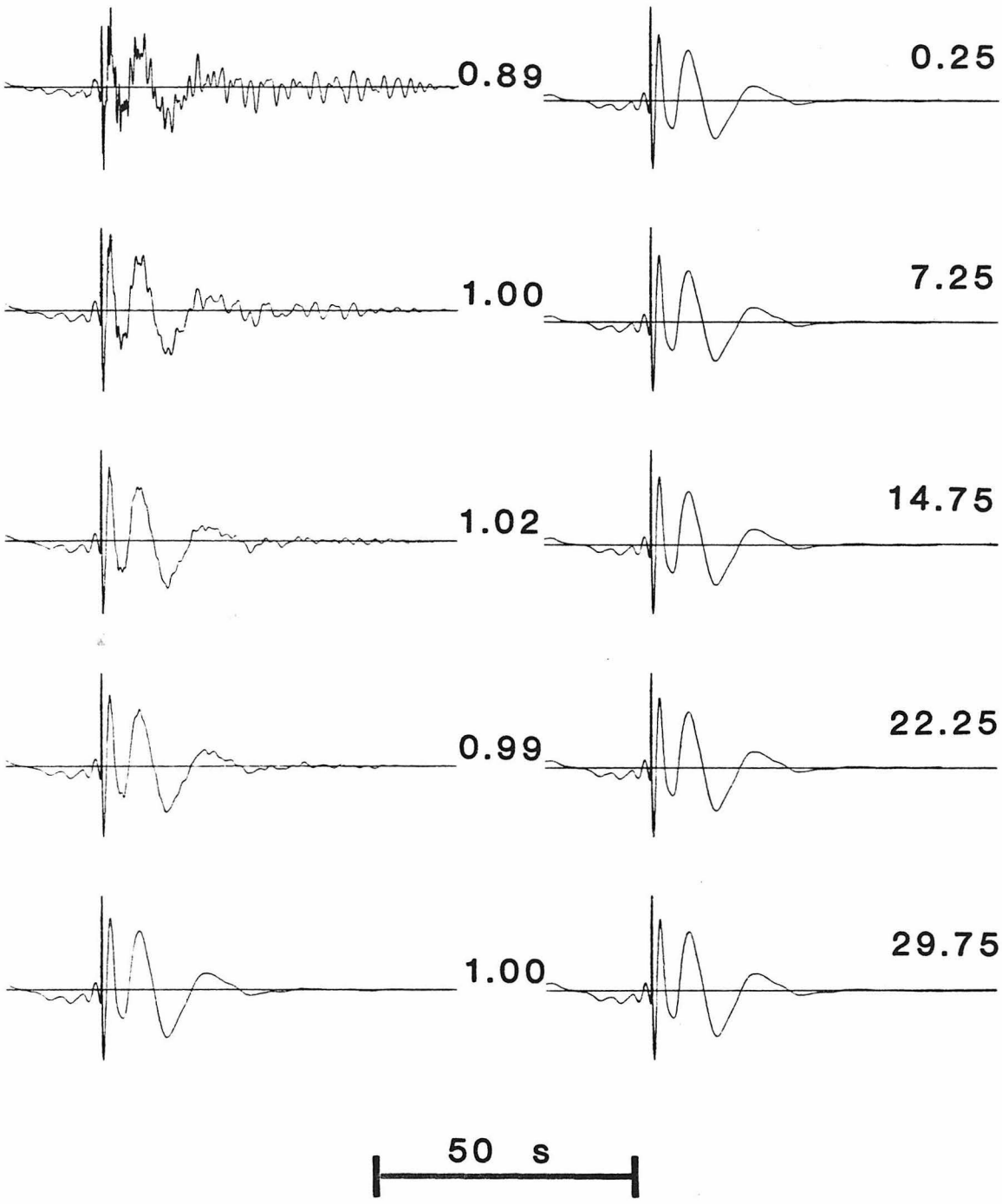

Figure 15: Comparison of hybrid synthetics at Δ=1600 km. The traces in the left column are calculated by RT convolution of the mode sum forcing functions calculated at Δ=1500 km with the fundamental mode Green's functions for 100 km further propagation. The traces in the right column are determined by RT convolution of fundamental mode forcing functions for DELTA=1500 km and the same Green's functions as the left column. The numbers to the right of each pair of seismograms show the depth to which integration along the RT integration surface has been completed. The central numbers show the RMS amplitude ratio of the the right trace to the left trace.

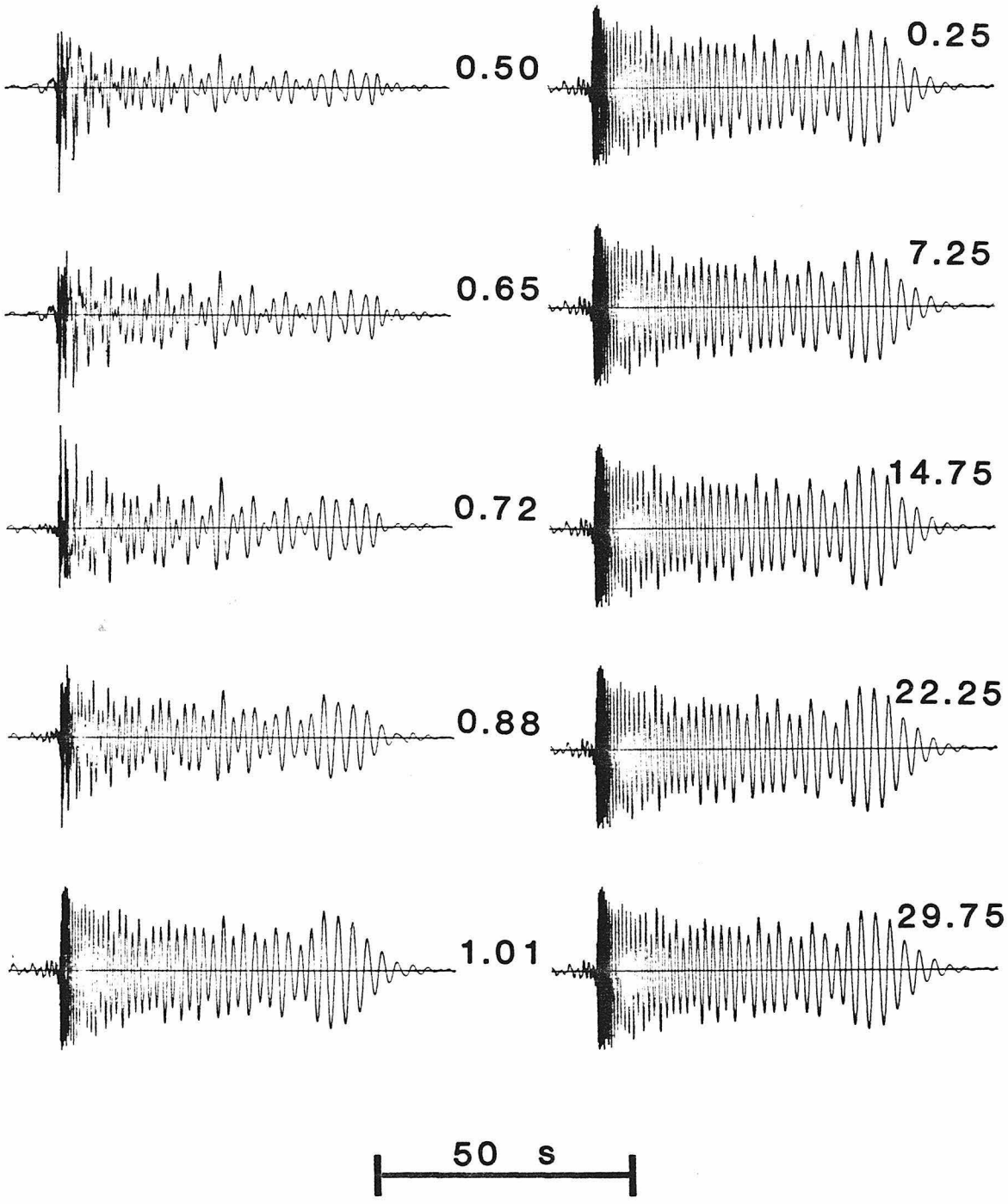

Figure 16: Comparison of hybrid synthetics at Δ=1600 km. The traces in the left column are calculated by RT convolution of the mode sum forcing functions calculated at Δ=1500 km with the third higher mode Green's functions for 100 km further propagation. The traces in the right column are determined by RT convolution of third higher mode forcing functions with the same Green's functions as the left column. The numbers to the right of each pair of seismograms and between each pair of seismograms have the same meanings as for Figure 14.

seismogram to reach that of the single mode hybrid results. For the modes investigated it was determined that the amplitude ratios stabilized near or above the base of the crustal layer, and that when the amplitudes had stabilized the waveforms of the two calculations showed little difference and remained relatively stable. Figures 17 and 18 illustrate the mode by mode results of the test discussed above. Rather than show the detailed progression to the stable result as in the previous two figures, a depth of thirty kilometers was chosen as the vertical extent of integration. This allows the illustration of the results of all six modes in two figures. In these figures two columns of seismograms are illustrated. The left column shows the results using the mode sum forcing functions and the single mode Green's functions. The right column shows the results using the single mode forcing functions and the single mode Green's functions. The numbers between each pair of seismograms indicate the ratio of the RMS amplitude of the left trace to the RMS amplitude of the right trace. Below each pair of seismograms the mode of the Green's functions is indicated. These seismograms appear different from those shown in Figures 12 and 13 since they have not been filtered before plotting. In summary, the effect of using a set of Green's functions containing a subset of the modes present in the set of forcing functions is to produce an efficient filter that allows only the modes common to both sets to appear in the hybrid result.

Now it is time to return to the analysis of the accuracy of the RT integration for a given single frequency mode. Rearranging equation (15) gives

$$2\underline{A}_L I_1 = 1 \tag{17}$$

Evaluation of this simple equation provides a direct estimate of the accuracy of the integration on a mode by mode basis. The estimate of the accuracy is obtained by evaluating the I_1 integrand at each integration point used in the RT integration, for each frequency on each branch of the dispersion curve used. For each single frequency

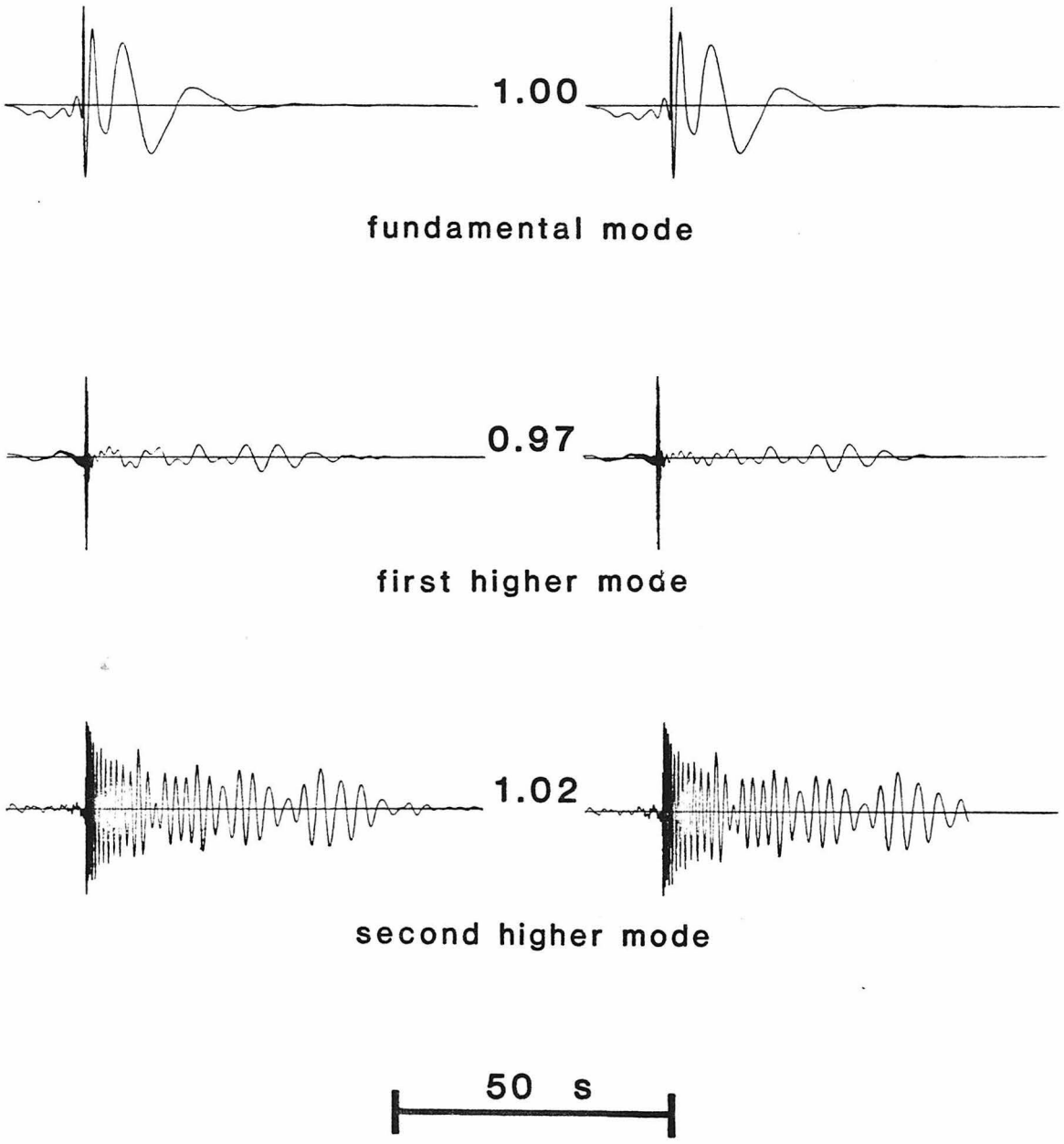

Figure 17; Comparison of synthetics at Δ=1600km. The synthetics are transmitted the first 1500 km using the propagator method, and the remaining 100 km using RT integration with propagator generated Green's functions. The left column of seismograms shows the RT convolution of the mode sum forcing functions and the Green's functions of the indicated mode, the right column shows synthetics resulting from RT integration of forcing functions and Green's functions of the indicated mode only. The results are presented mode by mode, and the mode is identified below each pair of traces. The number between each pair of traces is the ratio of the RMS amplitude of the left trace to right trace.

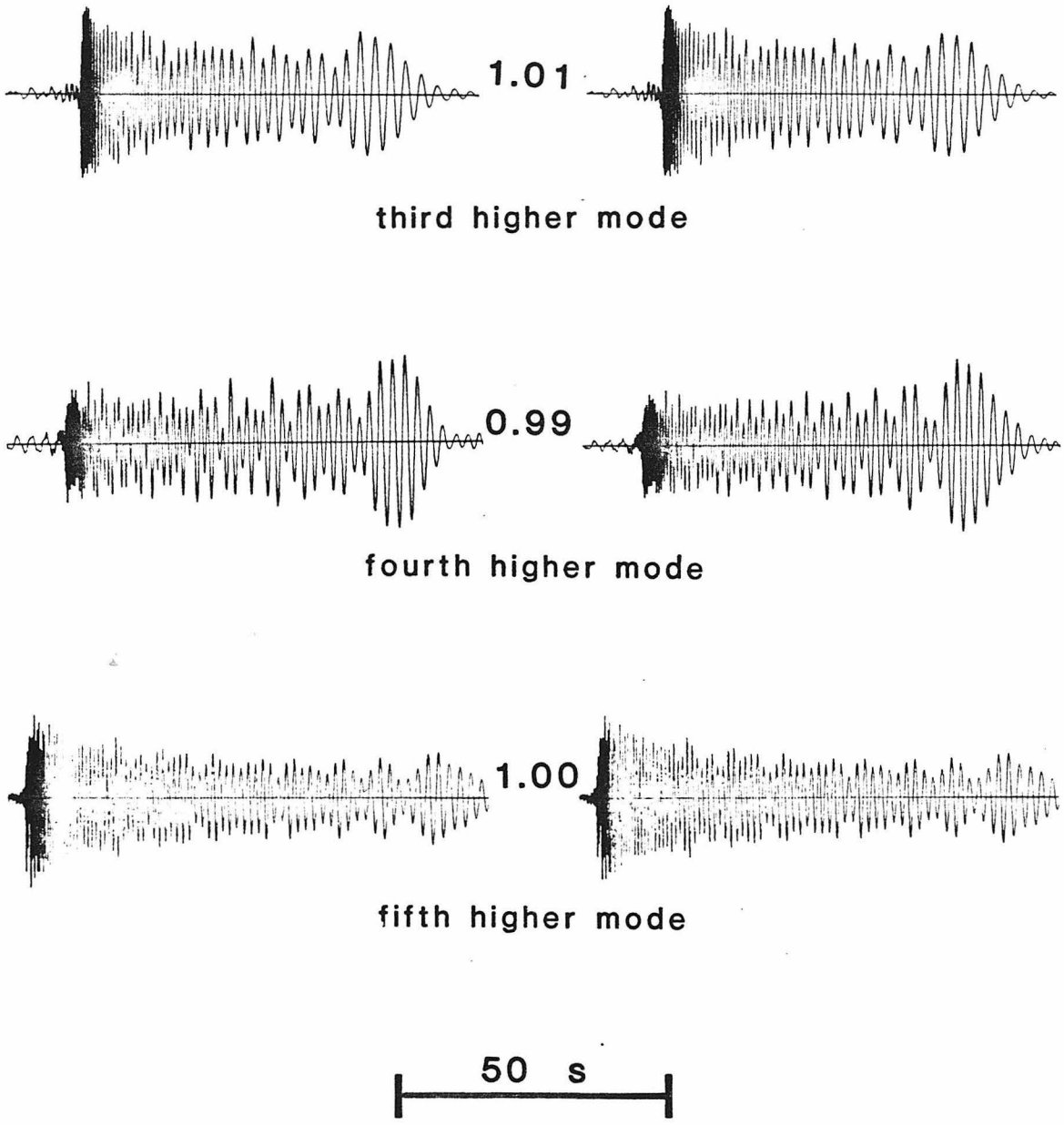

Figure 18: Comparison of synthetics at Δ=1600 km. This figure is a continuation of Figure 12 showing the remaining modes. Other details are the same as for Figure 12.

mode the quantity on the right hand side of equation 17 is determined at each integration point and summed over the integration surface. If the solution were perfect with no error present, then the sum would be exactly one. In practice the sum departs from one by some amount which gives and estimate of the size of the minimum error that could be expected in that mode in the RT integration results. The estimate is a minimum since it does not account for the phase of the arrivals nor for possible errors in that phase. The evaluation of the error using this relation is much faster than comparing results from multiple applications of RT theorem coupling. For example generating the tables on pages 219 and 220 which show the effects of varying grid spacing or of varying the vertical extent of the RT integration surface on the errors took less than 25% the time needed for a single RT integration example.

The tables on pages 219 and 220 show the effects of grid spacing and vertical extent of the integration surface. In the tables z indicates the depth in kilometers to which the integration surface extends, Δx indicated the spacing between successive integration points on that surface, and T indicates the period of the given mode. For each combination of these parameters illustrated the numbers in the table are the values of $2\underline{A}_L I_1$. It is clear from examining these tables that the grid spacing is fine enough to yield good results. Halving or doubling the grid spacing makes less than one percent difference in the error estimates which are at a level of about 98.5%. Reducing the time spacing by as much as a factor of four made no significant differences in the estimates of accuracy. So no table was included to illustrate how accuracy changed with time spacing. Seeing the errors on a frequency by frequency basis also helps to understand the causes of the inaccuracies noted in the actual RT integration results. The only variation that made noticeable changes in the accuracy of individual modes was variation in the depth to which the integration surface was extended. This change was, as expected, largest in the longest period modes. At

fundamental mode

T	z=40 km			dx=0.5 km		
	dx=,25	dx=0.5	dx=1.0	z=40	z=70	z=100
1000.	.00071	.00071	.00071	.00091	.00208	.00325
500.0	.00287	.00261	.00284	.00364	.00831	.01296
250.0	.01151	.01147	.01139	.01457	.03295	.05098
90.00	.09059	.09027	.08964	0.1123	0.2336	0.3384
70.00	0.1509	0.1503	0.1492	0.1843	0.3613	0.4998
60.00	0.2057	0.2049	0.2033	0.2480	0.4617	0.6145
55.00	0.2443	0.2433	0.2414	0.2920	0.5248	0.6808
50.00	0.2937	0.2926	0.2902	0.3473	0.5974	0.7513
45.00	0.3574	0.3559	0.3529	0.4169	0.6787	0.8223
40.00	0.4389	0.4370	0.4332	0.5034	0.7654	0.8881
35.00	0.5404	0.5379	0.5329	0.6070	0.8500	0.9408
30.00	0.6584	0.6551	0.6486	0.7216	0.9203	0.9738
25.00	0.7793	0.7752	0.7669	0.8314	0.9653	0.9873
20.00	0.8817	0.8766	0.8664	0.9160	0.9841	0.9893
18.00	0.9134	0.9079	0.8969	0.9397	0.9865	0.9889
16.00	0.9390	0.9331	0.9215	0.9576	0.9874	0.9883
14.00	0.9586	0.9525	0.9402	0.9701	0.9874	0.9877
12.00	0.9729	0.9664	0.9535	0.9782	0.9870	0.9871
10.00	0.9825	0.9757	0.9623	0.9827	0.9865	0.9865
8.000	0.9883	0.9813	0.9674	0.9848	0.9861	0.9861
6.000	0.9913	0.9841	0.9697	0.9854	0.9856	0.9856
4.000	0.9924	0.9850	0.9702	0.9852	0.9852	0.9852
2.000	0.9924	0.9848	0.9696	0.9848	0.9848	0.9848
1.800	0.9924	0.9848	0.9695	0.9848	0.9848	0.9848
1.600	0.9923	0.9847	0.9694	0.9847	0.9847	0.9847
1.400	0.9923	0.9847	0.9693	0.9847	0.9847	0.9847
1.200	0.9923	0.9846	0.9693	0.9846	0.9846	0.9846
1.000	0.9924	0.9847	0.9693	0.9847	0.9847	0.9847
0.8000	0.9924	0.9847	0.9692	0.9847	0.9847	0.9847
0.7000	0.9924	0.9847	0.9692	0.9847	0.9847	0.9847
0.6000	0.9917	0.9839	0.9684	0.9839	0.9839	0.9839
0.5000	0.9924	0.9847	0.9691	0.9847	0.9847	0.9847
0.4000	0.9925	0.9847	0.9692	0.9847	0.9847	0.9847
0.3000	0.9925	0.9848	0.9692	0.9848	0.9848	0.9848
0.2500	0.9966	0.9889	0.9733	0.9889	0.9889	0.9889
0.2000	0.9927	0.9849	0.9693	0.9849	0.9849	0.9849
0.1500	0.9928	0.9849	0.9692	0.9849	0.9849	0.9849
0.1000	0.9930	0.9851	0.9694	0.9851	0.9851	0.9851

fifth higher mode

T	z=40 km			dx=0.5 km		
	dx=,25	dx=0.5	dx=1.0	z=40	z=70	z=100
2.2960	.08099	.08054	.07972	0.1171	0.3077	0.4571
2.2900	0.2266	0.2253	0.2230	0.3185	0.6836	0.8523
2.2860	0.2996	0.2980	0.2949	0.4144	0.8015	0.9312
2.2000	0.8010	0.7963	0.7877	0.9187	0.9901	0.9902
2.1000	0.9213	0.9155	0.9050	0.9748	0.9880	0.9880
2.0000	0.9619	0.9555	0.9440	0.9839	0.9870	0.9870
1.9000	0.9784	0.9717	0.9596	0.9855	0.9863	0.9863
1.8000	0.9858	0.9788	0.9663	0.9857	0.9859	0.9859
1.7000	0.9892	0.9822	0.9694	0.9856	0.9856	0.9856
1.6000	0.9909	0.9837	0.9708	0.9854	0.9854	0.9854
1.5000	0.9917	0.9845	0.9714	0.9853	0.9853	0.9853
1.4000	0.9921	0.9848	0.9716	0.9852	0.9852	0.9852
1.3000	0.9923	0.9849	0.9717	0.9851	0.9851	0.9851
1.2000	0.9923	0.9850	0.9716	0.9850	0.9850	0.9850
1.1000	0.9923	0.9849	0.9716	0.9850	0.9850	0.9850
1.0000	0.9923	0.9849	0.9715	0.9849	0.9849	0.9849
0.9501	0.9923	0.9849	0.9715	0.9849	0.9849	0.9849
0.9001	0.9923	0.9849	0.9714	0.9849	0.9849	0.9849
0.8501	0.9923	0.9849	0.9714	0.9849	0.9849	0.9849
0.8001	0.9923	0.9849	0.9714	0.9849	0.9849	0.9849
0.7501	0.9923	0.9848	0.9714	0.9848	0.9848	0.9848
0.7001	0.9923	0.9848	0.9713	0.9848	0.9848	0.9848
0.6501	0.9923	0.9848	0.9713	0.9848	0.9848	0.9848
0.6000	0.9923	0.9848	0.9713	0.9848	0.9848	0.9848
0.5500	0.9923	0.9848	0.9713	0.9848	0.9848	0.9848
0.5000	0.9923	0.9848	0.9713	0.9848	0.9848	0.9848
0.4500	0.9923	0.9848	0.9713	0.9848	0.9848	0.9848
0.4000	0.9922	0.9847	0.9712	0.9847	0.9847	0.9847
0.3501	0.9922	0.9847	0.9712	0.9847	0.9847	0.9847
0.3000	0.9922	0.9847	0.9712	0.9847	0.9847	0.9847
0.2500	0.9927	0.9851	0.9715	0.9851	0.9851	0.9851
0.2000	0.9928	0.9852	0.9716	0.9852	0.9852	0.9852
0.1500	0.9921	0.9846	0.9710	0.9846	0.9846	0.9846
0.0000	0.9924	0.9849	0.9721	0.9849	0.9849	0.9849

longer periods the wavelength increases and the integration surface needs to be extended downward to maintain accurate results. When the depth to which the integration surface extends is less than n wavelengths then significant error occurs. This relation is clearly visible in the tables on pages 222 and 223. These tables show the mode by mode values of $2\underline{A}_L I_1$ for each separate overtone, and for the fundamental. It is easily seen that the error is very small until n+1 wavelengths, for the nth higher mode, become longer than the depth extent of the RT integration surface. This explains why the RT integration results and the analytic synthetics needed to have the long periods removed to yield a good fit. Those long period components had large errors due to incomplete representation caused by the truncation of the integration surface at depth and thus contaminated otherwise accurate results.

Using the RT Integration Method for Long Oceanic Paths

Now that the reliability of the RT coupling of FE results to a receiver distant from the FE grid has been demonstrated it can be applied to the problem of investigating the propagation of Lg when the intermediate oceanic path is too long to be handled using FE alone. The amount of calculation needed to determine each seismogram using the coupling technique is large enough that the calculation of an entire depth section for reentry into another FE calculation would be worthwhile only if a specific example were to be considered, and detailed structure were known. Thus, the approach taken here is to calculate seismograms at the surface at receivers distant from the end of the FE grid, and to examine what the remaining modal energy looks like after propagation for a large distance through the oceanic crust. Then by knowing the proportion of surface amplitude that is removed by transmission through a reverse transition an estimate of the RMS amplitude of the Lg energy that travels through the transition can be made.

fundamental		1st		2nd	
T		T			
1000.	.00090	11.49	0.0000	5.750	0.0000
500.0	.00036	11.40	.00370	5.700	0.1350
250.0	.01457	11.20	0.1135	5.600	0.3522
90.00	0.1123	11.00	0.1868	5.500	0.5069
70.00	0.1843	10.80	0.2572	5.400	0.6219
60.00	0.2480	10.60	0.3249	5.300	0.7091
55.00	0.2920	10.40	0.3899	5.200	0.7758
50.00	0.3473	10.20	0.4521	5.100	0.8269
45.00	0.4169	10.00	0.5113	5.000	0.8660
40.00	0.5034	9.800	0.5672	4.900	0.8958
35.00	0.6070	9.600	0.6196	4.800	0.9184
30.00	0.7216	9.400	0.6681	4.700	0.9355
25.00	0.8314	9.200	0.7126	4.600	0.9485
20.00	0.9160	9.000	0.7530	4.500	0.9582
18.00	0.9397	8.800	0.7890	4.400	0.9654
16.00	0.9576	8.600	0.8210	4.300	0.9708
14.00	0.9701	8.400	0.8488	4.200	0.9748
12.00	0.9782	8.200	0.8729	4.100	0.9778
10.00	0.9827	8.000	0.8935	4.000	0.9800
8.000	0.9848	7.800	0.9108	3.800	0.9827
6.000	0.9854	7.600	0.9254	3.600	0.9842
4.000	0.9852	7.400	0.9374	3.400	0.9849
2.000	0.9848	7.200	0.9474	3.200	0.9852
1.800	0.9848	7.000	0.9555	3.000	0.9852
1.600	0.9847	6.500	0.9695	2.500	0.9851
1.400	0.9847	6.000	0.9775	2.000	0.9849
1.200	0.9846	5.500	0.9818	1.900	0.9849
1.000	0.9847	5.000	0.9839	1.800	0.9849
0.8000	0.9847	4.500	0.9848	1.700	0.9848
0.7000	0.9847	4.000	0.9851	1.600	0.9848
0.6000	0.9839	3.500	0.9852	1.500	0.9848
0.5000	0.9847	3.000	0.9851	1.400	0.9848
0.4000	0.9847	2.500	0.9850	1.300	0.9847
0.3000	0.9848	2.000	0.9848	1.200	0.9847
0.2500	0.9889	1.800	0.9848	1.100	0.9847
0.2000	0.9849	1.600	0.9847	1.000	0.9847
0.1500	0.9849	1.400	0.9847	0.9001	0.9846
0.1000	0.9851	1.200	0.9846	0.8001	0.9846
0.0000	0.0000	1.000	0.9846	0.7001	0.9846
0.0000	0.0000	0.9001	0.9846	0.6001	0.9844
0.0000	0.0000	0.8001	0.9845	0.5001	0.9843
0.0000	0.0000	0.7001	0.9849	0.4501	0.9844
0.0000	0.0000	0.6001	0.9843	0.4000	0.9845
0.0000	0.0000	0.5001	0.9844	0.3500	0.9845
0.0000	0.0000	0.4001	0.9841	0.3000	0.9845
0.0000	0.0000	0.3001	0.9841	0.2500	0.9849
0.0000	0.0000	0.2501	0.9844	0.2000	0.9850
0.0000	0.0000	0.2000	0.9849	0.1500	0.9851
0.0000	0.0000	0.1500	0.9851	0.100E	0.9865
0.0000	0.0000	0.1001	4.234	0.0000	0.0000

3rd		4th		5th	
T		T		T	
3.831	0.0000	2.873	0.0000	2.299	0.0000
3.824	.07248	2.869	.09512	2.296	0.1171
3.808	0.2093	2.860	0.2664	2.290	0.3185
3.800	0.2651	2.854	0.3519	2.286	0.4144
3.700	0.6640	2.800	0.7295	2.200	0.9187
3.600	0.8238	2.700	0.9145	2.100	0.9748
3.500	0.9005	2.600	0.9624	2.000	0.9839
3.400	0.9400	2.500	0.9777	1.900	0.9855
3.300	0.9609	2.400	0.9830	1.800	0.9857
3.200	0.9722	2.300	0.9848	1.700	0.9856
3.100	0.9784	2.200	0.9854	1.600	0.9854
3.000	0.9818	2.100	0.9855	1.500	0.9853
2.900	0.9836	2.000	0.9855	1.400	0.9852
2.800	0.9846	1.900	0.9854	1.300	0.9851
2.700	0.9851	1.800	0.9853	1.200	0.9850
2.600	0.9853	1.700	0.9852	1.100	0.9850
2.500	0.9854	1.600	0.9851	1.000	0.9849
2.400	0.9854	1.500	0.9850	0.9501	0.9849
2.300	0.9853	1.400	0.9850	0.9001	0.9849
2.200	0.9853	1.300	0.9849	0.8501	0.9849
2.000	0.9851	1.200	0.9849	0.8001	0.9849
1.800	0.9850	1.100	0.9848	0.7501	0.9848
1.600	0.9849	1.000	0.9848	0.7001	0.9848
1.500	0.9849	0.9501	0.9848	0.6501	0.9848
1.400	0.9848	0.9001	0.9848	0.6000	0.9848
1.300	0.9848	0.8501	0.9848	0.5500	0.9848
1.200	0.9848	0.8001	0.9848	0.5000	0.9848
1.100	0.9848	0.7501	0.9847	0.4500	0.9848
1.000	0.9847	0.7001	0.9847	0.4000	0.9847
0.9001	0.9847	0.6501	0.9847	0.3501	0.9847
0.8001	0.9847	0.6000	0.9847	0.3000	0.9847
0.7501	0.9846	0.5500	0.9847	0.2500	0.9851
0.7001	0.9847	0.5000	0.9847	0.2000	0.9852
0.6501	0.9846	0.4500	0.9847	0.1500	0.9846
0.6001	0.9846	0.4000	0.9847	0.1000	0.9849
0.5500	0.9846	0.3500	0.9846	0.0000	0.0000
0.5000	0.9846	0.3000	0.9846	0.0000	0.0000
0.4500	0.9846	0.2500	0.9851	0.0000	0.0000
0.4000	0.9849	0.2000	0.9846	0.0000	0.0000
0.3500	0.9846	0.1500	0.9847	0.0000	0.0000
0.3000	0.9845	0.1000	0.9849	0.0000	0.0000
0.2500	0.9844	0.0000	0.0000	0.0000	0.0000
0.2000	0.9837	0.0000	0.0000	0.0000	0.0000
0.1500	0.9853	0.0000	0.0000	0.0000	0.0000
0.1000	0.9856	0.0000	0.0000	0.0000	0.0000

In order to perform the RT integration that propagates the FE results across the oceanic portion of the path sets of Green's functions must first be calculated for each distance at which the seismogram is to be examined. It should be noted that these Green's Functions are not identical to those used in the tests above. Since the propagation path has an oceanic crustal structure a different set of modes appropriate for an oceanic structure rather than a continental one must be used to determine the Green's functions. Since the oceanic crust is thinner than the continental crust the modes tend to concentrate at higher frequencies. Thus, more (eight) higher modes were used in the oceanic mode set than in the continental mode set. This does not give complete coverage in the period range considered, but should give an adequate Green's function.

To illustrate the effect that the oceanic propagation has on the FE results sampling a wavefield that has already propagated through a transition region three sample distances, from FE node to receiver, of one hundred, two hundred and fifty, and one thousand kilometers were chosen. Mode sum Green's functions for receivers at the crustal surface and sources where the FE displacements and stresses were recorded were calculated to be used in the RT integral. The seismograms resulting from the RT integrations are illustrated in Figure 19. In this figure the RT integration results for the two shortest paths are compared to FE results at the same locations with respect to the source. The result for the longer path is also shown below the upper two pairs of seismograms. In each of the pairs of illustrated seismograms the upper trace shows the FE result. This result includes propagation through an oceanic path length of 125 km, for the upper pair, or 275 km, for the lower pair. These seismograms are taken from the reverse reference model FE calculation which uses a column of nodes recorded in the fifty kilometer forward transition calculation as forcing functions. Displacements and stresses recorded at the same horizontal distance from the source as these forcing functions are used as the u_2, and $\mu u_{2,1}$, terms in the RT

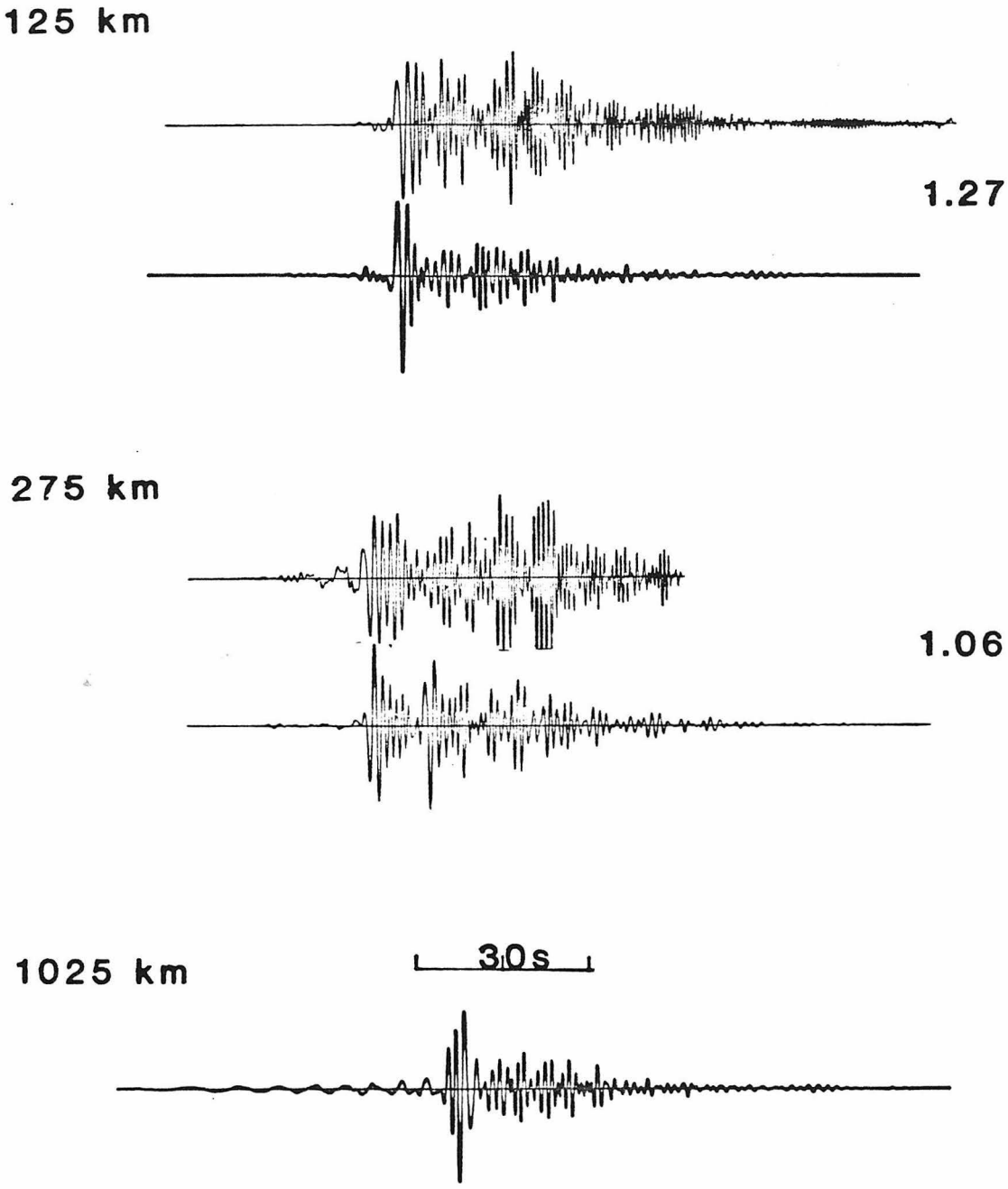

Figure 19: Seismograms for different oceanic path lengths. Each of the upper two pairs of traces compare FE and RT integration results at the indicated distances. The single seismogram at 1025 km shows RT integration results for a distance to long to treat using FE. The number to the right of each pair of seismograms give the RMS amplitude ratio of the upper trace to the lower trace.

integration. The seismograms resulting from the RT integration of these terms with Green's functions for propagation through a path length of oceanic structure are shown as the lower seismograms. The upper pair of seismograms is for Green's functions for a one hundred kilometer path length, the lower pair for a Green's function path length of two hundred fifty kilometers. The numbers to the right of each pair indicate the RMS amplitude ratio of the upper seismogram to the lower one. The upper pair of seismograms shows reasonable agreement. At least half the difference between the two traces could easily be due to truncation errors caused by terminating the integration surface at 35 km depth. The remaining differences in amplitude and waveform can be explained as being due to a small component of non-modal energy which is filtered out of the result when using the RT integration but not when using the FE method. Thus, this pair of seismograms shows that after propagation through 125 km of oceanic path most of the non-modal energy is no longer visible at the surface. From the FE calculations whose time slices are shown in chapter two it is clear that at this distance some of the non-modal energy is still present at depth. This energy is probably a source of the amplitude discrepancy between the two uppermost seismograms. The lower pair of seismograms shows excellent agreement in amplitude but discrepancies in waveform for all but the initial arrivals. This is expected since the FE result is contaminated with small reflections from the nearby grid edge that can change the waveform significantly but have been shown to change the RMS amplitudes by at most a couple of percent. Thus the amplitude agreement at this distance implies that the non-modal energy remaining at depths included in the integration is not significant. However, the remaining amplitude of the Lg phase is still fifty five to seventy percent of the incident amplitude. Using longer transitions this can be reduced another five to ten percent, and adding the effects of intrinsic or scattering attenuation, which are not considered

in the calculations presented here, might produce a further small reduction in the the Lg wave amplitude. Thus, it is apparent that the attenuation due to passage through a transition region is not sufficient to explain the entire observed attenuation of Lg waves.

In conclusion, the FE results show several effects which are significant mechanisms for the attenuation of Lg as it passes through ocean continent or continent ocean transition regions. The most important of these effects, associated with the path length of oceanic structure, is the transmission of energy across the crust half-space boundary in the forward transition region and the conversion of that energy into downgoing non-modal phases. As the length of the oceanic path increases the amplitude of these downgoing phases increase and they are able to propagate far enough towards the base of the grid that they are not transmitted back into the crustal layer through the half-space crust boundary in the reverse transition region. The FE results illustrated in this chapter show that significant portions of the energy originally trapped in the continental crust can be carried out of the system in this manner. The RT integration results show that, for a 125 km path length, much of the downgoing energy has passed out of the depth region above the base of the continental crust, and that after propagation through an oceanic path of length 275 km the non-modal energy has become negligable. The attenuation of Lg passing through the reverse transition should be maximal for path lengths in excess of that length at which the non-modal energy has reached depths below the base of the continental crust. The oceanic path length necessary for complete escape of the non-modal component of the wavefield is on the order of 200 to 250 km but significant portions of the energy is able to escape for path lengths as short as eighty kilometers. The results presented here are for a fifty kilometer long transition. Since a longer transition region produces more rapid downward propagation these lengths should be expected to be an

overestimate of the observed Lg data which is on average associated with longer transitions. However, the amount of attenuation seen in the Lg phase is not large enough to explain the observed attenuation of Lg. These simple models show that geometry of the transition region alone produces at most a reduction of a factor of five or six in amplitude. Thus, the observed attenuation, which has frequently been attributed to the propagation effects caused by passage through a transition, cannot be entirely due to these propagation effects.

REFERENCES

Abramowitz, M., Stegun, I., *Handbook of Mathematical Functions,* Dover, New York, 1972.

Aki, K., Richards, P. G., *Quantitative Seismology,* W. H. Freeman & Co., San Francisco, 1980.

Alsop, L. E., Transmission and Reflection of Love Waves at a Vertical Discontinuity, *J. Geophys. Res., vol. 71,* pp. 3969-3984, 1966.

Alsop, L. E., An Orthonormality Relation for Elastic Body Waves, *Bull. Seismol. Soc. Am., vol. 58,* pp. 1949-1954, 1968.

Baker, R. G., Determination of Magnitude from L_g, *Bull. Seismol. Soc. Am., vol. 60,* pp. 1907-1919, 1970.

Barker, B. W., Der, Z. A., Mrazek, C. P., The Effect of Crustal Structure on the Regional Phases P_g and L_g at the Nevada Test Site, *J. Geophys. Res., vol. 86,* pp. 1686-1700, 1981.

Barton, P., Matthews, D., Hall, J., Warner, M., Moho beneath the North Sea Compared on Normal Incidence and Wide-Angle Seismic Records, *Nature, vol. 308* , 1984.

Basham, P. W., A New Magnitude Formula for Short Period Continental Rayleigh Waves, *Geophys. J. R. Astr. Soc., vol. 23,* pp. 255-260, 1971.

Bath, M., The Elastic Waves L_g and R_g along Euroasiatic Paths, *Arkiv for Geofysik, vol. 2,* pp. 295-342, 1954.

Bath, M., Channel Waves, *J. Geophys. Res., vol. 63,* pp. 583-587, 1958.

Blandford, R., Seismic Event Discrimination, *Bull. Seismol. Soc. Am., vol. 72,* pp. s69-s87, 1982.

Bolt, B. A., Velocity of the Seismic Waves L_g and R_g across Australia, *Nature, vol. 180,* pp. 495, 1957.

Bollinger, G. A., Attenuation of the L_g Phases and Determination of m_b in the Southeastern United States, *Bull. Seismol. Soc. Am., vol. 69*, pp. 45-63, 1979.

Boore, D., Love Waves in Nonuniform Wave Guides: Finite Difference Calculations, *J. Geophys. Res., vol. 75*, pp. 1512-1527, 1970.

Boore, D., A Note on the Effect of Simple Topography on Seismic SH Waves, *Bull. Seismol. Soc. Am., vol. 62*, pp. 275-284, 1972a.

Boore, D., Finite Difference Methods for Seismic-Wave Propagation in Heterogeneous Materials, Ch. 5 in *Methods in Computational Physics, Vol. II*, Academic Press, 1972b.

Boore, D., Larner, K. L., Aki, K., Comparison of Two Independent Methods for the Solution of Wave-Scattering Problems: Response of a Sedimentary Basin to Vertically Incident SH Waves, *J. Geophys. Res., vol. 76*, pp. 558-569, 1971.

Bose, S. K., Transmission of SH Waves across a Rectangular Step, *Bull. Seismol. Soc. Am., vol. 65*, pp. 1779-1786, 1975.

Bouchon, M., A Simple Method to Calculate Green's Functions for Elastic Layered Media, *Bull. Seismol. Soc. Am., vol. 71*, pp. 959-971, 1981.

Bouchon, M., The Complete Synthesis of Seismic Crustal Phases at Regional Distances, *J. Geophys. Res., vol. 87*, pp. 1735-1741, 1982.

Campillo, M., Bouchon, M., Massinon, B., Theoretical Study of the Excitation, Spectral Characteristics, and Geometrical Attenuation of Regional Seismic Phases, *Bull. Seismol. Soc. Am., vol. 74*, pp. 79-90, 1984.

Cara, M., Minster, J. B., Multi-Mode Analysis of Rayleigh-Type Lg. Part 1. Theory and Applicabilty of the Method., *Bull. Seismol. Soc. Am., vol. 71*, pp. 973-984, 1981.

Cara, M., Minster, J. B., LeBras, R., Multi-Mode Analysis of Rayleigh-Type Lg. Part 2. Application to Southern California and the Northwestern Sierra Nevada., *Bull. Seismol. Soc. Am., vol. 71*, pp. 985-1002, 1981.

Chinn, D. S., Isacks, B. L., Barazangi, M., High Frequency Seismic Wave Propagation in Western South America Along the Continental Margin, in the Nazca Plate, and across the Altiplano, *Geophys. J. R. Astr. Soc., vol. 60*, pp. 209-244, 1980.

Chung, D. H, Bernreuter, D. L., Regional Relationships among Earthquake Magnitude Scales, *Reviews of Geophys. Space Phys., vol. 19*, pp. 649-663, 1981.

Der, Z. A., Marshall, M. E., O'Donnell, A., McElfresh, T. W., Spatial Coherence Structure and Attenuation of the L_g Phase, Site Effects, and the Interpretation of the L_g Coda, *Bull. Seismol. Soc. Am., vol. 74*, pp. 1125-1147, 1984.

de Hoop, A.,T., Representation Theorems for the Displacement in an Elastic Solid and Their Application to Elastodynamic Diffraction Theory, Sc. D. Thesis, Technische Hogeschool, Delft, 1958.

Drake, L. A., Love and Rayleigh Waves in Nonhorizontally Layered Media, *Bull. Seismol. Soc. Am., vol. 62*, pp. 1241-1258, 1972.

Drake, L. A., Bolt, B. A., Love Waves Normally Incident at a Continental Boundary, *Bull. Seismol. Soc. Am., vol. 70*, pp. 1103-1123, 1980.

Dwyer, J. J., Herrmann, R. B., Nuttli, O. W., Spatial Attenuation of the L_g Wave in the Central United States, *Bull. Seismol. Soc. Am., vol. 73*, pp. 781-796, 1983.

Ebel, J. E., M_L Measurements for Northeastern United States Earthquakes, *Bull. Seismol. Soc. Am., vol. 72*, pp. 1367-1378, 1982.

Eittreim, S., Grantz, A., CDP Seismic Sections of the Western Beaufort Continental Margin, *Tectonophysics, vol. 59*, pp. 251-262, 1979.

Frazier, G. A., Alexander, J. H., Petersen, C. M., 3-D Seismic code for the ILLIAC IV. *Systems, Science and Software Report SSS-R-73-1506,* 1973.

Frazier, G. A., Petersen, C. M., 3-D Stress Wave Code for the ILLIAC IV. *Systems, Science and Software Report SSS-R-74-2103*, 1974.

Gilbert, F., Knopoff, L., Seismic Scattering from Topographic Irregularities, *J. Geophys. Res., vol. 65*, pp. 3437-3444, 1960.

Grantz, A., Eittreim, S., Dinter, D. A., Geology and Tectonic Development of the Continental Margin North of Alaska, *Tectonophysics, vol. 59*, pp. 263-269, 1979.

Gregersen, S., Possible Mode Conversion between Love and Rayleigh Waves at a Continental Margin, *Geophys. J. R. Astr. Soc., vol. 54*, pp. 121-127, 1978.

Gregersen, S., L_g Wave Propagation and Crustal Structure Differences near Denmark and the North Sea, *Geophys. J. R. Astr. Soc., vol. 79*, pp. 217-234, 1984.

Gregersen, S., Alsop, L. E., Amplitudes of Horizontally Refracted Love Waves, *Bull. Seismol. Soc. Am., vol. 64*, pp. 535-553, 1974.

Gregersen, S., Alsop, L. E., Mode Conversion of Love Waves at a Continental Margin, *Bull. Seismol. Soc. Am., vol. 66*, pp. 1855-1872, 1976.

Grow, J. A., Bowin, C. O., Hutchinson, D. R., The Gravity Field of the U. S. Atlantic Continental Margin, *Tectonophysics, vol. 59*, pp. 27-52, 1979.

Gumper, F., Pomeroy, P. W., Seismic Wave Velocities and Earth Structure on the African Continent, *Bull. Seismol. Soc. Am., vol. 60*, pp. 651-668, 1970.

Gupta., I. N., Barker, B. W., Burnetti, J. A., Der, Z. A., A Study of the Regional Phases from Earthquakes and Explosions in Western Russia, *Bull. Seismol. Soc. Am., vol. 70*, pp. 851-872, 1980.

Gupta, I. N., von Seggern, D. H., Wagner, R. A., A Study of Variations in the Horizontal to Vertical L_g Amplitude Ratio in the Eastern United States, *Bull. Seismol. Soc. Am., vol. 72*, pp. 2081-2088, 1982.

Gutenburg, B., Channel Waves in the Earth's Crust, *Geophysics, vol. 20* pp. 283-294, 1955.

Harkrider, D. G., Surface Waves in Multilayered Media I, Rayleigh and Love Waves from Buried Sources in a Multilayered Elastic Half-Space, *Bull. Seismol. Soc. Am., vol. 54*, pp. 627-679, 1964.

Harkrider, D. G., Surface Waves in Multilayered Elastic Media, Part II. Higher Mode Spectra and Spectral Ratios from Point Sources in Plane Layered Earth Models, *Bull. Seismol. Soc. Am., vol. 60*, pp. 1937-1987, 1970.

Harkrider, D. G., Coupling Near Source Phenomena into Surface Wave Generation, pp. 277-326 in *Identification of Seismic Sources- Earthquake or Underground Explosion*, ed. Husebye, E. S., Mykkeltveit, S., eds, Reidel, 1981.

Herrin, E., On $\overline{P}$ and L_g, *J. Geophys. Res., vol. 66*, pp. 334-335, 1961.

Herrin, E., Minton, P. D., The Velocity of L_g in the Southwestern United States and Mexico, *Bull. Seismol. Soc. Am., vol. 50*, pp. 35-44, 1960.

Herrin, E., Richmond, J., On the Propagation of the L_g Phase, *Bull. Seismol. Soc. Am., vol. 50*, pp. 197-210, 1960.

Herrmann, R. B., Kijko, A., Modeling Some Empirical Vertical Component L_g Relations, *Bull. Seismol. Soc. Am., vol. 73*, pp. 157-171, 1983a.

Herrmann, R. B., Kijko, A., Short Period L_g Magnitudes: Instrument, Attenuation, and Source Effects, *Bull. Seismol. Soc. Am., vol. 73*, pp. 1835-1850, 1983b.

Herrmann, R. B., Nuttli, O. W., Ground Motion Modelling at Regional Distances for Earthquakes in a Continental Interior, I. Theory and Observations, *Int. J. Earthq. Engng. Struct. Dyn., vol. 4*, pp. 49-58, 1975a.

Herrmann, R. B., Nuttli, O. W., Ground Motion Modelling at Regional Distances for Earthquakes in a Continental Interior, II. Effect of Focal Depth, Azimuth, and Attenuation, *Int. J. Earthq. Engng. Struct. Dyn., vol. 4*, pp. 59-77, 1975b.

Herrmann, R. B., Nuttli, O. W., Magnitude: the Relation of M_L to m_{bL_g}, *Bull. Seismol. Soc. Am., vol. 72*, pp. 389-397, 1982.

Herrera, I., On a Method to Obtain a Green's Functions for a Multi-Layered Half Space, *Bull. Seismol. Soc. Am., vol. 54*, pp. 1087-1096, 1964a.

Herrera, I., A Perturbation Method for Elastic Wave Propagation: I. Nonparallel Boundaries, *J. Geophys. Res., vol. 69*, pp. 3845-3851, 1964b.

Hinz, K., Schluter, H.-U., Grant, A. C., Srivastava, S. P., Unpleby, D., Woodside, J., Geophysical Transects of the Labrador Sea: Labrador to Southwest Greenland, *Tectonophysics, vol. 59*, pp. 151-183, 1979.

Hudson, J. A., The Passage of Elastic Waves through an Anomalous Region-IV. Transmission of Love Waves through a Laterally Varying Structure, *Geophys. J., vol. 49*, pp. 645-654, 1977.

Hudson, J. A., Scattered Surface Waves from a Surface Obstacle, *Geophys. J., vol. 13*, pp. 441-458, 1967.

Hudson, J. A., Knopoff, L., Transmission and Reflection of Surface Waves at a Corner: I. Love Waves, *J. Geophys. Res., vol. 69*, pp. 275-280, 1964.

Isacks, B. L., Stephens, C., Conversion of S_n to L_g at a Continental Margin, *Bull. Seismol. Soc. Am., vol. 65*, pp. 235-244, 1975.

Jones, F. B., Long, L. T., McKee, J. H., Study of the Attenuation and Azimuthal Dependence of Seismic Wave Propagation in the Southeastern United States, *Bull. Seismol. Soc. Am., vol. 67*, pp. 1503-1513, 1977.

Kadinsky-Cade, K., Barazangi, M., Oliver, J., Isacks, B., Lateral Variation of High Frequency Seismic Wave Propagation at Regional Distances across the Turkish and Iranian Plateaus, *J. Geophys. Res., vol. 86*, pp. 9377-9396, 1981.

Kazi, M. H., The Love Wave Scattering Matrix for a Continental Margin (Theoretical), *Geophys. J. R. Astr. Soc., vol. 52*, pp. 25-44, 1978a.

Kazi, M. H., The Love Wave Scattering Matrix for a Continental Margin (Numerical), *Geophys. J. R. Astr. Soc., vol. 53*, pp. 227-243, 1978b.

Keen, C. E., Hyndman, R. D., Geophysical Review of the Continental Margins of Eastern and Western Canada, *Can. J. Earth Sci., vol. 16*, pp. 712-747, 1979.

Kennett, B. L. N., The Interaction of Seismic Waves with Horizontal Velocity Contrasts, *Geophys. J. R. Astr. Soc., vol. 33*, pp. 431-450, 1973.

Kennett, B. L. N., Guided Wave Propagation in Laterally Varying Media-I. Theoretical Development, *Geophys. J. R. Astr. Soc., vol. 79*, pp. 235-256, 1984.

Kennett, B. L. N., Mykkeltveit, S., Guided Wave Propagation in Laterally Varying Media-II. L_g-Waves in North-Western Europe, *Geophys. J. R. Astr. Soc., vol. 79*, pp. 257-267, 1984.

Kennett, B. L. N., L_g Waves and Structural Boundaries, *Bull. Seismol. Soc. Am., vol. 76*, pp. 1133-1142, 1986.

Knopoff, L., Hudson, J. A., Transmission of Love Waves Past a Continental Margin, *J. Geophys. Res., vol. 69*, pp. 1649-1653, 1964.

Knopoff, L., Mal, A. K., Phase Velocities of Surface Waves in the Transition Zone of Continental Margins-I. Love Waves, *J. Geophys. Res., vol. 72*, pp. 1769-1776, 1967.

Knopoff, L., Mal, A. K., Alsop, L. E., Phinney, R. A., A Property of Long-Period Love Waves, *J. Geophys. Res., vol. 75*, pp. 4084-4086, 1970.

Knopoff, L., Schwab, F., Nakanishi, K., Chang, F., Evaluation of L_g as a Discriminant among Different Continental Crustal Structures, *Geophys. J. R. Astr. Soc., vol. 39*, pp. 41-70, 1975.

Knopoff, L., Schwab, F., Kausel, E., Interpretation of L_g, *Geophys. J. R. Astr. Soc., vol. 33*, pp. 389-404, 1973.

Kosloff, D., Frazier, G. A., Treatment of Hourglass Patterns in Lower Order Finite Element Codes, *International Journal for Numerical and Analytical Methods,*

vol. 2, pp. 57-72, 1978.

Kovach, R. L., Anderson, D. L., Higher Mode Surface Waves and Their Bearing on the Structure of the Earth's Mantle, *Bull. Seismol. Soc. Am., vol. 54*, pp. 161-182, 1964.

Lapwood, E. R., Hudson, J. A., The Passage of Elastic Waves through an Anomalous Region-III. Transmission of Obliquely Incident Body Waves, *Geophys. J. R. Astr. Soc., vol. 40*, pp. 255-268, 1975.

Lapwood, E. R., Hudson, J. A., Kembhavi, K., The Passage of Elastic Waves through an Anomalous Region-II. Transmission through a Layer between Two Different Media, *Geophys. J. R. Astr. Soc., vol. 40*, pp. 241-254, 1975.

Lapwood, E. R., Hudson, J. A., Kembhavi, K., The Passage of Elastic Waves through an Anomalous Region-I. Transmission of Body Waves through a Soft Layer, *Geophys. J. R. Astr. Soc., vol. 31*, pp. 457-467, 1973.

Le Douaran, S., Burrus, J., Avedik, F., Deep Structure of the North-Western Mediterranean Basin: Results of a Two-Ship Survey, *Marine Geology, vol. 55*, pp. 325-345, 1984.

Lehmann, I., On Short Period Surface Wave L_g and Crustal Structures, *Bull. D'information L'UGGI* 2^e Aneé, pp. 248-251, 1952.

Lehmann, I., On L_g as read in North American Records, *Annali di Geofisica, vol. 10*, pp. 1-28, 1957

Love, A. E. H., *A Treatise on the Mathematical Theory of Elasticity*, 4th edn. Cambridge University Press, Cambridge, 643 pp.

Lysmer, J., Drake, L. A., The Propagation of Love Waves across Nonhorizontally Layered Structures, *Bull. Seismol. Soc. Am., vol. 61*, pp. 1233-1251, 1971.

Lysmer, J., Drake, L. A., A Finite Element Method for Seismology, Ch. 6 in *Methods in Computational Physics 11, Seismology,* Alder, B., Fernbach, S., Bolt, B. A., editors, Academic Press, 1972.

Makris, J., Ben Abraham, Z., Behle, A., Ginzburg, A., Giese, P., Steinmetz, L., Whitmarsh, R. B., Eleftheriou, S., Seismic Refraction Profiles Between Cyprus and Israel and Their Interpretation, *Geophys. J. R. Astr. Soc., vol. 75*, pp. 575-591, 1983.

Makris, J., Stobbe, C., Physical Properties and State of the Crust and Upper Mantle of the Eastern Mediterranean Sea Deduced from Geophysical Data, *Marine Geology, vol. 55*, pp. 347-363, 1984.

Mal, A. K., Herrera, I., Scattering of Love Waves by a Constriction in the Crust, *J. Geophys. Res., vol. 70*, pp. 5125-5133, 1965.

Martel, L., Love Wave Propagation Across a Step by Finite Elements and Spatial Filtering, *Geophys. J. R. Astr. Soc., vol. 61*, pp. 639-677, 1980.

Mantovani, E., Generation of Complete Theoretical Seismograms for SH-III, *Geophys. J. R. Astr. Soc., vol. 53*, pp. 55-60, 1978.

Mantovani, E., Schwab, F., Liao, H., Knopoff, L., Generation of Complete Theoretical Seismograms for SH-II, *Geophys. J. R. Astr. Soc., vol. 48*, pp. 531-535, 1977.

Nakanishi, K., Schwab, F., Knopoff, L., Generation of Complete Theoretical Seismograms for SH-I, *Geophys. J. R. Astr. Soc., vol. 48*, pp. 525-530, 1977.

Ni, J., Barazangi, M., High-Frequency Seismic Wave Propagation beneath the Indian Shield, Himalayan Arc, Tibetan Plateau, and Surrounding Regions: High Uppermost Mantle velocities and Efficient S_n Propagation Beneath Tibet, *Geophys. J. R. Astr. Soc., vol. 72*, pp. 663-689, 1983.

Nicolas, M., Massinon, B., Mechler, P., Bouchon, M., Attenuation of Regional Phases in Western Europe, *Bull. Seismol. Soc. Am., vol. 72*, pp. 2089-2106, 1982.

Nuttli, O. W., Seismic Wave Attenuation and Magnitude Relations for Eastern North America, *J. Geophys. Res., vol. 78*, pp. 876-885, 1973.

Nuttli, O. W., A Time Domain Study of the Attenuation of 10-Hz Waves in the New Madrid Seismic Zone, *Bull. Seismol. Soc. Am., vol. 68*, pp. 343-355, 1978.

Nuttli, O. W., The Excitation and Attenuation of Seismic Crustal Phases in Iran, *Bull. Seismol. Soc. Am., vol. 70*, pp. 469-485, 1980.

Nuttli, O. W., On the Attenuation of L_g Waves in Western and Central Asia and Their Use as a Discriminant between Earthquakes and Explosions, *Bull. Seismol. Soc. Am., vol. 71*, pp. 249-261, 1981.

Oliver, J., Dorman, J., Sutton, G., The Second Shear Mode of Continental Rayleigh Waves, *Bull. Seismol. Soc. Am., vol. 49*, pp. 379-389, 1959.

Oliver, J., Ewing, M., Press, F., Crustal Structure of the Arctic Regions from the L_g Phase, *Bull. Seismol. Soc. Am., vol. 66*, pp. 1063-1074, 1955.

Oliver, J., Ewing, M., Higher Modes of Continental Rayleigh Waves, *Bull. Seismol. Soc. Am., vol. 47*, pp. 187-204, 1957.

Oliver, J., Ewing, M., Normal Modes of Continental Surface Waves, *Bull. Seismol. Soc. Am., vol. 48*, pp. 33-49, 1958a.

Oliver, J., Ewing, M., The Effect of Surficial Sedimentary Layers on Continental Surface Waves, *Bull. Seismol. Soc. Am., vol. 48*, pp. 339-354, 1958b.

Panza, G. F., Calcagnile, G., Comparison of Multimode Surface Wave Response in Structures With and Without a Low Velocity Channel (Part I: Dip Slip Sources on a vertical Fault Plane), *Pure Appl. Geophys., vol. 112*, pp. 583-596, 1974.

Panza, G. F., Calcagnile, G., L_g, L_i and R_g from Rayleigh Modes, *Geophys. J. R. Astr. Soc., vol. 40*, pp. 475-487, 1975.

Panza, G. F., Schwab, F. A., Knopoff, L., Channel and Crustal Rayleigh Waves, *Geophys. J. R. Astr. Soc., vol. 30*, pp. 273-280, 1972.

Péč, K., Theoretical Dispersion Tables for Love Waves Propagating in a Wedge and in a Single Nonhomogeneous Layer with a Linear Velocity Gradient, *Pub. of Dominion Obs. Ottawa, vol. 35*, 1967.

Pomeroy, P. W., Best, W. J., McKevilly, T. V., Test Ban Treaty verification with Regional Data: A Review, *Bull. Seismol. Soc. Am., vol. 72*, pp. s89-s129, 1982.

Press, F., Velocity of L_g Waves in California, *Trans. A. G. U., vol. 37* , pp. 615-618, 1956.

Press, F., Ewing, M., Two Slow Surface Waves across North America, *Bull. Seismol. Soc. Am., vol. 42*, pp. 219-228, 1952.

Press, F., Ewing, M., Oliver, J., Crustal Structure and Surface-Wave Dispersion in Africa, *Bull. Seismol. Soc. Am., vol. 46*, pp. 97-103, 1956.

Press, F., Gutenburg, B., Channel P Waves Π_g in the Earth's Crust, *Trans. A. G. U., vol. 37*, pp. 754-756, 1956.

Ruzaikin, A. I., Nersesov, I. L., Khalturin, vol. I., Molnar, P., Propagation of L_g and Lateral Variations in Crustal Structure in Asia, *J. Geophys. Res., vol. 82*, pp. 307-316, 1977.

Sato, R., Love Waves Propagated across Transitional Zone, *Japan J. Geophys., vol. 2*, pp. 117-134, 1961a.

Sato, R., Love Waves in Case the Surface Layer is Variable in Thickness, *J. Phys. Earth., vol. 9*, pp. 19-36, 1961b.

Schlue, J. W., Love Wave Propagation in Three-Dimensional Structures Using Finite Element Techniques, *Bull. Seismol. Soc. Am., vol. 69*, pp. 319-328, 1979.

Savarensky, E., Valdner, N., Observations of L_g and R_g Waves from the Black Sea Basin Earthquakes, *Annali di Geofisica, vol. 13*, pp. 129-134, 1960.

Schwab, F., Kausel, E., Knopoff, L., Interpretation of S_a for a Shield Structure, *Geophys. J. R. Astr. Soc., vol. 36*, pp. 737-742, 1974.

Sheridan, R. E., Grow, J. A., Behrent, J. C., Bayer K. C., Seismic Refraction Study of the Continental Edges of the Eastern United States, *Tectonophysics, vol. 59*, pp. 1-26, 1979

Shurbet, D. H., The High Frequency P and S Phases from the West Indies, *Bull. Seismol. Soc. Am., vol. 52*, pp. 957-962, 1962.

Shurbet, D. H., The High Frequency S Phase and Structure of the Upper Mantle, *J. Geophys. Res., vol. 69*, pp. 2065-2070, 1964.

Shurbet, D. H., Conversion of S_n at a Continental Margin, *Bull. Seismol. Soc. Am., vol. 66,* 327-329, pp. 1976.

Singh, S., Herrmann, R. B., Regionalization of Crustal Coda Q in the Continental United States, *J. Geophys. Res., vol. 88*, pp. 527-538, 1983.

Smith, W. D., A Nonreflecting Plane Boundary for Wave Propagation Problems, *J. Comp. Phys., vol. 15*, pp. 492-503, 1974.

Stephens, J. L., Day, S. M., The Physical Basis of m_b:M_s and Variable Frequency Magnitude Methods for Earthquake/Explosion Discrimination, *J. Geophys. Res., vol. 90*, pp. 3009-3020, 1985.

Stephens, C., Isacks, B. L., Toward an Understanding of S_n: Normal Modes of Love Waves in an Oceanic Structure, *Bull. Seismol. Soc. Am., vol. 67*, pp. 69-78, 1977.

Street, R., Scaling Northeastern United States/Southeastern Canadian Earthquakes by Their L_g Waves, *Bull. Seismol. Soc. Am., vol. 66*, pp. 1525-1537, 1976.

Street, R., Some Recent L_g Phase Displacement Spectral Densities and Their Implications with Respect to the Prediction of Ground Motions in Eastern North America, *Bull. Seismol. Soc. Am., vol. 74*, pp. 757-762, 1984.

Street, R., Herrmann, R. B., Nuttli, O. W., Spectral Characteristics of the L_g Wave Generated by Central United States Earthquakes *Geophys. J. R. Astr. Soc.,*

vol. 41, pp. 51-63, 1975.

Street, R., Turcotte, F. T., A Study of Northeastern North American Spectral Moments, Magnitudes, and Intensities, *Bull. Seismol. Soc. Am., vol. 67*, pp. 599-614, 1977.

Sutton, G. H., Mitronovas, W., Pomeroy, P. W., Short-Period Seismic Energy Radiation Patterns from Underground Nuclear Explosions and Small Magnitude Earthquakes, *Bull. Seismol. Soc. Am., vol. 57*, pp. 249-267, 1967.

Uchupi, Austin, J. A., The Geologic History of the Passive Margin off New England and the Canadian Maritime Provinces, *Tectonophysics, vol. 59*, pp. 53-69, 1979.

Utsu, T., Observations of the L_g Waves and Crustal Structure in the Vicinity of Japan, ..., *vol.* .., pp. 499-508, ...

Wetmiller, R. J., Crustal Structure of Baffin Bay from Earthquake Generated L_g Phases, *Can. J. Earth Sci., vol. 11*, pp. 123-130, 1974.

Zienkiewicz, O. C., *The Finite Element Method in Engineering Science*, McGraw-Hill, 1971.

Zienkiewicz, O. C., Cheung, ., *The Finite Element Method in Structural and Continuum Mechanics*, McGraw-Hill, 1967.